Mixing Procedures for Lithium-Ion Electrode Slurries

– Understanding and Design Considerations –

Zur Erlangung des akademischen Grades eines
DOKTORS DER INGENIEURWISSENSCHAFTEN

von der KIT-Fakultät für Chemieingenieurwesen und Verfahrenstechnik des
Karlsruher Instituts für Technologie (KIT)
genehmigte

DISSERTATION

Von
Dipl.-Ing. Peter Haberzettl
aus Eberbach am Neckar

Tag der mündlichen Prüfung:	12. November 2025
Erstgutachter:	Prof. Dr. Norbert Willenbacher
Zweitgutachter:	Prof. Dr.-Ing. Wilhelm Schabel

Acknowledgments

The process of establishing a laboratory that also requires construction and research cannot be accomplished without the assistance and collaboration of numerous individuals with diverse expertise. My gratitude goes out to all those who have contributed to the creation of this work.

I would like to express my profound gratitude to Prof. Dr. Norbert Willenbacher, Head of the Applied Mechanics Group (AME) at the Institute of Mechanical Process Engineering and Mechanics (MVM) at KIT, for his invaluable guidance and support. His guidance throughout the doctoral program, and the well-balanced challenging encouragement he provided, had a significant positive impact on the outcome of this work. Furthermore, I would like to express my gratitude to Prof. Dr. Jens Tübke, a member of KIT's MVM, who acted as the second referee.

Moreover, I would like to express my gratitude to Dr. Martin Frey, Dr. Thomas Soczka-Guth and Mr. Franz Nietfeld for fostering an environment conducive to academic excellence and for providing a facility which enables this within the eCampus at Mercedes-Benz Untertürkheim.

I would also like to thank Dr. Dragoljub Vrankovic for his invaluable scientific experience and knowledge in the field of LICs, which has significantly contributed to the development of this work and enhanced my personal understanding of the subject matter. Furthermore, I would like to acknowledge Dr. Ingolf Bauer and Dr. Sören Thieme for their insightful discussions on cell data and its interpretation.

In addition, I would like to acknowledge the contributions of Dr. Aline Desjean, Dr. Kerem Aylar, and Mr. Nicholas Filipovic, as well as Mr. Mustafa Celik, Mr. Xu Han, Mr. Tobias Thaidigsmann, Ms. Kim Zi Tan, and Dr. Anja Paulus, whose input has had the most significant impact on the outcome of this work. I am indebted to you all for your invaluable assistance.

Finally, I would like to express my gratitude to my family and loved ones for their unwavering support and understanding during this challenging period.

Abstract

This study examines the production of lithium-ion electrode suspensions, with a particular emphasis on the intricate flow dynamics of slurries comprising of diverse material compositions and processing techniques. Experimental series were conducted on cathodic $LiFePO_4$ (LFP) and anodic materials, including graphite and SiO_x, utilizing current, industrially relevant materials and equipment. The flow behavior of slurries was demonstrated to be influenced by a number of factors, including their composition and the production method. The addition of dissolved polymers, macroscopic and microscopic particles, all contributed to an increase in viscosity. Furthermore, the processing techniques employed, in particular the choice of mixing sequence and energy input, were found to significantly affect the slurry's microstructure and flow properties.

On the cathodic side, the addition of conductive additives, namely carbon black (CB) and single-walled carbon nanotubes (SW-CNTs), resulted in the formation of strong colloidal interactions, which in turn led to a notable alteration in the flow behavior, to a greater extent than that observed with the LFP material. In the case of anodic slurries, carboxymethyl cellulose (CMC) proved to be a crucial factor in modifying viscosity through adsorption on the particle, which resulted in the emergence of complex flow behaviors, including shear thinning, Newtonian, and shear thickening. The degree of adsorption was observed to be contingent upon the energy input during mixing, which could be optimized by adjusting the solid content and machine parameters, like tool speed and sequence duration.

Furthermore, the study investigated the influence of mixing procedure sequencing on the mechanical and structural properties of positive electrodes. The dry mixing of CB, active material, and binder resulted in the production of a slurry with significantly reduced viscosity while maintaining a good peel strength. It was postulated, that this is due to the dispersity of the conductive additive that not just affected the flow behavior, but also the peel strength. This mixing method proved effective in minimizing the formation of carbon agglomerates, as confirmed by scanning electron microscopy (SEM) and energy-dispersive X-ray (EDX) mapping and required the least energy input. In addition, a procedure which pre-dispersed both conductive additives prior to mixing the active material resulted in a different state of dispersity, causing web-like structures around LFP particles, also displaying reduced viscosity of the slurry and pronounced mechanical properties of the resulting electrode. The electrochemical performance of the LFP cell specimens was evaluated, with a particular focus on their C-rate capability and cycle stability. A procedure in which the CB was dispersed first and the SW-CNTs last, resulted in slurries with the highest viscosity and electrodes with a low peel strength. Yet, they showed the highest C-rate performance and cyclability for approximately 2,000 cycles. Conversely, procedures that altered the dispersion sequence of the conductive additives or applied a dry mixing sequence of the conductive additive and active material resulted in slurries with reduced viscosity and a substantially higher peel strength of the electrode. However, the originating cells did not demonstrate equivalent performance, with the capacity to cycle for approximately 1,000 cycles.

This research highlights the necessity of optimizing processing methods to balance flow behavior, mechanical strength, and electrochemical performance. It underscores the pivotal role of mixing sequences and energy input in determining the quality of lithium-ion electrodes. In particular, dry mixing techniques and optimized conductive additive dispersion represent promising avenues for enhancing both the processability and performance of electrode slurries, particularly in roll-to-roll coating processes for large-scale battery production.

Kurzfassung

In dieser Arbeit wird die Herstellung von Lithium-Ionen-Elektrodensuspensionen untersucht, wobei der Schwerpunkt auf dem komplexen Fließverhalten von Slurries aus unterschiedlichen Verarbeitungstechniken und Materialzusammensetzungen liegt. Es wurden Versuchsreihen mit kathodischen $LiFePO_4$ (LFP) und anodischen Materialien, einschließlich Graphit und SiO_x unter Verwendung aktueller, industriell relevanter Materialien und Anlagen durchgeführt. Es wurde demonstriert, dass das Fließverhalten von Slurries von einer Reihe von Faktoren beeinflusst wird, einschließlich ihrer Zusammensetzung und der Herstellungsmethode. Die Zugabe von gelösten Polymeren, makroskopischen und mikroskopischen Partikeln trug zu einem Anstieg der Viskosität bei. Darüber hinaus wurde festgestellt, dass die angewandten Verarbeitungstechniken, insbesondere die Wahl der Mischsequenz und der Energieeintrag, die Mikrostruktur und die Fließeigenschaften der Slurries erheblich beeinflussen.

In kathodischen Formulierungen führte die Zugabe von Leitadditiven wie Leitruß (CB) und Single-Walled Carbon Nanotubes (SW-CNTs) zur Bildung starker kolloidaler Wechselwirkungen, was das Fließverhalten der Slurry stärker als das LFP beeinflusste. Im Fall der anodischen Slurry erwirkte die Adsorption von Carboxymethylcellulose (CMC) signifikante Veränderungen der Viskosität, was auch das Fließverhalten veränderte und zu einer komplexen Überlagerung von scherverdünnender, newtonscher und scherverdickender Charakteristiken führte. Es wurde festgestellt, dass der Grad der Adsorption vom Energieeintrag während des Mischens abhängt, der durch Anpassung des Feststoffgehalts und der Maschinenparameter wie Werkzeuggeschwindigkeit und Sequenzdauer beeinflusst werden kann.

Außerdem wurde der Einfluss der Mischreihenfolge auf die mechanischen und strukturellen Eigenschaften der positiven Elektroden untersucht. Das Trockenmischen von CB, Aktivmaterial und Bindemittel führte zur Herstellung einer Slurry mit deutlich verringerter Viskosität unter Beibehaltung einer guten mechanischen Stabilität. Es wurde vermutet, dass dies auf die Dispersität des Leitadditivs zurückzuführen ist, was nicht nur das Fließverhalten, sondern auch die Heftfestigkeit der Elektrode beeinflusst. Wie die Rasterelektronenmikroskopie (SEM) und die energiedispersive Röntgenanalyse (EDX) bestätigten, konnte mit dieser Mischmethode die Bildung von Kohlenstoffagglomeraten auf ein Minimum reduziert werden und der Energieeintrag geringgehalten werden. Darüber hinaus führte ein Verfahren, bei dem die beiden Leitadditive vor dem Mischen des Aktivmaterials dispergiert wurden, zu einer anderen Dispersität, welche sich durch netzartige Strukturen an dem LFP-Partikel auszeichnet, eine geringere Viskosität der Slurry bedingt und ausgeprägte mechanische Eigenschaften der resultierenden Elektrode aufweist.

Die elektrochemischen Charakteristiken der LFP-Zellen wurde mit besonderem Augenmerk auf ihre C-Rate-Fähigkeit und Zyklenstabilität bewertet. Ein Verfahren, bei dem das CB zuerst und die SW-CNTs zuletzt dispergiert wurden, führte zu Slurries mit der höchsten Viskosität und Elektroden mit einer geringen Schälfestigkeit. Dennoch zeigten sie die höchste C-Ratefähigkeit und Zyklierbarkeit für etwa 2.000 Zyklen. Umgekehrt führten Verfahren, bei denen die Dispergierreihenfolge der Leitadditive geändert oder eine trockene Mischreihenfolge von Leitadditiven und Aktivmaterial angewendet wurde, zu Slurries mit geringerer Viskosität und einer wesentlich höheren Haftfestigkeit der Elektrode. Diese Zellen wiesen jedoch keine gleichwertige Leistungsfähigkeit mit einer Zyklenstabilität von etwa 1.000 Zyklen auf.

Diese Arbeit unterstreicht die Notwendigkeit die Verarbeitungsmethoden zu optimieren, um ein Gleichgewicht zwischen Fließverhalten, mechanischer Stabilität und elektrochemischer Leistung herzustellen. Sie hebt die zentrale Rolle der Mischsequenzen und des Energieeintrags bei der Bestimmung der Qualität von Lithium-Ionen-Elektroden hervor. Insbesondere Trockenmischtechniken und eine optimierte Dispersion von leitfähigen Additiven sind vielversprechende Wege, um sowohl die

Verarbeitbarkeit als auch die Leistung von Elektrodenslurrys zu verbessern, vor allem bei Rolle-zu-Rolle-Beschichtungsprozessen für die großtechnische Batterieproduktion.

Abbreviations

AM	*Active material*
BET	Brunauer-Emmett-Teller
CA	*Conductive additive*
CADB	*Conductive additives dispersed in dissolved binder sequence*
CA_i	Variations of CA-Series
CB	*Carbon Black*
CBD	*Carbon-binder domain*
CC	*Constant current*
$CH_3COO–$	Carboxymethyl group
CMC	*Carboxymethyl cellulose*
CMC_{500}	CMC (M_w = 500 kDa)
CMC_{875}	CMC (M_w = 875 kDa)
CNT	Carbon nanotubes
CV	*Constant voltage*
D_i	*De Brouckere mean diameter*
DM	*Dry mixing sequence*
DMC	*Dimethyl carbonate*
DS	*Degrees of substitution*
e^-	Electron
EC	*Ethylene carbonate*
EV	*Electric vehicle*, electric vehicle
FCC	Full coin-cell
FEC	*Fluoroethylene carbonate*
Gr	*Graphite*
H_2	Hydrogen
HF	*Hydrofluoric acid*
HSCM	High solids content mixing
HSV	High shear viscosity
KS	*Kneading sequence*
KS_{ij}	Variations of Kneading-Series 1
LFP	*Lithium iron phosphate*
Li^+	*Lithium-ion*
LIC	*Lithium ion cell*
$LiCoO_2$	lithium cobalt oxide
LiOH	*Lithium hydroxid*
$LiPF_6$	*Lithium hexafluorophosphate*
LSL	Lower stability limit
LSV	Low shear viscosity
NMC	*Lithium nickel manganese cobalt oxide*
NMP	*N-methyl-2-pyrrolidone*
NV&V	*Non-volatile and volatile*
–OH	hydroxyl group
OPM	*One-pot method sequence*
P1 / P2	Variations of Preliminary-Series
PFA	*Perfluoroalkoxy alkanes*
P_i	Variations of Kneading-Series 2
P_{low}	Low energy input reference of Kneading-Series 2
Pro_i	Variations of Procedure-Series
PTFE	Polytetrafluoroethylene
PVDF	*Polyvinylidene fluoride*
Q_{tsg}	*Theoretical specific gravimetric capacity*
SBR	*Styrene-butadiene rubber*
SEI	*Solid electrolyte interface*
Si	*Silicon*
SiO_2	Silicon dioxide
SiO_x	*Silicon oxide*
SOC	State of charge
SPC	Small-format pouch cells
SPC_{20}	Small-format pouch cells (20 cm²)
SPC_{46}	Small-format pouch cells (46 cm²)
SSA	Specific surface area
SW-CNT	Single-walled carbon nanotubes
TSC_i	Variations of TSC-Series
USL	Upper stability limit
VC	*Vinylene carbonate*
VCM	Visco-Capillary Model
x_i	TSC within HSCM of Kneading-Series 2

Latin Symbols

G^*	Dynamic gap [-]
U_i.	Voltage of a cell [V]
Ca_R	Capillary number after Ruschak [-]
A_{CAM}	Cell’s cathodic surface area [cm²]
A_h	Hamaker constant [J]
A_O	Surface of an object [m²]
BC	Blue channel [-]
c	Concentration [g L^{-1}]
Ca	Capillary number [-]
CE	Coulombic efficiency
d	particle distance [nm]
e	Electron charge [C]
E	Energy consumption [Wh]
E_{eff}	Effective energy input [Wh L^{-1}]
E_{idle}	Idle energy consumption [Wh L^{-1}]
E_{sp}	Specific energy input [Wh L^{-1}]
$\vec{F}$	Force [N]
F_{peel}	Peel strength [N m^{-1}]
F_{total}	Measured force [N]
G_S	Slot-die gap [µm]
GC	Green channel [-]
H_c	Hight of the coating [Ω cm^2]
H_{cc}	Hight of the current collector [Ω cm^2]
H_E	Total thickness [µm]
I	Electric current [A]
I_{SIR}	Discharging / charging current [A]
k	Number of ion species [-]
$m_{Component}$	Component's non-volatile mass [g]
m_{liquid}	Liquid's mass [g]
m_{solid}	Solid's mass [g]
n_0^k	Number density [mol]
NV	Non-volatile [wt%]
P_{el}	Power consumption [W]
Q_s	Double layer overlap [µF cm^{-2}]
r	Particle radius [nm]
R_{cell}	Electronic resistivity of a cell [Ω cm²]
RC	Red channel [-]
RCFA	Residue occupied foil area [%]
SC	Solids content [wt%]
t_{disp}	CADB sequence duration [min]
t_{dm}	Dry mixing sequence duration [min]
t_k	Kneadin sequence duration [min]
t_{seq}	Sequence duration [min]
TSA	Total surface area [m² g^{-1}]
TSC	Total solids content [wt%]
U_L	Line speed [m s^{-1}]
V	Volume [m³]
V_{liquid}	Liquid's volume [L]
V_{seq}	Sequence’s occupied volume [L]
V_{solid}	Solid's volume [L]
W	Wet film [µm]
W_{sample}	Width of the sample [m]
YC	Brightness channel [-]
z^k	Valency of the ion [-]

Greek Symbols

g_i	Gravimetric loading [mg cm^{-2}]
M_w	Molar weight [g mol^{-1}]
$V_{component}$	Solid component's volume [L]
γ	Deformation [-]
$\dot{\gamma}$	Shear rate [s^{-1}]
ε_r	Dielectric constant [-]
η	Dynamic viscosity [Pa·s]
η_0	Zero shear viscosity [Pa·s]
η_R	Relative viscosity [-]
η_S	Solvent viscosity [Pa·s]
η_{SP}	Specific viscosity [-]
κ^{-1}	Debye length [nm]
ρ_C	Volume resistivity [Ω cm]
ρ_{CN}	Specific contact resistance [Ω cm^2]
ρ_I	Interface resistance [Ω cm^2]
ϱ_i	Electrode density [g cm^{-3}]
ρ_M	Electrical resistivity [Ω cm^2]
σ	Tensile stress [Pa]
σ_{ij}	Tensile stress [Pa]

τ	Shear stress (x-y plane) [Pa]
τ_0	Yield stress [Pa]
τ_{ij}	Shear stress [Pa]
Φ	Solid volume fraction [-]
Φ_i	Individual volume fraction [L]
Ψ	Interaction potential [mV]
Ψ_{DLVO}	DLVO interaction potential [mV]
Ψ_S	Particle's surface potential [mV]
Ψ_{vdW}	London van der Waals force [N]
ω_{pan}	circumferential speed pan [m s^{-1}]
ω_{tool}	Circumferential speed dispersion tool [m s^{-1}]
ω_w	Tool speed of dry mixing sequence [m s^{-1}]
ω_{wdisp}	Tool speed of CADB Sequence [m s^{-1}]
ω_{wk}	Tool speed of dry kneadin sequence [m s^{-1}]

Content

1 Introduction

It is impossible to deny the importance of consumer electronics in our everyday lives. These can include items such as mobile phones and cameras, as well as medical devices such as implantable pacemakers or attached insulin pumps, just to mention a few examples. The operation of these devices is contingent upon the availability of electrical energy, which is stored and provided by rechargeable batteries. As the development of such devices progresses, their size often decreases and their performance increases as well. This has resulted in the demand for the development of new, more adequate battery cells, which are often smaller and possess greater electric capacity. This iterative process gives rise to new materials that are capable of fulfilling these functions.

Lithium-ion cells (LICs) are widely used due to their lightweight nature, offering high energy densities and a versatile range of operational conditions, which has driven the development of electric vehicles (EVs) [1]. This field of application necessitates the development of a novel scale of LIC production capabilities, unprecedented in its scope. This is particularly the case given that numerous nations are trying to meet EV quotas on both public and private sectors, thereby further accelerating the pace of cell development [2]. It is evident that this initiative is driven by a desire to mitigate global warming and curtail the consumption of fossil fuels [3, 4].

However, the creation of a product that demonstrates excellent performance requires the development of new or adjusted manufacturing procedures for the utilization of novel materials. This is particularly crucial when developing cells from novel material compositions, as the requisite Quality Gates are rigorously defined and the demonstration of the new composition must be conducted in a representative manner. As the production chain of LICs comprises numerous steps, the propagation of errors can have significant adverse consequences in terms of safety and key performance indicators. This is particularly the case in the initial production phase, namely the creation of the suspension, or slurry, which is employed in the coating and drying process to manufacture electrodes. The particle distributions created here serve as the foundation for the subsequent electrode's microstructure, which in turn determines the cell's electrochemical characteristics [5].

This work is dedicated to the topic of mixing electrode suspensions, which are used for the creation of lithium-ion electrodes, with the goal of developing a deeper understanding of the correlations between the mixing procedure and the subsequent intermediate and final products.

2 State-of-the-art

This chapter sets forth the theoretical background that is necessary for the interpretation of this work. Firstly, the fundamental principles of rheology are presented, with a particular focus on their application to the analysis of complex fluids. Secondly, the colloidal aspects of suspensions are elucidated. Thirdly, the engineering principles and functions of lithium-ion cells are described, with an emphasis on the inactive, active, conductive and binding components of modern cells. In a fourth segment, the production chain of modern lithium-ion cell electrodes is presented, with a particular focus on the mixing and processing of electrode suspensions.

2.1. Rheology and colloids

Rheology is the scientific discipline concerned with the behavior of fluids and other viscous substances when they are in a state of flow. By measuring parameters such as deformation and force, it is possible to characterize a medium, thereby enabling interpretations of its structure.

In everyday life, food products such as emulsions (e.g. mayonnaise) or other products (e.g. sorbet, yoghurt, milkshakes) are received and individually judged by consumers in terms of not only taste but also structure. The latter is frequently characterized by its viscosity, which refers to the resistance of a fluid to deformation. This seemingly intuitive analysis does not necessarily reflect the fact that the structure is the result of a complex superposition of numerous interactions, involving solids, liquids or even gases or microscopic particles, as well as dissolved polymers with diverse characteristics.

This section aims to provide an overview of the rheological and colloidal interactions that are pertinent to this work, in a concise manner. For a more detailed explanation of the topics covered in this section on rheology, please refer to the following sources: [6–8]. For further insight into the subject of colloids and polymers, please refer to the following sources: [9, 10] and [11–13] respectively.

2.1.1. Rheological principles

Within the scope of this work the term rheology refers to rotational rheology, hence viscosity refers to the dynamic viscosity of a medium or suspension.

The application of a force $\vec{F}$ to the surface of an object A_O results in the generation of stress σ, to be seen in (1). If the stress is along an axis, it is referred to as tensile stress σ_{ij}. If the stress is tangential to the surface, it is designated as shear stress τ_{ij}. This can be further simplified under the following assumptions: the fluid is incompressible and Newtonian (i.e. $\tau \sim \dot{\gamma}$); with constant density; applied pressures do not cause deformation; Z-axis influences are neutral; and opposing stresses in the plane are equal in magnitude.

$$\sigma = \frac{\|\vec{F}\|}{A_O} = \begin{bmatrix} \sigma_{xx} & \tau_{xy} & \tau_{xz} \\ \tau_{yx} & \sigma_{yy} & \tau_{yz} \\ \tau_{zx} & \tau_{zy} & \sigma_{zz} \end{bmatrix} = \begin{bmatrix} \sigma_{xx} & \tau & 0 \\ \tau & \sigma_{yy} & 0 \\ 0 & 0 & \sigma_{zz} \end{bmatrix} \quad (1)$$

Thus, from a rotational rheometric point of view, the stress tensor is defined by the normal stresses (N_1, N_2), the shear stress in the x-y plane τ, shown in the following two equations.

$$N_1 = \sigma_{xx} - \sigma_{yy} \quad (2)$$

$$N_2 = \sigma_{yy} - \sigma_{zz} \quad (3)$$

In a plane, the deformation γ of a volume V is equivalent to the offset dx in the direction of flow over its height dy, as illustrated in the two-plate model in Figure 2-1. The deformation derived according to time results in the velocity gradient $\dot{\gamma}$ of this deformation, which is also referred to as the shear rate (4).

$$\dot{\gamma} = \frac{d}{dt}\frac{dx}{dy} = \frac{d\gamma}{dt} \qquad (4)$$

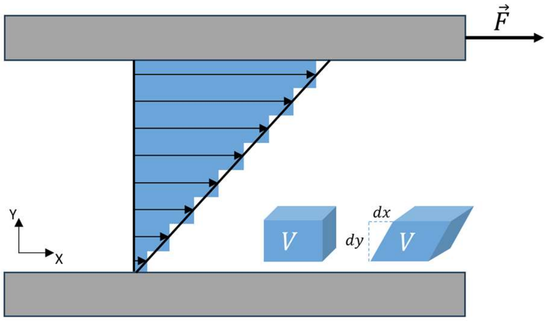

Figure 2-1: Two-plate model

The relationship between shear rate and shear stress is described by the viscosity η of the fluid. This is defined as the quotient of shear stress and shear rate (5).

$$\eta = \frac{\tau}{\dot{\gamma}} \qquad (5)$$

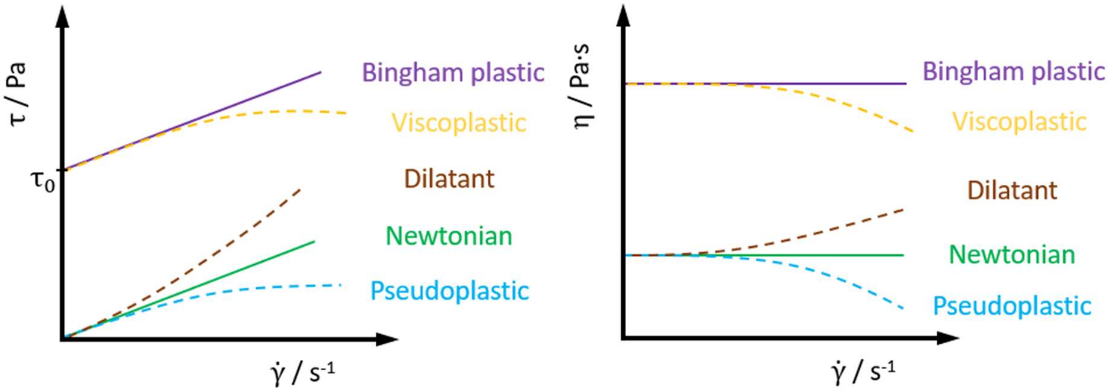

a) b)

Figure 2-2: Categorization of different fluids and plastics in dependence of shear rate; a) shear stress function; b) viscosity function

The aforementioned Newtonian fluid has a distinct shear stress function, which is proportional to the shear rate, to be seen in Figure 2-2a. This implies that the viscosity is independent of the shear rate, as illustrated in Figure 2-2b. However, the viscosity response of a fluid that experiences a shear rate is a complex superposition of several interactions. In certain instances, the viscosity of a fluid may diminish as the shear rate rises. This phenomenon is known as shear thinning, which is observed in pseudoplastic fluids. In contrast, other fluids exhibit an inverse behavior, displaying shear thickening or dilatant characteristics. It is a fallacy to assume that all fluids are, in fact, fluids from the outset. A notable illustration of this phenomenon can be observed in the case of ketchup, which initially remains in a static state within a bottle but begins to flow once a force exceeding the yield stress τ_0 is applied. Furthermore, the shear thinning behaviour indicates that this is a viscoplastic fluid. A fluid that lacks the shear thinning attribute is referred to as a Bingham plastic.

2.1.2. Colloidal principles of dispersions and suspensions

A dispersion is defined as a mixture of solid particles and a solvent. It is regarded as a disperse system, which is defined as a two- or multi-phase system comprising insoluble or immiscible components. In everyday life, one may encounter numerous examples of these systems in different forms, for this work, the dispersion is of relevance. All dispersions comprise a solid, liquid, or gas phase, which is designated the dispersed phase. The dispersed phase is constituted by particles that are dispersed in a solid, liquid, or gas phase, which is known as the continuous phase. For this work, the dispersed phase consists of solids dispersed in a solvent.

Dispersions are not thermodynamically stable, resulting in a tendency for the phases to separate over time. The following section will provide a more detailed examination of suspensions. A suspension, defined as a mixture of homogeneously dispersed solids in a solvent, will, over time, undergo a process of aggregation and sedimentation of the continuous phase's solid particles. In addition to the aforementioned characterization of their phases, there are a number of other defining characteristics of a suspension. To illustrate, the continuous phase is characterized by specific density, viscosity and polarity, whereas the dispersed phase is defined by particle size, particle shape, particle surface properties, e.g. charge, adsorbed surfactant of polymer, and density. A suspension may be described in simple terms by the solid volume fraction Φ, which is the ratio of the solid's volume V_{solid} to the sum of the solid's volume and the liquid's volume V_{liquid}. When increasing the quantity of solids, the individual volume fraction Φ_i is calculated as the ratio of the solid component's volume $V_{component}$ to the volume sum of the solid components and the liquid.

$$\Phi = \frac{V_{solid}}{V_{solid} + V_{liquid}}; \Phi_i = \frac{V_{component}}{\sum V_{component} + V_{liquid}} \tag{6}$$

In the context of the slurries presented in this work, the total solids content (TSC) is defined as the ratio of the solid's mass m_{solid} to the sum of the solid's mass and the liquid's mass m_{liquid}. This is a frequently employed parameter in the relevant literature.

$$TSC = \frac{m_{solid}}{m_{solid} + m_{liquid}} \tag{7}$$

Furthermore, the solids content (SC) can be described in two distinct ways: as the ratio of the non-volatile (NV)) components or as the ratio of the non-volatile and volatile (NV&V) components. Consequently, SC_{NV} is defined as the ratio of a mass of non-volatile components $m_{Component}$ divided by the sum of the non-volatile components' mass. Subsequently, the mass ratio of a non-volatile and volatile component's mass is divided by the sum of the components' mass and the mass of the liquid, resulting in $SC_{NV\&V}$.

$$SC_{NV} = \frac{m_{Component}}{\sum m_{Component}} \tag{8}$$

$$SC_{NV\&V} = \frac{m_{Component}}{\sum m_{Component} + m_{liquid}} \tag{9}$$

In the context of engineering, it is crucial to comprehend the utilization limits of a suspension, including its flow and stability behavior. This entails an understanding of the suspension's response when subjected to external forces. In this study, the particle size and solid volume fraction are of particular importance. However, there are additional correlations that must be considered, including dissipative interactions and the viscosity of the fluid, as well as the particle's specific surface area and particle-fluid compositions (e.g., salt, pH, etc.).

2.1.3. Effects related to particle size

The force between particles that are capable of forming a dipole is the van der Waals force, named after the Dutch physicist Johannes D. van der Waals. It is a non-covalent force that is always present in aqueous colloidal suspensions and is considered an attractive interparticle force or interaction potential Ψ, which causes the aggregation of colloidal particles. The attractive (London) van der Waals force Ψ_{vdW} can be calculated . In the case of two identical spherical particles of radius r and particle surface separation d, which are significantly smaller than the radius, the simplified equation is as follows: A_h is the so-called Hamaker constant.

$$\Psi_{vdW}(d) = \frac{A_h\, r}{12\, d} \tag{10}$$

In suspensions, however, these attractive forces may be counterbalanced by electrostatic or steric forces that are repellent. An example of the latter would be that caused by adsorbed polymers. Consequently, two identical particles with the same surface charge will experience a repulsive force. This force arises when particles are surrounded by a polar solvent in the presence of ions, thereby creating a double layer of charges surrounding them. The Poisson-Boltzmann equation describes the electric potential around the charged surface, assuming a Boltzmann statistics for the distribution of counter and co-ions around a single charged particle, utilizing the dielectric constant ε_r, the permittivity of free space ε_0, the number density n_0^k, the valency of the ion z^k, the number of ion species k and the electron charge e.

$$\varepsilon_r \varepsilon_0 \nabla^2 \Psi \;=\; -e \sum_k z^k n_0^k \left(exp\left({}^{-ez^k\Psi}\!/_{kT} \right) \right) \tag{11}$$

The derivation of the Debye-Hückel approximation, a function of the distance from the spheric particle's surface, is achieved through the linearization of equation (11) This approximation is based on the particle's surface potential Ψ_S.

$$\Psi(d) = \Psi_S \frac{r}{d} \exp\bigl(-\kappa((d-r)\bigr) \tag{12}$$

The Debye length κ^{-1}, also referred to as the Debye radius, represents the range of electrostatic repulsion. Its value can be determined through the application of the following equation, in which n_i denotes the ion concentration.

$$\kappa = \sqrt{\frac{e^2 \sum_i z_i^2 n_i}{\varepsilon_r \varepsilon_0 kT}} \tag{13}$$

This permits for the expression of the electrostatic interaction potential of the double layer overlap, as follows, in which Q_s represents the surface charge of the particle:

$$\Psi_{el}(d) = \frac{Q_s^2}{4\pi\varepsilon_r\varepsilon_0 d} \frac{exp(2r\kappa)}{1 + r\kappa} exp(-d\kappa) \tag{14}$$

The superposition of the attractive van der Waals force (10) and the repulsive electrostatic force (14) is described within the DLVO theory, which provides a quantitative explanation for the aggregation and stability of a colloidal suspension.

$$\Psi_{DLVO} = \Psi_{vdW}(d) + \Psi_{el}(d) \tag{15}$$

Figure 2-3 illustrates the DLVO theory. It shows, that that two colloid-scaled particles exert a repulsive force on one another due to the preponderance of electrostatic repulsion at distances $d \gg 0$. However, upon approaching one another, e.g. trough mixing, the particles overcome an energy barrier, resulting in the ascendance of an attractive force. This phenomenon culminates in the aggregation of the colloids.

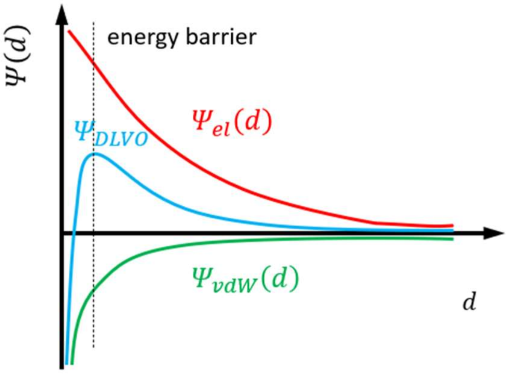

Figure 2-3: Exemplary interaction potentials described by the DLVO theory

2.1.4. Basics of dissolved polymers

Polymers are chain-like molecules. The smallest repeating segment of a polymer is called a monomer. The size of a polymer is described by the molar weight (M_w). In everyday life, polymers are encountered in the form of solid materials, such as plastic bags and containers. Synthetic polymers are not the only category of polymers; natural polymers, such as polysaccharides, also exist. When dissolved in a solvent, the flow behavior is affected by changing the viscosity, which for example enables the binding of a sauce when preparing a meal. Upon drying or cooling, polymers assume a rigid form, exemplified by the binding of a dried sauce on a plate after a meal or glue that has dried after application. This illustrates that polymers exhibit diverse structural characteristics contingent upon solubility in a solvent, the latter of which is pertinent to this investigation.

At the molecular level, a polymer exhibits a three-dimensional structure. Upon dissolution in a solvent, the structure undergoes alterations due to the influence of physical interactions with the solvent, temperature, and ions and the polymer occupies a larger volume. This results in a volume fraction of a solvent becoming immobilized within a solvent shell, as illustrated in Figure 2-4. This ultimately affects the solution's flow behavior.

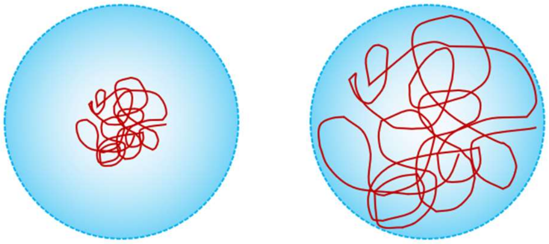

Figure 2-4: Schematic of a poorly dissolved polymer (left) and dissolved polymer (right)

Moreover, polymers may interact with one another or with particles. The following section, 2.1.5, provides a more detailed account of the concentration-related effects and correlations of polymers.

2.1.5. Effects related to concentration

It would appear reasonable to posit that the introduction of powder-sized solids to a liquid will result in an increase in the viscosity of the formed suspension. This phenomenon is not exclusive to hard particles; it also occurs with polymers.

2.1.5.1. Particle concentration

In the context of suspensions, the term relative viscosity η_R is frequently employed, representing the ratio of the suspension's viscosity and that of its continuous phase, described by the widely-known Stokes-Einstein equation (16). This provides an estimation of the viscosity relative to the solvent viscosity η_S, designated as η_R, as a function of the solid's volume fraction. However, due to the linear nature of this equation, its accuracy is limited to very small values of Φ, as will be demonstrated in the following paragraph.

$$\eta_R = \frac{\eta}{\eta_S} = 1 + 2.5\Phi \tag{16}$$

As the volume fraction of solids is increased, the average separation distance between particles will decrease. This is reflected in the relative viscosity η_R [9]. In the case of hard spheric particles with dominant attractive forces, this may results in the formation of three distinct rheological segments [14]. The initial segment is characterized by minimal shear rate. The second segment is characterized by a moderate shear rate, while the third is distinguished by a high shear rate. Figure 2-5a provides an illustrative representation of the three segments. Within segment *I*, the shear rates are low, hence the viscosity is often referred to as low shear viscosity (LSV) and an increase in Φ results in an increase in η_R. This even allows the formation of microstructures that are sufficiently robust to resist any plastic deformation, including flow, under the influence of gravity or shear stress, which is typical for suspensions with dominant attractive forces. In this instance, it is not possible to ascertain the viscosity, by definition. It is only when the critical yield stress is exceeded that the microstructure collapses, thereby allowing flow to be determined. In segment *II*, the microstructure undergoes collapse as hydrodynamic forces exert dominant influence on the microstructure's stress with increasing shear rate, leading to a shear thinning behavior. The value of η_R is higher than that of the solvent, yet not as high as in segment *I*. Figure 2-5b illustrates the relationship between $\eta_R$and Φ at the same shear rate as that observed in segment II. For moderate values of Φ, the value of η_R in segment *III* should remain constant in comparison to that of segment II. However, for high values of Φ, colloidal suspensions may experience an increase in viscosity, resulting in a shear thickening behaviour. This is due to the formation of an additional structure, the hydrodynamic cluster [15]. One hypothesis posits that at exceedingly high shear rates, particles are propelled in close proximity, whereupon lubrication hydrodynamic forces exert influence upon the colloidal system, thereby precipitating the formation of these hydroclusters [16].

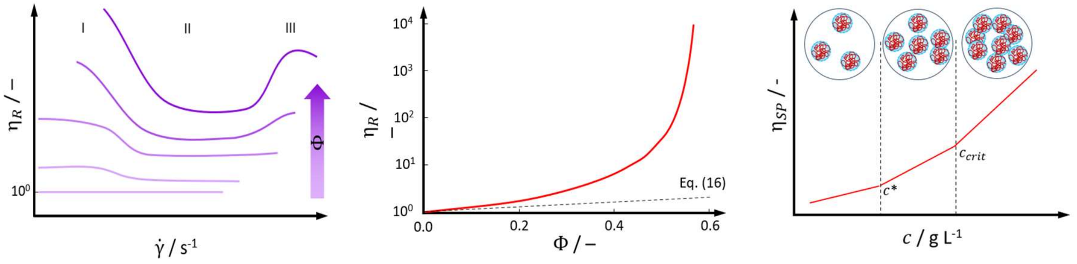

a) b) c)

Figure 2-5: a) exemplary relative viscosity as a function of shear rate on a double-logarithmic scale for hard sphere suspensions with increasing solid volume fraction, recreated after Laun et al [14]; b) exemplary correlation between volume fraction and relative viscosity recreated after Russel et al [17]; c) exemplary η_{SP}-c relation of polymer solutions on a double-logarithmic scale, displaying three distinct polymer regimes, dilute (left), semi-dilute unentangled (center) and semi-dilute entangled (right)

It should be noted that in the shear rates in segment *III* are significantly higher, hence the viscosity is often referred to as high shear viscosity (HSV).

2.1.5.2. Polymer concentration

The concentration of a polymer solution exerts a significant influence on both pure polymer systems and colloidal systems.

The viscosity of a solution is increased by the presence of a dissolved polymer, which causes an increase in the immobilized solvent within the polymer's solvent shell [18]. As the concentration c of the solution increases, the specific viscosity η_{SP} of the solution also increases. This refers to the solvent-specific relative change in viscosity, which in this study is defined as the zero shear viscosity η_0, which is the viscosity value of the viscosity plateau at very low shear rates of a suspension or polymer solution [13].

$$\eta_{sp} = \frac{\eta_0 - \eta_s}{\eta_S} = \frac{\eta_0}{\eta_S} - 1 \tag{17}$$

In general, the relationship between η_{SP} and c can be divided into distinct polymer regimes. In the present study, this refers to the dilute and semi-dilute regimes. They describe the interaction between the polymers. The dilute regime is a system of dissolved polymers that do not interact with each other and are predominantly influenced by hydrodynamic interactions. In the semi-dilute regime, polymers may interact with each other. This regime is divided into two sub-regimes: semi-dilute unentangled and semi-dilute entangled. The critical concentration separates these two sub-regimes. In this context, the polymers may entangle or are already entangled due to the high concentration and an appropriate high molar weight. The resulting viscosity is higher than that observed in the dilute system. The shear thinning behavior is more pronounced. The relationship between specific viscosity and concentration (η_{SP}-c) follows a polymer-specific power-law within the aforementioned regimes, as illustrated in Figure 2-5c. [19]

2.1.5.3. Adsorption

In the presence of suitable conditions, polymers are capable of adsorbing onto solid surfaces, including particles. In the initial stages, a polymer must come into contact with the solid surface, for example, through Brownian motion or flow. It may occur as a result of hydrogen bonding between the polymer and the surface. [12]

The adsorption of polymers onto colloidal systems, such as slurries [20], can give rise to a number of effects, which can be grouped into three categories that affect the stability of the system. The interaction between polymers and particles can result in bridging flocculation, whereby multi-particle-polymer aggregates are bonded by the polymer, thereby accelerating the process of sedimentation. Particles undergo steric stabilization, when polymer shells overlap and the osmotic pressure pushes the particles apart. The range of repulsion is more pronounced in cases where the molecular weight (M_w) is greater and the solubility in the surrounding liquid is higher. In the presence of non-adsorbed polymers, depletion flocculation may occur. This phenomenon occurs when the osmotic pressure of the dissolved polymer is greater than the repulsion of the overlapping double layer, causing the particles to aggregate. [10]

2.2. Rechargeable Lithium-ion cells

Battery cells can be classified into two principal categories: primary and secondary. In contrast to secondary cells, which are rechargeable, primary cells lack this property. A number of books have been published on the subject of battery cells, providing comprehensive overviews of the topic, e.g. [21–24]. This section will focus on secondary lithium-ion cells with applications in electric vehicles (EVs), as well as the cell components that fall within the scope of this topic.

2.2.1. Principles and function

A lithium-ion cell represents a specific type of electrochemical energy storage device, wherein lithium-ions (Li^+) are employed as a positive charge. The cell is composed of two electrodes: a negative electrode, designated the "anode," and a positive electrode, referred to as the "cathode." The two electrodes are encased in an electrolyte solution comprising a salt dissolved in an organic solvent, which facilitates the transfer of lithium-ions. The electrodes are separated from one another by a separator, which is a membrane that permits the electrolyte to pass through it while preventing electrical contact between the electrodes. A schematic representation of a cell is provided in Figure 2-6.

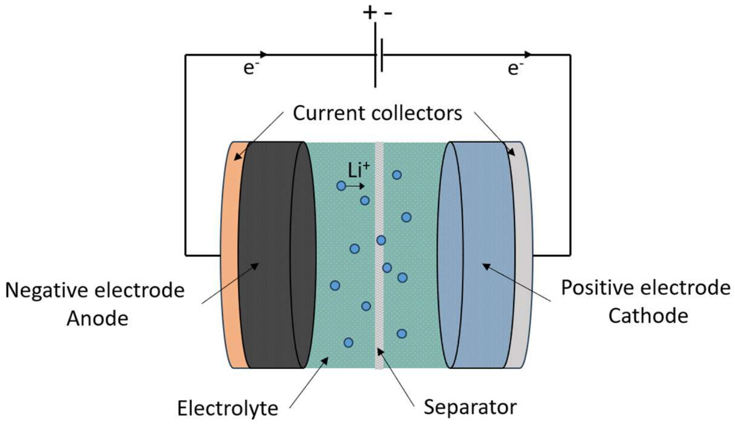

Figure 2-6: Schematic drawing of a LIC

When the current collectors of a charged LIC are connected via an external circuit, redox reactions occur at the electrodes. The negative electrode undergoes oxidation, whereby Li^+ are transported into the electrolyte solution and electrons (e^-) are released. Consequently, the cathode undergoes lithiation by reduction of lithium, whereby the electrolyte's Li^+ and e^- are received, as provided by the external circuit. The reactions occurring at the electrodes, as well as the overall reaction of the cell, are described by the following redox equations (18 to 25). In this instance, graphite (C_6) was employed as the anodic active material (AAM), while lithium cobalt oxide ($LiCoO_2$) constituted the cathodic active material (CAM).

neg. $$Li_xC_6 \rightleftharpoons xLi^+ + xe^- + C_6 \qquad (18)$$

pos. $$xLi^+ + xe^- + Li_{1-x}CoO_2 \rightleftharpoons LiCoO_2 \qquad (19)$$

total $$LiCoO_2 + C_6 \rightleftharpoons Li_{1-x}CoO_2 + Li_xC_6 \qquad (20)$$

The stored energy of a LIC is defined by the quantity of free Li+, which is primarily introduced into the cell by the CAM and to a lesser extent as a component of the electrolyte salt. During the process of cycling from charge to discharge and vice versa, the cell's components undergo a change in redox potential. For example, a $LiCoO_2/C_6$ cell will undergo a change from [25] e.g. 3.0 to 4.2 V. This process gives rise to a number of parasitic reactions, which ultimately result in the formation of passivating layers, most commonly referred to as solid electrolyte interfaces (SEI). This results in the consumption of Li^+ and electrolyte components, which consequently reduces the capacity of the LIC. The accompanying gas formation also affects the wetting of the electrodes' active surface. Nevertheless, despite the deleterious effects, an intact SEI serves to safeguard the cell from the progressive formation of SEI, thereby stabilizing the cell electrochemically and chemically. It is therefore essential that every newly constructed cell undergoes a formation process, which allows the formation of the aforementioned layers to occur under controlled conditions.

2.2.2. Inactive materials in LICs

As previously outlined, a LIC is a complex entity comprising a multitude of components, each of which exerts a profound influence on the cell and its functional capabilities. Subsequently, the LIC's inactive materials are briefly outlined to facilitate a rapid yet comprehensive grasp of their nature and functionality.

It should be noted that conductive additives and binders are also classified as inactive materials. However, they are of significant importance in this work and therefore addressed in individual subsections 2.2.4 and 2.2.5.

2.2.2.1. Cell casing

The cell is encased in a casing that serves the function of sealing the interior from the exterior. This is of particular importance in preventing the ingress of water, whether in the form of atmospheric moisture or liquid. The reactivity of water with the LIC's components is such that it can potentially cause the exothermic creation of lithium hydroxide (LiOH), flammable gaseous hydrogen (H_2) and the formation of harmful hydrofluoric acid (HF). These reactions have the potential to result in catastrophic events such as a thermal runaway. In addition to the electrode's metallic current collector, the case has the greatest impact on thermal conductivity, which is a significant driving force behind the advancement of modern fast-charge cell technology. This is due to the fact that these cells require cooling and heating in order to maintain optimal performance. Furthermore, the case provides stability and resistance against mechanical deformation. [26–28]

For larger LICs, there are three principal types of casing: a cylindrical metallic can, a rectangular metallic can, and a pouch bag comprising a combination of plastic and metallic compounds. In the case of smaller LICs, coin cells are widely used in a variety of everyday applications [29]. They are also an excellent format for rapid material characterization in research and development contexts [22]. The casing types under consideration in this study are coin cells and pouch cells.

2.2.2.2. Electrolyte

The liquid phase and the dissolved salts enable the movement of Li^+ between the positive and negative electrodes. Lithium hexafluorophosphate ($LiPF_6$), is one of the most commonly utilized electrolytes, which is dissolved in a mixture of organic solvents, for example, ethylene carbonate (EC) and dimethyl carbonate (DMC) [30, 31]. The specific composition of the electrolyte and the addition of additives, such as vinylene carbonate (VC) and fluoroethylene carbonate (FEC), are of great consequence in achieving optimal cell performance [32]. The advancement of active material (AM) development represents a significant driving force in the development of new electrolytes and the evolution of safety expectations.

2.2.2.3. Separator

It is imperative that the separator physically separates the electrodes from one another, with a porous structure that enables the migration of lithium-ions between the electrodes [33]. However, the material must also be chemically inert and non-conductive [34]. In addition, the material must be mechanically resistant to deformation during lithiation of the electrodes. The most commonly used separators are made of polyethylene or polypropylene, or are ceramic-coated compounds. A challenge in the development of these materials is to reduce their thickness, which affects the stack size of a cell and therefore the energy density [35].

2.2.2.4. Current collector

The metallic foil of the electrode serves the function of a current collector, a role which is also referred to as that of a substrate. The choice of metallic element utilized in this context is contingent upon the particular coated electrodes under consideration. Copper is typically used for the negative electrode and aluminum for the positive electrode, all in accordance with the galvanic potential of the AM [36]. In the case of LICs employed in high-performance applications such as electric vehicles, the current collector is confronted with a delicate trade-off in terms of its thickness. A thick foil is beneficial for achieving good thermal and electrical conductivity, yet a thin foil is necessary to reduce weight and volume, both of which affect the energy density of the cell [37]. It should also be noted that the current collector foil, in addition to the electrode coating, provides mechanical stability to the latter cell and also contributes to the cell's electric resistance [38].

2.2.3. Active materials in LICs

AMs represent a fundamental element of the LIC. They serve to store the electrochemical energy and to define the behavior of the cell in terms of charge and discharge. The distinctive configuration of these AMs permits reversible intercalation or the reversible formation of alloys. The following figure illustrates the three most common AM structures in EVs, which are summarized in this section.

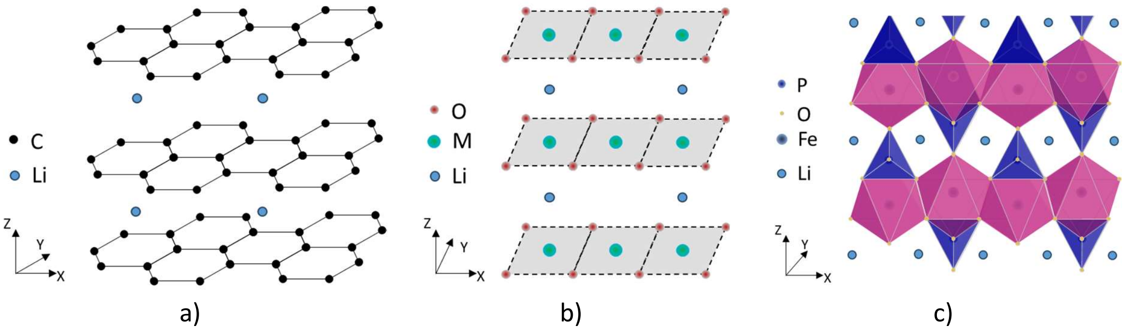

Figure 2-7: Schematic drawing of; a) lithiated graphite; b) lithiated Li_xMO_2; c) lithiated LFP; recreated after [22, 39, 40]

2.2.3.1. Anode

With regard to the anode, the most advanced material is graphite (C_6; Gr), which is either naturally occurring or produced through a synthetic process [41]. Graphite is a structured carbon, as illustrated in Figure 2-7a, and is composed of multiple graphene layers [42], which are accompanied by excellent electrical conductivity [43]. Due to its layered structure, the through-plane resistivity is approximately 20 to 300 mΩ cm, which is higher than the in-plane resistivity, which is ca. 0.6 to 2 mΩ cm [44]. The intercalation of Li+ between these basal layers, which is the figure's X-Y plane, results in a theoretical specific gravimetric capacity (Q_{tsg}) of 372 mAh g^{-1}. Due to intercalation, the distance between the layers increases, resulting in a volume change of approximately 10 % [45]. This results in an AM demonstrating excellent, long-lasting, cycling efficiency.

Significant efforts are being made to implement silicon (Si) as an AM due to its potential for enhanced energy density. Nevertheless, silicon and silicon-containing materials continue to encounter obstacles in attaining stable, enduring, and cyclable performance [46]. The lithiation of silicon occurs through the formation of a silicon-lithium alloy, which subsequently causes a change in volume [47]. The stoichiometry of the alloy may permit the attainment of exceedingly high Q_{tsg} values. A fully lithiated silicon ($Li_{22}Si_5$) could potentially attain a Q_{tsg} of 4.200 mAh g^{-1} [48], however, this state of lithiation is not achievable under normal ambient temperature conditions. In the context of typical operational conditions, a Q_{tsg} of 3.579 mAh g^{-1} ($Li_{15}Si_4$) can be achieved, which is accompanied by a volume change of approximately 280 % [49]. It should be noted that alloys containing less Li and Si are also possible. In comparison to graphite, pure silicon exhibits a Q_{tsg} that is approximately 10 times higher and a 28 times higher change in volume. The rationale behind the use of silicon as an AM is clear. The substitution of silicon for graphite in the negative electrode results in a notable reduction in electrode weight and height, thereby facilitating the incorporation of additional electrode layers and consequently enhancing the energy density of the battery.

Nevertheless, the utilization of Si encounters difficulties in maintaining satisfactory and efficient cyclability, with the charge and discharge potential exhibiting hysteresis due to sluggish kinetics [50]. Moreover, the considerable volume alteration gives rise to particle fracturing, which in turn gives rise to the continuous formation of the SEI [51] and the electrical isolation of electrode segments [52]. In order to address these issues, a number of concepts are currently developed [53]. (i) The development of nano-structured silicon attempts to accommodate the volume changes due to its specific surface area [51, 54]. (ii) Core-shell composites adopt a strategy of embedding the "problematic" Si in materials with superior cyclability, such as carbon, in order to mitigate the formation of cracks and the development of the SEI [55, 56]. (iii) SiO_x particles, which comprise a mixture of Si, SiO_2 and metastable silicon oxides, offer the potential for significantly less volume expansion than pure Si, at a cost of less Q_{tsg} than that of pure Si and reduced electrical conductivity [57]. The effective Q_{tsg} is situated between that of silicon dioxide (SiO_2) (1.600 mAh g^{-1}) and Si [58]. (iv) The combination of silicon materials with graphite, which is sometimes referred to as a blend of AMs, is anticipated to offset the advantages and disadvantages associated with each material [59].

2.2.3.2. Cathode

One of the earliest commercially available CAMs was $LiCoO_2$; however, its use in BEVs is limited by its high cost, which is a consequence of its high stochiometric content of cobalt [60]. More cost-effective alternatives include lithium nickel manganese cobalt oxide (NMC), which offers a higher energy density and balance between performance, safety, and cost, and lithium iron phosphate (LFP), which exhibits excellent thermal stability, cycle life, and safety [53]. In terms of electrical resistivity, it is noteworthy that CAMs exhibit poor electrical conductivity. For instance, $LiCoO_2$ has a resistivity of approximately 1 kΩ cm [61].

NMC is a layered metal oxide compound that intercalates lithium-ions on a two-dimensional plane (X-Y). Figure 2-7b illustrates the typical crystal structure of a lithium metal oxide (Li_xMO_2), exemplified by NMC or $LiCoO_2$. There are numerous varieties in regard to its stoichiometry, the most prominent of which is NMC−111 (Q_{tsg} = 280 mAh g^{-1}) [53]. However, new cost-driven developments have introduced higher nickel contents, such as NMC-622 and NMC-811. The current challenges are the thermal stability and cycling performance [62]. The electrical resistivity is dependent upon the stoichiometry and the state of lithiation, with values ranging from approximately 455 kΩ cm (NMC−111) to 244 Ω cm (NMC-811) [63].

LFP is a lithium transition metal phosphate with a porous olivine structure, as illustrated in Figure 2-7c. In this structure, Li-ion diffuse in a one-dimensional plane, aligned with the z-axis. First introduced in 1997 [40], it has been the subject of numerous research studies and is a commercially well-established AM in EVs. Upon complete lithiation, the material exhibits a specific capacity of Q_{tsg} = 170 mAh g^{-1}. Given that the electrical resistivity of the AM particles is relatively high, at approximately 1 GΩ cm [64], the AM-particles are carbon coated in order to mitigate this issue. A recent publication by a cell manufacturer [65] details a new LFP-based cell that is capable of 4C charging, which is equivalent to a 15-minute charging time. The aforementioned cell will be employed in the context of electric vehicles. This illustrates that, despite the considerable research and development that has been undertaken over the past 27 years, there is still scope for enhancement in this field.

2.2.4. Conductive additives

The objective of utilizing conductive additives is to enhance the electrical conductivity throughout an electrode, thereby increasing the conductivity of AMs towards the current collector [66]. The additives in question are, for the most part, nanomaterials, including particulate amorphous carbons (so-called "carbon black," or CB), carbon nanotubes or fibers, graphene, and micro-scaled graphite [67]. For a more exhaustive overview of these additives, see Baumgärtner et al [68]. The objective of these conductive additives (CAs) is to establish a conductive network that percolates through the electrode and its components, thereby establishing a connection with the external circuit. As the majority of the electrode is the AM, the conductive additives and the binders share the same inter-(active)particle domain. This is why some authors refer to this as the carbon-binder domain (CBD) [69–71]. In this context is it widely differentiated between short, medium and long-range conductive networks in the context of CAs.

2.2.4.1. Carbon black

Due to its low cost and high availability, CB is a popular choice for the purpose of increasing the electric conductivity of an electrode. One of CB's most notable characteristics is its substantial Brunauer-Emmett-Teller (BET) specific surface area (SSA), which exerts a profound influence on the electrode in a multitude of ways. The large SSA provides a multitude of contact points with the AM, thereby enhancing the electrical conductivity. A greater BET surface area results in a lower percolation limit, indicating that a smaller quantity of CB is required to maintain a percolating carbon-binder domain [72]. Moreover, an increased SSA results in a greater range of pore sizes within the electrode. Moreover, a reduction in the particle size of CB is linked to an improvement in conductivity, both electrical and ionic [73].

The particulate nano-scaled particles are agglomerated by default and must be deagglomerated in order to facilitate their uniform distribution throughout a slurry and, subsequently, the latter electrode [74]. The smallest dimensions range from 10 to 100 nm, while the agglomerates can be in the micrometer range. Nevertheless, it is possible that a very finely dispersed CB may not be the optimal choice, as it could potentially lead to a reduction in electrode porosity and an increase in electrode stiffness [75].

2.2.4.2. High aspect ratio nano structures

In recent years, there has been a significant increase in interest in fibrous and tube-like nanostructures. A defining characteristic is the high aspect ratio and a higher specific surface area (SSA) than that observed for CB. The particles have a diameter of approximately a few nanometers, while their length is on the order of micrometers [76]. Given that CB tends to form short-to-medium range conductive networks, fibrous conductive particles offer the potential for the formation of a long-ranging conductive network [77]. Among the fibrous CAs, carbon nano fibers (BET 10 – 200 $m^2\ g^{-1}$) are the least expensive, although their cost is higher than that of CB. Multi-walled carbon nanotubes (CNT) (BET 100 – 10.000 $m^2\ g^{-1}$) are more costly than other fibrous conductive particles due to their tube-like morphology and the complexity of their manufacturing process. Single-walled carbon nanotubes (SW-CNTs ; BET 300 – 10.000 $m^2\ g^{-1}$) are the most expensive of the fibrous conductive particles, due to their advanced technological capabilities. The financial implications of these materials can be a significant obstacle when developing new electrode compositions, despite the relatively low concentration of fibrous or tubular carbon additives, which is typically less than 1 wt% of the electrode's mass.

2.2.5. Binders

Binders are polymers that have a wide range of applications in LICs. They provide mechanical stability of electrode coatings against both the cyclic swelling of the electrode and externally applied mechanical stress on the cell, which ultimately improves the cycle life of a cell. From an analytical perspective, this stability can be divided into two distinct categories: adhesive properties that emerge from the particle-binder-substrate interface and cohesive properties that result from the particle-binder-particle interface [78]. As a dissolved polymer in the slurry, it determines the flow behavior of the suspension, which is crucial for processing. Its impact on viscosity also enhances the slurry's stability, which is vital for processing. Moreover, the binder can facilitate the dispersion of material agglomerates during the slurry preparation process, contingent on the binder's adsorption properties. However, binders are inactive materials, which is why they only constitute a minor component of the electrode composition. Furthermore, binders display poor electrical and ionic conductivity, which would have a detrimental impact on the cell's performance [79, 80].

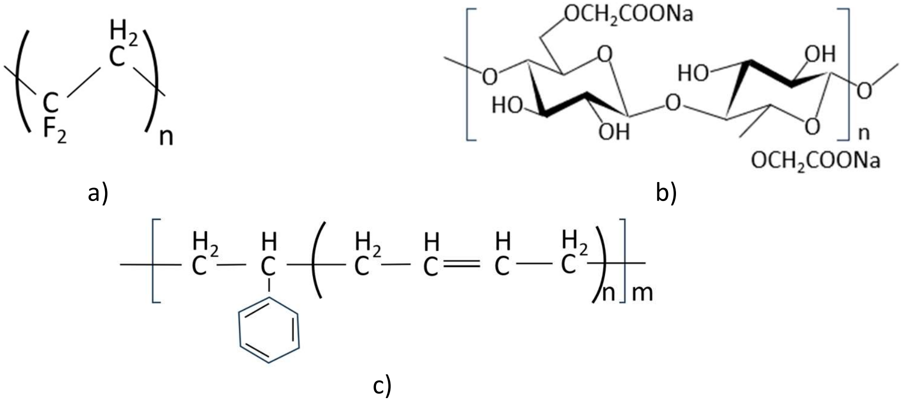

Figure 2-8: chemical structure of a) polyvinylidene fluoride; b) sodium carboxymethyl cellulose; c) styrene-butadiene rubber; recreated after [81, 82]

The two main solvents used in LICs, water and NMP (N-methyl-2-pyrrolidone), give rise to three binders that represent the economic majority within the LIC industry. The NMP-soluble polyvinylidene fluoride (PVDF), the water-soluble sodium carboxymethyl cellulose (CMC) and the finely dispersed styrene-butadiene rubber (SBR), which is insoluble in water, yet employed in aqueous processing due to its binding properties.

2.2.5.1. Polyvinylidene fluoride

Polyvinylidene fluoride (PVDF) is a thermoplastic fluoropolymer. Its structure is illustrated in Figure 2-8a. It is a linear type synthetic semi-crystalline homopolymer. It is renowned for its non-reactivity, as well as its thermal and electrochemical stability [81]. In the majority of LIC applications, the non-reactivity of PVDF also precludes its use as a dispersing agent. It has an impact on the flow behavior of the slurry and the mechanical stability of the electrodes in terms of adhesion and cohesion [83].

In conventional LIC processing, it is employed for both the cathode and anode electrodes. It is soluble in organic solvents, including NMP. While the solubility is advantageous in preventing contamination by water, particularly in cathodic electrode processing [84], PVDF presents certain environmental challenges. In January 2023, the European Chemical Agency proposed a ban on Perfluoroalkoxy alkanes (PFA) [85] due to their deleterious impact on the environment. These compounds do not decay and therefore accumulate. The production of PVDF is derived from PFA monomer, which would consequently be affected by the implementation of a ban. The toxicity of NMP serves to underscore the ecological concerns, thereby reinforcing the necessity for either the development of water-stable CAM or an alternative binder/solvent combination in cathodic electrode processing [86]

2.2.5.2. Carboxymethyl cellulose

The sodium salt of carboxymethyl cellulose is a common form of CMC. Its chemical structure is illustrated in Figure 2-8b. It is a linear derivative of cellulose and is available in a range of degrees of substitution (DS), which refers to the replacement of hydroxyl groups (–OH) by carboxymethyl groups (CH_3COO–) [87]. The maximum degree of substitution is three. In the presence of water, the carboxymethyl groups are dissociated, forming anionic groups that establish the solubility in water [88]. Moreover, CMC contains hydrophobic portions that permit its adsorption on hydrophobic surfaces, such as graphite or carbon. Meanwhile, the remaining carboxylate group forms a stabilizing layer around the particle-polymer complex. This creates a steric stabilization, acting as a dispersant [89, 90]. The molar weight of the CMC exerts a significant influence on both the slurry and the coating.

Specifically, an elevated Mw results in increased slurry viscosity, pronounced shear thinning, augmented adsorption, and a more brittle and rigid coating compared to one with a lower M_w. Furthermore, an increase in DS has been shown to increase the tendency for adsorption [91].

Despite its efficacy in maintaining electrode and cell cohesion, CMC exhibits minimal elastic properties and is brittle and rigid [92]. This is why recent developments for Si-containing electrodes are challenging the utility of CMC due to the high volume change during cycling. Potential alternatives include polyacrylic acid [93]. Nevertheless, the reactivity of CMC towards other surfaces offers the possibility of adapting it to new AMs, for example, by modifying the CMC's bonding mechanisms [94].

2.2.5.3. Styrene-butadiene rubber

Styrene-butadiene rubber is a synthetic rubber and is considered an elastomeric polymer, its structure is shown in Figure 2-8c. It is derived from the polymerization of styrene, the aromatic compound, and butadiene. Variations in, for example, styrene or butadiene content, polymerization process or cross-linking result in a wide range of product variations. LICs use the emulsified form, i.e. stabilized colloidal SBR particles [95].

Used in combination with CMC, colloidally dispersed SBR is an important additive for LIC processing as it increases the mechanical strength in both cohesion and adhesion of the electrode [96, 97], introducing a soft and deformable component alongside the brittle CMC. It has been documented that upon curing, the material exhibits elongations in excess of 100 % and tensile moduli in excess of 1 MPa [98]. Additionally, a glass transition has been observed at approximately -40 °C. Due to its particulate nature, it has little or no effect on the flow behavior of the slurries [99].

2.3. Production of liquid coated LIC electrodes

The electrode represents the point of convergence for the aforementioned components, and the process steps involved in this production chain are illustrated in Figure 2-9. Initially, the active and inactive components are combined with a solvent to create an electrode suspension, or slurry. This process is frequently designated as a mixing procedure. Subsequently, the slurry is coated onto a current collector and dried. In certain instances, these stages are delineated as two discrete processes. However, on an industrial scale, the entire process is conducted on a single machine in a roll-to-roll configuration, with coating and drying occurring concurrently. Subsequently, the electrode is compressed using a machine that resembles a pasta machine, which is referred to as a calender. The machine comprises two rollers that run in opposite directions, creating a gap through which the electrodes are compressed at a continuous line speed. Subsequently, the compressed electrode coils are subjected to a further drying process under vacuum prior to utilization in the cell assembly process. Depending on the scale of the production chain, the demand for coated electrodes can be so high that a single line coated electrode foil is insufficient, necessitating the addition of further lines and the implementation of a slitting process after the calendering. This involves the separation of a coil into numerous smaller coils. [100]

Figure 2-9: Illustration of a common electrode process chain

This process chain is typically conducted in a dry room atmosphere, as the presence of water can have detrimental effects on the components involved. At the component level, this primarily affects the CAM through redox and cation exchange reactions, as well as the participation of some binders [101]. A CAM's surface free lithium may undergo a reaction with gaseous atmospheric water to form lithium hydroxide, which in turn creates hydrogen (21) Lithium hydroxide then reacts with carbon dioxide to form lithium bicarbonate (22),which in turn facilitates the creation of lithium carbonate and water (23). The aforementioned reactions are facilitated by the outward lithiation and inward protonation, and continue until equilibrium is reached. This ultimately reduces the AMs capacity, resulting in the formation of passivating rock salt phases [102]. The assembly of a cell contaminated with water can result in the occurrence of additional parasitic and potentially dangerous reactions [102].

$$Li^+ + H_2O \rightarrow H^+ + LiOH \tag{21}$$

$$LiOH + CO_2 \rightarrow LiHCO_3 \tag{22}$$

$$LiOH + LiHCO_3 \rightarrow H_2O + Li_2CO_3 \tag{23}$$

The mixing of NMP-based slurries can result in two distinct effects due to the presence of water contamination, which is contingent upon the quantity of water present. The presence of water in trace amounts may result in the formation of an alkaline environment, which in turn can facilitate the defluorination and cross-linking of PVDF, ultimately leading to the gelation of the slurry [103]. Furthermore, the presence of an abundant water content has the effect of reducing the solubility of PVDF, resulting in its precipitation and flocculation into an undissolved state.

Given the evident issues associated with water contamination and the high costs of drying intermediate products, research is often conducted into the development of water-based CAMs and binders [104, 105] and the all-dry processing of electrodes [106, 107]. Furthermore, the environmental aspects of NMP-based processing are frequently the subject of investigation. One popular method for creating an electrode film through solvent-free means is to introduce a network by polymer fibrillation of PTFE (polytetrafluoroethylene) [108, 109]. Although promising, the process development is difficult and the machines needed require a lot of investment, which in terms requires materials that are demonstrating a high maturity level, which is why this research is mainly limited to the industry [110].

From a developmental standpoint, an electrode suspension is a complex composition of numerous components, representing the initial intermediate product in the product chain of a LIC. The requisite relationship between the coating application and product specifications is a delicate one. From a design perspective, the material composition is the result of a considered approach that takes both economic and technical requirements into account. These may include, for example, the energy density or charge behavior of the latter cells. Conversely, these design considerations are subject to continual challenge as the production process matures at different levels. A pragmatic approach is to initially develop compositions at the laboratory scale in order to precisely adjust the mass ratios. At the workshop or pilot line scale, the processing is then demonstrated and any necessary adjustments to the composition are made prior to utilization on a production line, which may involve further adjustments to the composition. However, laboratory equipment is highly versatile and adaptable, whereas industrial-level machinery is not. It is therefore essential to gain a comprehensive understanding of the slurry as an intermediate product, which is subject to a multitude of applications, in order to facilitate the precise development of the composition.

2.3.1. Composition of a slurry

A slurry is a suspension that primarily comprises the AM and a solvent. The proportion of the latter, however, is contingent upon the desired flow behavior. A significant proportion of technical compositions exhibit a rough non-volatile content, or solids content (SC), of 90 to 95 wt% AM, with the solvent content accounting for approximately 35 ± 18 wt%. The remaining portion is then divided between conductive additives and binders. Figure 2-10 depicts an illustrative slurry composition, showcasing the mass ratios. In certain applications, dispersants [111, 112] of surfactants [113] are employed to enhance processability throughout the product chain, however they hold no relevancy in this work.

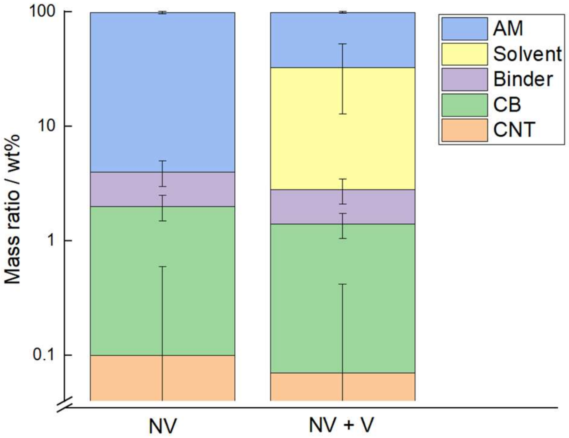

Figure 2-10: Exemplary composition of a generic electrode slurry, non-volatile composition (left), volatile and non-volatile composition (right)

Typically, graphite-based slurries exhibit a total solids content (TSC) of approximately 50 to 60 wt%, whereas cathodes with, for instance, NMC exhibit a considerably higher TSC, with values reported to be as high as 70 to 80 wt%. These significant discrepancies can be attributed primarily to the variations in AM density, which influences the packing density. However, additional factors such as SSA, the interaction between particles and binders and the solvent also contribute to the final TSC value, as discussed in section 2.1.2.

The slurry is employed in the coating process. A flowable slurry is required for a number of reasons. In order to prevent coating defects caused by air bubbles and to maintain a homogeneous mass loading, a slurry must be degassed. Furthermore, the slurry has to flow in and out of pumps. Given the inherent delicacy of the coating process, which is dependent upon the viscosity of the slurry, the η_R-Φ correlation imposes a limit on the maximum TSC, thereby influencing the design choices with respect to the mass ratio.

In addition to the requirements of the intended application, the final product, the cell, ultimately determines the composition. The mechanical stability and electric and ionic resistivities are pivotal in identifying the composition of any electrode, which is a consequence of the conductive additives and binder employed.

2.3.2. Mixing and dispersion of slurries

The slurry is a complex fluid, comprising a multitude of components. The objective of the mixing procedure is to combine the aforementioned components in a manner that is consistent with the desired outcome. This requirement may present particular challenges. With regard to dispersion or deagglomeration, the solid fraction particles are inherently diverse. Some AMs display particle sizes with a mean diameter D_i exceeding 30 µm, while others are in the nanoscale range, a phenomenon that is particularly prevalent among conductive additives. Moreover, some components may display a monomodal, bimodal, or polymodal particle size distribution. In a wet mixing procedure, dispersion is achieved primarily through three comminution mechanisms, as outlined in reference [114].

1. Collision of aggregates against each other or a surface
2. Shear of aggregates against each other or a surface
3. Electrostatic or steric repulsion of the aggregate particles that may be induced by the solvent, a dispersant or a polymer

As previously discussed in subsection 2.2.4, the carbon-binder domain must be facilitated, with the percolation correlating to the aggregate size. Achieving this in a mixing procedure can be quite challenging when approximately 90 wt% of the solids is AM, which should be fully dispersed. Additionally, CB should have the "right" aggregate size, as a too small size can cause the electrode to become brittle.

Binders can act as dispersants (subsection 2.2.5), but this function depends on their dissolution. The requisite time for this process may be considerable, contingent on the solubility of the solvent in question. Moreover, the binders may be susceptible to shear-induced mechanical degradation.

2.3.3. Sequencing of a mixing procedure in literature and motivation

Despite the absence of a consistent terminology in the existing literature, a common structure can be identified in the description of mixing procedures. In order to avoid confusion, this work defines the structure as follows:

> The slurry is created through a mixing procedure, which is comprised of a series of sequences. A sequence is defined by two key elements: material parameters and process parameters. Material parameters indicate the specific materials and quantities being treated in that sequence, while process parameters encompass the sequence duration, the speed of the tool and the mixtures temperature.

The number of sequences in a procedure may vary, which can complicate the design of the procedure. Firstly, the sequencing of the procedures is based on the constraints imposed by the utilized mixer, such as the minimum degree of filling. Secondly, the procedure is subject to limitations in tool speed, which may be attributed to the component's delicate nature or the limitations of the mixing machine itself. This ultimately restricts the range of potential operating options.

A relatively straightforward approach to mixing would be to combine all the slurry's components within a single sequence, which could be described as a ‘one-pot method’ (OPM). An alternative approach would be to disperse each component in a designated sequence, whereby one component is dispersed in the first sequence, another is added and dispersed in a subsequent sequence, and so on. A number of academic publications have compared slurries and electrodes produced by different mixing procedures. The distinguishing factor between these studies is the addition, removal, or alteration of specific sequences. In the context of the present study, three sequences merit particular attention.

1. The preliminary dry mixing (DM) of the components' powders is employed with the objective of expeditiously deagglomerating conductive and active materials within a single sequence.
2. Subsequently, a dedicated dispersion of conductive additives within a dissolved binder that is employed as a continuous phase (CADB) is prepared, followed by the incorporation of active materials and additional components.
3. The dispersion of the AM within a so-called kneading sequence (KS) is a common subsequent sequence following a CADB sequence. This process entails the creation of a mixture with minimal solvent content, resulting in the dispersion of a viscous or non-flowable plastic mass.

The following table, Table 2-1, provides an overview of some literature on the effect of mixing sequences. The publications are categorized according to the mixing sequences utilized within a given procedure, the machines employed, and the active material and solvent used, followed by a simplified summery of the key findings relevant for this work. It should be noted that the KS sequence in the tables does not always refer to the kneading character of a non-flowable mass. Rather, it refers to the dispersion of AM and CB under conditions of high enough solvent content, which results in a flowable mass.

It is evident that there is a substantial body of literature that addresses the topic of mixing procedures in this field of study, which has been in existence for over three decades and concerns the creation of slurry in a laboratory setting and beyond. Nevertheless, comparisons are frequently made between procedures that exhibit significant differences in their design. For example, one might undertake a comparison between different mixers or contrast sophisticated procedures with simple and crude ones. In essence, alterations to the microstructure were instigated, which inevitably influence the mechanical, electronic and electrochemical characteristics of the resulting electrodes. Given the scientific nature of the subject matter, it is to be expected that significant contrasts are being displayed in order to investigate a phenomenon. However, the specific characteristics of mixing procedures, such as the variation of tool speeds and component concentrations, are particularly relevant in the context of industrial applications. Consequently, the impact of such changes on technical compositions is often the subject of debate and remains unresolved. It is important to note that the investigation of the impact of procedures is a time-consuming endeavor, given the number of variables that must be considered. This is due to the fact that the analysis of mixing procedures can only be conducted by modifying a single parameter at a time. Moreover, the aforementioned variations have an impact on the entirety of the powder-to-cell product chain, which must remain constant in order to obtain quantitative results. Furthermore, the extensive range of globally available electrode components, which are subject to their own inherent limitations, may require the performance of a multitude of tests.

Table 2-1: Selected overview of publications that are addressing the effects of different mixing procedures

Author, AM, solvent	**–** **○**	**Sequences / procedure variations** **Equipment**	**Simplified key finding / conclusion**
Bauer et al. [115], NMC, NMP	– – ○ ○	DM & subsequent wet mixing KS & subsequent wet mixing DM in high shear powder mixer Slurry dispersion via dispersion disc	Intensive dry mixing facilitated the coating of CB on the AM's particles, thereby lowering viscosities in slurries and lower resistivities in electrodes. In contrast, liquid processing did not achieve this level of dispersion. The lower resistivity had a positive effect on cell performance.
Park et al. [116], Graphite, Water	– – – ○	CADB & subsequent KS / wet mixing KS of AM and Binder subsequent wet mixing OPM & subsequent wet mixing Ultra-turrax; Anchor type stirrer	The sequencing of a procedure significantly affected the adsorption of CMC on both, CB and Graphite, leading to different dispersibility and flow behavior. Enabling a selectivity of CMC- adsorption between the two carbon materials.
Li et al. [90], LFP, Water	– – ○	OPM with preliminary SBR addition OPM with a subsequent SBR addition Slurry dispersion via ball milling	It is essential to design the utilization moment within a mixing procedure, taking into account the varying interaction and adsorption priorities of the binder. This design choice has been demonstrated to exert an influence on the microstructure of the slurry and the subsequent cell performance.
Liu et al. [117], NMC, NMP	– – ○ ○	DM of CB & subsequent wet mixing CADB via diverse sequences & subsequent KS Slurry dispersion via ball milling Slurry dispersion in a custom-built mixer using several dispersion tools	Similar flow behaviors were created by both dry mixing sequences and all liquid processing, indicating that rheological results are not exclusive to one mixing machine or procedure.
Nakajima et al. [118], LiCoO₂, NMP	– – ○ ○	DM & subsequent wet mixing at different energy input levels OPM & subsequent wet mixing DM in a ball mill Slurry dispersion via magnetic mixer	Utilized dry mixing procedures of moderate energy input displayed most performant cycling behavior and ideal resistivities, which was reasoned by microstructural differences regarding the dispersion state of CB.
Kim et al. [119], LiCoO₂, NMP	– – – ○	DM & subsequent wet mixing CADB & subsequent KS / wet mixing KS of AM and Binder subsequent wet mixing OPM & subsequent wet mixing Machinery not disclosed	The employment of a dry mixing sequence of AM and CB, in conjunction with a pre-dissolved binder, has been demonstrated to yield optimal results at the cell level.
Wang et al. [120], NMC, NMP	– – ○	DM & subsequent KS / wet mixing CADB & subsequent KS / wet mixing Slurry dispersion via planetary mixer	In the course of the comparison, slurries with gel-like properties were created by the CADB procedure, in contrast to the DM procedure, which demonstrated superior peel strength, but inferior ionic and electronic conductivity. The CADB procedure exhibited superior c-rate capabilities, emphasizing the significance of ionic conductivity as a result of the mixing procedure.
Tang et al. [121], NMC, NMP	– ○	CADB and alternations in sequence TSC, tool speed and duration Planetary centrifugal mixer	As the energy input in mixing procedures is increased, there is a concomitant decrease in slurry viscosity. Tool speed variations demonstrated the greatest effect on this behavior.
Takeno et al. [122], LiCoO₂, NMP	– – ○	DM & subsequent KS / wet mixing CADB & subsequent KS / wet mixing Planetary mixer	The utilization of a dry mixing sequence yielded superior electronic resistances and impacted the viscoelastic behavior of the slurry.
Kuratani et al. [123], LiCoO₂, NMP	– – – ○	OPM KS of AM and Binder subsequent wet mixing KS of AM and Binder subsequent wet mixing at higher shear rate Planetary centrifugal mixer	An increase in mixing intensity affects the CA dispersion, leading to electrode microstructures with a dispersion state of highly aggregated CA at low energy input and vice versa finely dispersed at high energy input. The results indicate that an optimal state of dispersion is achieved at moderate energy input.
Huber et al. [124], Graphite, Water	– – – ○ ○	CADB & subsequent KS / wet mixing KS of AM and Binder subsequent wet mixing CADB & subsequent KS / wet mixing with different degrees of CADB premix transfer in the subsequent sequences at varying TSC Planetary mixer Slurry dispersion via dispersion disc	It was demonstrated that an elevated sequence TSC resulted in enhanced energy input, leading to diminished slurry viscosity and a less homogeneous pore structure. This led to an augmentation in the electrode's tortuosity, thereby facilitating lithium plating.
Konda eta al. [125], LFP, NMP	– – ○ ○	CADB & subsequent KS / wet mixing DM & subsequent KS / wet mixing Slurry dispersion via dispersion disc DM of CB and AM in a ball mill	The utilization of a DM sequence resulted in a superior electrode, as evidenced by its enhanced c-rate performance, resistivity, peel strength, and particle size distribution. Furthermore, its slurry viscosity was found to be significantly reduced.

3 Hypothesis, goals, and limitations of this work

The objective of this dissertation is to gain insight into the topic of mixing electrode suspensions and the procedure's impact on the slurry, which represents an intermediate product in a production chain. In order to achieve this, commercially available electrode materials are employed and subjected to mixing machinery that is intended for industrial use. This approach allows for the derivation of conclusions applicable to process development and for optimized LIC production, which can be applied to the same mixing machinery.

As has been demonstrated in numerous publications, significant alterations to the mixing procedure have a profound impact on the resulting slurry's microstructure, which in turn affects subsequent cell performance. In the present work, the overarching hypothesis is that minor procedure variations, such as tool speed, sequence duration and the TSC of a sequence, have a considerable effect on both the product itself and the production chain. This is particularly relevant for industrial equipment, given that their capabilities are constrained.

In order to remain consistent with the prevailing trends in component development, the anodic compositions employ a combination of graphite and SiO_x as anodic active material. Conversely, the cathodic compositions utilize single-walled carbon nanotubes as a conductive additive and LFP as a cathodic active material. The following list outlines the structure of the result-bearing chapters in this work, which address different topics:

Chapter 5	The interaction of the active material (LFP) and conductive additives (CB and SW-CNT) is investigated through the application of a unimodal and bimodal content variation of the latter. This is followed by an investigation of mixing procedure's sequence variations of a selected composition.
Chapter 6	The influence of process parameters, specifically tool speed and sequence duration, on the resulting slurry of graphite and SiO_x, dispersed with a high molar weight binder are examined. Two distinct mixing procedures were designed, and the parameters were varied in order to ascertain the impact of these variables on flow behavior and cell performance.
Chapter 7	The impact of the total solids content and energy input is being investigated by varying the sequence's water content. This variation was applied to two anodic compositions: one comprising a pure graphite slurry with a low molar weight binder and the composition utilized in the previous chapter.

4 Experimental

4.1. Intensive mixer

The principal instrument employed for the dispersion of a slurry in this study is an intensive mixer, manufactured by Maschinenfabrik Gustav Eirich GmbH & Co KG, Germany. An illustration of the mixer can be observed in Figure 4-1a, while the schematic drawing of the interior is presented in Figure 4-1b. The machine's defining characteristics are the relatively large dispersion tool and the rotating batch vessel, which is referred to as the pan. The rotating pan makes the machine particularly suited to the processing of highly viscous and amorphous masses, such as high solids content suspensions, i.e. slurries. During the processing stage, the pan rotates with a circumferential speed of ω_{pan}, thereby setting the mixer's content in motion. The scraper then directs the mass towards the center of the pan. The tool is positioned slightly off-center, with a circumferential speed of ω_{tool}, which ensures a uniform energy input and prevents the formation of pockets of untreated material. The bottom of the pan may become visible, depending on the degree of filling and the viscosity of the processed bulk. In this study, two versions of the intensive mixer were employed: a one-litre model (EL1) and a five-litre model (C5), revering to the useable volume. It should be noted that the nominal volume exceeds the useable volume.

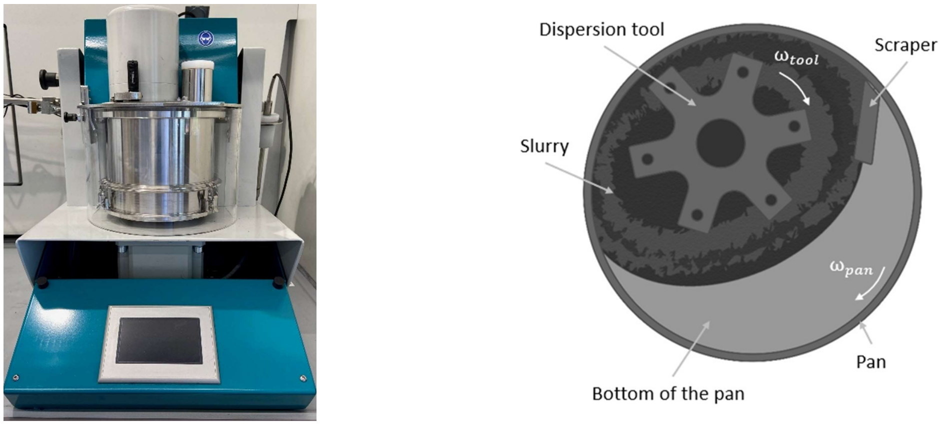

a) b)

Figure 4-1: a) image of an Intensive mixer "EL1"; b) schematic drawing of the intensive mixers interior while processing a slurry

The production of each slurry is the consequence of a meticulously devised mixing procedure. This procedure commences with the mise en place, whereby the components are weighed and the binder is pre-dissolved overnight. Subsequently, the pre-weighed components were introduced into the mixer in bulk. Each sequence is characterized by specific machine settings, including ω_{tool} and sequence duration t_{seq}, as well as process parameters such as the sequence's material ratios (TCS) and the degree of filling, which was calculated using the component's density values and their mass. In this study, the data is presented in two figures: a procedure diagram (Figure 4-3a) and a procedure sequence diagram (Figure 4-3b).

The procedure diagram presents the sequence titles on the x-axis and the TSC, the degree of filling, $\omega_{tool}$and t_{seq} on the y-axis. The procedure sequence diagram illustrates the sequence names and the components that are introduced.

4.2. Experimental series

This section describes the various procedures employed in the work, including the experimental series components, compositions, and the sequencing of the procedures.

4.2.1. Cathodic compositions

Two cathodic experimental series are employed to pursue the subject matter of Chapter 5. In both series, a slurry is prepared using the components enumerated in Table 4-1.

Table 4-1: Component details of cathodic slurry

Component	Designation, manufacturer, country	Properties*
Lithium iron phosphate (LFP)	A19, Aleees Eco Ark (Ningbo) Co., Ltd., Taiwan	D_{50} = 12 µm BET SSA = 7.40 $m^2 g^{-1}$
Carbon black (CB)	LITX® HP, CABOT Corporation, USA	BET SSA = 45.5 $m^2 g^{-1}$
Single walled carbon nanotubes (SW-CNT)	TUBALL®, OCSiAl, Luxembourg	BET SSA = 400 $m^2 g^{-1}$
Polyvinylidene fluoride (PVDF)	Solef® 5140; Solvay Specialty Polymers Germany GmbH, Germany	M_W = 1.300 kDa
N-methyl-2-Pyrrolidone (NMP)	Battery grade, BASF SE, Germany	-

* According to the manufacturer

4.2.1.1. CA-Series

The compositions of the CA-Series exhibit considerable variation, with the components of Table 4-1 being employed in each case. All slurries have a total solids content (TSC) of 45 wt% and a total of 5 wt% binder (non-volatile). Nevertheless, the content of CA ultimately determines the CAM content. Figure 4-2 provides an overview of the CA-Series variation, which comprises a total of nine slurries. Four of the compositions are produced by varying the carbon black content, which ranges from 0 to 2.5 wt%. These are designated as CB_i. A further four can be identified by the variation in CNT content, ranging from 0 to 0.12 wt%, designated as CNT_i. The cross-over of both designations is referred to as CA_{alt}, which is also labelled as $CB_{1.5}$ or $CNT_{0.08}$, depending on the context of the comparison, whether it is a uni- or bimodal investigation. Slurry CA_{opt} is another variation that represents a smaller concentration of both CAs of CA_{alt}. Slurry CAM_{ref} refers to the sample with no conductive additives.

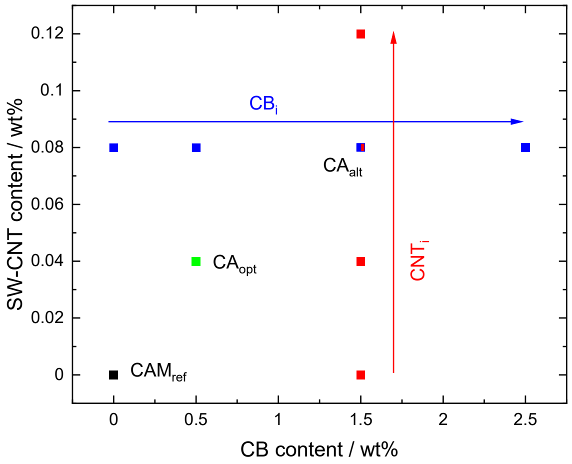

Figure 4-2: variation matrix of the CA-Series' conductive additive variation

The composition of CA_{alt} is presented in Table 4-2. The CA-Series alternations of CA_i represent variations of CA that affect the CAM content of the slurry. The PVDF content was maintained at a constant level. It should be noted that the SW-CNT was employed as a pre-prepared product; it is a single-wall carbon nanotube dispersion with PVDF used as a kinetic stabilization agent. The values presented in the table for the PVDF content represent the sum of the added PVDF and the PVDF present in the SW-CNT dispersion.

Table 4-2: Composition of slurry CA_{alt}

Components	**SC_{NV} / wt%**	**$SC_{NV\&V}$ / wt%**	**Φ_i / vol%**
LFP	93.42	42.04	17,71
CB	1.50	0,68	0,66
SW-CNT	0.08	0.04	0,03
PVDF	5.00	2.25	2,88
NMP	-	*65.00	**78,72
**1 - TSC; **1* $- \sum \Phi_i$			

The methodology employed to create the series' slurries is illustrated in Figure 4-3, wherein panel a) depicts the sequence-dependent TSC, degree of filling, tool speed and duration. Figure 4-3b presents a procedure sequence diagram, indicating the sequence in which each component was utilized. It should be noted that the other variations of the CA-Series are not shown, as the changes are too minor to be discernible in this form. The rationale behind this procedure is that, in the initial sequence, the carbon black is dispersed before the kneading phase of the added CAM. Given that the SW-CNTs are already pre-dispersed, there is no necessity for a high TSC, and thus a high energy input, dispersion. This is why they are added after the suspension has been diluted.

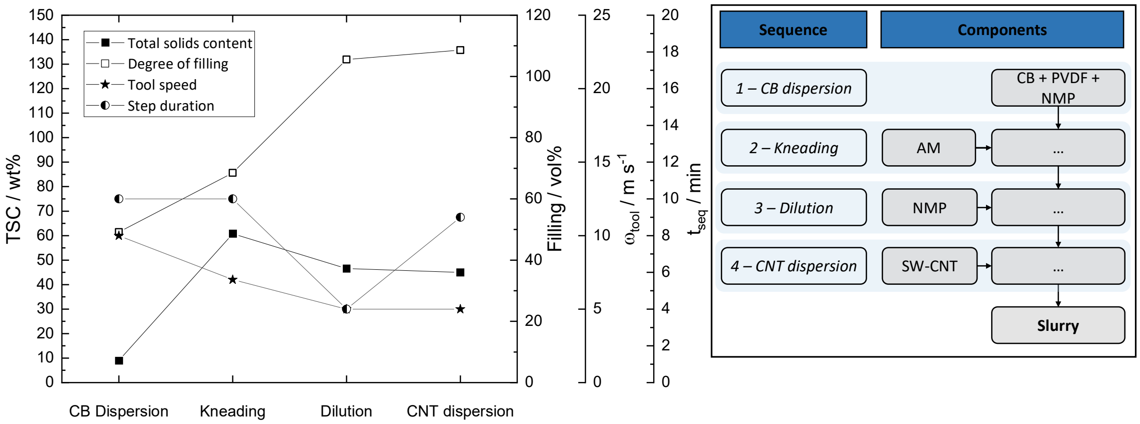

a) b)

Figure 4-3: Procedure details of slurry CA_{alt}; a) procedure diagram displaying TSC, degree of filling, tool speed and sequence duration b) procedures sequence diagram;

The procedure demonstrates that the initial sequence facilitates the dispersion of CB in a dissolved PVDF/NMP solution. The dispersion occurs within the sequence at a TSC of 9 wt% and a degree of filling of 49 vol%, with ω_{tool} set to 10 m s^{-1} circumferential speed for a t_{seq} of 10 minutes. In the subsequent kneading sequence, the AM (LFP) is introduced, resulting in an increased TSC of 61 wt% and a modified filling of 69 vol%. The kneading process is conducted at a tool speed of 7 m s^{-1} for a duration of 10 minutes. In the dilution sequence, NMP is added, resulting in a change to the sequence's TSC to 47 wt% at a filling of 105 vol%, which exceeds of the mixer's useable volume but lies within the nominal volume. The sequence then proceeds to homogenize the mixture for a period of 4 minutes at a speed of 5 m s^{-1}. The final sequence disperses the SW-CNT, finishing the slurry, with a TSC of 45 wt% and a filling of 109 vol%. This is achieved through a nine-minute mixing period at a speed of 5 m s^{-1}.

4.2.1.2. Procedure-Series

The second series of cathodic compositions examines the impact of varying specific mixing procedure sequences utilizing the components outlined in Table 4-1. In this instance, the composition of slurry CA_{opt} is employed, with detailed specifications presented in Table 4-3. The distinguishing factor between CA_{opt} and CA_{alt} is the reduction of CB and SW-CNT.

Table 4-3: Composition of slurry CA_{opt} and the procedure variations Pro_i

Components	**SC_{NV} / wt%**	**$SC_{NV\&V}$ / wt%**	**Φ_i / vol%**
LFP	94.46	42.51	17.95
CB	0.50	0,23	0.22
SW-CNT	0.04	0.02	0.01
PVDF	5.00	2.25	2.89
NMP	-	*65.00	**78,92
*$1 - TSC$; **$1-\sum \Phi_i$*			

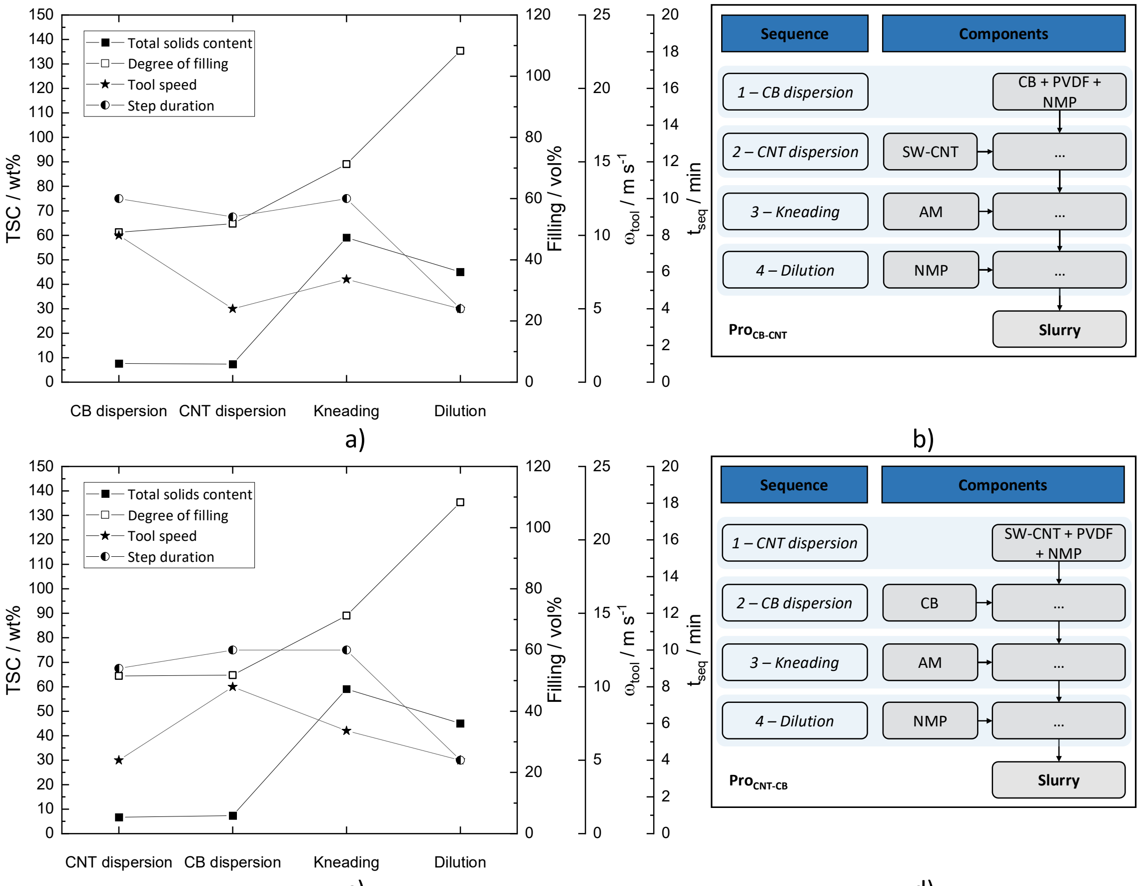

a) b) c) d)

Figure 4-4: Procedure details of slurry Pro_{CB-CNT}: a) procedure diagram displaying TSC, degree of filling, tool speed and sequence duration b) procedures sequence diagram; Procedure details of slurry Pro_{CNT-CB}: c) procedure diagram displaying TSC, degree of filling, tool speed and sequence duration d) procedures sequence diagram

The procedure variations are designated as Pro$_{\mathrm{i}}$ and are described in the following manner. The designation "Pro$_{\mathrm{opt}}$" is used to refer to a slurry that has been prepared in accordance with the procedure outlined in Figure 4-3, whereby CB is dispersed in the initial stage and SW-CNTs in the final stage. The slurry Pro$_{\mathrm{CB\text{-}CNT}}$ is the result of a procedure that involves the dispersion of CNTs in sequence two, subsequent to a prior dispersion of CB in the first sequence. The details of this procedure are illustrated in Figure 4-4a and b. The slurry Pro$_{\mathrm{CNT\text{-}CB}}$ is created by first dispersing SW-CNTs, followed by the dispersion of CB. The details of this procedure can be seen in Figure 4-4c and d.

The Slurry Pro$_{\mathrm{DM\ A\text{-}C}}$ procedure commences with a dry mixing sequence, whereby LFP is combined with CB. This is followed by a kneading sequence, during which the dissolved binder is applied. The full procedure is illustrated in Figure 4-5a and b. Furthermore, the slurry Pro$_{\mathrm{DM\ A\text{-}C\text{-}B}}$ employs a dry mixing sequence, whereby the dry binder powder is combined with LFP and CB, followed by a kneading sequence in which the solvent is introduced. This is illustrated in Figure 4-5c and d.

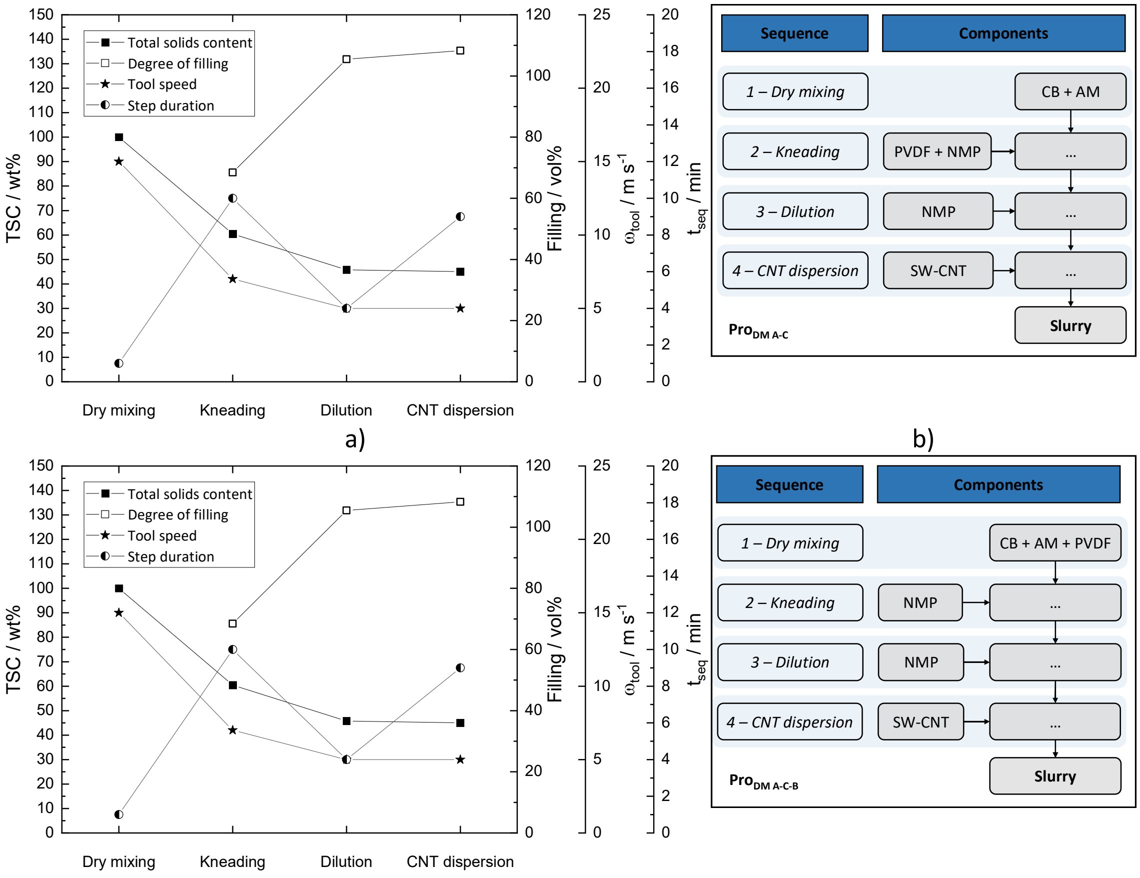

a) b) c) d)

Figure 4-5: Procedure details of slurry Pro$_{\mathrm{DM\ A\text{-}C}}$: a) procedure diagram displaying TSC, degree of filling, tool speed and sequence duration b) procedures sequence diagram; Procedure details of slurry Pro$_{\mathrm{DM\ A\text{-}C\text{-}B}}$: c) procedure diagram displaying TSC, degree of filling, tool speed and sequence duration d) procedures sequence diagram

4.2.2. Anodic compositions

In contrast to the cathodic compositions, the research subjects of the anodic compositions demonstrate a high TSC and a subsequently high Φ, as well as an adsorbable binder, the CMC. A total of five anodic experimental series were conducted in order to pursue the subject matter of Chapters 6 and 7.

The series originate from three slurry compositions, namely an all-graphite slurry that utilizes a CMC binder, a graphite-SiO_x blended slurry that utilizes a CMC binder with slightly higher M_w. The third slurry employs the same components as the blended slurry, however SiO_x is not utilized. This composition is exclusive for the preliminary test series. The remaining components of the remaining compositions were maintained at the same levels. The specific components are listed in the following three tables.

The components of the all-graphite slurry with the low molar weight CMC are shown in Table 4-4.

Table 4-4: Component details of the all-graphite slurry

Component	**Designation, manufacturer, country**	**Properties***
Artificial graphite (Graphite)	Not to be disclosed	D_{50} = 15.3 µm BET SSA = 1.7 $m^2\ g^{-1}$
Carbon black (CB)	C-NERGY SUPER C45, Imerys Graphite & Carbon, Switzerland	SSA = 45.5 $m^2\ g^{-1}$
sodium carboxymethyl cellulose (CMC_{500})	TEXTURECEL™ 2000 PA, DDP Specialty Products Germany GmbH & Co. KG, Germany	M_W = 500 kDa DS = 0.9
Styrene-butadiene rubber emulsion (SBR)	BM-451, Zeon Europe GmbH, Germany	TSC = 40 wt%
Deionized water	In-house	-

* According to the manufacturer

The components of the graphite-SiO_x blended slurry are presented in Table 4-5. The slurry comprises two blended AMs, with a smaller D_{50} and higher molar weight.

Table 4-5: Component details of graphite-SiO_x slurry

Component	**Designation, manufacturer, country**	**Properties***
Artificial graphite (Graphite)	SCMG-CD-C, Showa Denko Materials (Europe) GmbH, Germany	D_{50} = 6.2 µm BET SSA = 3.5 $m^2\ g^{-1}$
Silicon containing active material (SiO_x)	H80; Daejoo Electronic Materials Co. Ltd. Republic of Korea	D_{50} = 5.5 µm BET SSA = 8.0 $m^2\ g^{-1}$
Carbon black (CB)	C-NERGY SUPER C45, Imerys Graphite & Carbon, Switzerland	SSA = 45.5 $m^2\ g^{-1}$
sodium carboxymethyl cellulose (CMC_{875})	WALOCEL CRT 30.000 P BA, DDP Specialty Products Germany GmbH & Co. KG, Germany	M_W = 875 kDa DS = 0.9
Styrene-butadiene rubber emulsion (SBR)	BM-451, Zeon Europe GmbH, Germany	TSC = 40 wt%
Deionized water	In-house	-

* According to the manufacturer

The second all-graphite slurry is employed exclusively in the Preliminary-Series. Its components are delineated in Table 4-6.

The Parameter-Series is a dedicated investigation into the subject matter of Chapter 6. It utilizes the graphite-SiO_X composition, which is produced through a range of mixing procedures at varying tool speeds and durations. Chapter 7 addresses the issue of composition concentrations, with a particular focus on the TSC of a sequence, and employs a number of experimental series. The Preliminary-Series displays two distinct techniques for dispersing a slurry are employed, following the graphite-SiO_X blend. Secondly, the variation of a slurry's TSC was investigated within a series designated as TSC-Series, following a variety of pure graphite slurry compositions. This resulted in the emergence of two additional series, designated as Kneading-Series 1 and Kneading-Series 2. The initial series of kneading variations employs an exclusively graphite composition and a low molar weight binder, and utilizes two procedures of different process parameters, each of which varies the TSC within the kneading sequence. The Kneading Series 2 employs a graphite-SiO_x blend composition and a high molar weight binder and modifies the procedure's kneading sequence's TSC.

The experimental series are outlined in the following paragraphs, with a description of the component ratios and procedure details.

Table 4-6: Component details of the all-graphite C slurry, employed in the Preliminary-Series

Component	**Designation, manufacturer, country**	**Properties***
Artificial graphite (Graphite)	SCMG-CD-C, Showa Denko Materials (Europe) GmbH, Germany	D_{50} = 6.2 µm BET SSA = 3.5 $m^2\ g^{-1}$
Carbon black (CB)	C-NERGY SUPER C45, Imerys Graphite & Carbon, Switzerland	SSA = 45.5 $m^2\ g^{-1}$
sodium carboxymethyl cellulose (CMC_{875})	WALOCEL CRT 30.000 P BA, DDP Specialty Products Germany GmbH & Co. KG, Germany	M_W = 875 kDa DS = 0.9
Styrene-butadiene rubber emulsion (SBR)	BM-451, Zeon Europe GmbH, Germany	TSC = 40 wt%
Deionized water	In-house	-

* According to the manufacturer

4.2.2.1. Preliminary-Series

The preliminary tests demonstrate the impact of the mixing technique on the slurry's flow behavior. The tests were conducted using the preliminary graphite slurry composition, as detailed in Table 4-7. The component ratios are presented in Table 4-6.

Table 4-7: Composition of the preliminary test

Components	**SC_{NV} / wt%**	**$SC_{NV\&V}$ / wt%**	**Φ_i / vol%**
Graphite	96.20	48.10	29.49
CB	2.00	1.00	0.91
CMC	0.90	0.45	0.60
SBR	0.90	0.45	0.42
Water	-	*50.00	**68.57

**1 - TSC; **1 − $\sum \Phi_i$*

The slurry composition was employed in two distinct mixing procedures, designated as P1 and P2. The two procedures differed in that P1 was predominantly mixed by hand using a stainless-steel spatula to knead the solid components into a smooth paste prior to the fine dispersion using a dispersion disc mixer (Dispermat, LC disperser series, VMA-Getzmann GmbH, Germany). This was followed by the addition of SBR and water. In the case of P2, the mixing process was conducted using an intensive mixer (EL1, Maschinenfabrik Gustav Eirich GmbH & Co KG, Germany). This involved the kneading and dispersion of all the solids with a CMC solution, followed by the addition of SBR and water to achieve the final TSC.

4.2.2.2. TSC-Series

The present experimental series is designed to investigate the correlation between TSC and flow behavior. To this end, a number of graphite slurries, comprising the components listed in Table 4-4 and following the composition set out in Table 4-8, were prepared. The TSC-Series was developed with the objective of creating slurries with a range of final TSC values, and the solvent content of this series was therefore adjusted to achieve the desired range of 33.5 to 46.0 wt%.

Table 4-8: Composition of the TSC-Serie's slurry - TSC_i

Components	**SC_{NV} / wt%**	**$SC_{NV\&V}$ / wt%**	**Φ_i / vol%**
Graphite	94.5	51.03 – 62.84	32.14 – 43.71
CB	2.0	1.08 – 1.33	1.01 – 1.38
CMC	1.0	0.54 – 0.67	0.74 – 1.02
SBR	2.5	1.35 – 1.66	1.31 – 1.78
Water	-	*46.00 – 33.50	**64.80 – 52.12
**1 - TSC; **1* $- \sum \Phi_i$			

The creation of a slurry with a specific TSC inevitably affects the individual sequence's TSC, given that no solvent can be removed from the mixing procedure. This ultimately constrains the design considerations that can be made with regard to the sequence's degree of filling, which is of particular importance in the context of the dispersion tool, given that it must be immersed in order to operate as intended. The TSC-Series procedures' process parameters and sequence diagram are illustrated in Figure 4-6. Six slurries with a TSC ranging from 54 to 69 wt% in increments of 3 wt% were prepared. The slurries are designated as TSC_i, where the index number represents the slurry TSC. In this procedure, the machine parameters were maintained at a constant level, while the total amount of water was adjusted in order to achieve the desired final slurry TSC. It should be noted that slurry TSC_{69} was produced in accordance with the aforementioned figure; however, the resulting slurry was not flowable, which is why this slurry was diluted to a TSC of 66.5 wt% after mixing.

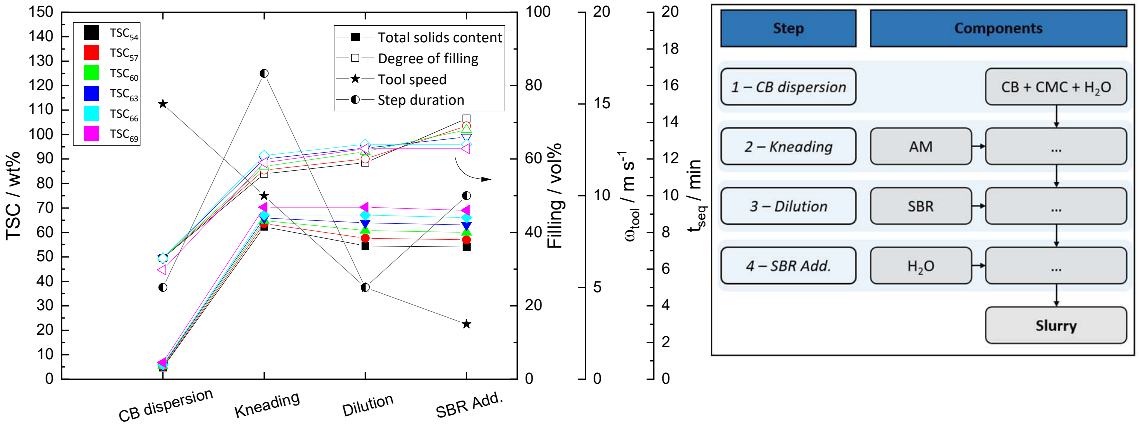

a) b)

Figure 4-6: Procedure details of the TSC-Series: a) procedure diagram displaying TSC, degree of filling, tool speed and sequence duration, b) procedures sequence diagram

4.2.2.3. Kneading-Series 1

The objective of this series of experiments is to investigate the effect of the TSC within the mixing procedure's kneading sequence on a slurry and the subsequent electrode. For this purpose, a pure graphite slurry composition with a TSC of 60 wt% and a low molar weight CMC was used. The details of this composition can be found in the following table. The slurry's components are listed in Table 4-4.

Table 4-9: Composition of Kneading-Series 1

Components	**SC_{NV} / wt%**	**$SC_{NV\&V}$ / wt%**	**Φ_i / vol%**
Graphite	94.5	56.70	37.41%
CB	2.0	1.20	1.18%
CMC	1.0	0.60	0.87%
SBR	2.5	1.50	1.52%
Water	-	*40.00	**59.03%

**1 - TSC; **1* $-\sum \Phi_i$

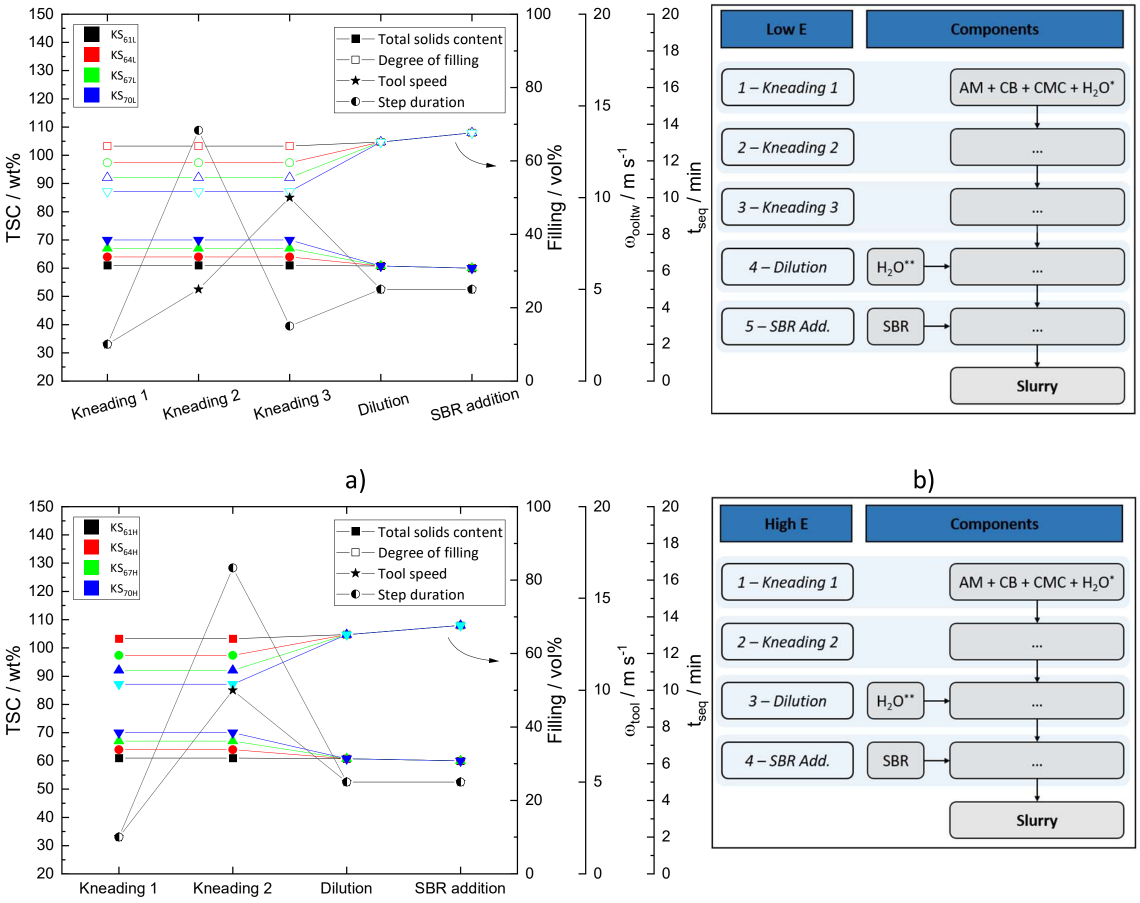

a) b)

c) d)

Figure 4-7: Procedure details of the Kneading-Series 1: Low energy input procedure a) procedure diagram displaying TSC, degree of filling, tool speed and sequence duration, b) procedures sequence diagram; High energy input procedure: c) procedure diagram displaying TSC, degree of filling, tool speed and sequence duration d) procedures sequence diagram; H_2O^* and H_2O^{**} represents the adjusted amount of solvent to create the desired TSC of that sequence depending on the sample

The series is distinguished by a series of gradual alterations to the TSC concentration, ranging from 61 to 70 wt%. The slurries are designated as "KS$_{ij}$", where "i" represents the TSC of the kneading sequence and "j" denotes the procedure from which it originates. The sequence variations were conducted using two distinct mixing procedures. One procedure is characterized by low energy input, with low tool speeds and a short sequence duration (see Figure 4-7a and b). This results in the slurry designation ending in "L". The alternative mixing procedure employs higher tool speeds and longer sequence durations, as illustrated in Figure 4-7c and d. This results in a slurry designation with an "H" ending. The low-energy input procedures set of slurries was produced in three individual kneading sequences, each with a distinct ω_{tool} and t_{seq}. Subsequently, they were diluted before the finalisation with the SBR emulsion. The high-energy input procedure employed two kneading sequences, utilising a high ω_{tool} for an extended t_{seq}, before dilution and SBR addition.

4.2.2.4. Parameter-Series

The investigation of the mixing procedure's machine parameters was conducted on the basis of the composition of the following table. The slurry comprises two AMs (artificial graphite and SiO$_x$), as well as the high molar weight CMC$_{875}$. The component details are provided in Table 4-5.

Table 4-10: Slurry composition of Parameter-Series and Kneading-Series 2

Components	**SC$_{NV}$ / wt%**	**SC$_{NV\&V}$ / wt%**	**Φ_i / vol%**
Graphite	86.58	51.95	34.25
SiO$_x$	9.62	5.77	4.24
CB	2.00	1.22	1.20
CMC	0.90	0.54	0.77
SBR	0.90	0.54	0.55
Water	-	*40.00	**58.99

**1 - TSC; **1* $-\sum \Phi_i$

In this series of experiments, the parameters of the intensive mixer were varied on the basis of the procedures designated as "Ref. 1" and "Ref. 2". The procedure and sequence diagram are illustrated in the following figure. The procedure outlined in Ref. 1 (see Figure 4-8 a and b) comprises a dry mixing sequence, followed by a kneading sequence, and then the SBR addition and dilution. The variation affected the tool speed ω and the sequence duration t of the dry mixing sequence (ω_w and t_{dm}) , as well as the kneading sequence (ω_{wk} and t_k). The procedure designated as Ref 2 (Figure 4-8 c and d) commences with the utilization of a carbon black dispersion sequence, wherein the tool speed and the sequence duration (ω_{wdisp} and t_{disp}) are subjected to variation. The subsequent sequences are the kneading, SBR addition and dilution sequences. The sequence variations were conducted in a one-factor-at-a-time approach, with each sequence resulting in an individual slurry. The series' parameter variations of the dispersion tool and the duration can be seen in Table 4-11, in which the baseline setting is listed in brackets, hence the value of the variation is added on top.

Table 4-11: Variation of the Parameter-Series' parameters

Sequence	Parameter (standard)	Parameter variation	Unit	Procedure
Kneading duration	$t_k(10)$	+5; +10	min	Ref. 1
Kneading speed	$\omega_{wk}(10)$	+5; +10	m s^{-1}	Ref. 1
Dry mixing duration	$t_{dm}(1)$	+5; +10	min	Ref. 1
Dry mixing speed	$\omega_w(10)$	+5; +10	m s^{-1}	Ref. 1 (t_{dm}=10)
Carbon Black dispersion duration	$t_{disp}(10)$	+5; +10	min	Ref. 2
Carbon Black dispersion speed	$\omega_{wdisp}(10)$	+5; +10	m s^{-1}	Ref. 2

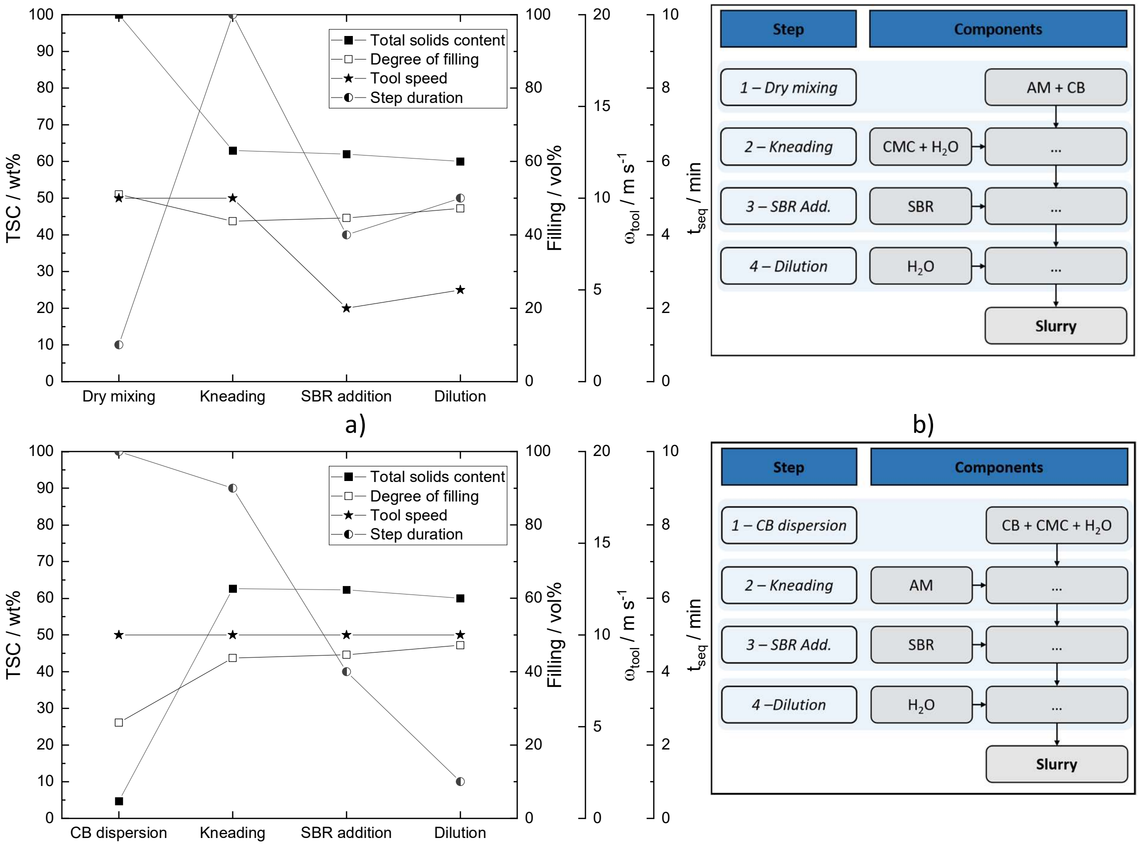

Figure 4-8: Procedure details of the Parameter-Series; Ref. 1: a) procedure diagram displaying TSC, degree of filling, tool speed and sequence duration b) procedures sequence diagram; Procedure details of slurry Ref. 2: c) procedure diagram displaying TSC, degree of filling, tool speed and sequence duration d) procedures sequence diagram; Procedure details of slurry

4.2.2.5. Kneading-Series 2

The second series of kneading variations employs the same slurry composition as that of the parameter series. For further details, please refer to Table 4-10 and Table 4-5. In contrast to the other kneading series, this second series utilizes a blend of AMs with a lower D_{50}, a high molar weight CMC and an overall low concentration of CMC and SBR. The procedure details and sequence diagram for the second kneading series are presented in Figure 4-9. The majority of sequences have two distinct settings: a "slow" and a "fast" setting. The "slow" setting involves a brief sequence with a low ω_{tool}, which serves to prevent splashing or the formation of dusk clouds. This is followed by a sequence with a higher ω_{tool} and a longer t_{seq}. The samples exhibit variations in an incremental change of the kneading sequence's TSC (x_i) , designated as high solids content mixing (HSCM), with TSC values ranging from 60 to 69 wt%, varying in increments of 3 wt%. This resulted in the creation of four distinct procedures, which were labelled P_{60} to P_{69}.

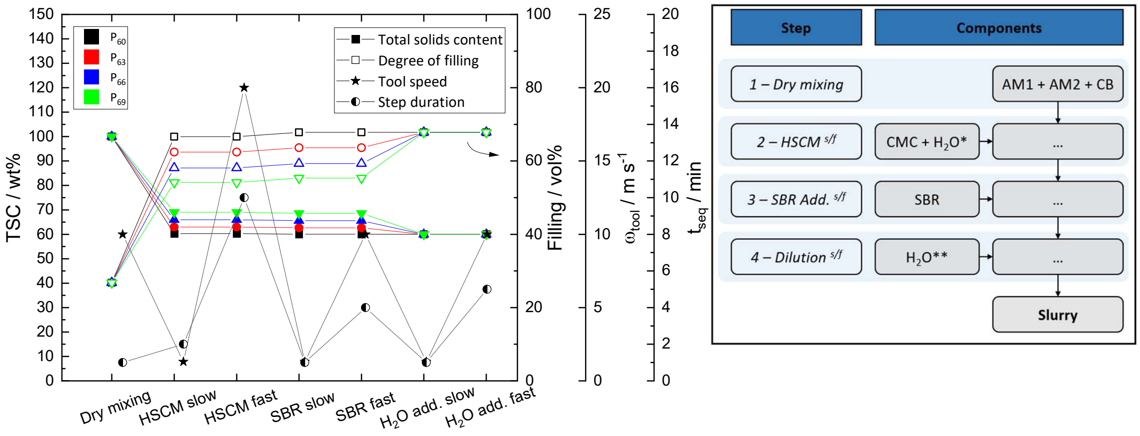

a) b)

Figure 4-9: Procedure details of the Kneading-Series 2: a) procedure diagram displaying TSC, degree of filling, tool speed and sequence duration b) procedures sequence diagram; H_2O* and H_2O** represents the adjusted amount of solvent to create the desired TSC of that sequence depending on the sample; $^{s/f}$ slow tool speed prior to the sequences faster tool speed

In addition to the series' four samples, a low E_{sp} reference, designated P_{low}, was produced following the same composition and components. The procedure details and sequence diagram are presented in Figure 4-10. The TSC of this mixing procedure's kneading sequence was maintained at 60 wt%, however, there are four kneading sequences with a very low ω_{tool} of $3\ m\ s^{-1}$.

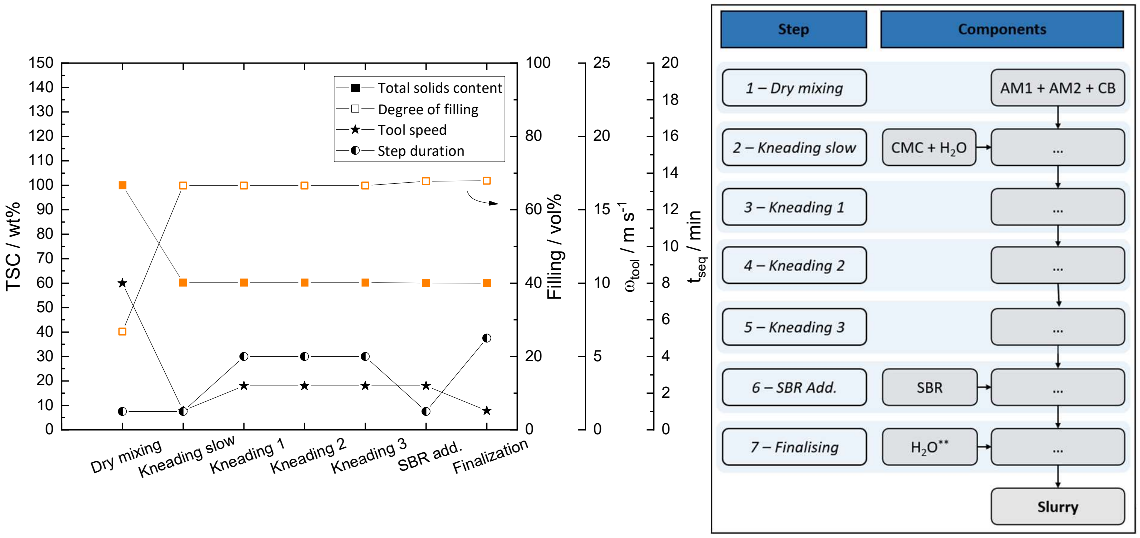

a) b)

Figure 4-10: Procedure details of low-energy reference procedure of the Kneading-Series 2: a) procedure diagram displaying TSC, degree of filling, tool speed and sequence duration b) procedures sequence diagram

4.3. Slurry characterization and treating

4.3.1. Rheometry

Rheological measurements were conducted utilizing a rotational rheometer (MCR 302e, Anton Paar Germany GmbH, Germany). A plate–plate configuration with a diameter of 50 mm and a gap height of 0.3 mm was employed as the measurement geometry. The temperature was maintained at 25 degrees Celsius.

Shear-rate-controlled measurements were conducted using a logarithmic shear rate ramp, spanning a range of $\dot{\gamma}$ = 0.05 to 1000 s^{-1}, with a corresponding measurement duration varying from 80 seconds at the lowest shear rate to 2 seconds at the highest shear rate. In the case of stress-controlled measurements, the shear stress τ was increased logarithmically, from 0.01 to 1000 Pa, with a measurement time of 18 seconds for each stress value.

4.3.2. Coating experiment

In order to analyze the coating experiments, it was necessary to calculate the shear rate within the coating layer. This was achieved by dividing the line speed, U_L, by the slot-die gap, G_S, which is the distance between the slot-die lips and the substrate. Please refer to Figure 4-11.for further details.

$$\dot{\gamma} = \frac{U_L}{G} \tag{24}$$

The dynamic viscosity η was calculated by interpolating the experimental data for viscosity versus shear rate.

In order to establish the relationship between surface tension σ, η, and U_L, the dimensionless capillary number Ca was calculated as follows, in accordance with the methodology set forth by [126, 127].

$$Ca = \frac{\eta \cdot U_L}{\sigma} \tag{25}$$

The surface tension of the slurry was set equal to that of pure water at 22 °C, σ = 72.3 mN m^{-1} [128], which was deemed a reasonable approximation for this quantity, given that no surface-active ingredients were added during the preparation of the slurry.

The viscosity data employed to calculate Ca were obtained at 25 °C; as the slot-die coating was conducted at 22 °C, this results in a minor systematic discrepancy. Given that the temperature dependence of slurry viscosity is essentially determined by that of water , which constitutes the main ingredient of the slurry's dispersed phase [9], it can be estimated that this error is smaller than 7 %.

The dynamic gap G^* was calculated as the ratio of the slot-die gap G and the height of the wet film W, as illustrated in Figure 4-11. The value of G is determined by the dimensions and configuration of the coating apparatus itself. In contrast, the value of W was calculated using the electrode loading, the TSC slurry concentration, and the slurry density, resulting in a value of W = 87.6 µm.

$$G^* = \frac{G}{W} \tag{26}$$

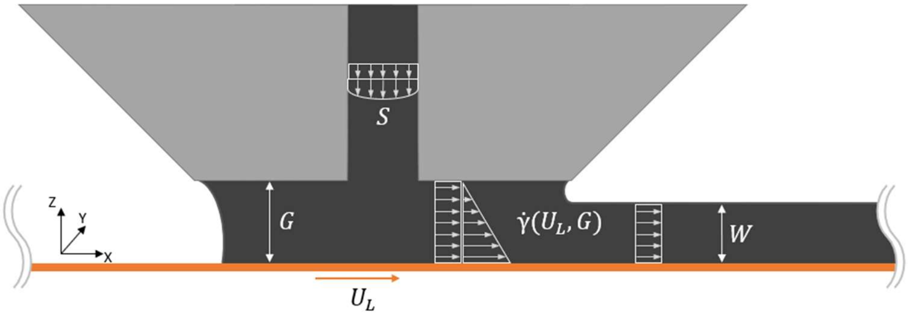

Figure 4-11: Schematic drawing of a slot-die, including flow pattern within the coating bead.

The coating trials of the Kneading-Series 2 were conducted utilizing a roll-to-roll coater, manufactured by Mathis AG (Switzerland). The slot-die apparatus was installed with a 300 µm thick shim sheet S and a slot width of 50 mm. The slurry was supplied by a progressing cavity pump. Prior to the commencement of the trials, the coater pump was calibrated at the highest stable G^* for each speed of the test run, thereby ensuring a constant capacity loading of 3.3 mAh cm^{-2} at each speed. This was achieved by coating, drying and weighing cut coins at line speeds ranging from 2 to 10 m per minute, with an increment of 2 m per minute. The experiments were conducted in a dry room (dew point < −45 °C) at a temperature of 22 °C.

Two coating defects, namely air entrainment and widening of the coating, were monitored visually as stability criteria. In this context, the upper stability limit (USL) represents the highest values of G^* where no air entrainment was observed, while the lower stability limit (LSL) denotes the lowest value of G^* where no increase in coating width was recorded. Figure 4-12a illustrates the occurrence of air entrainment, following the exceedance of the USL. Conversely, the widening of the coating after the exceedance of the LSL was quantified by the coater's camera measurement system. Figure 4-12b depicts the uniformity and absence of coating defects within the stability limits.

a) b)

Figure 4-12: Inline photographs of the roll-to-roll coating experiments, web's direction from bottom to top; a) coating outside stable operating window with visible air entrainment; b) coating within the stable operating window.

In order to estimate the USL, the visco-capillary model (VCM) proposed by Ruschak was employed, and the critical capillary number Ca_R was calculated with a numerical prefactor of 0.65 [126, 129].

$$Ca_R = 0.65\left(\frac{2}{G-1}\right)^{\frac{3}{2}} \tag{27}$$

4.3.3. Energy input

The power consumption P_{el} of the rotor of the dispersing tools was monitored by the machine and integrated over time, t, resulting in the energy consumption of the rotor, E.

$$E = \int P_{el}\, dt \tag{28}$$

The specific energy input E_{sp} was calculated by subtracting the idle energy consumption E_{idle} from the rotor energy consumption E. This effective energy input E_{eff} was then divided by the sample volume occupied during the mixing sequence V_{seq}, thus yielding E_{sp}.

$$E_{sp} = \frac{E - E_{idle}}{V_{seq}} = \frac{E_{eff}}{V_{seq}} \tag{29}$$

The relative specific energy input $E_{sp\,r}$ is the ratio between a procedure and another procedure.

4.3.4. Centrifugal treatment of the slurry

To gain further insight into the integrity and quantity of the binders of a slurry, the slurry was subjected to centrifugation (Z366, Hermle Labortechnik GmbH, Germany) for 12 hours at a relative centrifugal force of 6300, with the objective of separating the solid fraction from the liquid fraction. The resulting supernatant was then analyzed by rheological measurement.

4.4. Electrode characterization and treating

4.4.1. Peel-Test

The peel strength was determined utilizing a ZwickiLine Zo.5 (ZwickRoell GmbH & Co. KG, Germany) and a 90° peel-test configuration. The electrodes were cut into strips 30 mm in width, with a total substrate length of 200 mm and a coating length of 120 mm. Following calendering, the electrode samples were affixed to the setup with double-sided adhesive tape (Tesa 05696, Tesa SE, Germany) using a silicone roller to laminate the electrode foil onto the tape. The force measuring probe was attached to the electrodes' current collector, and the machine measured the force required to peel the substrate from the coating at a speed of 5 mm s^{-1}. The peel strength F_{peel} was calculated by dividing the measured force F_{total}) by the width of the sample W_{sample}. Figure 4-13 shows a schematic drawing of the tests.

$$F_{peel} = \frac{F_{total}}{W_{sample}} \tag{30}$$

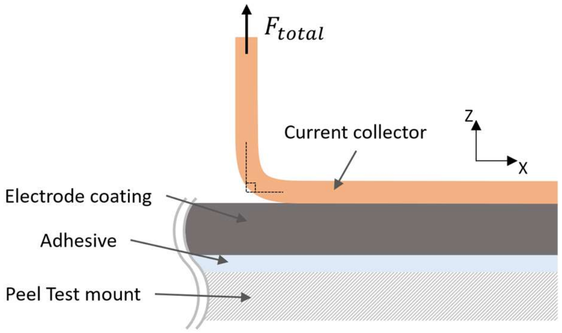

Figure 4-13: Schematic drawing of the peel-test

4.4.2. Post-Peel-Test Analysis

The microscopic examination of the electrode was conducted on a top light microscope (VHX 7000, Keyence Deutschland GmbH, Germany). For this, the post-peel-test current collector foils were punched into coins with a 14 mm diameter and images of the coins peeled surface were taken under constant conditions of lens distance, magnification, and lighting. The images were then analyzed using a raster graphics editor (GNU Image Manipulation Program, Spencer Kimball, Peter Mattis and GIMP Development Team, USA). An exemplary microscope image is shown in Figure 4-14a, a dark residue can be seen on the aluminum current collector foil. To determine the coating-residue's area that occupies the foil, the histogram of the images RGB-color-spectrum was analyzed. This spectrum defines a color by assigning a value of 0 to 255 to each of the three color channels: red (RC), green (GC) and blue (BC). In order to set a threshold value, the brightness channel (YC) is be calculated. This channel is the sum of the weighted channel values of RC, GC and BC, according to the following equation [130].

$$YC = 0.02126 \cdot \mathrm{RC} + 0.7152 \cdot \mathrm{GC} + 0.072 \cdot \mathrm{BC} \tag{31}$$

To separate the black residue's area from the current collector it was assumed that every color equal to or lower in value than 80 (YC) is considered residue, meaning every pixel higher in value is considered foil. The threshold-value's color can be seen in the bottom right corner of Figure 4-14a. The image's smallest areal unit is a pixel. The images pixel count, divided into the RGB-channel and the brightness channel can be seen in Figure 4-14b. The integral of the YC-channels curve from channel value 0 to 80 represents the occupied area (dark), the remainder of the YC integral is the foils unoccupied area. It should be noted that these areas are assumed to be the projected area.

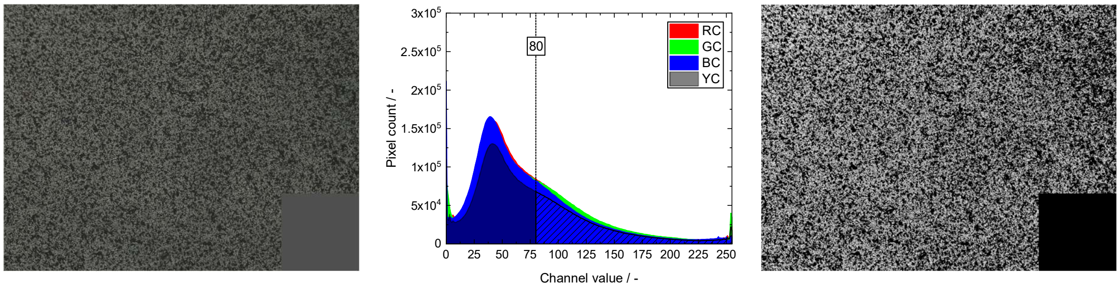

a) b) c)

Figure 4-14: a) original top light microscope image of a post-peel-test current collector foil, RGB-threshold bottom right corner; b) pixel count as a function of channel value; c) black (YC:0) and white (YC:255) recolored image – 0(YC) ≤ 80(YC) ≤ 255(YC), RGB-threshold after conversion

When applying this threshold onto the original image, it can be recolored white (YC:255) for every original pixel with a value greater than YC:80 and black (YC:0) for every other pixel's YC-value, see Figure 4-14c. The ratio of the black pixels and the total amount of pixels gives the percentage of residue occupied foil area (ROFA). In this exemplary case it is roughly 61.8 % (bottom right box excluded).

4.4.3. Electrode resistivity

The resistivity of the electrodes was measured using an electrode resistance measuring system (RM2610, Hioki E.E. Corporation, Japan). The system presses a 46-pin probe head against the surface of the electrode and measures two resistances: the volume resistivity ρ_C in the units of Ω cm, representing the resistivity of the electrode layer, and the interface resistance ρ_I in the units of Ω cm^2, representing the resistivity of the interface between the coating and the substrate. Figure 4-15 illustrates an electrode with the location of the named resistivities and its measuring principle. The system applies a constant current onto the electrode sheet and measures the potential-distribution throughout the pin-head. By generating a digital model of the electrode sheet, the resistances are computed by adjusting the model to fit the measured values. Essential for this numeric approach is the specific electrical resistivity of the current collector, copper foil (ρ_M = 1.68· µΩ cm), aluminum foil ((ρ_M = 2.69 µΩ cm) and the height of the coating H_c, as well as the height of the current collector H_{cc}.

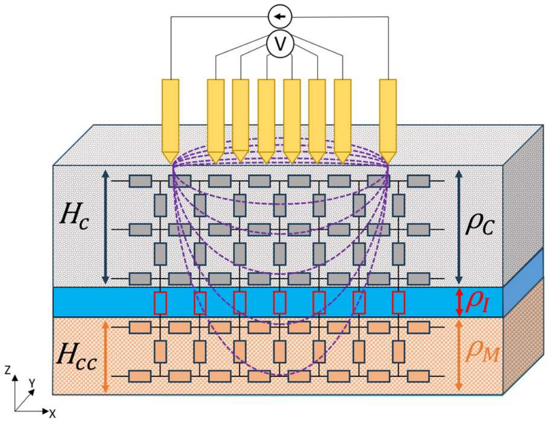

Figure 4-15: Schematic drawing of the electrode resistance measurements principle; recreated after [131]

Assuming that electron flow in the electrode is perpendicular to the current collector surface, the specific contact resistance ρ_{CN} is given by the product of ρ_C and H_c.

$$\rho_{CN} = \rho_C \cdot H_C \tag{32}$$

4.4.4. Manufacturing of electrodes

The electrode coatings were manufactured using a table coater. The slurries were degassed at 100 mbar for a period of two minutes, following which they were cast using a porous vacuum table (510XL, Erichsen GmbH & Co. KG, Germany) and a fixed film applicator frame (BYK-Gardner GmbH, Geretsried, Germany). The gap of the doctor blade was dependent on the targeted mass loading and the viscosity of the slurry. Electrodes with a loading of 3.3 mAh cm^{-2} were produced. The corresponding positive electrode had a loading of 3.0 mAh cm^{-2}, a mass loading of 16 mg cm^{-2} and a compressed electrode thickness of approximately 49 µm. The positive electrode contains an AM content of 94.5 wt% NCM 811. The LFP positive electrodes followed the same metrics.

4.4.5. Compression of electrodes

The dried electrodes were compressed using a laboratory calender (Ingecal SAS, Chassieu, France) operating at 0.8 kN mm^{-1}. For compression, the electrodes are cut into strips of a variable width, dependent on the intended subsequent use and cell format. The intensity of compression was controlled by adjusting the roll gap distance. The electrodes were characterized in terms of current collector thickness and total thickness H_E, with the difference between the two representing the thickness of the coating. Given the gravimetric loading g_i of the coating, the electrode density ϱ_i can be calculated using the following formula.

$$\varrho_i = \frac{g_i}{H_E - H_C} \tag{33}$$

The electrodes were cut into stripes with a width of 70 mm (30 mm for peel-tests) and subsequently compressed using a laboratory calender (Ingecal SAS, France). Prior to calendering, the electrodes were heated to 80 °C and the machine's desired gap, defined as the distance between the two compressing rolls, was set. The gap height was dependent upon the mass loading of the electrode and the desired coating density. Subsequent to compression, the electrodes were cut to the dimensions of the latter cell. Prior to the assembly of the cut electrodes to the cells, the electrodes underwent a drying process for a period of 12 hours under a vacuum (60 to 120 mbar absolute pressure) at a temperature of 80 °C.

4.4.6. SEM and EDX

The topographical and cross-sectional images of the electrodes were obtained using a scanning electron microscope (SEM; MIRA3, Tescan Orsay Holding a.s., Brno, Czech Republic). The electrode coins were stamped with a diameter of 15 mm and bisected. For the cross-sectional images, the straight-cut edge was then treated using an ion milling system (IM4000Plus, Hitachi High-Tech Europe GmbH, Krefeld, Germany). The topographical images originate from the same electrode's surface.

The SEM is also furnished with an energy-dispersive X-ray (EDX) module, thereby enabling EDX-mapping. The fundamental tenets of this methodology are as follows. A beam of electrons is emitted onto a sample. The electrons interact with the sample material at the atomic level, thereby emitting an electromagnetic radiation that is characteristic of the atomic structure of the sample material. By analyzing the intensity and the number of counts in the emission spectrum, an investigated segment of the sample can be mapped in terms of atomic integrity.

4.5. Cell manufacturing

For electrochemical testing, cells in different formats were constructed. The following subsections will describe the various cell formats. In order to achieve optimal cell performance while maintaining a high degree of safety, the ratio of positive to negative capacity (P:N) was set to 1.1. This means that the negative electrode has a 10% larger capacity than the positive electrode. Additionally, the negative electrode always has a slightly larger surface area than the positive electrode.

4.5.1. Coin-cell assembly

The full coin-cells (FCC) were assembled in an argon-filled glovebox atmosphere with less than 0.1 ppm O_2 and 0.1 ppm H_2O, utilizing single-sided electrodes. The positive electrode was positioned in the lower portion of the coin-cell casing, followed by a 21 µm thick ceramic separator (Enpass D22AEGK, SK innovation Co., Ltd., Korea), the negative electrode, a stainless-steel spacer coin, a spring, and the upper section of the coin-cell casing. A total of 100 µl of electrolyte, comprising $LiPF_6$ and a carbonate-solvent mixture with additives, was employed. Thereafter, the coins were sealed using an electric crimper (MSK−160E, MTI Corporation, USA) at a force of 1 kN.

4.5.2. Small format pouch cell assembly

Two distinct types of small-format pouch cells (SPC) " were built in this study. The primary distinction between the two types is the dimensions of the positive electrode, which differs by 26 cm^2. To enhance clarity, the format types are labelled according to their positive electrode dimensions, designated as "SPC_{20}" and "SPC_{46}” ".

4.5.2.1. SPC20

The positive electrode of this format has dimensions of 25 mm by 40 mm. Two single-sided negative electrodes and one double-sided positive electrode were employed. The negative electrode exhibits a slight increase in dimensions when compared to the positive electrode, with a size of 27 mm by 42 mm. The cells were filled with 0.4 ml of an electrolyte solution containing $LiPF_6$ (carbonate solvent mixture and additive, Soulbrain, Northville Township, MI, USA). The same 21 µm-thick separator as that used for the coin cells was employed. The assembly of the cells was conducted in a dry room (dew point < −45 °C), and the electrolyte was filled in an argon-filled glovebox atmosphere with less than 0.1 ppm O_2 and 0.1 ppm H_2O. The pouches were evacuated and sealed in the same glovebox.

4.5.2.2. SPC46

The dimensions of the positive electrode are 48 mm × 48 mm, while the negative electrode has dimensions of 50 mm × 50 mm. In this format, 0.7 ml of electrolyte, which is the same as in the other formats, was utilized. The assembly occurred in the same dry room as the other format, and the filling occurred in the glove box in the same manner. All SPCs were placed between two acrylic plastic plates and pressed tight by using clamps to guarantee a uniform pressure.

4.6. Electrochemical characterization

The cells were characterized using a CTS (Basytec GmbH, Germany). The coin-cells were subjected to cycling under room temperature conditions (22.5 °C), while the SPCs were held in a climate chamber at a constant temperature of 25 °C. The full cell’s cut-off potential was set to 2.8 and 4.2 V for the NCM containing cells and 2.5 and 3.7 V for the LFP containing cells. Each electrode sample was characterized by cycling multiple cells, with a minimum of three per variation.

4.6.1. Formation

A formation plan was implemented for each cell in this study. This entails multiple cycles of charging and discharging at a low C-rate subsequent to a CCCV regime. The C-rate is reversed to a charge rate that represents a percentage of the cell’s capacity. For example, 2C holds a current that is sufficient to charge or discharge the cell within half an hour, whereas a C-rate of 0.5C would take two hours to charge or discharge. In contrast, CCCV reverses to a cycling regime with an initial constant current (CC) until the cut-off potential is reached, subsequently continuing in a constant voltage (CV) phase. This maintains the cut-off potential by adjusting the current down to a minimum of 10 % of the last C-rate.

The NMC containing cells were subjected to the cycling regimen depicted in Table 4-12, the LFP containing cells have adjusted voltage ranges. In the initial two cycles, the cells were charged at 0.1C until they reached the cancellation criteria of 4.2 V, as specified in the CC step. Subsequently, a CV) regime was initiated, maintaining a potential of 4.2 V by adjusting the current until the cancellation criteria of 0.01C was reached. Subsequently, a discharge was conducted with a CC regime and a cancelation criteria of 2.8 V. The subsequent two steps were cycled at 0.2C, with cycles 5–7 at 0.33C, in accordance with the aforementioned methodology. Finally, the cells were charged to 30% state of charge (SOC). At the conclusion of each charge and discharge step, a 10-minute interval was incorporated.

Table 4-12: Formation plan of Parameter-Series 1

Cycles	C-rate	Regime	Cancel criteria
1 – 2	+ 0.1C	CC / CV	4.2 V / 0.01C
	- 0.1C	CC	2.8 V
3 – 4	+ 0.2C	CC / CV	4.2 V / 0.01C
	- 0.2C	CC	2.8 V
5 – 7	+ 0.33C	CC / CV	4.2 V / 0.01C
	- 0.33C	CC	2.8 V
8	+ 0.33C	CC	0.3 SOC

4.6.2. C-Rate

The C-Rate testing plan has been devised with the objective of evaluating the C-Rate capability of a cell. In order to achieve this, a series of cycles with an increasing C-Rate is applied to the cell. The testing plan comprises six 0.33C check-up cycles, two of which are conducted prior to the C-Rate variation of the discharge step, two prior to the C-Rate variation of the charge step and two more at the conclusion of the test. This examination provides an assessment of the cell's condition subsequent to a constant current charging (CCCV) regimen. The discharge C-rate is varied in increments of 0.5C, ranging from 0.5C to 5.0C, following a constant current (CC) regime. Each C-rate step comprises three cycles, with each charging occurring at 0.33C. Moreover, a 10-minute interval of rest is included between each stage of the procedure. Similarly, the charging C-rate variation is conducted in a comparable manner. The charging C-rate is varied in increments of 0.5C, ranging from 0.5C to 5.0C. The complete plan is presented in Table 4-13.

Table 4-13: C-rate plan of Parameter-Series 1

Cycles	C-rate	Regime	Cancel criteria
1 – 2	+ 0.33C	CC / CV	4.2 V / 0.01C
"Check-Up"	- 0.33C	CC	2.8 V
3 – 32	+ 0.33	CC	4.2 V
(3 cycles per 0.5C step)	- 0.5C to 5.0C	CC	2.8 V
33 – 34	+ 0.33C	CC / CV	4.2 V / 0.01C
"Check-Up"	- 0.33C	CC	2.8 V
35 – 64	+ 0.5C to 5.0C	CC	4.2 V
(3 cycles per 0.5C step)	- 0.33C	CC	2.8 V
65 – 66	+ 0.33C	CC / CV	4.2 V / 0.01C
"Check-Up"	- 0.33C	CC	2.8 V

It should be noted that this table refers to the C-rate test of the Kneading-Series 2. It is possible that other tests may have been altered with a view to focusing on either the cell's cathode or anode, for reasons of time-saving. The adjustments can be seen in the test figures.

4.6.3. Endless cycling

The LFP-containing cells were subjected to an endless cycling test. A CCCV regime at 0.3C was applied every 50 cycles. The cycles between the aforementioned check-up cycles were conducted using a 1C/1C charge and discharge CCCV regime, with a constant voltage (CV) phase of 5% of the previous C-rate.

4.6.4. Cell resistivity

The resistivity of a cell R_{cell} was calculated using two distinct methods: the simplified DCIR method and the DCIR method [132]. The simplified DCIR is based on Ohm's law, which states that resistance is the ratio between voltage U and current I . This methodology was subsequently applied to the cyclic voltammetry data set, with an illustrative example provided in Figure 4-16a. The data set demonstrates a 10-minute pause step and the subsequent decline in cell potential following the CV step. The potential recorded at the conclusion of the pause step is designated U_1. Upon commencing the CC step, a current I_{SIR} is applied to the cell. In response, the measured voltage declines immediately. A second voltage reading U_2 was then obtained 250 ms later, and the voltage drop across the resistances ΔU was calculated by subtracting U_2 from U_1. Subsequently, the voltage drop was divided by the current and multiplied by the cathodic area of the cells A_{CAM} , resulting in R_{cell}.

$$R_{cell} = \frac{U_1 - U_2}{I_{SIR}} \cdot A_{CAM} = \frac{\Delta U}{I_{SIR}} \cdot A_{CAM} \tag{34}$$

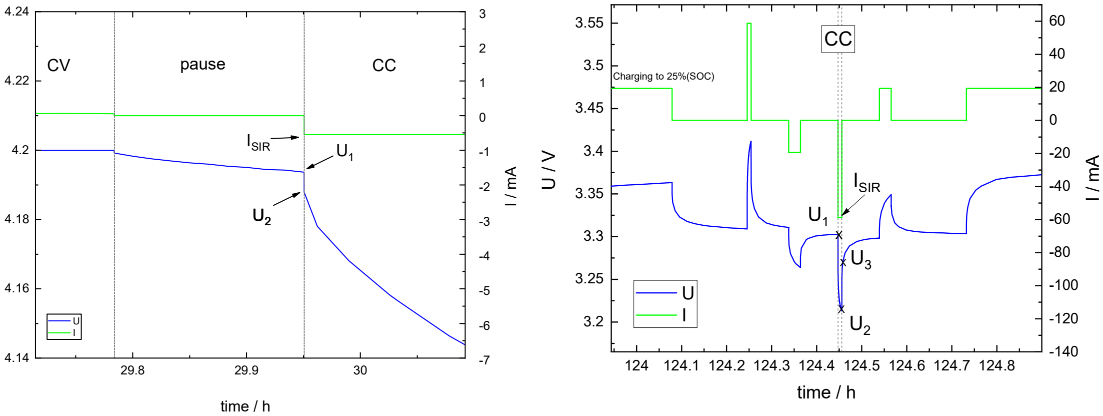

a) b)

Figure 4-16: Cyclic voltammetry data of a cell showcasing the voltage response after applying a current to calculate R_{cell}; a) using the simplified DCIR method b) using the DCIR method

The DCIR method is illustrated in Figure 4-16b. Similar to the simplified method, the voltage difference is calculated from the average relaxation voltage of U_1 and U_3 and the peak value of U_2. The full pulse was measured for 10 seconds and was taken at a 25% state of charge.

$$R_{cell} = \frac{\frac{U_1 + U_3}{2} - U_2}{I_{SIR}} \cdot A_{CAM} = \frac{\Delta U}{I_{SIR}} \cdot A_{CAM} \tag{35}$$

5 Conductive additive’s concentration and mixing procedure

In order to gain a deeper insight into the interrelationship between active material (AM), conductive additives (CA), and Binder, two experimental series were conducted in this chapter. In subsection 5.1, a series of slurries were prepared in which the AM content was substituted by a range of CA variations addressing the carbon black (CB) and single-walled carbon nanotubes (SW-CNT) content, both unimodal and bimodal, as illustrated in Figure 5-1. The binder content was maintained at a constant level. Electrodes were made and their characteristics were determined in order to obtain a well-suited candidate for the following procedure variation.

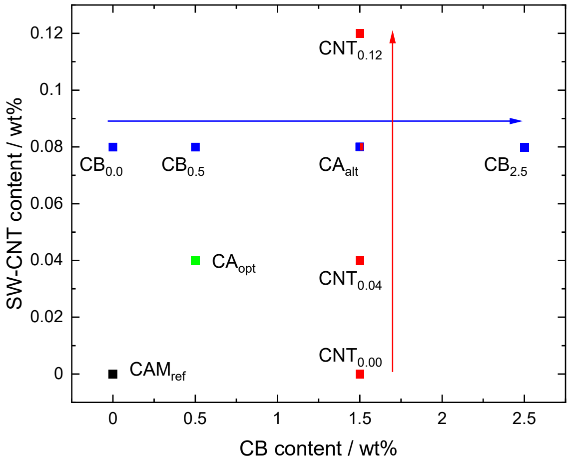

Figure 5-1: Illustration of the CA-Series’ composition variations

Once a preferred composition had been identified, the sequencing of the mixing procedure used to create the slurry was varied in order to gain a deeper understanding of the impact of the mixing procedure on not just the slurry, but also on the electrode and, finally, the cell (subsection 5.2). The following figure outlines the key differences between the investigated procedures in a simplified way.

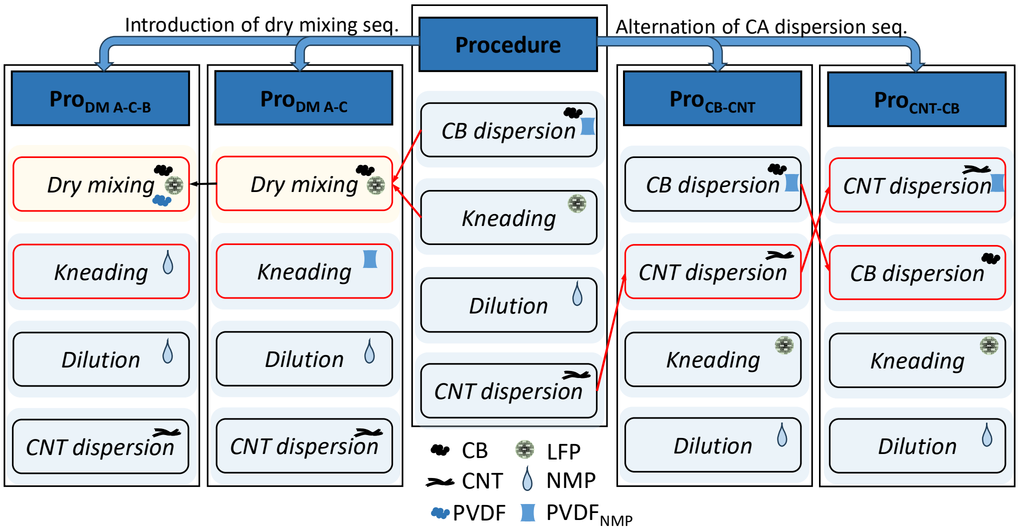

Figure 5-2: Illustration of the Procedure-Series’ variations

5.1. CA-Series

The following subsection investigates the effects correlating with the change of conductive additive while keeping the binder constant and adjusting the active material content. The components used are that of Table 4-1 the ratio of one slurry and its variations is listed in and the applied mixing procedure in detail is shown in Table 4-2 and Figure 4-2. The mixing procedure by which the components were processed is shown in Figure 4-3.

5.1.1. Unimodal CA variation

The following two figures illustrate the viscosity function of the CB_i and the CNT_i variation. It is important to note that all CB-containing slurries ($CB_{0.0}$ to $CB_{2.5}$) have a non-volatile SW-CNT solid content of 0.08 wt%, while all CNT-containing slurries ($CNT_{0.00}$ to $CNT_{0.12}$) have a CB solid content of 1.5 wt% and slurry CAM_{ref} has no CA at all. The designation’s index represents its SC_{NV}.

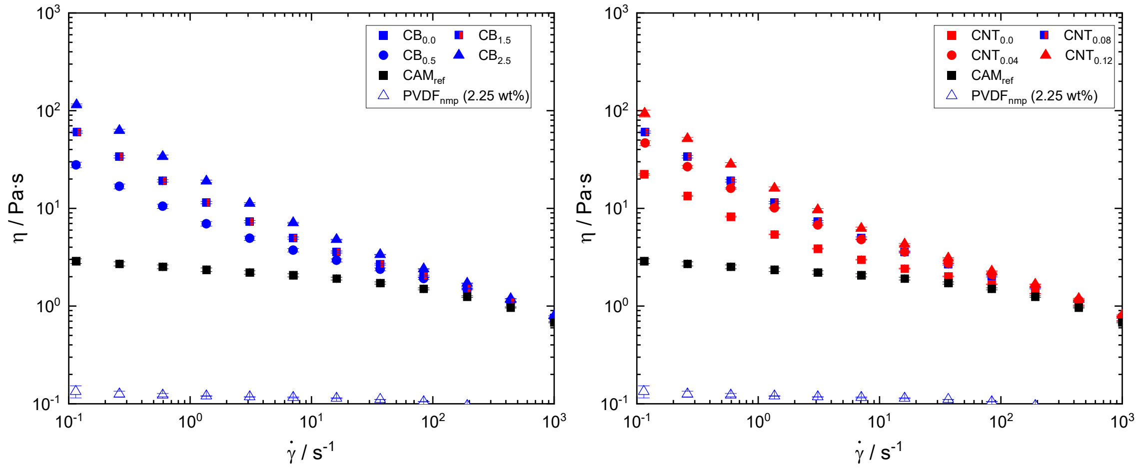

a) b)

Figure 5-3: Viscosity function of the CA-Series’ including CAM_{ref} and a PVDF solution of 2.25 wt%; a) CB_i variation; b) CNT_i variation

Figure 5-3a and b illustrate that CAM_{ref} exhibits the lowest viscosity across all shear rates. It is a suspension of LFP in a dissolved PVDF matrix. It is notable that the viscosity of the suspension exhibits minimal variation within the shear rate range of 0.1 to 100 s^{-1}. This observation suggests that the interaction between particles is relatively weak, given that no interaction such as adsorption between PVDF and the slurry components occurs [83]. The suspension has a volume fraction of approximately 16.5 vol% of LFP, the particle is of a spherical, polycrystalline, form and the D_{50} of it is 12 µm (D_{90} = 33 µm; D10 = 3 µm). It can be reasonably assumed that no strong colloidal interactions are to be expected among the CAM. The relative viscosity of CAM_{ref} is roughly 22 times that of its PVDF solution, which can be explained by the LFP acting as hard spheres, however the particles deviate from a perfect spherical form, thus leading to such an increase in viscosity. This implies that the flow behavior of the suspension CAM_{ref} is largely determined by the PVDF network and the containing particles. The viscosity function of a dilution row of PVDF solutions can be seen in the appendix, A 9-1a. To display the reproducibility of the procedure, slurry $CB_{1.5}$ (“CA_{alt}”) and its reproduction is displayed in the appendix A 9-1b. At a shear rate of roughly 0.1 s^{-1} the viscosity of two slurries lies between 61 and 73 Pa·s at an average value of 67 Pa·s, indicating a systemic error of roughly ± 9% between slurries. It should be noted that this is a very simplified estimation.

As the concentration of CB and SW-CNT is increased, the viscosity of the slurry rises. This rise also affects the shear-thinning behavior. It can be seen, that an increase in the CB content gives rise to a more pronounced monotonic shear thinning behavior, a phenomenon that is similarly evident upon the addition of SW-CNTs. This phenomenon can be attributed to the interaction between CB and CNT colloidal particles, leading to the formation of a network-like structure. This, in turn, strengthens the slurry’s structure in addition to the PVDF network. This leads to an increase in low shear viscosity (LSV), which is ultimately dominated by hydrodynamic forces as the shear rate increases, causing the structure to collapse and resulting in shear thinning behavior. However, the viscosity-increase of the CNT containing slurries is stronger, considering comparable small solids contents next to that of CB. At shear rates beyond 100 s^{-1} all viscosity curves superimpose irrespective of the CA content as no colloidal structure is maintained.

Figure 5-4 illustrates the LSV at a shear rate of 0.1 s^{-1} for both variations. It should be noted that the slurry designated CB$_{alt}$ is the alternative designation of CB$_{0.5}$ and CNT$_{0.08}$.

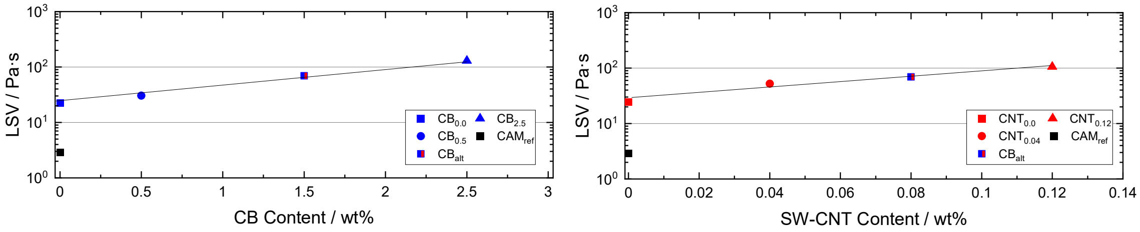

a) b)

Figure 5-4: Low shear viscosity at a shear rate of 0.1 s^{-1} as a function of the CA-Series’ variations in a) CB$_i$ and b) CNT$_i$

The slurry devoid of CB content (CB$_{0.0}$) exhibits an LSV of approximately 25.6 Pa·s the highest viscosity value is 130 Pa·s at a CB-SC of 2.5 wt%. An increase in CB-SC results in an exponential increase in LSV. A comparable trend is evident in the CNT variation. The LSV of the sample devoid of SW-CNT (CNT$_{0.00}$) is approximately 24.1 Pa·s, whereas an increase in the concentration of SW-CNT to 0.12 wt% results in an LSV of 105.8 Pa·s. As previously stated, the increase in LSV is more pronounced for the SW-CNT. This can be explained by the aspect ratio of the CNTs in comparison to the CB, as well as the high SSA. It is anticipated that the dimensions of the CNTs and their high specific surface area (approximately 400 m^2 g^{-1}) will result in a lower (electronic) percolation threshold, thereby facilitating a greater increase in viscosity. However, the fiber-typical stronger shear thinning behavior due to particle orientation cannot be observed, which is most likely due to its small SC.

Electrodes with a capacity loading of 2.85 mAh cm^{-2} were manufactured via table coating using the CA-Series’ slurries. The electrodes were calendered using three different calender gap sizes. The non-calendered electrode was incorporated into a set of four distinct electrode densities ϱ_i for each slurry, roughly referring to 1.7, 2.1 and 2.2 g cm^{-3}, in addition to the native density of ca. 1.1 g cm^{-3}.

Figure 5-5 shows the peel strength (F$_{peel}$) of the CA-Series electrodes in dependence of the electrode density. Figure 5-5a illustrates the variation in CB content. Prior to compression, the peel strength of all CB variations falls within the range of 7.5 to 14.5 N m^{-1}. The initial compression density of approximately ϱ_i=1.7 g cm^{-3} exhibited a modest enhancement in peel strength, with CB$_{2.5}$ exhibiting the most pronounced increase from 14.5 to 20 N m^{-1}. However, as the compression increases, the peel strength decreases. This resulted in an overall reduction in F$_{peel}$ for all CB-containing samples, with CB$_{1.5}$ exhibiting the lowest peel strength (5.4 ± 0.5 N m^{-1}) among the samples. The behavior of electrodes devoid of carbon black was somewhat distinct. The CAM$_{ref}$ electrode contains no CA. The peel strength increased from 7.6 ± 0.7 N m^{-1} at the lowest density to 16.6 ± 1.1 N m^{-1} at the highest. Additionally, Sample $CB_{0.0}$ does not contain any carbon black, but it does contain 0.08 wt% of non-volatile solids content SW-CNT. No notable alteration in peel strength was discerned for this electrode.

The peel strength of the CNT_i samples (Figure 5-5b) exhibits a comparable trend, indicating that the incorporation of CNTs enhances peel strength under slight compression. For samples with a density exceeding 2 g cm^{-3}, the peel strength was determined to be either equivalent to that of the uncalendared electrode or lower. The sample comprising no CNTs but containing a non-volatile SC of 1.5 wt% carbon black ($CNT_{0.00}$) exhibits a similar behavior to the other CNT-containing electrodes. A comparison of this observation with that of the viscosity function indicates that the CA-Binder microstructure collapses during compression, resulting in a weaker peel strength.

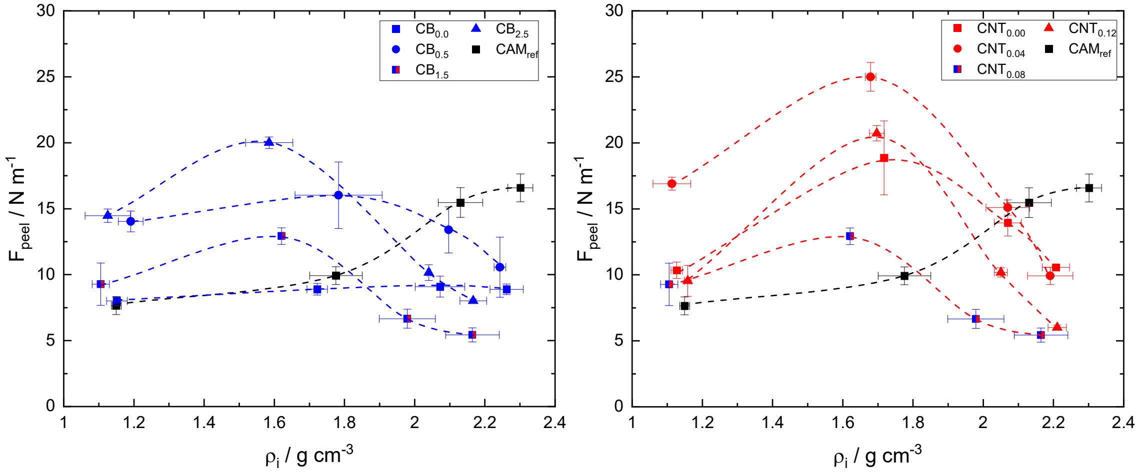

a) b)

Figure 5-5: Peel strength in dependence of electrode density of the CA-Series electrodes; variations in a) CB content and b) CNT content

The peel-test is a methodical process that measures the force present during delamination of coating and carrier foil. Such a collapse may occur either within the coating itself or at the interface between the coating and the current collector. In the event of an interfacial collapse, the measurement can be attributed to an adhesive failure mode. Conversely, in the case of an intra-coating collapse, it can be considered a cohesive failure mode. Subsequent to the completion of the measurements, an investigation was conducted on the samples’ substrate. It was observed that some samples exhibited a neat peeling action, while others left a residual coating on the substrate. The subsequent table presents the post-measurement images of the current collector foil of sample $CB_{0.0}$, which is of particular interest since it demonstrates a constant F_{peel} regardless of the electrode’s density. Please refer to Table A 9-7 for better visibility.

It can be observed that the remaining coating on the foil varies in accordance with the electrode density. The electrodes of the neat density of roughly 1.1 g cm^{-3} and the compressed density of 1.7 g cm^{-3} exhibit a considerable quantity of remaining material, in contrast to the electrodes with a density of 2.1 and 2.2 g cm^{-3}, where the remaining material appears to be distributed in a fine film on the surface. The second row displays the YC channel spectrum of the microscope images captured of the post-peeled foils. It is notable that the two electrodes with the lowest density exhibit a distinct peak, while the other densities display a less pronounced peak, which is likely attributed to the finely dispersed residue. Row "iii" presents the top light microscope images of the previous row’s YC spectrum. Here, the threshold condition of subsegment 4.4.2 was applied, resulting in a conversion to a black and white image. It can be validated that electrodes $\varrho_{CB_{0.0}}$ = 2.1 and 2.2 exhibit a fine dispersion of residue on the foil surface, in contrast to the other electrodes, which display clusters of remnants. The data in row “ROFA” represents the calculated area of residue on the foil surface, expressed as a percentage of the total image area. The electrodes with densities of roughly 1.1 and 1.7 g cm^{-3} exhibited a calculated ROFA of 72.0 and 70.7%, respectively. The ROFA for densities 2.1 and 2.2 g cm^{-3} is significantly lower, at 59.1% and 56.4%, respectively.

Table 5-1: Post-measurement images of electrode CB$_{0.0}$; $\varrho_{CB_{0.0}}$– electrode’s approximate density; i – image of current collector with the coating’s remainder; ii – color value spectrum of the original microscope image; iii – top light microscope images after threshold filter application; ROFA – percentage of the remainder’s occupied area (YC-range 0-80)

$\varrho_{CB_{0.00}}$	1.1	1.7	2.1	2.2
i				
ii	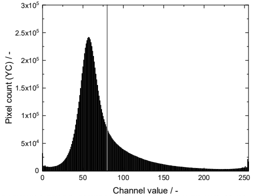	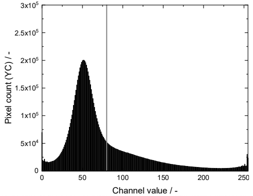	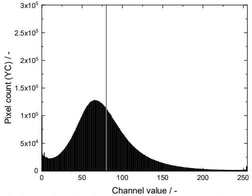	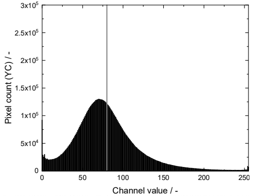
iii	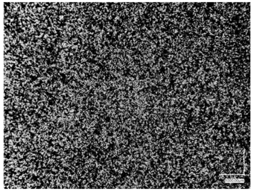	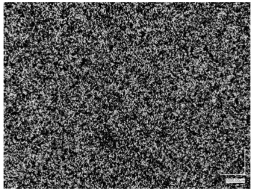	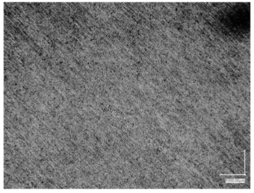	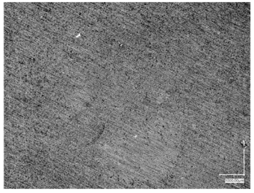
ROFA	72.0 %	70.7 %	59.1 %	56.4 %

Assuming that a ROFA of more than 60 % can be interpret as an cohesive peel strength failure. The electrodes of CB$_{0.0}$ with a density of 1.1 and 1.7 g cm^{-3} have a predominantly mechanical cohesive failure mode, whereas the other densities have a predominantly adhesive failure mode. While the failure mode varies with density, the peel strength of CB$_{0.0}$ does not appear to exhibit a strong dependence on density, displaying instead a relatively constant value. A similar behavior is observed when comparing the other unimodal variations of CB$_i$ and CNT$_i$, whereby the measured peel strength is found to depend on the calendered density.

The subsequent Figure 5-6a illustrates the ROFA in relation to the electrode’s density. While the individual values of the samples vary throughout the series, all CA-containing samples exhibit a similar behavior in that, with increasing electrode density, the ROFA decreases, as indicated by the dashed line. This demonstrates that the failure mode undergoes a significant transformation at varying rates of compression, exhibiting independence from the compositions of CA content, whether CB or SW-CNTs. At the outset, all electrodes with a neat density of approximately 1.1 g cm^{-3} exhibit a predominantly cohesive failure mode, indicating that the adhesive forces at the interfacial layer, between the substrate and the coating, are more pronounced than the coating’s cohesive forces. This phenomenon can be observed up to a density of approximately 1.7 g cm^{-3}. Nevertheless, further compression of the coating results in a predominantly adhesive failure, indicating that the structure providing the cohesive strength becomes stronger. Figure 5-6b illustrates the peel strength as a function of CA content, categorized according to the series’ approximate electrode densities. The data demonstrate that the highest measured peel force is observed in all variations at a density of approximately 1.7 g cm^{-3}. The highest density is associated with the weakest F_{peel}, and the slightly less compressed electrode density of 2.1 g cm^{-3} exhibits reduced peel strength in respect to the others.

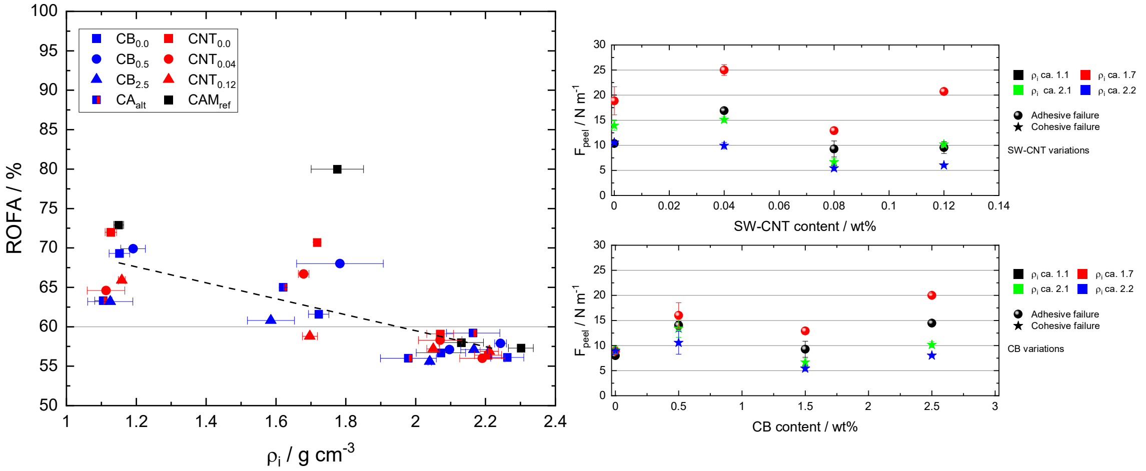

a) b)

Figure 5-6: a) Residue occupied foil area (ROFA) after peel strength measurement of the CA-Serie’s electrodes in dependence of density, dashed line to guide the eye; b) Peel strength in dependence of approximate electrode density of the CA-Serie’s variations in CA

One potential explanation for the aforementioned behavior is as follows. The mechanical strength of the electrode is primarily determined by the PVDF. The polymer, is distributed throughout the coating, and may partially or fully encapsulate the CAM, the CA, and void spaces. The electrode’s compression causes deformation of the coating, which increases the packing density of its components. This results in the polymer domain encapsulating and binding a greater area of particle surface, thereby enhancing the mechanical strength of both the coating and the interfacial layer between the coating and the current collector. Nevertheless, as the deformation persists, an increasing portion of the polymer network approaches must exceed its elastic stage and approach the stage of plastic deformation, which results in a reduction in the structure’s mechanical strength. The coating used for the electrodes was applied on one side only. It is possible that the compression resulted in a lack of uniformity in the deformation, leading to a deformation along the foil’s plane. It is possible that this deformation could be compensated within the three-dimensional coating, however, it is also conceivable that portions of the relatively two-dimensional polymer layer situated between the coating and the foil may have delaminated partially, which would ultimately result in a weakening of its mechanical structure. Consequently, the initial compression enhances the structural integrity of both the coating and the interface, leading to an increase in F_{peel}. Further compression serves to reinforce the coating, but simultaneously compromises the integrity of the interfacial layer. This transition to an adhesive failure mode and a concomitant reduction in peel strength are the inevitable consequences of such compression.

In addition to the preceding theory, it should be noted that electrodes approaching peak compression tend to deform within the foil’s plane, which can result in a wider coating. Furthermore, the thickness of the foil may also be affected, resulting in planar deformation. In both instances, the weight of the electrode and the foil is reduced. Neither of these changes was observed in the electrodes of this series.

The volume resistivity of the series’ CB$_i$ and CNT$_i$ variations are illustrated in Figure 5-7a and b respectively. It can be observed that as the CA increases, the value of ρ_C decreases, indicating an increase in conductivity. However, an increase in compression results in a reduction in volume resistivity. As the name suggest, an increase of the conductive additives exerts the most significant influence on the reduction in resistivity. Nevertheless, the discernible compression dependence suggests that the percolation of the carbon binder domain (CBD) is being enhanced. Furthermore, an improvement in conductivity is evident in higher densities of 2.1 and 2.2 g cm^{-3}. In light of these observations, it can be postulated that progressing compression enhances the CBD percolation in terms of conductivity, however the peel strength data suggest that the polymer network is partially weakened.

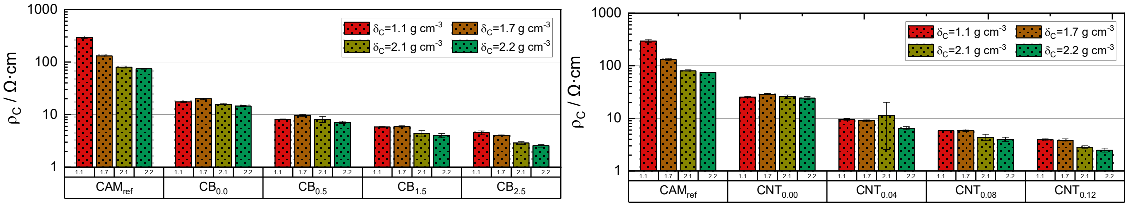

a) b)

Figure 5-7: Volume resistivity (ρ_C) of the CB$_i$ (a) and CNT$_i$ (b) variations

The following two figures illustrate the total electrode resistivity, which can be expressed as the sum of the interface resistance (ρ_I) and the specific contact resistance (ρ_{CN}), the latter of which is the volume resistivity normalised by the coating height (32).

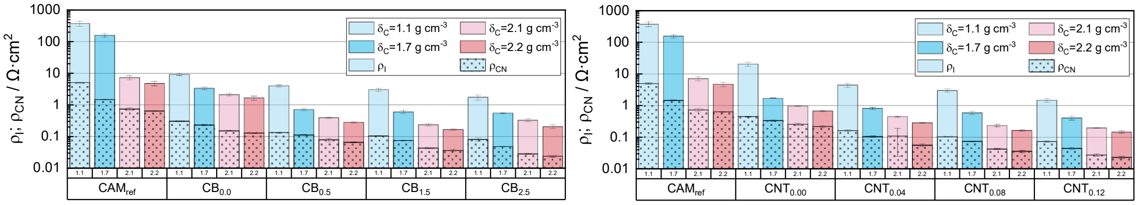

a) b)

Figure 5-8: Total resistance of the CB$_i$ (a) and CNT$_i$ (b) variations; total resistance divided into specific contact resistance ρ_{CN} and interface resistance ρ_I

As anticipated, the sample devoid of a conductive additive exhibits the highest total resistance. Upon the introduction of CA, the resistance markedly decreases. The largest contribution to the total resistance is that of the interface resistance, with the specific contact resistance accounting for approximately 10 to 20 % of the total resistance. The compression of the electrode resulted in an improvement in conductivity, manifested as a reduction in total resistance. This effect was more pronounced in electrodes with minimal CA and diminished with increasing CA. The addition of a high concentration of conductive additive had a negligible impact on the conductivity of the electrodes when subjected to compression. It seems plausible to suggest that this is due to the fact that the CBD’s percolation threshold has already been exceeded, which consequently results in only a minor improvement when further compression is applied. The same reasoning can be applied to explain the minimal change in interfacial resistance at higher densities.

5.1.2. Bimodal CA variation

The variation observed in both CB and CNT within the CA-Series resulted in slight differences in behavior in the slurry and the subsequent electrode. Figure 5-9a illustrates the viscosity function of the bimodal variation of CA. It was determined by the ambition to reduce CA.

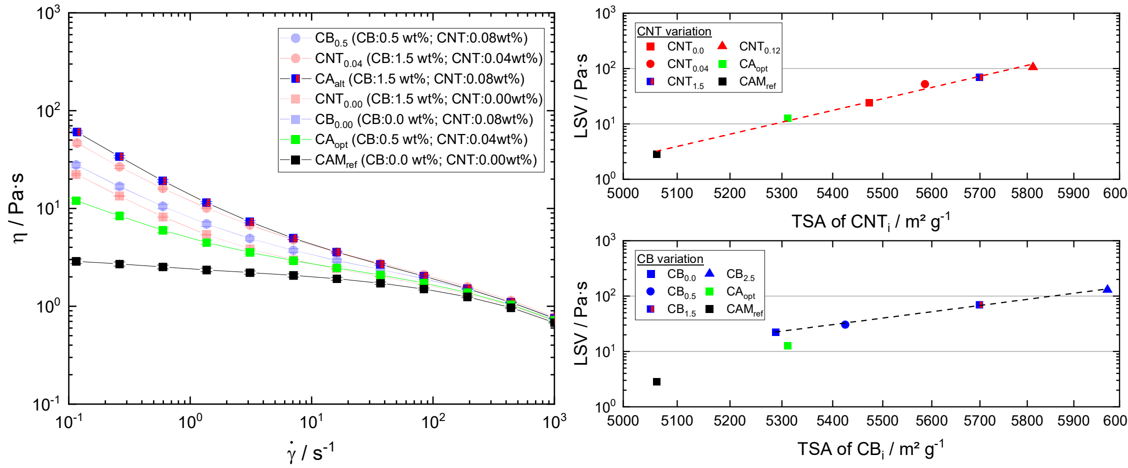

a) b)

Figure 5-9: a) Viscosity function of the CA-series’ bimodal CA-variation (the content of CB and SW-CNT listed for transparency; b) LSV at 0.1 s^{-1} as a function of the solid’s (CAM, CB and SW-CNT) total surface area (TSA)

The CA content of slurries CA_{opt} and CA_{alt} is a mixture of $CB_{0.5}$ and $CNT_{0.04}$, and $CB_{0.0}$ and $CNT_{0.00}$, which are considered to be complementary compositions. A comparison of the viscosity functions of slurries CA_{opt} and CA_{alt} with those of the CB_i and CNT_i variations suggests that the CA_{opt} viscosity function may lie between that of CAM_{ref}, representing no CA, and $CB_{0.5}$ and $CNT_{0.04}$. The viscosity value of the slurry CA_{alt} is higher than that of either $CB_{0.0}$ or $CNT_{0.00}$. The specific surface area of the CA has an impact on the CBD percolation threshold. It can be assumed that the higher the total surface area (TSA) of the CA, the greater the effect on the viscosity of the slurry. Figure 5-9b illustrates the low shear viscosity at a shear rate of 0.1 s^{-1} in relation to the solid’s total surface area (TSA). The reference sample without CA (CAM_{ref}) has a total surface area (TSA) of approximately 5.060 m^2 g^{-1}, provided by the CAM. The addition of CA resulted in a decrease in the CAM’s TSA contribution, but the TSA was ultimately increased due to the high specific surface area (SSA) of the CA substitution. It can be observed that the variation in CB content results in a linear increase in LSV within the $CB_{0.0}$ to $CB_{2.5}$ range in the semi-log plot, which corresponds to an exponential relationship. However, the data points for CB_{opt} and CAM_{ref} do not align with this linear prediction. Upon analysis of the varying contents of the SW-CNTs, it was observed that each LSV value exhibited a linear correlation. This suggests that within this bimodal CA variation, the SW-CNT predominantly determines the flow behavior of the slurry, likely due to its high aspect ratio and SSA. This non-linearity may also introduce another microstructure.

Figure 5-10a shows the peel strength of the electrodes represented in the preceding figure’s slurry. Upon analysis of the peel strength, it was observed that the CA_{opt} variation of the neat electrode exhibited a F_{peel} value of approximately 13.8 ± 0.8 N m^{-1}, which was found to be lower than that of $CB_{0.5}$ and $CNT_{0.04}$. Furthermore, this finding differs from the previously observed trend. It was observed that the initial compression to a density of 1.7 g cm^{-3} did not result in an increase in F_{peel}. Further compression to approximately 2.1 g cm^{-3} resulted in a reduction in the electrode’s peel strength value, while the highest compression led to an improvement in this parameter. The structural composition that provides mechanical resistance appears to be distinct from that observed in the other electrodes. However, the failure mode of CA_{opt} is analogous to that observed in the previously studied electrodes, as illustrated in Figure 5-10b. It is possible that this peel strength behavior is not distinct from that observed in the other electrodes, but the minimal and maximal peel strength values are not presented in this series of experiments, as the structure’s maximum might be observed at a different point, for example, at 1.4 g cm^{-3}.

It can be hypothesized that the significantly reduced CA content of CA_{opt} may result in a more extensive PVDF network, given that less total surface area must be encompassed by the polymer. Consequently, the compression’s deformation enhances the peel strength. Furthermore, additional compression results in a reduction in structural integrity, ultimately leading to the formation of a new structure that strengthens again.

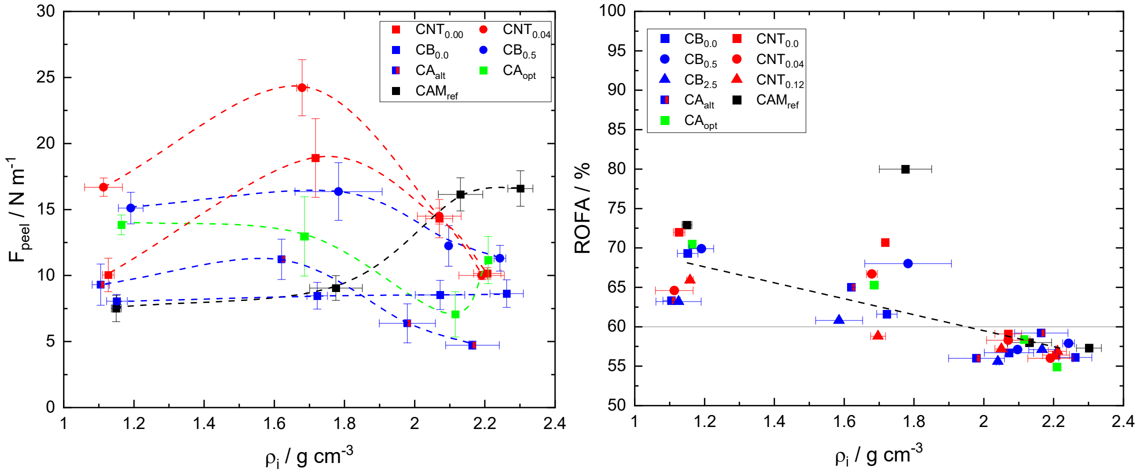

a) b)

Figure 5-10: a) Peel strength in dependence of electrode density of the CA-Series’ bimodal CA variation; b) residue occupied foil area (ROFA) after peel strength measurement of the CA-Serie’s electrodes in dependence of density, dashed line to guide the eye

Figure 5-11a illustrates the volume resistivity of CA_{opt} and CA_{alt}, which is presented in the context of the preceding discussion on electrical resistances. The electrode designated CAM_{ref}, which lacks CA, exhibits the highest volume resistivity. As compression increases, conductivity improves. The electrode’s CA content is illustrated in Figure 4-2 (p. 24). The CA_{opt} electrodes exhibited a resistivity of greater than 10 Ω cm, while the respective complementary electrodes, $CNT_{0.04}$ and $CB_{0.5}$, demonstrated a resistivity slightly lower than 10 Ω cm. It is to be expected that the complementary electrodes will exhibit superior conductivity, given that they contain a greater quantity of conductive additives than CA_{opt}. The electrodes of CA_{alt} were found to have a resistance of approximately 6 Ω cm, while their complementary electrodes, $CNT_{0.00}$ and $CB_{0.0}$, exhibited a resistance greater than 14 Ω cm. A comparable trend was observed in the analysis of the specific contact resistance and interface resistance, as illustrated in Figure 5-11b. CA_{opt} demonstrated a slightly higher total resistance than $CNT_{0.04}$ and $CB_{0.5}$, while CA_{alt} exhibited the lowest total resistance.

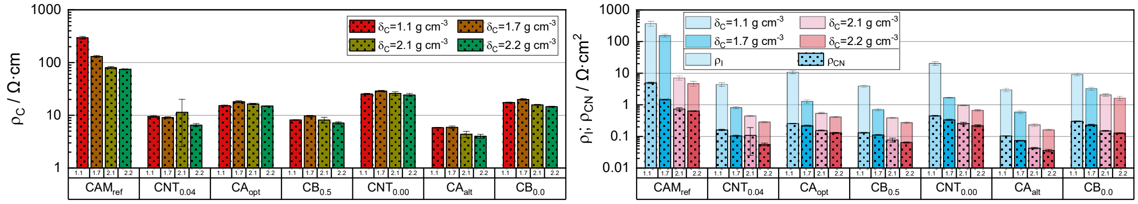

a) b)

Figure 5-11: Resistances of CA-Series’ bimodal CA variation; a) volume resistivity ρ_C; b) total resistance divided into specific contact resistance ρ_{CN} and interface resistance ρ_I

A further analysis of the electrode structure was conducted using mercury intrusion, with the objective of gaining insights into the pore structure of the electrode. The results of this analysis are presented in Figure 5-12. The electrodes of CA_{opt} and CA_{alt} are shown, both with a respective density of approximately 1.1 and 2.2 g cm^{-3}. The full set of samples is shown in A 9-2

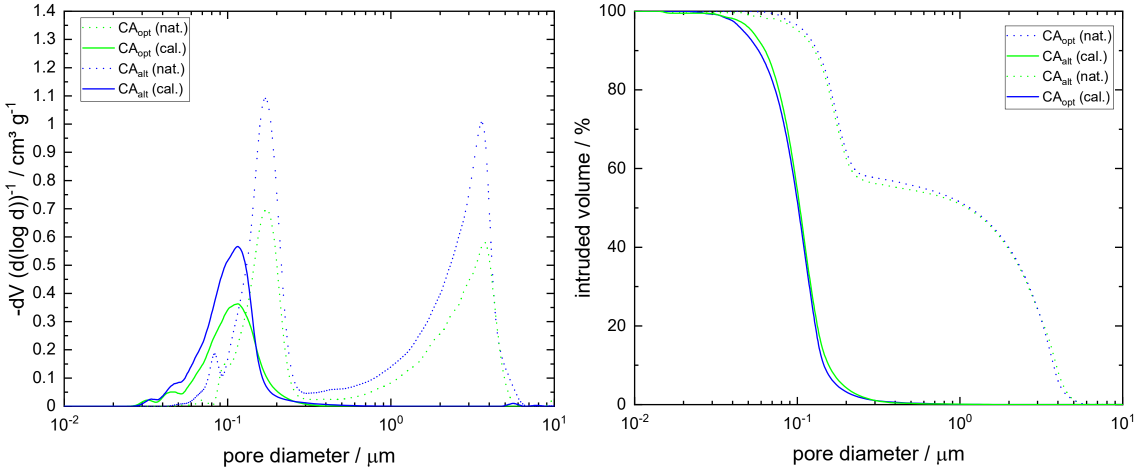

a) b)

Figure 5-12: HG-porosimetry data of electrodes CA_{opt} and CA_{alt}, calendered (cal.) and native (uncompressed; nat.); a) pore size distribution; b) accumulated volume

The native electrodes exhibit two peaks at approximately 0.2 and 3.7 µm, as illustrated in Figure 5-12a. These peaks accommodate the largest pore-volume fraction of the electrode, which is approximately 40 and 60 vol%, respectively (Figure 5-12b). The pore size distribution is highly comparable between the two materials, however the pore volume of CA_{opt} is significantly lower than that of CA_{alt}. It is counterintuitive that CA_{opt} has lower pore volume than CA_{alt}, given that it has a less CA. However, the PVDF binder may encapsulate more particles and voids, which could affect the pore volume. This is reflected in the previously introduced theory regarding the mechanical strength and the CBD distribution. It might be attributed to the differences in CA. The calendered electrodes only showed one peak for both electrodes at a pore diameter of approximately 0.1 µm. Furthermore, CA_{alt} exhibited less specific infiltrated mercury.

This discrepancy is likely attributable to the inherent differences in CA. The calendered electrodes exhibited a single peak for both electrodes at a pore diameter of approximately 0.1 µm. Once more, the CA_{alt} measurement exhibited a diminished degree of infiltrated mercury.

In light of the peel strength data pertaining to the bimodal variations, it can be posited that CA_{opt} represents an adequate compromise between acceptable mechanical strength and equally acceptable electronic resistivity. This conclusion is particularly supported by the fact that the electrode contains only 0.04 wt% SW-CNT, which is half that of the CA_{alt} electrode. Furthermore, this results in the composition having the highest CAM content of all the electrodes. Both of these factors represent significant economic incentives that cannot be overlooked. Consequently, the composition of CA_{opt} will be employed in the subsequent Procedure Series.

5.2. Procedure-Series

The procedure for producing CA_{opt} and CA_{alt} is identical. It begins with the dispersion of CB in a binder solution, followed by the addition of CAM, and concludes with the incorporation of SW-CNT. The remaining four variations are as follows: $Pro_{CB\text{-}CNT}$ represents the initial dispersion of CB in a binder solution, followed by the addition of SW-CNTs and subsequent components. $Pro_{CNT\text{-}CB}$ represents a variation in which the CB dispersion sequence has been swapped with that of the SW-CNT. The $Pro_{DM\ A\text{-}C}$ procedure commences with the dry mixing of the CAM and CB, followed by their dispersion in a binder solution, which is then completed with the addition of SW-CNTs. The $Pro_{DM\ A\text{-}C\text{-}B}$ procedure, on the other hand, begins with the dispersion of the CAM, CB, and undissolved binder powder, which is then completed with the addition of SW-CNTs. The aforementioned procedures are meticulously delineated in subsection 4.2.1, Figure 4-4 and Figure 4-5.

Figure 5-13a illustrates the viscosity function of the series' slurries. The alteration of the mixing sequence results in notable discrepancies in the viscosity function of the slurry, with the exception of CA_{alt} and CAM_{ref}, which remain consistent across all compositions. The variations of the CA sequencing ($Pro_{CB\text{-}CNT}$ and $Pro_{CNT\text{-}CCB}$) exhibit slightly lower low shear viscosity at 0.1 s^{-1} than CA_{opt} and the slurries of the dry mixing variation ($Pro_{DM\ A\text{-}C}$ and $Pro_{DM\ A\text{-}C\text{-}B}$), which in turn exhibit even lower values. However, these values are not as low as those observed for the no-CA reference (CAM_{ref}). This suggests that there is a reduction in colloidal interaction, resulting in a structure that is less resilient to deformation than CA_{opt}. Furthermore, as LSV decreases, the shear thinning behavior becomes less evident. In contrast to the CA series, the alterations in viscosity are not confined to the low shear viscosity at 0.1 s^{-1}. The magnification demonstrates that the high shear viscosity of the procedure variations at 1000 s^{-1} is not aligned with that of CA_{opt} (0.73 Pa·s) and, for instance, 0.57 Pa·s of $Pro_{DM\ A\text{-}C}$. This may be indicative of a change in the polymer's structure; however, the changes in value are relatively minor, suggesting that no significant mechanical degradation of the PVDF has occurred.

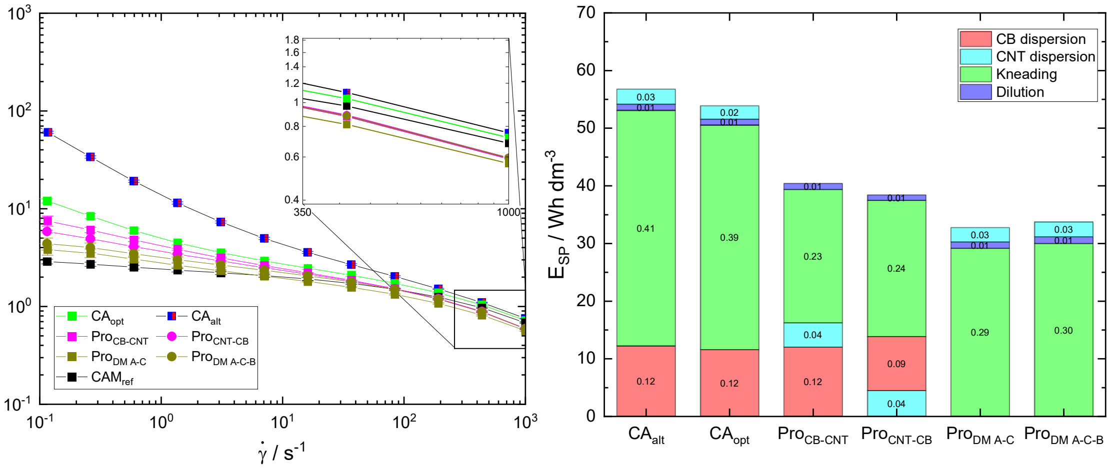

a) b)

Figure 5-13: a) Viscosity function of the Procedure-Series' variations; b) energy input of the Procedure-Series mixing procedure sequences

The mixing procedures exhibit disparate sequences and, consequently, disparate TSC and degrees of filling per sequence. The details are presented in subsection 4.2.1. Nevertheless, the fundamental elements of the procedure can be classified into four distinct sequences. The four principal stages of the procedure are the dispersion of CB, the dispersion of CNT, kneading and dilution. Figure 5-13b illustrates the specific energy input of each mixing procedure, classified according to the four aforementioned sequences. In general, the energy input required for the production of CA_{opt} and CA_{alt} was comparable, with a value of approximately 54 and 57 Wh dm^{-3}, respectively. Furthermore, the individual sequences exhibited a high degree of similarity. The remaining procedures exhibit a lower energy input. The energy input of the $\text{Pro}_{\text{CB-CNT}}$ and $\text{Pro}_{\text{CNT-CB}}$ procedures was found to be 40 and 39 Wh dm^{-3}, respectively. The $\text{Pro}_{\text{DM A-C}}$ and $\text{Pro}_{\text{DM A-C-B}}$ procedures exhibited energy inputs of 33 and 34 Wh dm^{-3}.

It can be observed that, within the CA sequence variations, the $\text{Pro}_{\text{CNT-CB}}$ procedure requires less energy input when dispersing CB and CNT than the $\text{Pro}_{\text{CB-CNT}}$ procedure. This is likely due to the fact that the CB dispersion sequence has a higher TSC in the $\text{Pro}_{\text{CB-CNT}}$ procedure than in the $\text{Pro}_{\text{CNT-CB}}$ procedure, which results in a higher viscosity and subsequently a higher energy input due to the constant tool speed of the aforementioned procedures. The same rationale can be extended to the kneading sequence. Both procedures exhibit a TSC of approximately 59 wt%, while CA_{opt} and CA_{alt} demonstrate a TSC of 60.4 and 60.8 wt%, respectively.

It should be noted that the procedures $\text{Pro}_{\text{DM A-C}}$ and $\text{Pro}_{\text{DM A-C-B}}$ are somewhat distinct from the others. These procedures have the lowest viscosity and the lowest energy input while kneading, with a significantly lower energy input than CA_{opt}, although they have the same TSC in the kneading sequence. It is established that dry mixing alters the morphology of the mixture, by coating the CAM with CB [133, 134]. This subsequently establishes a lower viscosity due to the fact that the less voluminous carbon black is present in the continuous phase, and consequently, there are fewer colloidal particle interactions [115]. This also explains why $\text{Pro}_{\text{DM A-C-B}}$ is slightly higher in viscosity than $\text{Pro}_{\text{DM A-C}}$, as the dry binder was initially coated with CB, and following its dissolution, the fraction of CB in the continuous phase is larger than that of $\text{Pro}_{\text{DM A-C}}$, which results in a slightly higher viscosity.

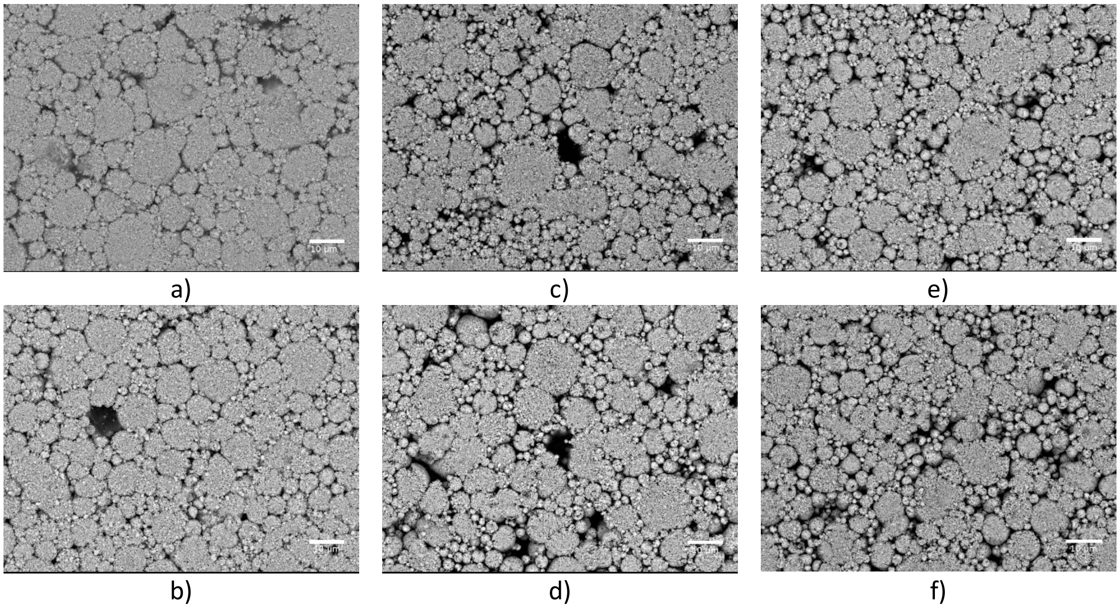
a) c) e)
b) d) f)

Figure 5-14: SEM Images of the Procedure-Series' electrodes at a density of roughly 2.2 g cm^{-3}; a) CA_{alt} b) CA_{opt} c) $\text{Pro}_{\text{CB-CNT}}$ d) $\text{Pro}_{\text{CNT-CB}}$ e) $\text{Pro}_{\text{DM A-C}}$ f) $\text{Pro}_{\text{DM A-C-B}}$

The morphology of the slurries' electrodes was characterized via scanning electron microscopy (SEM). Figure 5-14 illustrates the surface images of the electrodes with a density of approximately 2.2 g cm^{-3}. As illustrated in Figure a), the surface of CA$_{alt}$ exhibits a notable difference in grain border sharpness when compared to the other surface images. The LFP particle, which is a polycrystalline particle with a D$_{50}$ of 12 µm, displays a less defined grain border than the other images. This can be attributed to the markedly elevated proportion of conductive additives incorporated into this particular composition. In terms of particle size distribution, it appears that CA$_{alt}$ exhibits larger particle aggregates on the surface than the other electrodes. The particle size distribution of CA$_{opt}$ (b), which is produced using the same mixing procedure but with a reduced CA content, is comparable. On the surface of the Pro$_i$ electrodes (c-f), the presence of particles below 10 µm is evident. It is probable that the distribution of CA is finer and more homogeneous than in the CA$_i$ electrodes, which allows for a more precise optical recognition.

The topographically emphasized images of the surface are illustrated in Figure 5-15. The figure's first Column, designated as "1," illustrates the magnification of an electrode segment. This magnification is further enhanced in the second column. Column 3 illustrates the formation of conductive aggregates, while column 4 presents the same segment at a higher magnification. No image indicated the formation of fissures in the particles as a result of compression. The magnification of CA$_{alt}$ (a1) reveals structures that are likely to be smaller LFP particles. However, as with the overview images, the borders are not sharp, and further magnification does not alter this effect. It is possible that a combination of single crystals may have chipped off the polycrystalline LFP particles distributed with carbon black in the cavities between the particles. Ultimately, the electrode's slurry underwent the greatest energy input and exhibited the highest viscosity, which may facilitate the grinding of a limited quantity of CAM at the dispersion tool. With regard to the conductive additive, it can be observed that some of the particles with a diameter of less than 10 µm are embedded in the CA compound of carbon black (a4) and SW-CNTs (red arrows: a3 and a4). It should be noted that single SW-CNTs have dimensions smaller than the resolution of the scanning electron microscope can detect. It can thus be concluded that these must be bundle-like aggregates, which appears to be a plausible conclusion, since the stabilization of the CNT dispersion is of a kinetic nature and not steric. Therefore, it is possible that a portion of the SW-CNT particles may coagulate once they are introduced into a slurry. The electrode CA$_{opt}$ displays a more acute appearance, with discernible clusters of carbon black (red arrow b1 and image b4) and smaller LFP particles. Additionally, SW-CNT bundles (red arrow b2) are evident. Once more, some areas display the presence of CA compounds (b3). The images in rows c) and d) illustrate the Pro$_{CB\text{-}CNT}$ and Pro$_{CNT\text{-}CB}$ electrodes, respectively. The two samples exhibit a striking resemblance in their visual appearance (c1 and d1). Of particular note is the observation of a web-like structure in the electrodes of both procedures, as indicated by the marking in c2 and d2. Given that the polymer binder is not visible using this SEM, it is reasonable to conclude that it is a cluster of a finely percolating CB and SW-CNT network. The presence of CA agglomerates on the surface is apparent in images c3 and d3. These agglomerates are composed of CB and CNT, as illustrated in images c4 and d4. The images in rows e) and f) depict the Pro$_{DM\ A\text{-}C}$ and Pro$_{DM\ A\text{-}C\text{-}B}$ electrodes, respectively. No notable differences are perceptible between the two (e1 and f1). The CAM demonstrates that no damage was incurred as a consequence of the mixing sequence. In addition to some fiber-like structures, which are presumed to be bundles of SW-CNT (f2), there are also CA compounds of CB (e3 and f3) and SW-CNT (red arrows: e4 and f4) visible. It is important to note that the magnification in question does not disprove the previously mentioned effect of a dry mixing sequence on the coating of carbon black, given that only 0.5 wt% of CB was used in these compositions, which resembles a significantly smaller volume than that of the LFP.

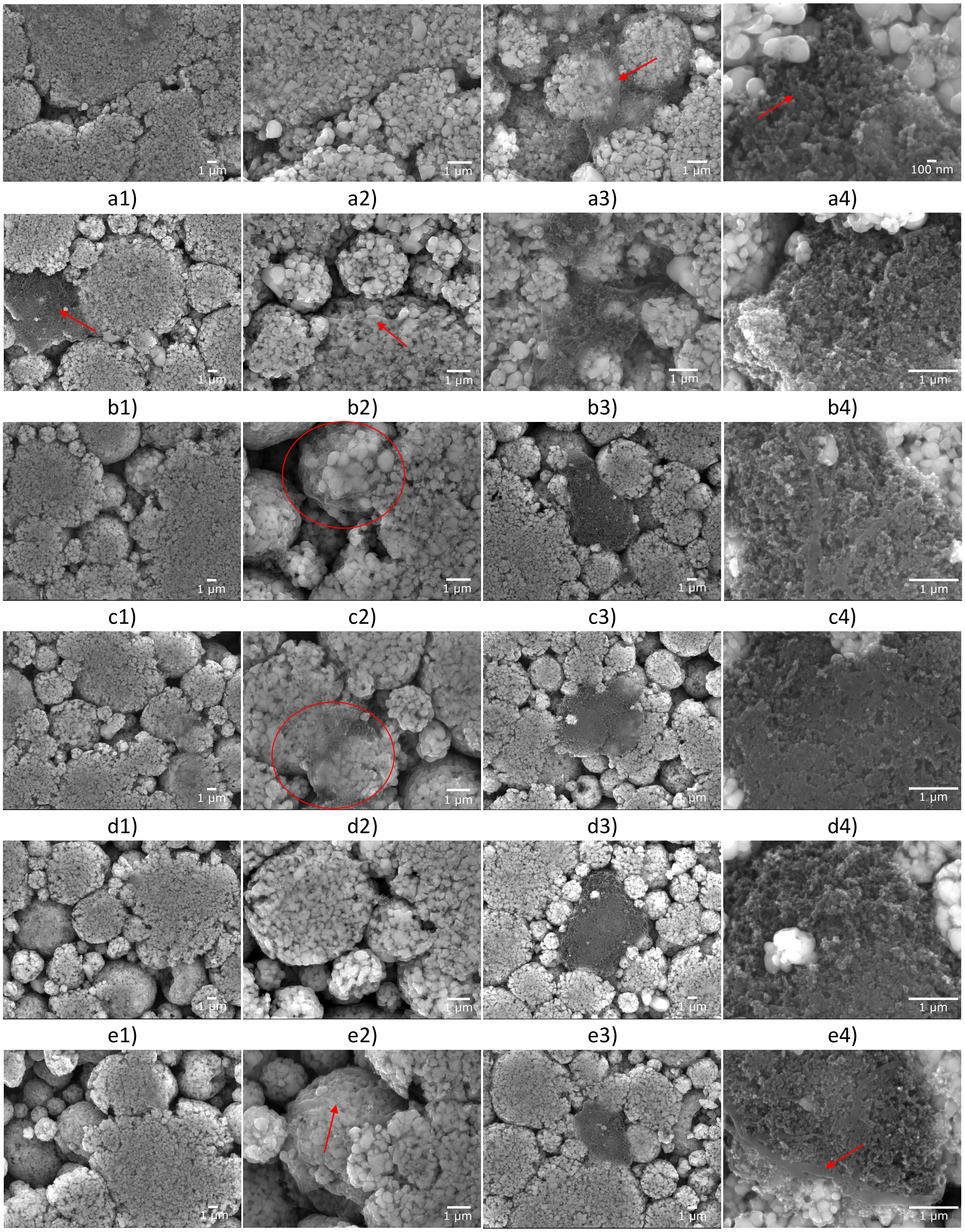

a1) a2) a3) a4)
b1) b2) b3) b4)
c1) c2) c3) c4)
d1) d2) d3) d4)
e1) e2) e3) e4)
f1) f2) f3) f4)

Figure 5-15: SEM Images of the Procedure-Series’ electrodes at a density of roughly 2.2 g cm^{-3}; a) CA$_{alt}$ b) CA$_{opt}$ c) Pro$_{CB\text{-}CNT}$ d) Pro$_{CNT\text{-}CB}$ e) Pro$_{DM\ A\text{-}C}$ f) Pro$_{DM\ A\text{-}C\text{-}B}$

Figure 5-16 presents an EDX mapping of the electrode surface, which reveals the presence of carbon signals. It is noteworthy that a substantial area is encompassed by these images.

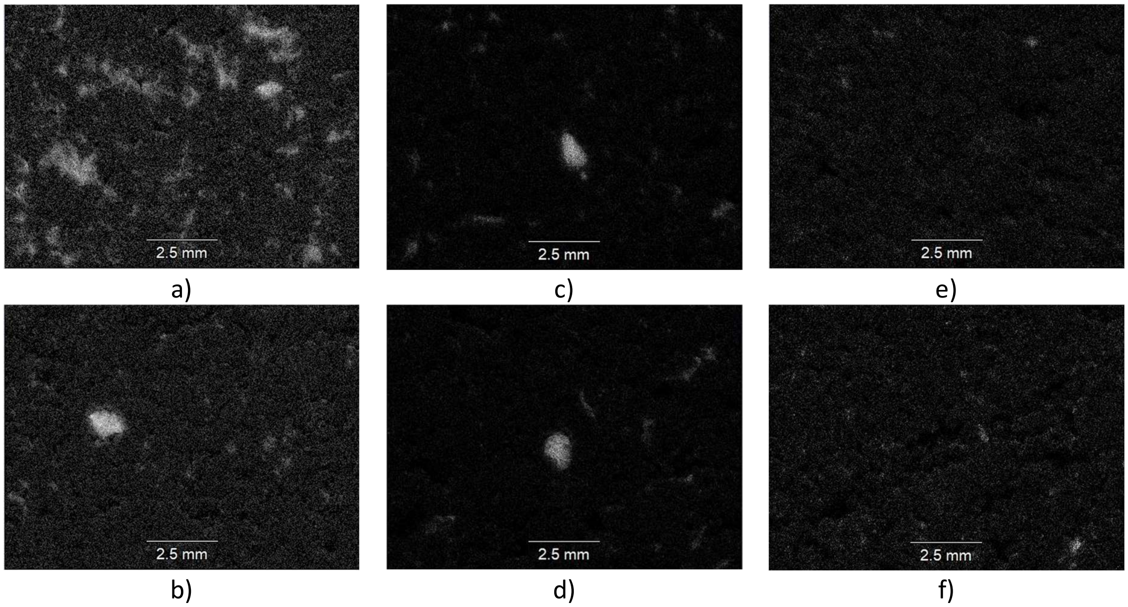

Figure 5-16: Carbon-signal EDX mapping of the Procedure-Series electrodes at a density of roughly 2.2 g cm^{-3}; a) CA$_{alt}$ b) CA$_{opt}$ c) Pro$_{CB-CNT}$ d) Pro$_{CNT-CB}$ e) Pro$_{DM\ A-C}$ f) Pro$_{DM\ A-C-B}$

It is evident that CA$_{alt}$ (a) exhibits the highest number of carbon signals in this comparison, given that it possessed the highest CA content. The CA$_{opt}$ electrode (b) displays both aggregates of CA, which appear as bright clusters, and more finely dispersed carbon, which manifest as small bright dots. The sequence variations Pro$_{CB-CNT}$ (c) and Pro$_{CNT-CB}$ (d) exhibit a single bright agglomerate in each image, accompanied by several faint clusters. It is reasonable to hypothesize that this is in accordance with the CB agglomerates and web-like structure of the electrodes (Figure 5-15 c2 and d2), but on a larger scale. However, the mapping of the signals between the clusters is minimal. It can be assumed, that the initial mixing of both CA leads to the formation of larger CA clusters that distribute a few mm apart and finely dispersed CA, which is to be found in voids between the CAM. The mapping of the dry mixing electrodes Pro$_{DM\ A-C}$ (e) and Pro$_{DM\ A-C-B}$ (f) reveals the presence of many small clusters, displayed as numerous dots. It appears that the carbon black was dispersed in the finest manner due to the dry mixing sequence. However, the number of signals observed is less than that of the CA$_{opt}$ electrode. As the majority of electrodes exhibit a similar CA content, the carbon counts observed in this EDX mapping must be consistent. It is possible that a volume fraction of the CB is so finely dispersed that it is not detected by EDX, perhaps hidden within the polycrystal LFP particle structure, indistinguishable from the carbon coating of the LFP or simply too small for the method to detect.

Figure 5-17a illustrates the outcomes of the peel strength measurements for the various procedure variations of the series. In the preceding CA-Series, the CA content was modified, resulting in a peel strength variation within the range of 5 to 15 N m^{-1}. In this Procedure-Series, it has been demonstrated that the variation of the mixing procedure has a significant impact on the peel strength. The CA$_{opt}$ electrodes demonstrate a peel strength of approximately 15 N m^{-1}, while the procedure variations exhibit peel strength values ranging from 50 to 93 N m^{-1}. In view of the peel test results for the anode, as presented subsequently in subsection 7.2, these values appear to be relatively elevated. Nevertheless, it should be noted that these values are actually lower than those reported in other publications [120, 135]. It is noticeable, that the Procedure-Series’ neat electrodes were measured at slightly elevated densities of roughly 1.3 g cm^{-3} (CA-Series ca. 1.1 g cm^{-3}). The aforementioned absence or smaller concentrations of CA in the voids between the CAM may result in the formation of a more robust PVDF percolation, which in turn is likely to exhibit significantly enhanced strength compared to previously observed values, parallel to a higher neat packing density.

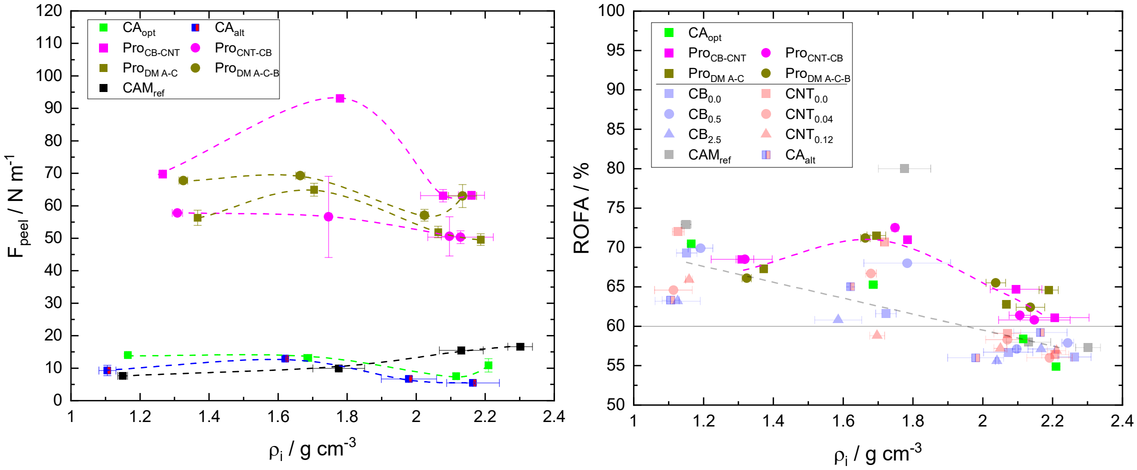

a) b)

Figure 5-17: a) Peel strength in dependence of electrode density of the Procedure-Series variation and selected CA-Series electrodes; b) residue occupied foil area (ROFA) after peel strength measurement of the CA-Serie’s electrodes in dependence of density, dashed line to guide the eye (black – CA-Series; pink – Procedure-Series)

The residue occupied foil area of the peeled current collector is presented in Figure 5-17b, which validates the significant changes in peel strength. The behavior of an initial decrease in ROFA followed by an increase can be observed in a manner similar to that observed in the CA-Series (transparent data point). However, the ROFA value is significantly higher than that observed in the CA-Series, indicating that all failure modes are predominantly cohesive in nature and that the structure must therefore be stronger. This observation may prove useful in optimizing the mixing procedure for electrode compositions that exhibit difficulties with mechanical stability.

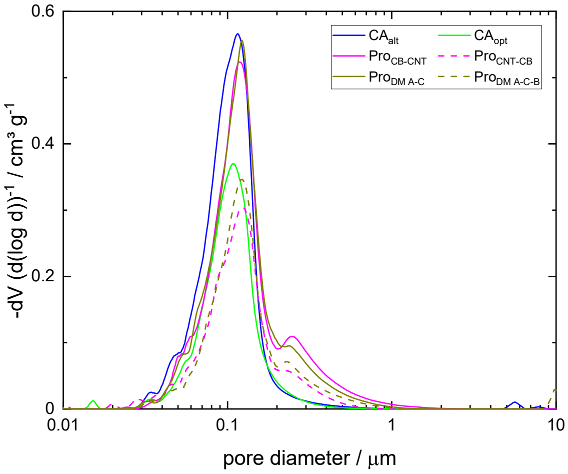

Figure 5-18: a) Pore size distribution of the Procedure-Series variation and selected CA-Series compressed electrodes measured by mercury intrusion

With regard to pore size distribution, only minor differences are evident, as illustrated in Figure 5-18. All electrodes exhibit a peak in the compression distribution at approximately 0.1 µm, which appears to be independent of CA content and mixing procedure. This is evidenced by the similarity of the peak observed in CA$_{\text{alt}}$ to those observed in Pro$_{\text{CB-CNT}}$ and Pro$_{\text{DM A-C}}$. It can be observed that the specific intrusion volume of CA$_{\text{opt}}$ is comparable to that of Pro$_{\text{CNT-CB}}$ and Pro$_{\text{DM A-C-B}}$. It is possible that the electrodes’ densities may fluctuate to some extent, which could account for these observed differences. However, there is no significant discrepancy beyond that of the aforementioned intrusion volume. Consequently, it can be assumed that the microstructure, in terms of pore size distribution, is consistent across all samples.

Figure 5-19a illustrates the correlation between electrode volume resistivity and density. In contrast to the CA Series, an increase in compression does not result in a corresponding decrease in resistivity. All procedural variations demonstrate an increase in resistivity as the density increases. A comparison of the resistivity values reveals that CA$_{\text{alt}}$ exhibits the lowest resistivity, which can be attributed to its higher CA content. The electrodes of Pro$_{\text{CNT-CB}}$ exhibit a markedly elevated resistivity, with a maximum value of 20 ± 0.1 Ω cm. No significant differences are evident for the remainder of the series.

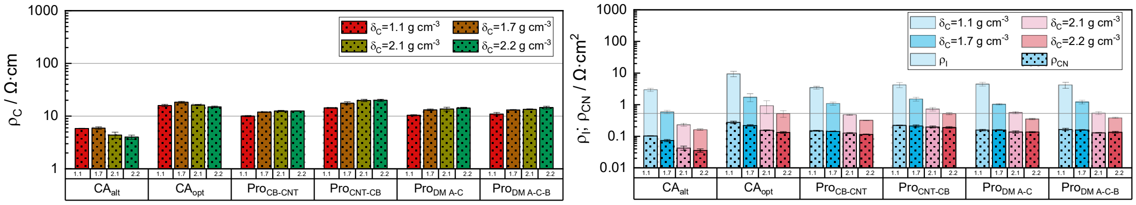

a) b)

Figure 5-19: Resistances of Procedure-Series’ variation; a) volume resistivity ρ_C; b) total resistance divided into specific contact resistance ρ_{CN} and interface resistance ρ_I

The total resistance can be observed in Figure 5-19b, wherein the Pro$_{\text{i}}$ variation’s specific contact resistance appears to be unchanging. By normalizing by height, the increase in resistance is offset, resulting in a ρ_{CN}-value that remains approximately constant. With regard to the interface resistance, it is observed that as the density increases, this resistance also decreases. At their respective highest densities, Pro$_{\text{CNT-CB}}$ and CA$_{\text{opt}}$ exhibit approximately the same total resistance of 0.53 Ω cm² (horizontal line), while the other variations display lower total resistance. For instance, Pro$_{\text{CB-CNT}}$ was measured at 0.32 ± 0.01 Ω cm^2.

On basis of this chapters rheological, mechanical, and electrical data, three types of microstructures are postulated and displayed in Figure 5-20, the illustration of the PVDF network is inspired of that of a thin film coating [136, 137]. It is shown, that electrodes produced via the CA-Series’ procedure (e.g. CA$_{\text{alt}}$) exhibit inferior peel strength in comparison to those produced via the Procedure-Series’ procedure. Consequently, it is hypothesized that the mechanical strength of the PVDF network may be compromised. Figure 5-20a provides an illustrative representation of this microstructure, showing that carbonous aggregates interrupt the binder percolation, which leads to voids of PVDF and a significantly lower peel strength. This also provides an explanation for the slightly higher low shear viscosity of CA$_{\text{alt}}$, as the aggregates initially resist deformation under shear rates, up to a point at which they collapse due to hydrodynamic forces. Given the higher peel strength of Pro$_{\text{i}}$ electrodes and significantly less residue on the substrate after peeling, it can be assumed that the PVDF network strength of procedures Pro$_{\text{CB-CNT}}$ and Pro$_{\text{CNT-CB}}$ is superior to that of CA$_{\text{opt}}$. Furthermore, the SEM imagery revealed the presence of web-like structures on the LFP particles, illustrated as a less dense CA aggregate in Figure 5-20b. Its EDX mapping indicated the presence of carbonaceous clusters on a larger scale, although there are noticeable voids of carbonaceous material between those clusters, which should be predominantly CB. The third microstructure is illustrated in Figure 5-20c and demonstrates the electrode structure that arises from Pro$_{\text{DM A-C}}$ and Pro$_{\text{DM A-C-B}}$. Here no web-like structures could be seen, and the EDX-mapping data indicated that the carbon signals are more finely dispersed, resulting in a reduction in the number of CB clusters observed compared to the other procedures. Given the markedly lower viscosity value, it can be postulated that the carbon black is predominantly located on the surface of the particles, which would explain this behavior. In a manner similar to the other Pro_i procedures, the CA-dispersion appears to be more advanced than that of CA_{opt}. As stated, this postulation is the conclusion of several results of different methods. However, the findings and interpretation is supported by similar publications, although the graphical illustration may differ [97, 118, 121, 123, 138].

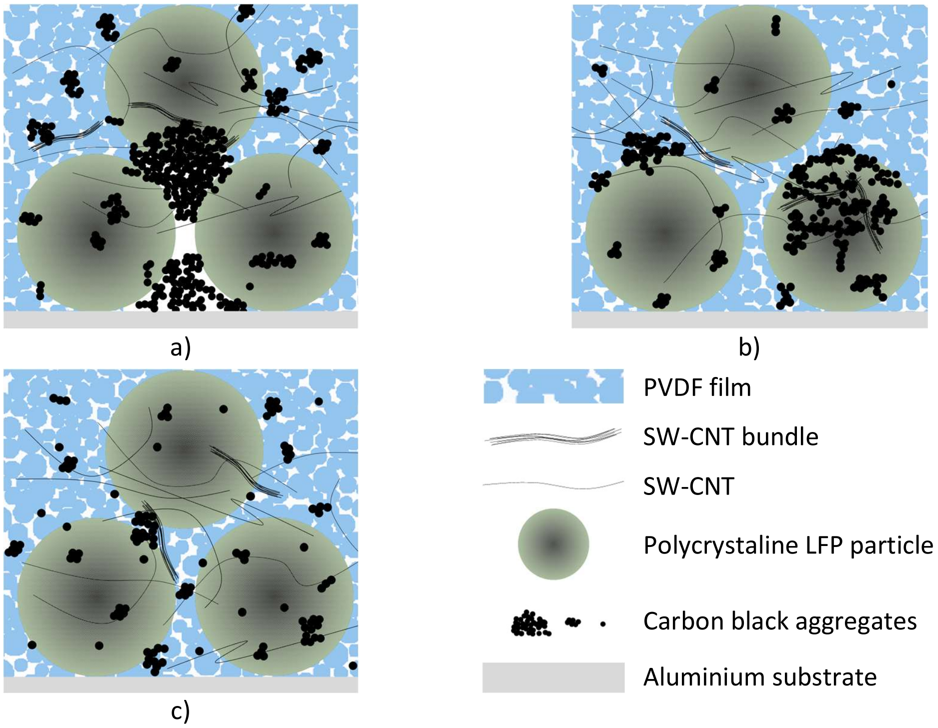

Figure 5-20: Illustration of the three main microstructures of LFP electrodes in this work respectively originating from different procedures; a) procedure CA_{alt} and CA_{opt}; b) procedure $\mathrm{Pro}_{CB\text{-}CNT}$ and $\mathrm{Pro}_{CNT\text{-}CB}$; c) procedure $\mathrm{Pro}_{DM\ A\text{-}C}$ and $\mathrm{Pro}_{DM\ A\text{-}C\text{-}B}$

Single-layer pouch cells (SPC_{46}) were constructed and subjected to electrochemical characterization. The initial phase of formation is illustrated in Figure 5-21a, wherein the most efficacious cells were selected for analysis. A comparison of the cells reveals no discernible differences in the voltage profile during charging and discharging. The only notable discrepancies are observed at the cut-off voltages, which are 2.5 and 3.7 V, respectively. Despite exhibiting a lower total resistance of the dry electrode, the cell of CA_{alt} ($Q = 150\ \mathrm{mAh\ g^{-1}}$) reaches a lower capacity than CA_{opt} ($Q = 155\ \mathrm{mAh\ g^{-1}}$). The variations of Pro_i were measured in between. However, the initial cycle loss of CA_{alt} ($13\ \mathrm{mAh\ g^{-1}}$) is less than that of CA_{opt} ($Q = 18\ \mathrm{mAh\ g^{-1}}$) in terms of first cycle efficiency.

The C-rate test yielded some notable discrepancies, as illustrated in Figure 5-21b. Initially, all the cells exhibited a similar specific gravimetric capacity, with a mean value of $132 \pm 4\ \mathrm{mAh\ g^{-1}}$. As the C-rate increases, the discrepancies become apparent. At the highest C-rate, 5C, CA_{alt} exhibited the highest stable value of $70 \pm 0.8\ \mathrm{mAh\ g^{-1}}$, while $\mathrm{Pro}_{CNT\text{-}CB}$ demonstrated the poorest performance with $58. \pm 1.2\ \mathrm{mAh\ g^{-1}}$. Cells with the CA_{opt} electrode variation exhibited a stable value of $66 \pm 1.0\ \mathrm{mAh\ g^{-1}}$. The check-up cycles at 54 and 55 cycle-count exhibited a high degree of similarity to the initial cycles of the test, with an average Q_{dis} of $129 \pm 3.5\ \mathrm{mAh\ g^{-1}}$. The results of this test indicate that, in terms of C-rate capability, the CA_{alt} electrode exhibits superior performance compared to the CA_{opt} electrode.

This finding is corroborated by the measured total resistance of the dry electrodes.

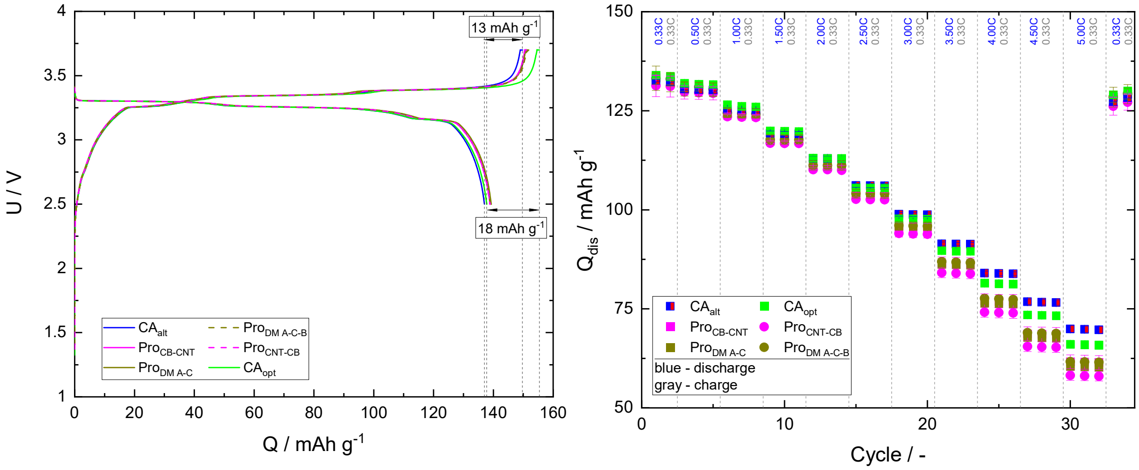

a) b)

Figure 5-21: a) charge and discharge curves of Procedure-Series cells; b) C-Rate test of the Procedure-Series cells

Furthermore, a cyclability test was conducted and the results are displayed in Figure 5-22a. It should be noted that over the course of several months, some test data was lost due to a global system failure which affected numerous computers. The missing data points are indicated by gaps in the plot. Following this event, some cells exhibited altered behavior, resulting in the average values no longer reflecting the previously observed trends. Consequently, only the most performing cell of each variation is presented, with the complete data set available in A 9-6. At 50-cycle intervals, a discharge and charge cycle of 0.33C was conducted as a quality control measure.

Despite the uniformity in component composition across all samples, with the exception of $\mathrm{CA_{alt}}$, which exhibited a higher CA content, the cyclability test revealed notable differences in capacity loss across the various samples. The cyclability behavior of $\mathrm{CA_{alt}}$ and $\mathrm{CA_{opt}}$ is more superior than that of $\mathrm{Pro_i}$. Initially, all cells exhibit a $\mathrm{Q_{dis}}$ of approximately 135 ± 1 mAh g^{-1}. However, with the progression of the cycle count, the cells derived from $\mathrm{Pro_i}$ demonstrate a pronounced capacity retention in comparison to the other two. The examination cycle at 600 cycles of the $\mathrm{Pro_i}$ procedures yielded a measurement of approximately 113 ± 2.0 mAh g^{-1}, while $\mathrm{CA_{alt}}$ and $\mathrm{CA_{opt}}$ exhibited a measurement of 121 ± 0.5 mAh g^{-1}. The capacity retention remains consistent as the cycle count progresses. It may be postulated that the capacity retention of $\mathrm{CA_{opt}}$ is less pronounced than that of $\mathrm{CA_{alt}}$, which could ultimately result in a higher cycle count. Though it must be noted, that one of the $\mathrm{CA_{opt}}$ cells failed at cycle 652. The 80% capacity barrier ($\mathrm{SOH_{80}}$) was predicted for $\mathrm{CA_{alt}}$ and $\mathrm{CA_{opt}}$ by means of linear regression. In order to ascertain this, four assessment cycles of all cells were employed, as illustrated in Figure 5-22b. It should be noted that in the case of $\mathrm{CA_{opt}}$ the last four check-up cycles of all three cells were used. The prediction indicates that, although $\mathrm{CA_{opt}}$ initially exhibited inferior performance relative to $\mathrm{CA_{alt}}$, its composition not only utilizes less CA, but also promises a more durable cell in terms of cyclability. The anticipated $\mathrm{SOH_{80}}$ of $\mathrm{CA_{opt}}$ is estimated to be 2020 cycles, while that of $\mathrm{CA_{alt}}$ is projected to be 1750 cycles. The variations of $\mathrm{Pro_i}$ did not perform as well, with a $\mathrm{SOH_{80}}$ ranging from 901 to 1051 cycles.

In order to validate the previously measured total dry electrode resistance, the cell resistance was determined using the DCIR method (35). The results are presented in Figure 5-23. With respect to the cell failure and data loss, the cycle count was limited as shown.

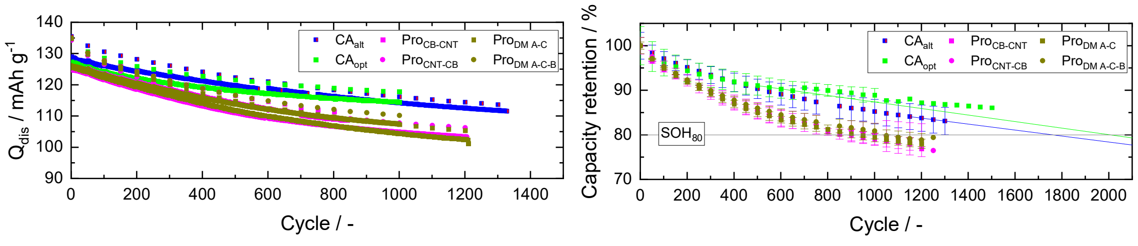

a) b)

Figure 5-22: a) full cyclability test of the sets' best performing cell including 1C cycling and 0.33C check-up every 50 cycles; b) cyclability test of the sets displaying the average capacity retention of the 0.33C check-up every 50 cycles; the lines represent the cycling prediction by means of linear regression

The majority of cells can be readily distinguished from one another. However, this is not the case for $\text{Pro}_{\text{CB-CNT}}$ and $\text{Pro}_{\text{DM A-C-B}}$. The lowest R_{cell} was observed in cells derived from CA_{alt} electrodes, with a value of approximately 24 Ω cm^2. The cells of CA_{opt} exhibited the highest cell resistance, with values of approximately 32 ± 1.2 Ω cm^2 and 34 ± 2.5 Ω cm^2, respectively, at the initial and final cycles. The variations observed in Pro_{i} are situated between the values recorded for CA_{alt} and CA_{opt}. It can be postulated that the superior cycling behavior observed in CA_{opt} is attributable to a microstructure that enhances cyclability. It may be the case that this is due to the measured lower pore volume, which results in fewer parasitic reactions and a greater capacity for the cathodes. Nevertheless, the remaining electrodes exhibit a comparable pore size distribution, with some displaying a volume identical to that of CA_{opt}.

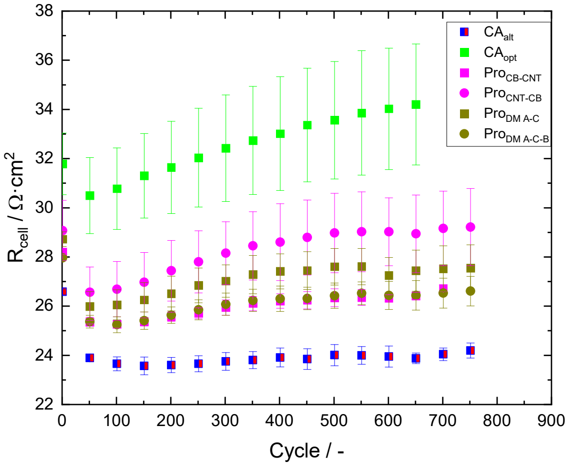

Figure 5-23: Calculated cell resistance using DCIR method of Procedure-Series' cells

It must be acknowledged that the conclusions presented here are contingent upon the limitations of the experimental design. The cells were balanced at a P:N ratio of approximately 1.1 with the opposing electrodes. This provides a plausible explanation for the observed low discharge capacity of approximately 135 mAh g^{-1}, which is below the manufacturer's stated value. However, the systematic error is identical for all cells. Consequently, this experimental series effectively demonstrates not only the rheological and physical distinctions between the slurries and their subsequent electrodes, but also the electrochemical variations.

5.3. Summary and conclusion

This chapter presents a number of design considerations pertaining to the development of electrodes. Initially, the impact of conductive additives on rheological properties, mechanical strength, and failure mechanisms, as well as the electrical properties of dry electrodes was addressed by creating slurries of different CA content (CA-Series) by an unchanged mixing procedure sequencing. It was demonstrated that the utilized LFP with a D_{50} value of 12 µm affects the flow behavior of a PVDF/NMP solution. However, it was observed that the conductive additives exert a more pronounced effect on this behavior due to the percolation of the carbon and binder domain, which underlies stronger colloidal interactions than those exhibited by the LFP. This behavior had previously been observed [139]. The peel strength of the table-coated electrodes exhibited variability in dependence on the CA content, yet no discernible trend was evident, which contradicts the sometimes stated correlation between the utilized CA's specific surface area and mechanical strength [78, 140, 141]. The density variation of the aforementioned electrodes affected the peel strength, and it was observed that the mechanical failure mode changed from a cohesive failure to a more adhesive failure in electrodes subjected to a 90° peel-test as the electrode density increased. It was demonstrated that the compression of an electrode initially enhances the peel strength by improving both the adhesive and cohesive forces. However, additional compression appears to have a detrimental effect on the mechanical integrity of the electrodes. This outcome is counterintuitive, as an increase in density is typically associated with an enhancement in peel strength [142, 143]. It was speculated that the calendering caused a deformation along the foil-coating-plain, weakening the peel strength. The enhancement in conductivity arising from an increase in CA content was measured by determining the dry electrode resistances, thus validating the differences in effectiveness of CB and SW-CNT [122, 131, 144]. A relatively modest increase in single-walled carbon nanotubes yielded outcomes comparable to those of a substantially larger increase in carbon black content. The second subsegment of the chapter demonstrated a bimodal variation of CB and SW-CNTs, indicating that SW-CNTs exert a greater influence on the slurry's flow behavior than carbon black, in accordance with the literature [143, 145], This phenomenon can be attributed to the significantly larger specific surface area of SW-CNTs. The mechanical strength of the electrode exhibited a trend analogous to that observed in the unimodal variation and the electrical resistances. On the basis of these observations, a composition was selected for utilization in the third subsegment's mixing procedure variation.

The Procedure-Series demonstrated that the sequencing of the mixing procedure exerts a significant influence on the characteristics of the slurry and its subsequent products. This was demonstrated by four "alternative" mixing procedures next to the aforementioned "original" procedure. The original slurry, which was produced by an initial dispersion of carbon black in a dissolved binder, followed by CAM, followed by dilution with a solvent, and finally by the dispersion of SW-CNTs, exhibited the highest viscosity value and the most pronounced shear thinning behavior. The slurries in which the conductive additives were dispersed in the initial and subsequent sequences exhibited a slightly reduced viscosity value and a less pronounced shear thinning behavior. The slurries that dispersed the conductive additives in the initial and subsequent sequences exhibited a slightly reduced viscosity value and a less pronounced shear thinning behavior. The slurries resulting from the dry mixing of CB, CAM and PVDF exhibited an even lower viscosity value and subsequent shear thinning behavior. It is suspected that this change in behavior is a consequence of the sequencing of the mixing procedure, rather than a result of the specific energy input, as the energy input must be interpreted with the sequence conditions. The employment of a dry mixing sequence has been shown to facilitate the fine dispersion of CB, and potentially the coating of the larger CAM particles [115, 133, 141], which consequently results in a reduction in colloidal interaction within the slurry's continuous phase, thereby lowering the viscosity. The SEM analysis of the electrodes has revealed structural differences that can be attributed to the mixing procedure. When the CAs, CB and SW-CNT, were mixed prior to the remaining components, web-like structures were observed to cover LFP particles and a finer CA distribution than the original mixing procedure was shown. The application of dry mixing resulted in the most finely distributed CA. It is notable that the peel strength of the electrodes produced using the alternative procedures was approximately five times greater than that of the CA-Series' original mixing procedure. This can be reasoned by differences in the microstructure, addressing the carbon binder domain as a consequence of the mixing procedure's sequencing [125, 145]. Hence, three different microstructures were postulated: The original mixing procedure resulted in an electrode that shows more CA aggregates, which must cause a structural disruption of the binder, inhibiting the networks percolation and therefore its mechanical strength, causing significantly lower peel strength than the following procedures. In contrast, the alternative procedures involving all-liquid sequences led to a reduction in CA aggregates within the electrode, resulting in the formation of web-like structures of CA and only a few larger clusters of CA. This approach established a microstructure that lay between the original procedure and the dry mixing procedures, with reduced CA aggregates between the AM [121, 123, 146]. Notably, the dry mixing procedures yielded electrodes that exhibited the least detectable CA aggregates between the AM particles.

The pore size distribution of the compressed electrodes exhibited notable similarity, although some electrodes demonstrated a lower specific pore volume than others. It is documented that differences in microstructure resulting from variations in the mixing procedure can affect the pore size distribution [124, 133, 141], however, no variations of significance were observed in this study. The variation in electronic resistances indicated a trend of rising volume resistivity with increasing density, which was not observed in the CA-Series. Pouch cells were constructed and characterized, revealing a high degree of similarity in the formation throughout the cells. The C-rate capability test demonstrated that the original mixing procedure of the CA-Series exhibited superior performance, a trend that was also observed in the cyclability tests. It was predicted that cells of the CA-Series mixing procedure would reach an SOH_{80} at approximately 1,750 to 2,020 cycles. In contrast, the alternative Procedure-Series cells were predicted to last for approximately 900 and 1,050 cycles. The CA-Series procedure exhibited the highest cell resistance and demonstrated the most stable cyclability, with its C-rate performance being surpassed only by another electrode composition with a higher CA content, prepared using the same procedure. This latter composition exhibited the highest conductivity. The Procedure-Series exhibited a cell resistance value intermediate to the aforementioned electrodes, indicating that the procedure affected the carbon binder domain. The relevance of the mixing procedure is often stated to affect the cyclability of the latter cells [123, 124, 133, 135], concluding that superior cycle behavior comes from superior conductivity, which may also come with a weakened peel strength. Nevertheless, the data in this series indicates that, for the materials selected in this study, the overall conductivity is sufficient. It is plausible that other factors, such as tortuosity [120, 147], contribute to the performance of the cells with both the highest and the lowest resistance, which surpass the performance of cells derived from alternative mixing procedures.

This chapter's results illustrate the broad range of effects of CA, encompassing carbon black and single-walled carbon nanotubes. These effects surround not only rheological and electronic aspects of subsequent slurry products but also mechanical properties. The outcomes of variation in the mixing procedure are particularly encouraging, as they suggest the potential for developing new, more sophisticated mixing procedures to address specific challenges. Compositions exhibiting elevated low shear viscosity may benefit from a dry mixing sequence to mitigate viscosity-related issues, for instance, when using slot dies. However, it is imperative to consider mixing the CA in portions or well-considered mixing sequences to maintain optimal electronic and potentially ionic performance. The findings further suggest that electrodes with inadequate mechanical strength can be enhanced through the design of a mixing procedure that incorporates a more focused CA dispersion, e.g. via a dry mixing sequence and a partial CA-addition, to achieve a balance between mechanical strength and electrochemical performance.

6 Influence of the mixing procedures parameters

To gain insight into the influence of the mixer's parameters – specifically, the mixing time and speed – a series of experiments were conducted, in which the durations (t_i) and speeds (ω_i) of the sequences were varied. The following figure provides a simplified illustration of the mixing procedure and its variations applied in this series.

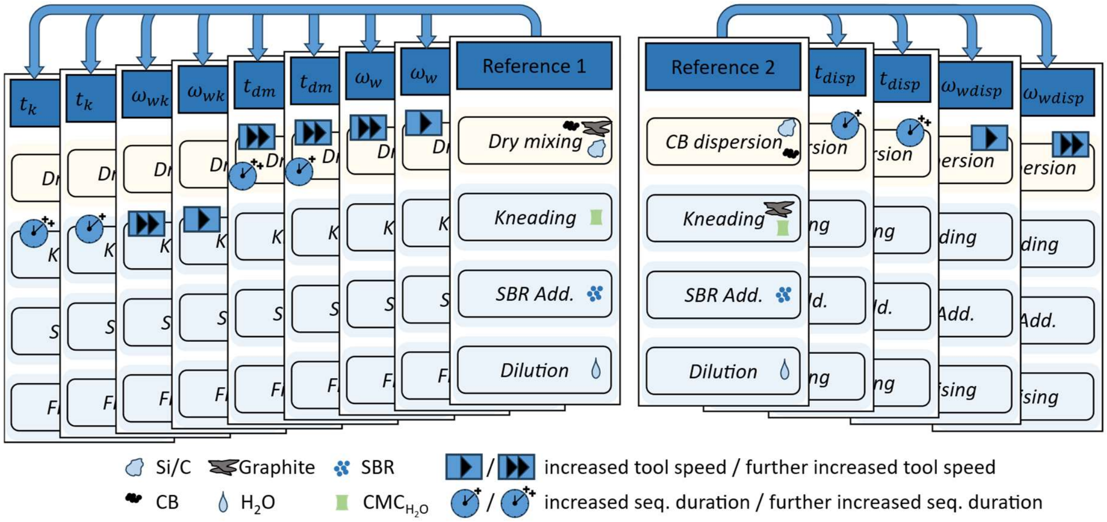

Figure 6-1: Illustration of the Parameters-Series' procedure variations

The composition employed in this study is that of Table 4-5. Two procedures were employed: Ref. 1 (Figure 4-8a), in which the dry mixing sequence and the kneading sequence were varied, and Ref. 2 (Figure 4-8b), in which the carbon black dispersion sequence was varied. The parameter values that were varied can be seen in Table 4-11.

6.1. Characterization of Slurries

To address the topic of reproducibility, two slurries origination of the Ref 1 procedure are displayed in the appendix A 9-1b. At a shear rate of roughly 0.15 s^{-1} the viscosity of two slurries lies between 66 and 86 Pa·s at an average value of 76 Pa·s, meaning the simplified reproducibility error lies roughly within ±13%.

For enhanced visualization, the variations in tool speed and sequence duration are categorized into three sets in accordance with the dry mixing sequence, the kneading sequence, and the dispersion of CB in dissolved binder. Figure 6-2a illustrates the viscosity function of slurry Ref. 1. The variations in procedures within the dry mixing sequence, dry mixing duration (t_{dm}) and tool speed (ω_w). An increase in the duration of the dry mixing sequence, by 5 and 10 minutes, resulted in a low shear viscosity (LSV) reduction of roughly 19 and 23 % at a shear rate of 0.15 s^{-1}. This suggests that a subtle change in the particle-particle structure may have occurred, leading to a decrease in viscosity. However, maintaining the dry mixing duration at 11 minutes and increasing the tool speed resulted in an increase of roughly 22 to 30 % in LSV. Subsequently, the shear thinning flow behavior was also observed to increase, yet both variations resulted in slurries that exhibited a similar flow behavior and high shear viscosity (HSV) at 1,000 s^{-1}. In conclusion, the dry mixing sequence resulted in a reduction in the total specific energy input of the mixing procedure when compared to the Ref. 1, which can be seen in Figure 6-2d, which illustrates the relative specific energy input ($E_{sp\ r}$), which is relative to procedure Ref. 1. This is most evident in the variation of t_{dm}, which has resulted in a reduction in energy input of approximately 17 % in comparison to Ref. 1 (E_{sp} = 35 Wh dm^{-3}). Although no definitive trend can be discerned, it is evident that the implementation of a dry mixing sequence has a mitigating effect on the total energy input of the subsequent procedure, due to the energy-efficient dispersion of agglomerates. Nevertheless, an extension of t_{dm} not only results in a reduction in E_{sp} for the procedure, but also a slight decrease in slurry viscosity.

Figure 6-2b illustrates the viscosity function of the kneading sequence's parameter variation. The extension of the sequence duration, in conjunction with the tool speed, resulted in a reduction of the overall viscosity value and a notable increase in energy input. This behavior is most evident in the LSV (28 to 46%), but it can also be observed in the HSV. A comprehensive investigation of its underlying causes will be presented in subsection 7.1.2.1. The third set of parameter variations, illustrated in Figure 6-2c, demonstrates that a modification within the carbon black dispersion of this mixing sequence results in a slight increase in viscosity. However, the magnitude of this change is the smallest among the series, and therefore, it is not further analyzed.

An overview of the parameter-series viscosity function is presented in Figure 6-3a. It can be stated that the selection of machine parameters does affect the viscosity function of the latter slurries, however, the magnitude of these changes is rather small. Among the tested variations, the alteration of the kneading time (t_k) and the tool speed (ω_{wk}) resulted in the most notable changes in viscosity and flow behaviour. A distinctive feature of the kneading sequence is its high TSC, which is observed during the mixing of the AM, CA, and binder with a solvent, resulting in a considerable energy input.

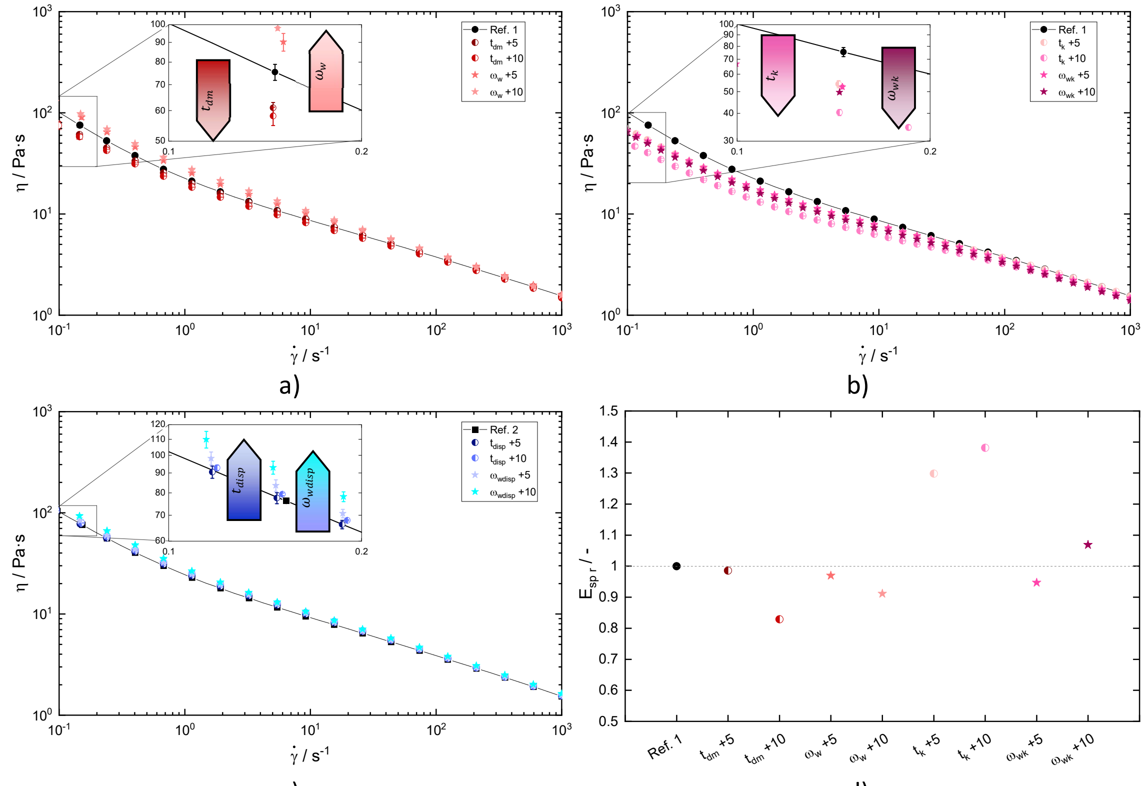

a) b) c) d)

Figure 6-2: Viscosity function; a) variation within the dry mixing sequence of Ref. 1; b) variation within the kneading sequence of Ref. 1; c) variation within the carbon black dispersion sequence of Ref. 2; d) specific energy input of mixing procedures

Since the tool speed and sequence duration showed little effect here, there might be instances in which a procedure needs adjustment in these metrics, which can easily be done without affection the slurry in a significant way.

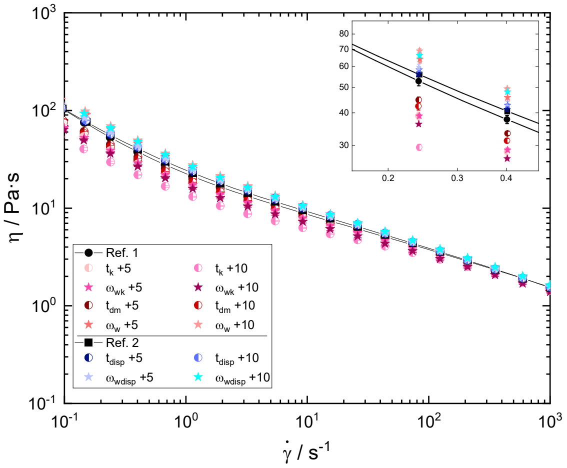

Figure 6-3: Viscosity function of the parameter series' variations

6.2. Electrode morphology

The five electrode variations of the Parameter-Series were chosen for further analysis: Ref. 1 and Ref. 2 and samples t_k +10, t_{dm} +10 ω_w +10 and ω_{wk} +10, as they show the biggest differences in viscosity from their respective references. The slurries were table coated and dried at room temperature. To investigate differences in microstructure that are suggested by the differences in viscosity, cross section SEM-images of the samples were made, to be seen in Figure 6-4 and Figure 6-5, respectively representing the overview and the magnification of agglomerates. The overview images were taken by a back scattered electron (BSE) detector. Here, the bright particles are those of the SiO_x, the dark particles are those of the Graphite – all electrodes show a homogeneous distribution of the two AM. It should be noted that the bright white residue is suspected to be debris from the current collector, caused by the ion polishing treatment. A larger magnification is displayed in Figure 6-5, a magnified view of the largest observed CB agglomerates is presented. A discernible variation in aggregate size is noticeable, with the range extending from 5 to 20 µm. Given the disparate energy inputs associated with the mixing procedures, it is reasonable to posit that the particles' health may be compromised. However, no evidence of cracking or a discernible reduction in particle size distribution was observed.

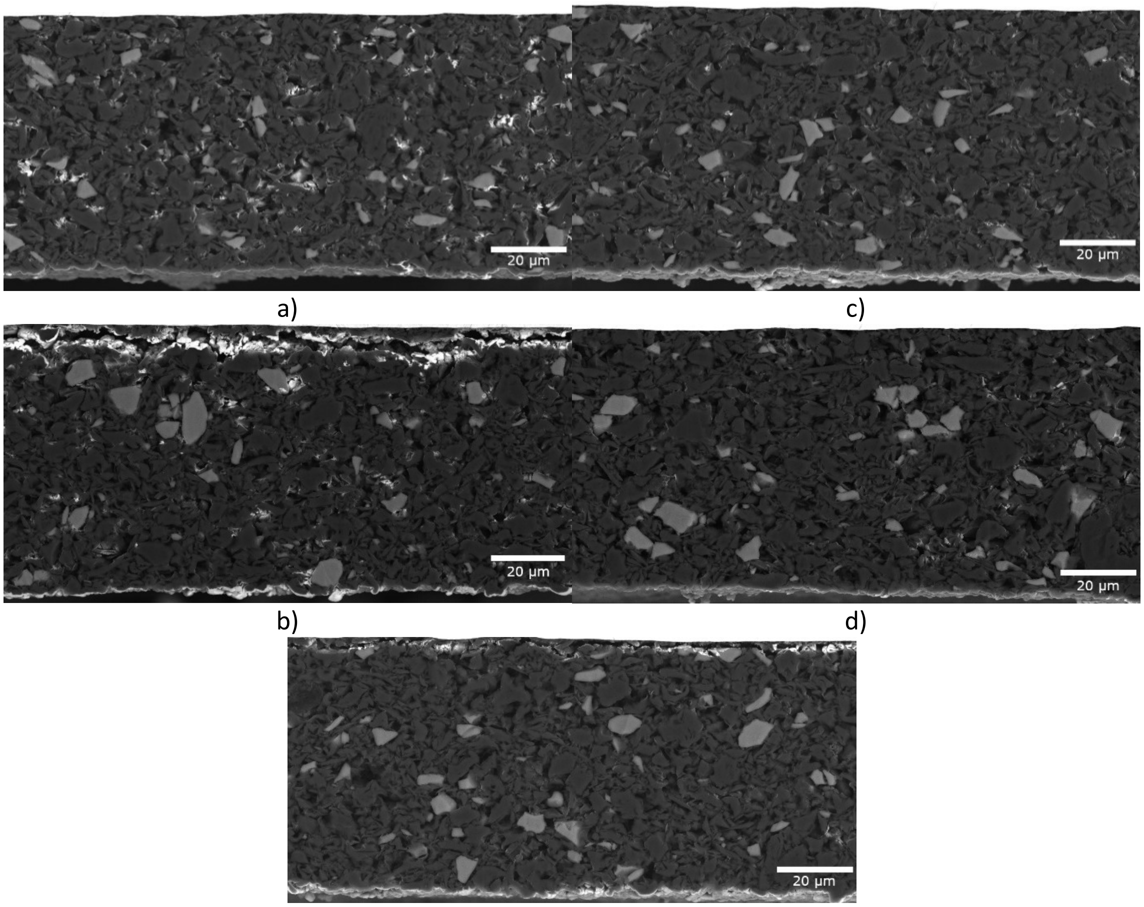

a) c)

b) d)

e)

Figure 6-4: SEM images overview of electrode cross sections; a) Ref. 1; b) ω_{wk} +10; c) t_k +10; d) Ref. 2; e) ω_{w} +10; images were taken via backscattered electron detector

Assuming that the mixing procedure Ref. 1 represents the baseline of the series' energy input a higher energy input caused by prolonged duration of faster tool seeds should decrease that agglomerate size [148]. Therefore, it is assumed that the agglomerate size of t_k +10 (Figure 6-5b) must be smaller than Ref. 1, hence the shown image must be a statistic outlier and the agglomerate size is significantly lower than Ref. 1.

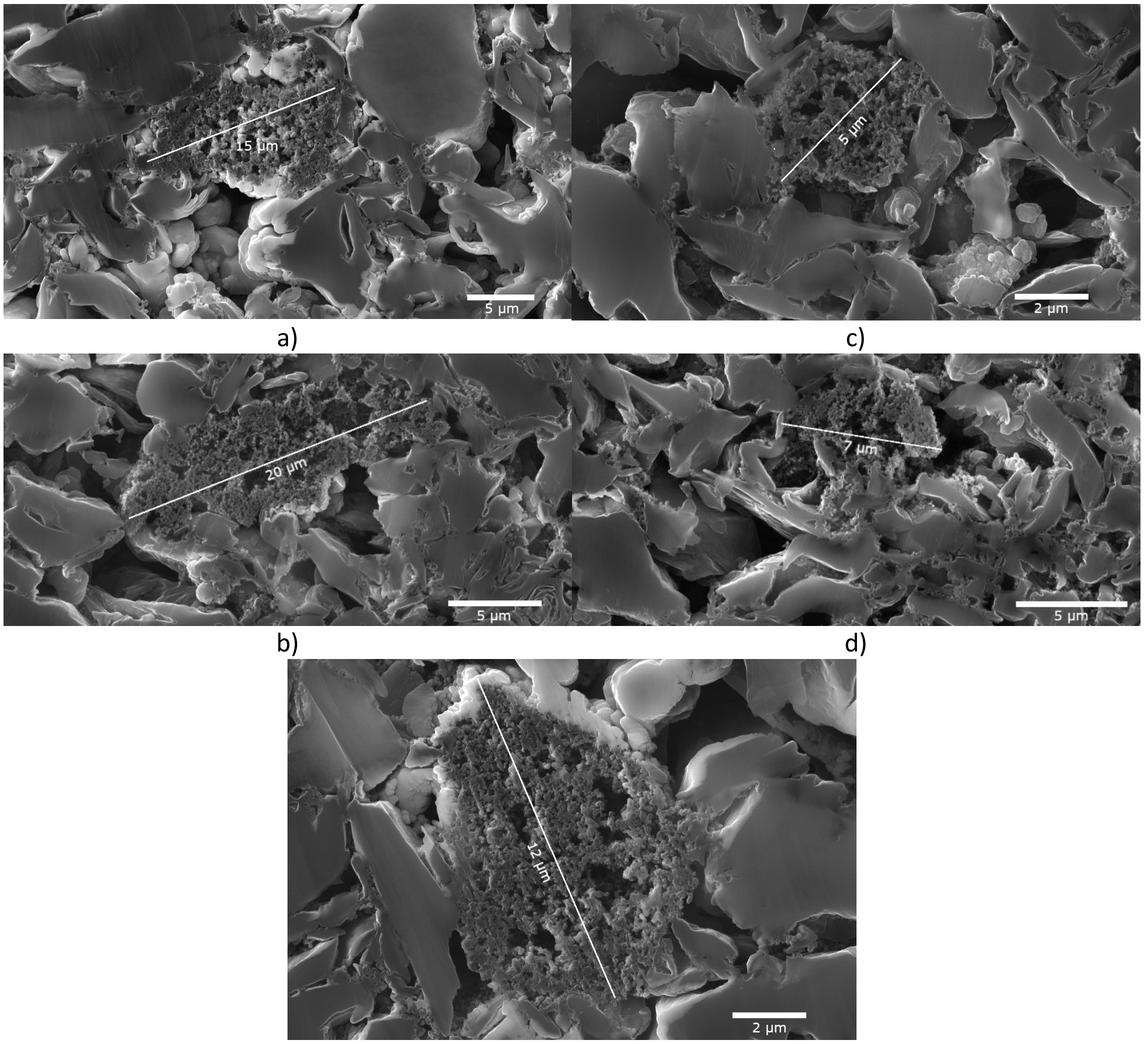

a) c)

b) d)

e)

Figure 6-5: SEM images of electrode cross sections - CB agglomerate; a) Ref. 1; b) ω_{wk} +10; c) t_k +10; d) Ref. 2; e) ω_w +10; images were taken via secondary electron detector

In regard of the porosity of the electrodes, it is feasible to assume a different degree in deagglomeration and differences in viscosity come along with changes of the electrode's pore structure. The histogram of the pore-volume distribution can be seen in Figure 6-6, here two differences among the samples can be observed: Ref. 1 has significant peak at roughly 1.2 µm at 0.7 cm³ g^{-1} and sample ω_{wk} +10 has less pore volume per mass than the remaining samples at roughly 0.6 to 0.7 µm. Smaller pores in the 100 nm range are shown in the magnification, although small quantities are measured, the variations of Ref. 1 showed an increase in pore volume per mass by one order of magnitude. However, the largest differences are rather focused on the large macro pore sizes in the range of 0.5 to 2.0 µm. Comparing these results with the SEM images, the roughly 1 µm pore size seems plausible. In the cell data it will be shown, that although there are measurable differences in porosity, no trend can be drawn between the porosity of the samples and the C-rate capability.

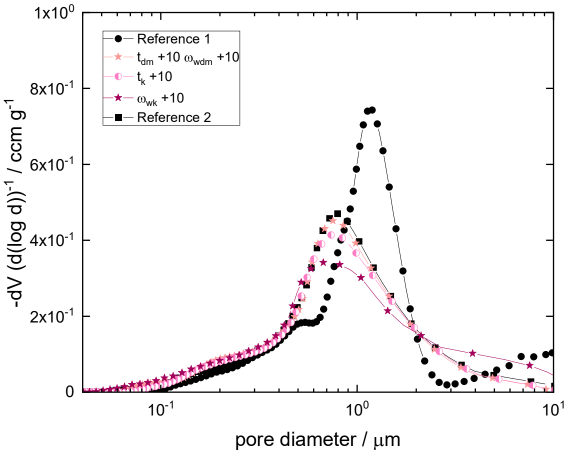

Figure 6-6: Mercury porosimetry histogram, selected samples of Parameter-Series

6.3. Characterization of cells

Full coin-cells were built out of the five selected Parameter-Series variations and cycled by applying a preliminary formation and C-rate testing plan on them.

The voltage profile of the first charge and discharge cycle of a representative FCC of Ref. 1 is displayed in Figure 6-7a. Here, the first charge cycle reaches a capacity of 221 mAh g^{-1} after applying a CCCV regime, the corresponding discharge cycles capacity reaches 184 mAh g^{-1} resulting in a first cycle efficiency of roughly 83.26 %. The voltage profile of cycle 6 changes in accordance with the change in C-rate and the capacity loss due to parasitic effects such as the SEI formation. The charge capacity reaches ca. 169 mAh g^{-1}, the discharge capacity lies at roughly 167 mAh g^{-1} (coulombic efficiency 98.82 %). This very similar behavior can be observed for all cells, only displaying minor differences, see Figure 6-7b. All cells of the Parameter-Series run at comparable capacity level during Formation, small differences can be seen, e.g. samples ω_{wk} +10 run at slightly higher capacity than samples t_k +10, however, the standard deviations overlap, therefore the samples cannot be deducted as significantly different in terms of specific gravimetric capacity.

The cell resistance (R_{Cell}) was calculated by the simplified DCIR method, after the resting phase was applied, additionally the voltage and current profile as a function of time can be seen in Figure 6-7c as well. The cells show a R_{Cell} of 13 to 21 Ω cm^2, the procedures that introduced higher energy input into the slurry (ω_{wk} +10 and t_k +10) have a lower R_{Cell} than the Ref. 1 and 2 and the cells of ω_{wk} +10 have the lowest resistance of roughly 17.5 Ω cm^2 at cycle 6.

The C-rate tests of the parameter series are illustrated in Figure 6-8a. The cells commence at a capacity of approximately 167 mAh g^{-1}, with the check-up cycle occurring 33 cycles after the discharge C-rate segment. This demonstrates average capacities of approximately 159 mAh g^{-1}, while the check-up at cycle 65 after the charge C-rate segment exhibits a capacity of approximately 152 mAh g^{-1}. This indicates that a decline in capacity is evident, although the extent of this decline is consistent across the cells. This indicates that the AAMs were not subjected to any significant damage, for instance, as a result of an excessive energy input. In the event of significant damage, the observed fading would be more pronounced following the stress of the C-rate test. When discharging at 5C, the highest average capacity of 104 ± 10 mAh g^{-1} was observed in sample ω_{wk} +10, while the lowest average capacity was 90 ± 4 mAh g^{-1} of the t_k +10 cells. When charging at 5C, the highest average capacity 41 ± 5 mAh g^{-1} was observed in cells ω_{wk} +10, while the lowest average capacity was 30 ± 6 mAh g^{-1} in cells t_k +10.

Despite exhibiting similar cycle behaviour during formation and C-rate testing, sample ω_{wk} +10 demonstrated a slightly higher C-rate capability than the other samples.

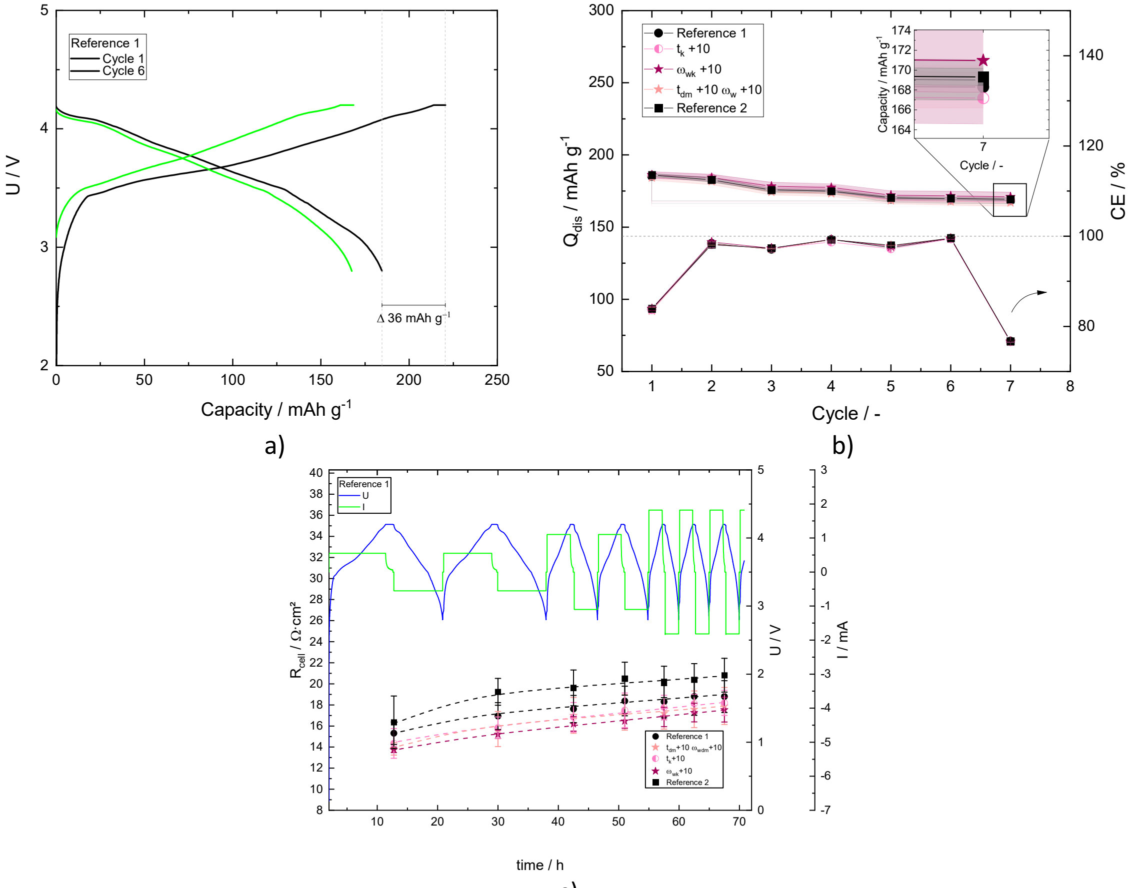

a)

b)

c)

Figure 6-7: a) Charge and discharge curves of a FCC of Ref. 1 of the Parameter-Series; b) average Capacity of the Parameter-Series' FCCs during formation; c) Voltage and current profile of selected FCCs of the Parameter Series with the calculated cell resistance using simplified DCIR method

In Terms of Cell resistance, the trend of the formation progresses throughout the C-rate test, Figure 6-8b. Although the resistance of t_k +10 is among the smallest measured R_{Cell}, the rate capability is not among the highest. Furthermore, Ref. 2 has the highest R_{Cell} of the series, yet it shows better rate capabilities than sample t_k +10 and has less fading at the test's final check-up. It must be noted that this DCIR based cell resistance does not cover all the complex resistances. It is measured within the first 20 ms after the pause step, so it is reasonable to assume that only the ohmic resistance, which in this case is a superposition of all the electronic resistances and the bulk electrolyte ionic resistance of the cell, is being measured here. Other resistances such as double layer capacitances, ionic resistance of the electrolyte, charge transfer resistances and polarization resistance would only contribute the pulses measurement if the pulse would be significantly longer [149]. Therefore, it could be speculated that there are other resistances at work, reducing the C-rate capability of sample t_k +10.

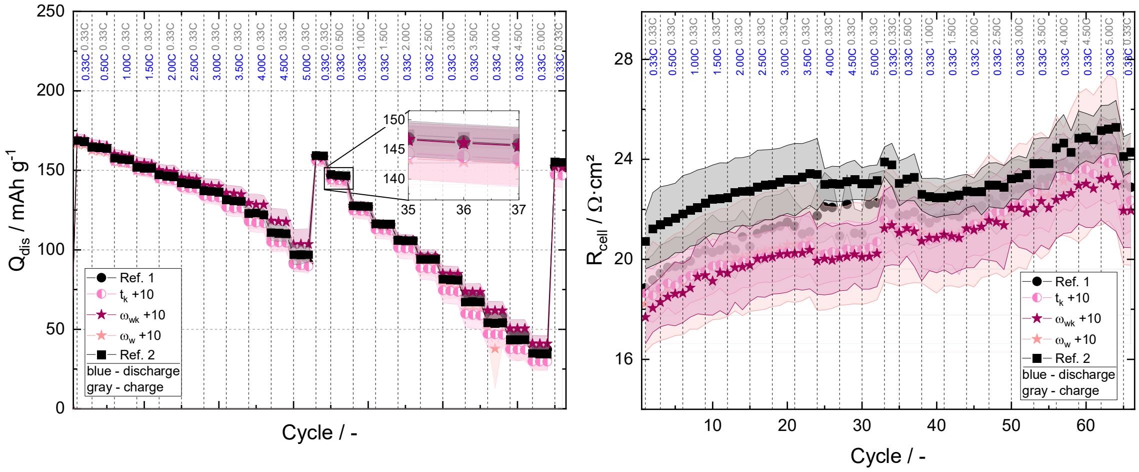

a) b)

Figure 6-8: a) C-rate test of the Parameter-Series’ FCCs; b) Cell resistance measured using the simplified DCIR Method

6.4. Summary conclusion

The objective of this chapter is to investigate the impact of variations in mixing parameters within a single slurry composition, establishing a baseline by analyzing two mixing procedures. One of the procedures entails a dry mixing sequence and the other a carbon black dispersion sequence. To investigate the impact of variations in tool speed and sequence duration, one procedure parameter was varied at a time. The variations affected the dry mixing sequence, the kneading sequence, and the sequence used to disperse CB in dissolved binder. It was established that the investigated selection of parameter values does affect the slurry’s flow behavior, though in a minor magnitude. Given that all variations, which increased the parameter of question, resulted in increased energy input throughout the series, it can be deduced that a finer dispersion must occur within the carbon binder domain [123, 148]. However, the flow behavior itself is insufficient to determine the degree of dispersity [150], and the SEM images do not suffice to quantitatively evaluate this matter. The mercury porosimetry did demonstrate some differences, yet literature values indicate that the differences are negligible [124, 151].

The full coin cells exhibited discrepancies in C-rate capability and cell resistance. The C-rate performance of all cells exhibited minimal variation. However, cells originating from higher tool speed procedure during kneading demonstrated slightly superior C-rate performance although this was not reflected in capacity retention, yet the differences are comparable modest [121].

In light of the findings presented in Chapter 5, it can be assumed that the enhanced C-rate capability correlates with a reduced cyclability. These findings substantiate the constraints of the experimental series, which was characterized by a not-extreme variation in machine parameters, tool speed and sequence duration. It is plausible that more pronounced alterations may impact the slurry and its subsequent products in a more pronounced manner. These findings illustrate that the design considerations of mixing procedures should be oriented towards the selection of beneficial sequences, rather than the pursuit of an optimal tool speed or duration. In particular, when considering production scale, variations within the scope of this series can be conducted without undue risk to a product or schedule.

7 Impact of composition-ratios within mixing procedures

The manner in which the processing is conducted, including the tools employed and the ratios of materials utilized within a given mixing sequence, can have a significant influence on the flow behavior of the resulting slurry. Figure 7-1 illustrates the viscosity function of four slurries of identical composition, as detailed in Table 4-6 and Table 4-7. The slurries were prepared according to the same sequences; however, in Procedure P1, the kneading sequence was conducted manually using a spatula and two different TSC. In the latter stage of Procedure P1, a dispersion disc was employed. In Procedure P2, the kneading occurred at two different TSC, and an intensive mixer was utilized in this procedure.

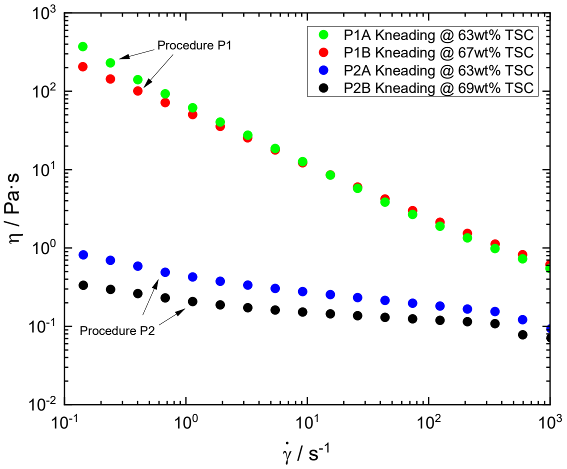

Figure 7-1: Viscosity function of four slurries; procedure P1: manually kneaded and mixed with dispersion disc; procedure P2: mixed with intensive mixer; variations in TSC while kneading

It is evident that the slurry originating from procedure P1 exhibits a higher viscosity, while the slurry derived from procedure P2 displays a lower viscosity. These two types of slurry exhibit a notable disparity in their low shear viscosity, with a difference exceeding two orders of magnitude. The slurry P1A was kneaded at a TSC of 63 wt%, exhibiting a slightly elevated low shear viscosity in comparison to P1B, which was kneaded at a TSC of 67 wt%. A similar trend is observed in slurries P2A and P2B, which were mixed at 63 and 69 wt%, respectively. This comparison indicates that the material ratios, specifically the TSC while kneading, and the mixing tools, such as kneading with a spatula or using an intensive mixer, have a significant impact on the flow behavior and, consequently, the microstructure of a slurry composition. It is apparent that the manual kneading of the slurries introduces a considerably lower energy input than the use of an electric mixer. Consequently, as the TSC is increased, the energy input also rises. The objective of this chapter is to investigate the effects of modifying the material ratios within the mixing procedure. For this purpose several experimental series were conducted.

7.1. Rheological characterization, interpretation and application

The following subsections present the rheological findings of the two series, Kneading-Series 1 and Kneading-Series 2, and offer an interpretation in the context of CMC adsorption and coating application.

7.1.1. Flow behavior of anodic lithium-ion slurries

As previously outlined in section 2.1.4, the total solids content of a pure solid/solvent suspension has a predictable impact on the suspension's viscosity. Figure 7-2a illustrates the TSC-Series' six slurries of identical non-volatile solids content (see Table 4-9). However, their TSC ranges from 54 to 66.5 wt%. It should be noted that the 66.5 wt% sample was created by making a 69 wt% TSC slurry, but the resulting slurry was not flowable and was diluted.

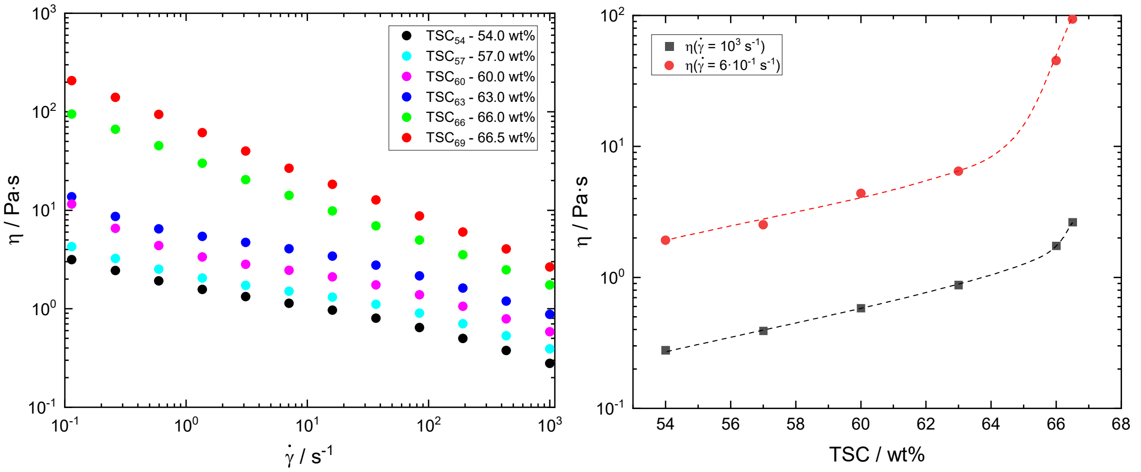

a) b)

Figure 7-2: Rheological data of the TSC-Series; a) Viscosity as a function of shear rate of slurries with six individual TSC ranging from 54 to 66.5 wt%; b) low and high shear viscosity of the six slurries

It is obvious that the overall viscosity rises in conjunction with an increase in slurry TSC. The shear thinning behavior of slurries TSC_{54} to TSC_{63} is less pronounced in shear rates from 0.1 to 7 s^{-1} than it is at higher shear rates. Furthermore, no purely linear behavior is observed. However, samples 66 and 66.5 wt% display a linear, monotonous shear thinning behavior throughout the full shear rate spectrum. However, the overall increase is not linear. This is evident when comparing the low and high shear viscosity as a function of the slurry's TSC (Figure 7-2b). When the TSC is increased from 54 to 63 wt%, both the low and high shear viscosity change in a linear logarithmic trend, according to a single exponential increase. However, greater TSC values diverge from this trend and are significantly higher in viscosity.

The slurry was produced on an individual basis, with the same mixing parameters applied in each case. These parameters included speed and sequence duration. In order to achieve the differences in TSC, the quantity of water in the sequence was varied. This also affected the degree of filling. Details of the procedure are provided in Figure 4-6. The differences in these parameters result in differences in the overall energy input and therefore the specific energy input.

The specific energy input (E_{sp}) of each sequence is illustrated in Figure 7-3a, while the accumulated E_{sp} is depicted in Figure 7-3b. In terms of the overall process, the CB-Dispersion and the water addition account for a relatively small proportion of the total energy input. The most substantial contribution is derived from the kneading sequence. The lowest accumulated energy input was observed for Slurry TSC_{54}, at approximately 30 Wh dm^{-3}, while the highest was recorded for Sample TSC_{66}, at around 58 Wh dm^{-3}. Despite TSC_{69} exhibiting the highest TSC, which would be expected to result in the highest viscosity and E_{sp}, the E_{sp} of the kneading sequence was found to be approximately 36 Wh dm^{-3}, which is comparable to that of TSC_{57}. This can be attributed to the fact that no flowable mass was formed; rather, a plastic mass was created that sporadically made contact with the dispersion tool. This resulted in fluctuations in the rotors' power consumption, which in turn led to a reduction in the energy input.

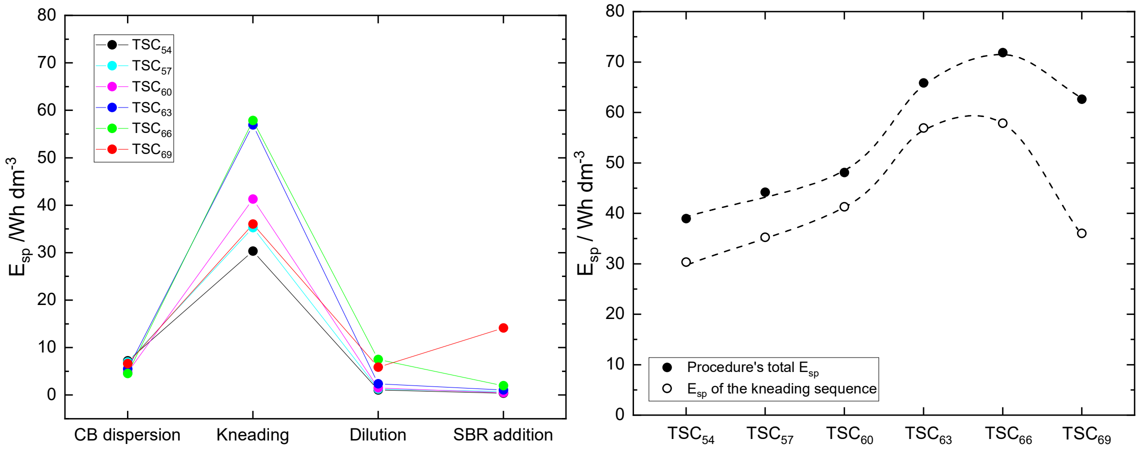

a) b)

Figure 7-3: a) sequential specific energy input of TSC-Series; b) total specific and specific energy input of the kneading sequence of TSC-Series

Figure 7-3b illustrates a linear correlation between the specific energy input and the TSC of slurry samples TSC_{54} to TSC_{60}. However, samples with a higher TSC deviate from this trend. The variations TSC_{63} and TSC_{66} demonstrate a comparable energy input within the kneading sequence of approximately 69 Wh dm^{-3} and a relatively consistent total energy input as well. Given that both samples underwent a procedure with 66 and 72 Wh dm^{-3}, it may be assumed that both viscosity functions exhibit a similar flow behavior. However, the difference in LSV and HSV is greater than that observed in the other 3 wt% increments. By correlating the differences in mass ratios and the change in flow behavior, it is possible to deduce a threshold of TSC somewhere between the procedures of samples 60 and 63 wt% TSC. This results in a change of microstructure and therefore a different flow behavior.

On basis of the previous chapter and this chapters results, it can be assumed that the kneading sequence affects the slurry's later flow behavior. The mass ratio in this sequence plays a significant role if the procedure parameters are unchanged since this then correlates with the energy input which affects the later microstructure [116, 124, 147, 148].

7.1.2. TSC as design considerations of mixing procedure sequences

As has been demonstrated previously, the total solids content has a pronounced effect on the flow behavior of a slurry. The following two subsections investigate the effects resulting from the total solids content (TSC) utilized in mixing procedures, with a particular focus on the adsorption behavior of CMC with a M_w of 875 and 500 kDa on carbonous particles, which mainly is graphite, that will be shown to result from that procedural design element.

7.1.2.1. Adsorption related flow behavior of aqueous anodic slurries utilizing low molar weight Carboxymethyl cellulose

The objective of the Kneading-Series 1 is to gain a deeper comprehension of the impact of kneading procedures on the flow behavior of slurries, the following figure illustrates the procedure variations of said series in a simplified manner.

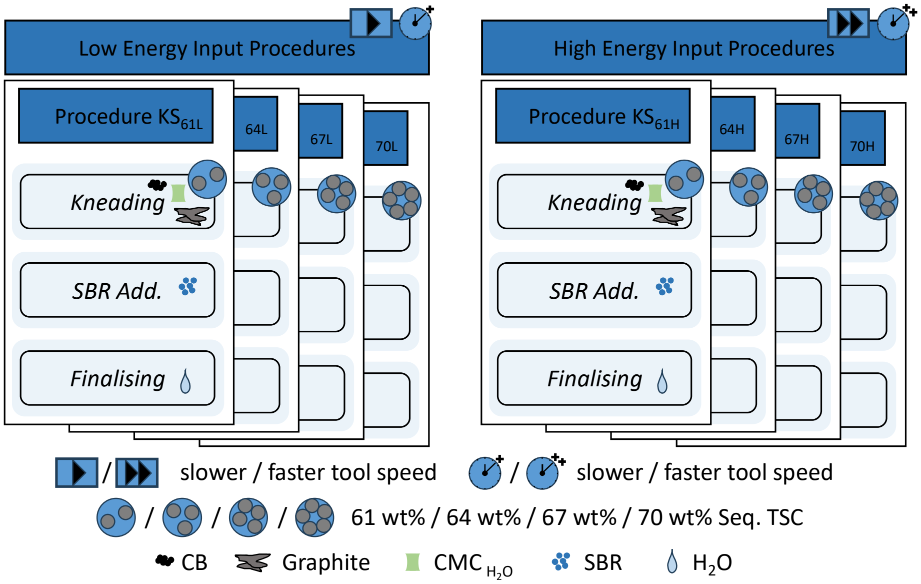

Figure 7-4: Illustration of the Kneading-Series 1 procedure variations

This is achieved by employing two distinct procedures, characterized by varying energy inputs, as a consequence of differing tool speeds and kneading durations. The variations are labelled according to the TSC of the kneading sequence, e.g. KS$_{60H}$. Consequently, 'H' denotes the high energy input procedure and 'L' denotes the low energy input procedure. The components of the slurries are listed in Table 4-4, the composition is listed in Table 4-9, and the procedure details are shown in Figure 4-7.

Table 7-1 shows the specific energy input of the procedures. As anticipated, the procedure utilizing the lower tool speed during the kneading sequences results in a reduction in total E_{sp}. The largest contributor to this reduction is the kneading sequences themselves. Moreover, as evidenced in the TSC-Series, an increase in TSC within the kneading sequence is accompanied by a corresponding rise in energy input. However, this phenomenon is only observable in the slurries KS$_{61}$, KS$_{64}$ and KS$_{67}$, L and H respectively. The slurries with a kneading TSC of 70 wt% were produced with a markedly reduced energy input. Figure 7-5a illustrates the procedures, total energy input and accumulated specific energy input of the kneading sequence, ordered in ascending order. It is noteworthy that a number of slurries were produced with comparable specific energy inputs. Two pairs were identified in the course of this experiment: KS$_{70L}$ & KS$_{64L}$ and KS$_{67L}$ & KS$_{70H}$. The pair KS$_{70L}$ & KS$_{64L}$ is of particular interest, as both slurries were manufactured with identical tool speed and sequence duration, yet with variations in TSC within the kneading sequences. The second pair, KS$_{67L}$ & KS$_{70H}$, was produced with disparate tool speed and sequence duration, and distinct TSC within the kneading sequences.

Table 7-1: Specific energy input of the Kneading-Series 1

	E_{sp} (Total procedure) /Wh dm^{-3}		**E_{sp} (accumulated kneading sequences) /Wh dm^{-3}**	
	Procedure L	Procedure H	Procedure L	Procedure H
KS$_{61}$	18.6	22.7	14.7	19.6
KS$_{64}$	26.6	35.4	23.9	32.9
KS$_{67}$	53.9	77.1	51.8	75.4
KS$_{70}$	25.6	56.9	22.9	54.9

The viscosity function of the slurry is illustrated in Figure 7-5b, which depicts the Kneading-Series 1. The slurries originating from procedure L typically exhibit higher viscosity values than those derived from procedure H. Additionally, variations in TSC within the kneading sequence have been observed to influence both the viscosity value and the flow behavior. Both KS_{61} slurries demonstrate slight alterations in their shear thinning behavior. In contrast, the slurries of KS_{67} exhibit a complex shift in flow behavior, encompassing a shear thinning segment between 0,1 – 1 s^{-1}, a plateau segment between 3 – 15 s^{-1}, and a subsequent shear thinning segment between 30 – 1000 s^{-1}. However, KS_{70} exhibits a distinct deviation from the observed trend of declining viscosity values and altered flow behavior with elevated TSC levels within the kneading sequence.

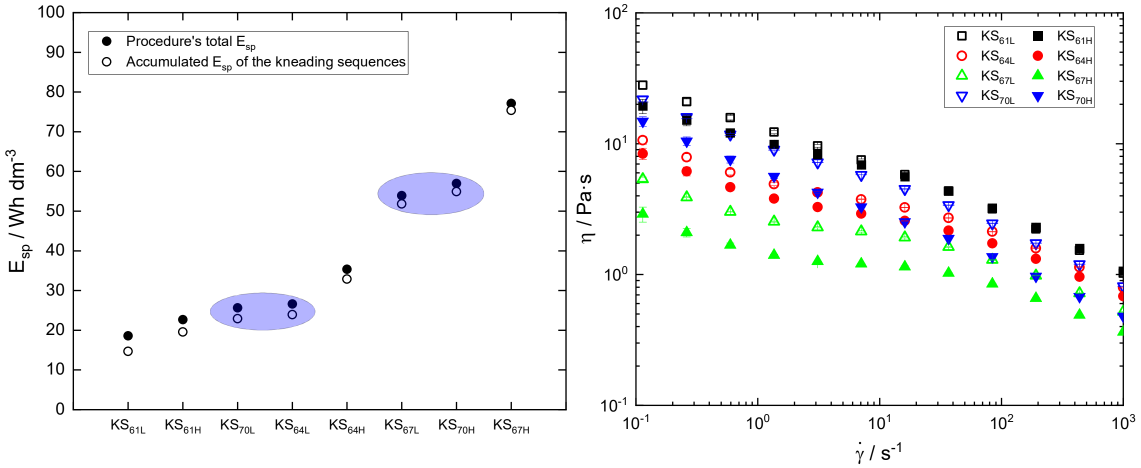

a) b)

Figure 7-5: a) Specific energy input of the Kneading-Series procedures, sorted in an ascending manner; highlighted samples with similar E_{sp}; b) Viscosity function of the Kneading-Series slurries, the slurries' compositions are identical

Figure 7-6 illustrates the previously identified pairs KS_{70L} & KS_{64L} and KS_{67L} & KS_{70H} with the addition of lines for enhanced visual clarity. While the energy input per pair is relatively similar, there are notable differences in the viscosity values and flow behavior. Slurry KS_{70L} can be characterized by a low shear viscosity of approximately 20 Pa·s at 0.1 s^{-1}, a high shear viscosity of approximately 0.8 Pa·s at 1,000 s^{-1}, and a relatively linear shear thinning behavior within the log-log plot. In contrast, slurry KS_{64L} exhibits an LSV of approximately 10 Pa·s, an HSV value of approximately 0.8 Pa·s, and a non-linear shear thinning behavior with two changes in slope at approximately 1 and 10 s^{-1}. Despite differing in viscosity value, the same behavior is evident in the pair KS_{67L} & KS_{70H}. The Slurry KS_{70H} exhibits a LSV of approximately 15 Pa·s, a HSV of approximately 0.5 Pa·s, and a linear shear thinning behavior. The slurry KS_{67L} displays a LSV of approximately 5 Pa·s, a HSV of approximately 0.5 Pa·s, and a non-linear shear thinning behavior at 1 and 10 s^{-1}.

It is evident that augmenting the kneading sequences TSC results in an escalation of E_{sp}; a similar outcome is observed with the enhancement of tool speed. It is less obvious that the viscosity of a slurry composition can be reduced in both low and high shear viscosity scenarios by modifying the water content within a mixing procedure sequence. Moreover, the flow behavior can be influenced. This can be achieved by modifying the tool speed, as demonstrated in samples KS_{61L} and KS_{61H}, or by modifying the energy input by increasing the kneading sequences TSC. However, this is only the case for a range of TSCs. If the TSC is too high and a non-flowable mass is formed during kneading, the energy input decreases, and the resulting slurry displays rather linear shear thinning behavior. As the volume ratio of the Kneading-Series solids remains unchanged, it can be inferred that this is caused by a change in the solvable polymer's microstructure, specifically the CMC.

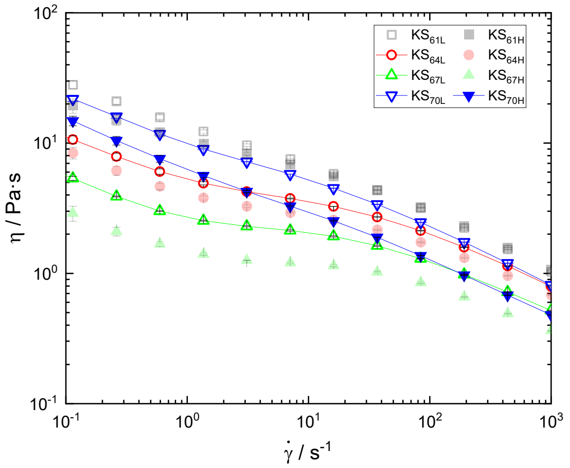

Figure 7-6: Viscosity function of the Kneading-Series 1 slurries, the slurries' compositions are identical

CMC has been demonstrated to exhibit adsorption behavior on graphite surfaces [91].To gain a deeper insight, it is essential to investigate the flow behavior of the CMC. Figure 7-7a illustrates the flow behavior of a range of CMC solutions (M_w = 500 kDa) with concentrations spanning from 30.9 to 0.5 g L^{-1}. Consequently, an increase in concentration results in a corresponding rise in the characteristic zero-shear viscosity (η_0). Moreover, the degree of shear thinning diminishes with declining concentration as the solution approaches the viscosity of the solvent (water), which is a Newtonian fluid. The specific viscosity (η_{SP}) was calculated using equation (17) with the values of η_0 from Figure 7-7a, and plotted as a function of the CMC concentration in Figure 7-7b. The slurry concentration of CMC in the Kneading-Series 1 is 15 g L^{-1}.

A correlation between concentration and η_{SP} was analysed, and it was found that there are two linear regions in the log-log plot. Region one has a slope of approximately 1.06 and ranges from approximately 0.5 to 7 g L^{-1}. Region two has a slope of approximately 3.94 and ranges from approximately 10.1 to 30.9 g L^{-1}. As is typical for polymer solutions, these regions correspond to the dilute and semi-dilute polymer regimes [152]. In dilute polymer solutions, the polymers are present in low concentration and do not interact with each other. In contrast, semi-dilute solutions have a higher concentration of polymers, allowing for overlap of the polymers.

The slurries of the Kneading-Series were subjected to centrifugation, and the viscosity function of the resulting supernatant is illustrated in Figure 7-8a. Additionally, several CMC solutions functions are plotted, with concentrations ranging from 30.9 to 0.5 g L^{-1}.

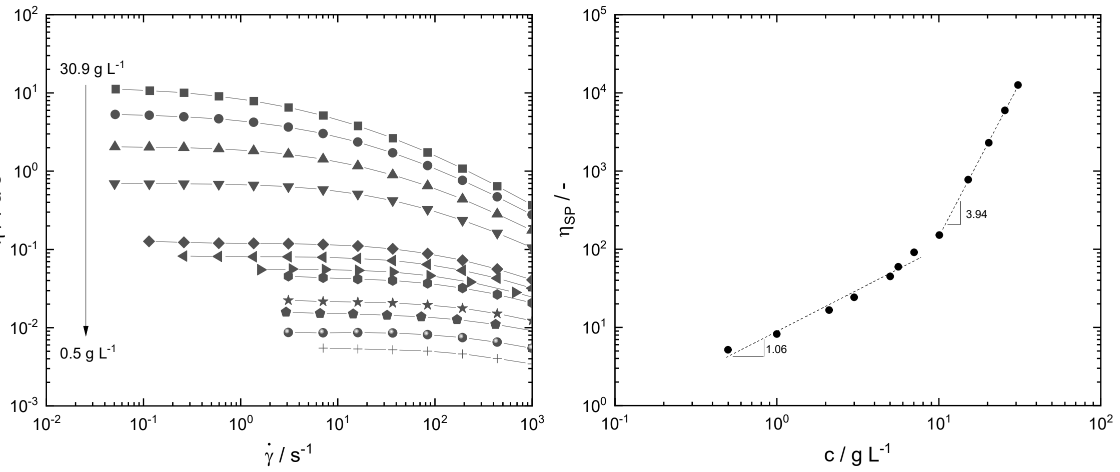

a) b)

Figure 7-7: a) Viscosity function of individual CMC-solutions (500 kDa) with concentrations ranging from 30.9 to 0.5 g L^{-1}, lines to guide the eye; b) Specific viscosity as a function of concentration

As with the slurry, the supernatant demonstrates a decrease in viscosity with an increase in energy input. This phenomenon can be observed in both procedures (L and H), in samples KS_{61}, KS_{64} and KS_{67}. In samples KS_{70L} and KS_{70H} this behavior is even more extreme. The viscosity of the supernatant is primarily determined by the concentration of dissolved CMC. However, there is a significant discrepancy in the viscosity of the supernatant samples, with a difference of approximately two orders of magnitude, indicating a change in CMC concentration.

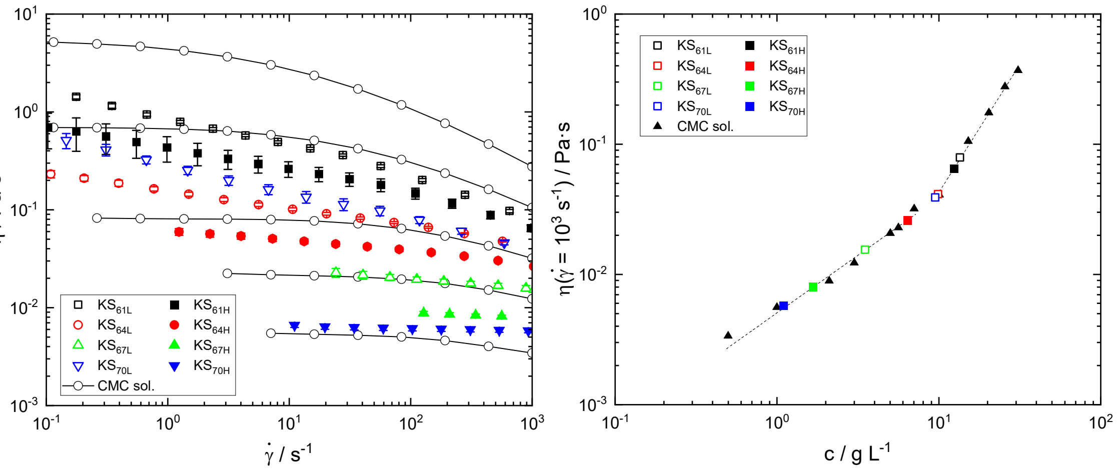

a) b)

Figure 7-8: a) Viscosity function of individual CMC-solutions (M_w = 500 kDa; c = 2.5, 1.5, 0.7, 0.3, 0.05 g L^{-1}, from top to bottom respectively) next to the supernatants of the series' slurries; b) Viscosity at a shear rate of 1,000 s^{-1} as a function of concentration and η_0 values of the series' slurry supernatants

It should be noted that not all of the supernatants displayed a clear zero-shear plateau (e.g. KS_{61L}), which precludes the accurate determination of the zero-shear viscosity (η_0). This may be attributed to the fact that the supernatants TSC ranges from approximately 3.5 up to 8.3 wt% (see A 9-3), which has the potential to cause particle-particle interactions that ultimately influence the flow behavior. This results in the absence of a zero shear plateau, and instead, a constant shear thinning behavior is observed. It was assumed that the microstructure of the CMC_{500} remained unaltered, for example, due to mechanical degradation. The high shear viscosity at a shear rate of 1,000 s^{-1} was determined by linear interpolation for each supernatant and CMC solution. This viscosity was plotted as a function of CMC concentration in Figure 7-8b. A comparable pattern to that observed in Figure 7-7b is evident, resulting in two discernible regimes, delineated by the dotted lines at the same concentrations as previously. The supernatant viscosity is evident in both regime segments, $\mathrm{KS}_{61\mathrm{L}}$ and $\mathrm{KS}_{61\mathrm{H}}$, within the range of the semi-diluted system. The remaining supernatants are either low in concentration, correlating to the dilute regime, or situated between the crossover points of the two regimes. The sample correlating viscosity and concentration values of Figure 7-8b are listed in the following table.

Table 7-2: Viscosity and CMC concentration of the Kneading-Series supernatants

Supernatant of	$\eta(\dot{\gamma} = 10^3 s^{-1})$ **/ Pa·s**	**C / g L^{-1}**	**Polymer regime**
$\mathrm{KS}_{61\mathrm{L}}$	0.079	13.5	Semi-dilute
$\mathrm{KS}_{64\mathrm{L}}$	0,041	9.9	-
$\mathrm{KS}_{67\mathrm{L}}$	0.016	3.5	Dilute
$\mathrm{KS}_{70\mathrm{L}}$	0.039	9.5	-
$\mathrm{KS}_{61\mathrm{H}}$	0.065	12.4	Semi-dilute
$\mathrm{KS}_{64\mathrm{H}}$	0.026	6.4	-
$\mathrm{KS}_{67\mathrm{H}}$	0.008	1.7	Dilute
$\mathrm{KS}_{70\mathrm{H}}$	0.006	1.1	Dilute

The initial concentration of the CMC in the Kneading-Series 1 solution is 15 g L^{-1}. Following Table 7-2, the CMC concentrations was roughly determined to be between 1.1 and 13.5 g L^{-1}, indicating that approximately 10 to 93 wt% of the CMC was absorbed, contingent on the mixing procedure employed. A comparison of the two procedures, designated as L and H, revealed that the slurries resulting from procedure L exhibited reduced adsorption due to the lower energy input. However, in contrast to procedure H, the degree of adsorption does not invariably increase in procedure L. Sample $\mathrm{KS}_{70\mathrm{L}}$ exhibited a higher supernatant concentration than $\mathrm{KS}_{67\mathrm{L}}$, while the corresponding supernatant $\mathrm{KS}_{70\mathrm{H}}$ displayed the lowest concentration of all the samples. This may be attributed to the observation that the supernatant viscosity of $\mathrm{KS}_{70\mathrm{H}}$ exhibits minimal shear thinning behavior, which suggest a mechanical degradation of the CMC. However, with a viscosity that closely approximates that of water and a shear thinning behavior that is indistinguishable between 100 and 1,000 s^{-1}, it is challenging to ascertain whether mechanical degradation did indeed occur.

7.1.2.2. Adsorption related flow behavior of aqueous anodic slurries utilizing high molar weight Carboxymethyl cellulose

To further investigate on the mechanical degradation parallel to polymer adsorption, another series of slurries was created, the “Kneading-Series 2”. The following figure illustrates the series’ procedure and its variations in a simplified way.

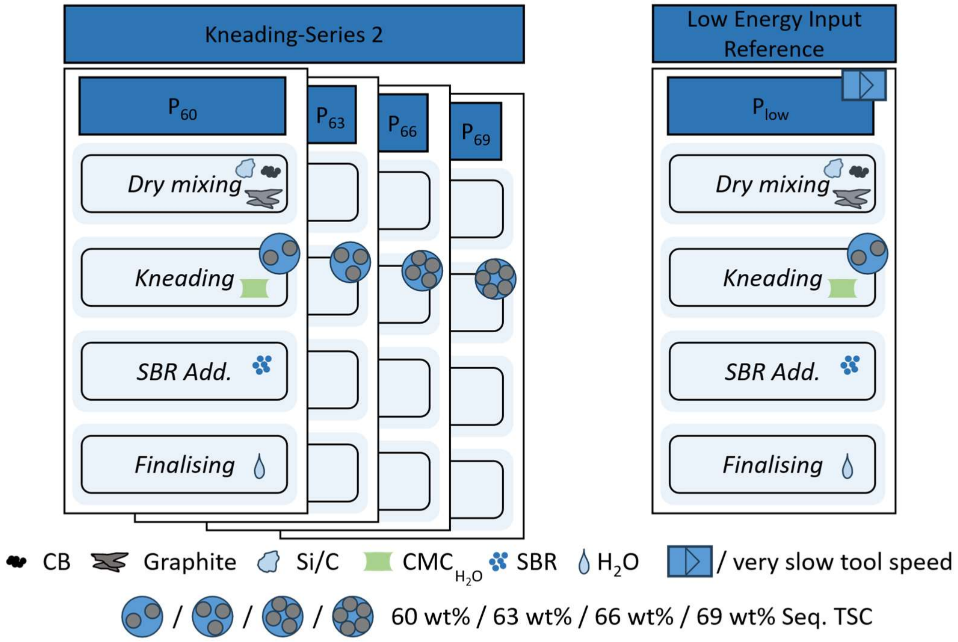

Figure 7-9: Illustration of the variations of Kneading-Series 2 and the low energy input reference

More detailed information can be seen in subsection 4.2.2.5. The components are listed in Table 4-5, the procedure and its details are shown in Figure 4-9. Characteristic for this series is that all the compositions final mass ratios are the same, to be seen in Table 4-10, and a CMC with a molar weight of 875 kDa. Two AM are present in this slurry composition, an artificial graphite, and a silicon-oxide. As with the previous segments Kneading-Series, the samples differ by the TSC of the mixing procedures kneading sequence “x_i”, the here called high solids content mixing – HSCM. The TSC within that HSCM varied from 60 to 69 wt% in four sequences, thus four different procedures – P_{60} to P_{69}. In addition to the variations in x_i, a low-energy input reference, P_{low}, was produced as well, it follows the composition, but another procedure, see Figure 4-10. The power consumption of the mixing procedures was monitored and is presented in Figure 7-10. It should be noted that only the solvent-containing sequences are presented here; these are sequences 2 to 4.

The power consumption profile observed during the processing of P_{60} is consistent with that typically observed for mixing suspensions [153]. This profile is most evident during the rapid HSCM sequence. At the outset of the process, the bulk mass underwent a transformation into a plastic mass, resulting in a peak in rotor power. As the wetting and dispersion of the particles progresses, the plastic mass transitions to a viscous suspension, accompanied by a reduction in power consumption, which ultimately reaches a constant level. It is evident that as x_i increases, there is a significant change in the total power consumption. While P_{63} and P_{66} exhibit a comparable power consumption pattern to that observed in P_{60}, the power consumption of procedure P_{69} undergoes a significant alteration, thereby resulting in a substantial change in the energy input. In this instance, the HSCM sequence does not result in the production of a fluid suspension; instead, a plastic mass is formed. This mass moves through the mixer and intermittently makes contact with the rotor, leading to the generation of a constant series of power peaks rather than a steady mass flow that eventually reaches a steady power level. Consequently, the duration of the HSCM sequence in procedure P_{69} has been extended by two minutes to accommodate the initial period of no mixing.

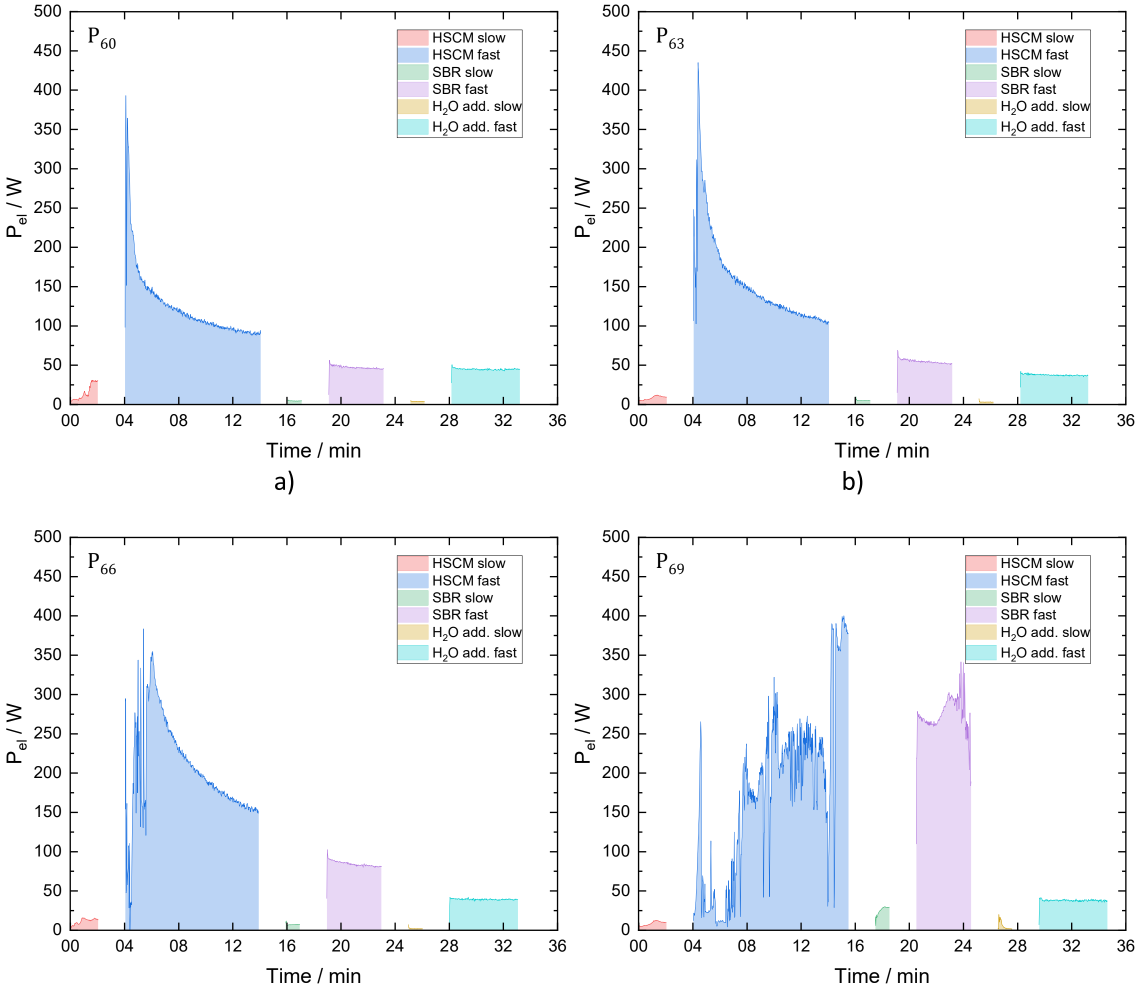

a)

b)

c)

d)

Figure 7-10: a) Rotor power consumption of the mixing procedure of Kneading-Series 2; high solids content mixing (HSCM) occurred at a) 60, b) 63, c) 66 and d) 69 wt% TSC; the legend refer to the mixing sequence as described in Figure 4-9

The accumulated specific energy input, as calculated using equation (29), is presented in Table 7-3. It can be observed that an increase in x_i results in a higher energy input. A comparison of the two most extreme variations, P_{60} and P_{69}, reveals a factor of approximately three between them. Consequently, it may be anticipated that a more pronounced deagglomeration will occur with increasing x_i. It is notable that the HSCM sequence represents the primary source of energy input, although the SBR addition sequence also makes a considerable contribution in the case of P_{69}. A comparison of P_{60} and P_{69} reveals a specific energy input for this sequence that differs by a factor of approximately 11. The H_2O addition fast sequence demonstrates comparable energy inputs for all slurries (see Figure 7-10), with an average value of 2.5 Wh dm^{-3}. This could lead to the erroneous assumption that all slurries exhibit analogous flow behavior. With regard to the low-energy reference, P_{low} exhibited an energy input of approximately one-third that of P_{60}. The detailed consumption data are presented in A 9-4.

Table 7-3 Specific energy input of all mixing procedure variations P_i originating from the change in x_i; total amount of specific energy input and specific energy input of sequence 3, the dispersion of SBR.

Specific Energy Input	$\mathbf{P_{60}}$	$\mathbf{P_{63}}$	$\mathbf{P_{66}}$	$\mathbf{P_{69}}$	$\mathbf{P_{Low}}$
E_{sp}/Wh dm^{-3}	29.1	45.0	59.0	85.9	11.5
E_{sp} of sequence 3 (SBR)/Wh dm^{-3}	3.0	4.1	7.7	31.9	0.6

To gain a more detailed understanding of the flow behavior, the flow curves of the Kneading-Series 2 five slurries as well as a CMC (M_w = 875 kDa) solution with a concentration of 13.5 g L^{-1}, which corresponds to the nominal CMC concentration in the slurry's continuous phase, are presented in Figure 7-11. Despite identical composition and TSC, the slurries exhibit markedly disparate flow behavior. In general, as x_i and, consequently, the energy input increase, the low shear viscosity of the slurries decreases by up to two orders of magnitude, despite their identical composition. In accordance with Stokes' law, it may be anticipated that slurries exhibiting reduced low shear viscosity will undergo sedimentation at a faster rate, resulting in a concomitant reduction in stability. In small batches, this may not be a significant issue. However, on an industrial scale, it could lead to stability problems when using the slurry over an extended period of time without stirring.

Slurry P_{Low}, which was produced at low energy input, demonstrates the highest viscosity values and exhibits uniform, power-law-type shear thinning behavior. Furthermore, slurries P_{60} and P_{63} also exhibit monotonic shear thinning behavior, albeit with lower absolute viscosity values and a less pronounced degree of shear thinning than that observed in P_{Low}. Additionally, the absolute viscosity values decrease with an increase in TSC or energy input during the HSCM mixing sequence. Moreover, slurries P_{66} and P_{69} do not exhibit strict shear thinning behavior. Slurry P_{66} displays weak shear thinning behavior exclusively at low shear rates, reaching a plateau between approximately 10 and 200 s^{-1}, and subsequently exhibiting a decline in viscosity at higher shear rates. Slurry P_{69} displays shear thickening behavior between 10 and 200 s^{-1}, which is followed by a shear thinning regime at higher $\dot{\gamma}$.

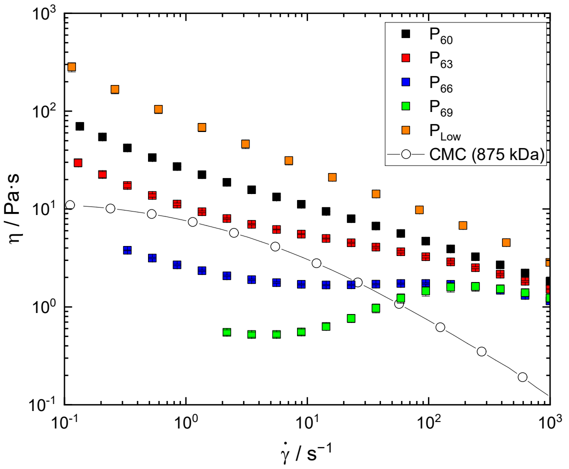

Figure 7-11: Slurries' viscosity function of the Kneading-Series 2; All compositions are identical, but mixed at different TSC during HSCM; TSC = 60 (black), 63 (red), 66 (blue), 69 wt% (green) and the low energy input reference slurry (orange). The CMC-solution (Mw = 875 kDa; open symbols) with the same concentration every slurry holds by composition (13.5 g L^{-1}).

These significant discrepancies in the behavior of slurries with an identical composition provide compelling evidence of disparate particle interactions and, consequently, distinct microstructures resulting from disparate slurry treatments, specifically varying energy inputs during mixing. One potential explanation for these alterations in flow behavior is a discrepancy in particle deagglomeration and the presence of particle clusters that capture a significant portion of the solvent, consequently resulting in an elevated effective particle volume fraction at low energy input. Nevertheless, all slurries exhibited satisfactory dispersion, and scanning electron microscopy images of the corresponding dry samples did not reveal the presence of residual particle clusters. It can be reasonably assumed that mechanical destruction of the solid fraction and a corresponding change in particle size distribution will not affect slurry viscosity, given that the overall particle loading of approximately 40 vol% is insufficient to do so. Furthermore, SEM images of corresponding dry samples do not provide experimental evidence to suggest that this is occurring. Ultimately, the flow behavior of suspensions is contingent upon the colloidal interactions among the suspended particles, in addition to the rheological properties of the solvent [9]. For the slurries under investigation, these phenomena are closely related to the adsorption of CMC on solid particle surfaces [91] and the mechanical degradation of CMC [154, 155] during slurry preparation. The relevance of CMC adsorption and degradation is already evident when comparing the low shear viscosity of slurries P_{66} and P_{69} to that of the CMC solution representing the disperse phase of these slurries. The low absolute viscosity values of slurries P_{66} and P_{69} can only be rationalized by taking into account the aforementioned adsorption and degradation phenomena, which will be discussed in more detail below.

The pronounced shear thickening of sample P_{69} can be attributed to the formation of hydrodynamic clusters. The formation of such clusters is contingent upon the absence or presence of weak, short-range repulsive interactions amongst the particles in question [9]. This phenomenon also results in low viscosity at low shear rates, as observed in the case of P_{69}. In this instance, the steric repulsion derived from the adsorbed CMC layer appears to serve only to offset the constant van der Waals attraction. In contrast, the latter appears to be the dominant phenomenon in the shear-thinning samples P_{60}, P_{63} and, in particular, P_{Low}. It is evident that the energy input during the HSCM mixing sequence has a considerable influence on the adsorption of CMC. Moreover, the mechanical degradation of CMC must be considered, as it affects both the viscosity of the solvent and the strength and range of the steric repulsion provided by the CMC adsorbed on the active particle surface. The reference sample P_{Low}, which was prepared using a different mixing procedure that resulted in a low energy input, exhibits the highest viscosity level and the strongest degree of shear thinning, which clearly indicates that attractive particle interactions are dominant in this slurry.

The slurries were centrifuged and the supernatants were analyzed. Figure 7-12a shows the flow curves for the Kneading-Series 2 supernatants. It should be noted that the supernatant of the slurry P_{Low} was diluted with deionized water in a ratio of 1:26 (supernatant/water) due to its high viscosity, which did not allow the determination of the zero shear viscosity; therefore, the dilution is denoted as P_{Low}. The viscosity functions of these supernatants are essentially determined by the concentrations and molecular weights of the dissolved CMC; the contribution of suspended SBR particles or residual active material is negligible, see A 9-5. The absolute viscosity values differ by about an order of magnitude, indicating that the amount of CMC removed from the disperse phase by adsorption on the active particles is strongly influenced by the slurry preparation procedure. The sample that underwent the greatest energy input during the HSCM mixing sequence exhibited the lowest disperse phase viscosity, indicating that a greater proportion of CMC was adsorbed on the particles in this instance. Moreover, the supernatants P_{60}, P_{63} and the diluted supernatant P_{Low} display shear thinning behavior, whereas samples P_{66} and P_{69} exhibit Newtonian flow behavior. This provides further insight into the processes of mechanically induced adsorption and degradation of CMC in these slurries. Highly dilute CMC solutions exhibit Newtonian flow behavior and solutions of different molecular weights and concentrations can have the same absolute viscosity value. However, solutions of greater concentration demonstrate shear thinning, and the absolute value of zero shear viscosity, along with the shape of the flow curve, constitute a distinctive signature of a solution at a given molecular weight and CMC concentration [11].

Figure 7-12a depicts the flow curves of CMC solutions with M_w = 875 kDa and M_w = 500 kDa, which correspond to the zero shear viscosity of the supernatants P_{60} and P_{low}, respectively. It is evident that the lower molecular weight CMC solution necessitates a higher concentration to attain the same zero shear viscosity as the higher molecular weight CMC solution. Moreover, the higher molecular weight CMC solution displays a markedly pronounced shear thinning behavior. The CMC_{875} solution with c_{CMC} = 0.3 g L^{-1} almost corresponds to the flow curve of the diluted supernatant P_{Low}. Its slightly more pronounced shear thinning indicates that some mechanical degradation also occurred in this case but is neglected for the sake of simplicity. Accordingly, the discrepancy between this concentration and the initial concentration of 13.5 g L^{-1} (see Table 4-10 and Figure 7-11) directly correlates with the quantity of CMC adsorbed onto the particles. In contrast, the behavior of the supernatant P_{60} is distinct from that of the CMC_{875} (M_w = 875 kDa) solution of 1.4 g L^{-1}, which exhibits similar zero shear viscosity, but displays a more pronounced shear thinning behavior. This provides clear evidence that the CMC molecules underwent degradation during the mixing process. In fact, the CMC_{500} solution with c_{CMC} = 5.8 g L^{-1} demonstrates a high degree of similarity in terms of both absolute values and the shape of the flow curve across the entire range of shear rates investigated. It can be concluded that the CMC has undergone mechanical degradation at approximately this average molecular weight. Consequently, the amount of CMC adsorbed can be calculated as the difference between the original concentration and the concentration of this CMC_{500} solution.

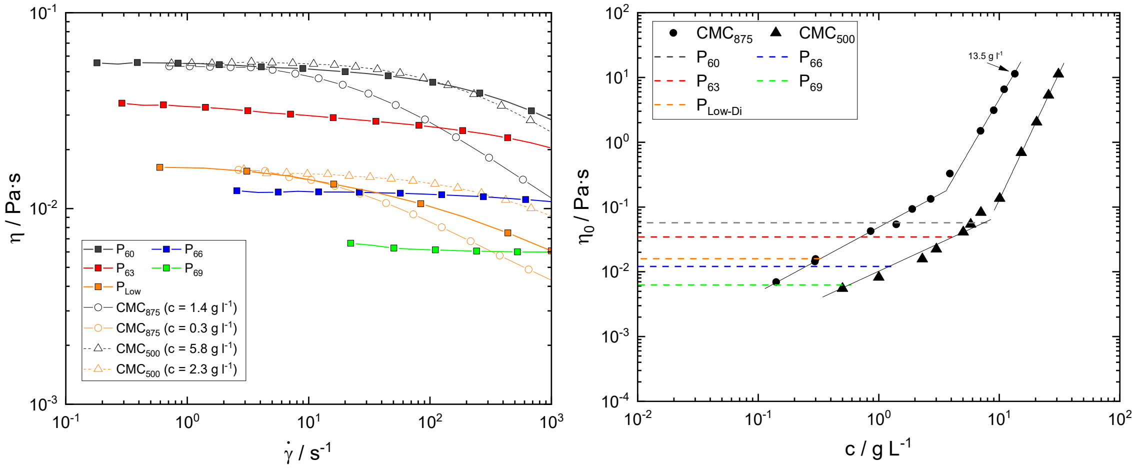

a) b)

Figure 7-12: a) Viscosity as a function of shear rate for supernatants of the Kneading-Series 2; TSC = 60 (black), 63 (red), 66 (blue), 69 wt% (green) for the procedures HSCM sequence and low energy input reference slurry TSC = 60 wt% (orange); CMC solution (875 kDa; circle) with 1.4 (black) and 0.3 (orange) g L^{-1} and CMC solution (500 kDa; triangle) with 2.3 (black) and 5.8 (orange) g L^{-1}; b) η_0 as a function of concentration of CMC solutions (875 kDa - circle; 500 kDa - triangle); dotted lines represent the η_0 value of the series' supernatants

It can be concluded that for P_{60}, approximately 57 wt% of the added CMC was adsorbed on the surface of the active particles. When taking the dilution of P_{Low} into account, the corresponding concentration is calculated to be c_{CMC} = 7.83 g L^{-1}, meaning that approximately 42 wt% was adsorbed. The supernatants P_{66} and P_{69} display Newtonian flow behavior, and it is not possible to assign the measured viscosity unambiguously to a specific M_w and concentration of the dissolved CMC. It may be assumed that, with increasing energy input, no further degradation of molecular weight takes place. Consequently, the CMC concentration in the supernatant can be determined from the data for a series of CMC solutions with M_w = 500 kDa, shown in Figure 7.10b, which relate the zero shear viscosity to the CMC concentration. Thus, it can be concluded that the proportion of adsorbed CMC increases with rising energy input. In the case of slurry P_{69}, nearly all the CMC is adsorbed onto the particles. This is consistent with the observed changes in the flow behavior of the corresponding slurries, which can be rationalized assuming a stronger steric repulsion for P_{69}, which ultimately balances the attractive van der Waals force. Conversely, should further degradation in the CMC chains occur in conjunction with a rise in energy input, the observed supernatant viscosity curves would indicate that a smaller proportion of shorter CMC chains was absorbed onto the active material particles. This is contrary to the observed reduction in slurry viscosity, which lends support to the assumption that no further mechanical degradation of CMC occurred in the slurries prepared with a higher energy input than that of P_{60}. Furthermore, the CMC of the slurries P_{60} to P_{69} is well within the dilute polymer regime of CMC_{500}. However, the CMC concentration of P_{Low} lies within the semi-dilute system of CMC_{875}, indicating that the energy input during the mixing process influences the polymer regime.

A similar effect of mechanical energy input on CMC adsorption was recently published by Park et al. [156]. However, the group did not consider mechanical degradation as they already used a low molecular weight CMC. Weber at al. [141] investigated the impact of dry mixing CB and Gr as a preliminary sequence before mixing it with the solvent in an extruder. Varying the tip speed during dry mixing resulted in different flow behavior in the final slurries, ranging from a rather monotonous shear thinning behavior to a discrete plateau. Perhaps the pretreatment of the powder resulted in different surface availability or different energy input during extrusion, resulting in a varying degree of polymer adsorption and degradation, finally changing particle-particle interactions and thus flow behavior as discussed above.

7.1.3. Coating considerations of slurries with complex flow behavior

In order to analyze the suitability of coating for slurries exhibiting considerable differences in flow behavior, slurries P_{60} and P_{69} of the Kneading-Series 2 were coated on a roll-to-toll coater utilizing a slot-die. The two slurries were coated at varying line speeds, with the maximum and minimum G values ascertained for the upper and lower stability limits, respectively. The results are presented in Figure 7-13a, which depicts the dynamic gap G^* of both stability limits as a function of line speed U_L. For slurry P_{60}, the upper stability limit (USL) exhibited a slight decrease with increasing line speed, with a dynamic gap range of 1.9 to 1.7. As the line speed (U_L) increases from 2 to 10 m min^{-1}, the difference between the upper and lower stability limits (ΔG^*) increases, reaching a value of approximately 0.3. The stability limits of slurry P_{69} exhibit a more pronounced shift. The initially high upper stability limit (USL) of approximately G^* = 2.5 at a line speed of 2 m min^{-1} decreases to G^* = 1.4 at 10 m min^{-1}. The corresponding lower stability limit (LSL) decreases in a similar manner; however, at 10 m min^{-1}, the lower limit approaches the upper limit, with G^* = 1.3. In contrast to P_{60}, which demonstrates a broad corridor of stable operation limits in this coater setup, P_{69} displays a rather narrow window of stable operating parameters. The narrow window of stable operating parameters makes the coating of P_{69} challenging, particularly at higher speeds.

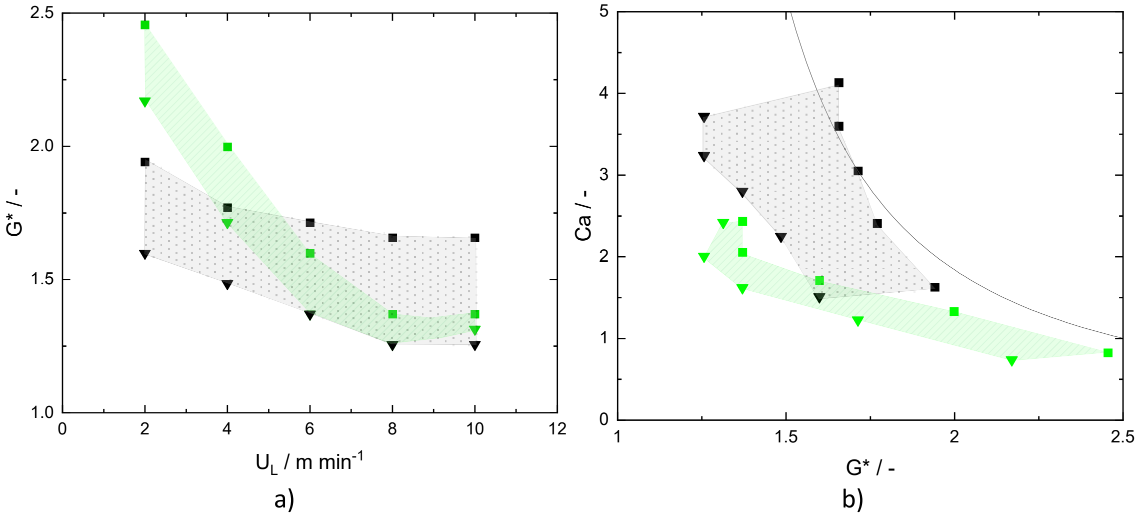

a) b)

Figure 7-13: Stability map for slot-die coating of slurries P_{60} (black) and P_{69} (green); USL—square symbol; LSL—triangle symbol; a) dynamic gap as a function of line speed; b) capillary number as a function of dynamic gap, including the VCM of Ruschak 1976 [129] (Eq. 27, line)

In order to facilitate a comparison between the results presented here and the visco-capillary model of Ruschak [129], a stability map was plotted in the Ca -G^* plane (Equations (25) and (26)), as illustrated in Figure 7-13b. It is important to note that the visco-capillary model (VCM) of Ruschak [28] was developed on the basis of Newtonian fluids. At the upper limit of 2 m min^{-1}, slurry P_{60} could be coated with G^* = 1.9 at Ca = 1.6, while at 10 m min^{-1}, a stable coating was achieved with G^* = 1.7 at Ca = 4.1. This upper stability limit (USL) border is in close proximity to that which was predicted by Ruschak; however, the decline in Ca with increasing shear rate is more pronounced. In contrast, slurry P_{69} demonstrated the ability to maintain an USL at 2 m min^{-1} with G^* = 2.5 at Ca = 0.8 and at 10 m min^{-1} with G^* = 1.4 at Ca = 2.4. In this instance, only for a very high G^* value of 2.5 is the VCM prediction approached. This comparison indicates that the coating behaviour of monotonically shear thinning slurries such as P60 can be predicted with respect to line speed and gap height settings. However, more complex slurries such as the shear thickening P_{69} are not represented by the model.

Upon exceeding the upper stability border, air entrainment was noted, which is indicative of the upstream meniscus's failure. In the case of P_{69}, this may be attributed to its comparatively lower viscosity. The resulting capillary number is significantly lower than that of P_{60}, indicating that the viscous forces are less pronounced. This ultimately results in the upstream meniscus closing towards the coating bead and the entrainment of air occurring at a lower G^* than it would with P_{60}. Given the narrow stability window of P_{69}, coating at higher speeds may prove challenging. In such cases, the installation of a vacuum box upstream could prove beneficial.

Despite the significant differences between the two slurries, the coating process was successfully completed by modifying the setup parameters. Nevertheless, it is crucial to underscore the fact that the electrodes ultimately manufactured are destined for integration within cells. It should be noted that the quality criteria of an electrode extend beyond the ability to coat, encompassing mechanical properties and electrical resistance. These aspects were not investigated in the context of the coating experiment.

7.2. Characterization of electrodes Kneading-Series 2

The table-coated electrodes, originating from the Kneading-Series 2, were characterized with a loading of 3.3 mAh cm^{-2} and an average compressed density of 1.2 g cm^{-3}. The electrodes, were subjected to analysis using a scanning electron microscope equipped with a backscattered electron (BSE) detector. The resulting images are presented in Figure 7-14 and Figure 7-15.

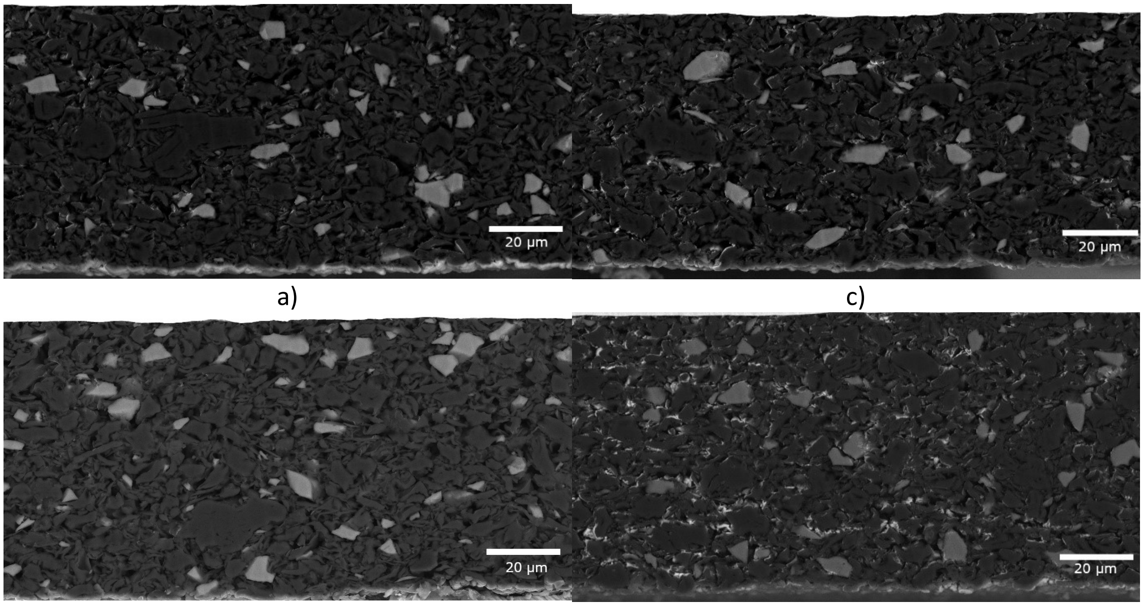

a) c)

b) d)

Figure 7-14: SEM cross-section of investigated compressed electrodes; a) P_{60}; b) P_{63}; c) P_{66}; d) P_{69}

Given the differences in the mixing procedures' E_{sp}, it is reasonable to hypothesise that particle deagglomeration, particularly of carbon black, may be influenced. Nevertheless, the overall distribution of the active material is found to be homogeneous. However, the P_{60} electrodes (Figure 7-15b) display a greater prevalence of larger CB aggregates than the P_{69} electrodes (Figure 7-15d).

Besides the progressing deagglomeration of CB, no noticeable degree of particle destruction was found. It should be noted that the bright white residue is suspected to be debris from the current collector, which is believed to have been caused by the ion polishing treatment.

Figure 7-16a illustrates the impact of dispersed CB on total electrode resistivity, which is divided into ρ_I and ρ_{CN}, eq. (32). The resistivity is observed to decrease with increasing energy input, from a total of approximately 4 ± 0.4 to 2.5 ± 0.2 mΩ cm^2. This trend is observable in both the coating and the interface. However, the most notable distinction in this series is the interfacial resistance, which exhibits a significant reduction: $\rho_{I;P_{60}}$= 3.0 ± 0.1 and $\rho_{I;P_{69}}$= 1.7 ± 0.2 mΩ cm^2. One potential explanation for this reduction in interfacial resistivity is that as the energy input increases, a greater proportion of CMC is adsorbed onto the active material particles, as previously discussed in the rheology section. Consequently, a reduction in CMC at the coating/substrate interface results in a decrease in interfacial resistivity. Conversely, the resistivity of the coating layer itself remains relatively constant $\rho_{CN;P_{60}}$= 1 ± 0.27 and $\rho_{CN;P_{69}}$= 0.8 ± 0.03 mΩ cm^2. Despite the reduction in CB agglomerate size with increasing x_i, this appears to have a minimal impact on the coating layer resistivity in these graphite-based electrodes. µ

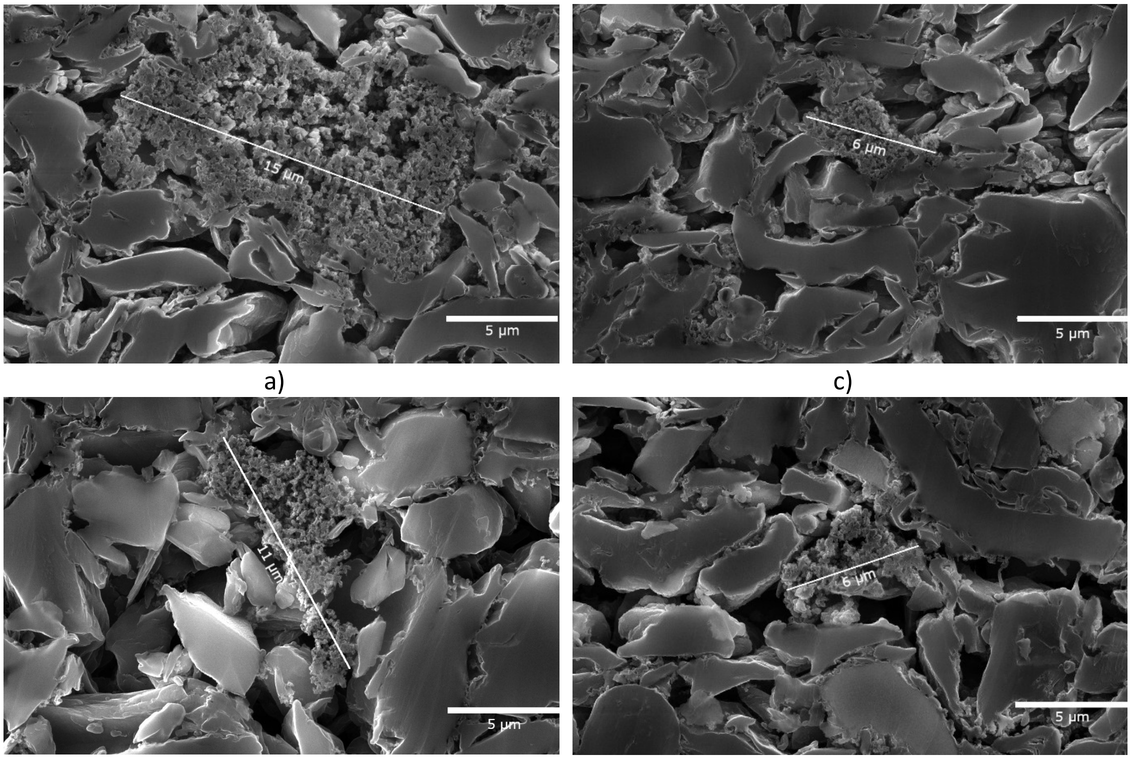

a) c)

b) d)

Figure 7-15: SEM cross-section of investigated compressed electrodes; a) P_{60}; b) P_{63}; c) P_{66}; d) P_{69}

The adhesion between the electrode and the current collector was characterized by a 90° peel-test, with the corresponding data for P_{60} to P_{69} presented in Figure 7-16b. While electrodes P_{60} to P_{66} exhibit a comparable peel strength of approximately 4.4 N m^{-1}, sample P_{69} displays a notable decline in adhesion, exhibiting a peel strength value of approximately 1.3 N m^{-1}. The low adhesion observed in sample P_{69} may present a challenge for automated processes within cell assembly, potentially leading to

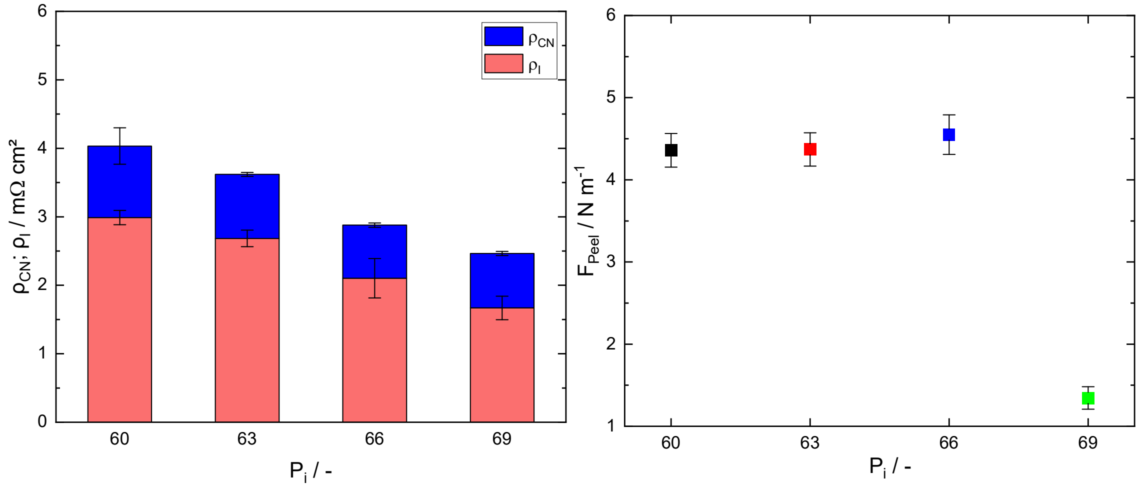

a) b)

Figure 7-16: Characterization of compressed electrodes originating from Kneading-Series 2; a) total resistance divided into specific contact resistance ρ_{CN} and interface resistance ρ_I; b) peel strength of compressed electrode coatings delamination of the coating. The adhesion is primarily provided by the added SBR [43]. The high energy input in sequence 2 (HSCM) of the procedure has a notable impact on SBR distribution, with a considerably lower SBR fraction at the current collector interface for P_{69}. This may be attributed to shear-induced agglomeration of SBR particles.

7.3. Characterization of cells

The following subsections present the electrochemical results of the two series, Kneading-Series 1 and Kneading-Series 2, in terms of C-rate capability and cell resistivity.

7.3.1. Kneading-Series 1

Full pouch cells (SPC_{46}) of the Kneading-Series 1's electrodes where electrochemically characterized by applying a formation and a C-rate test plan on them, described in section 4.6 . Six cells were used per variation.

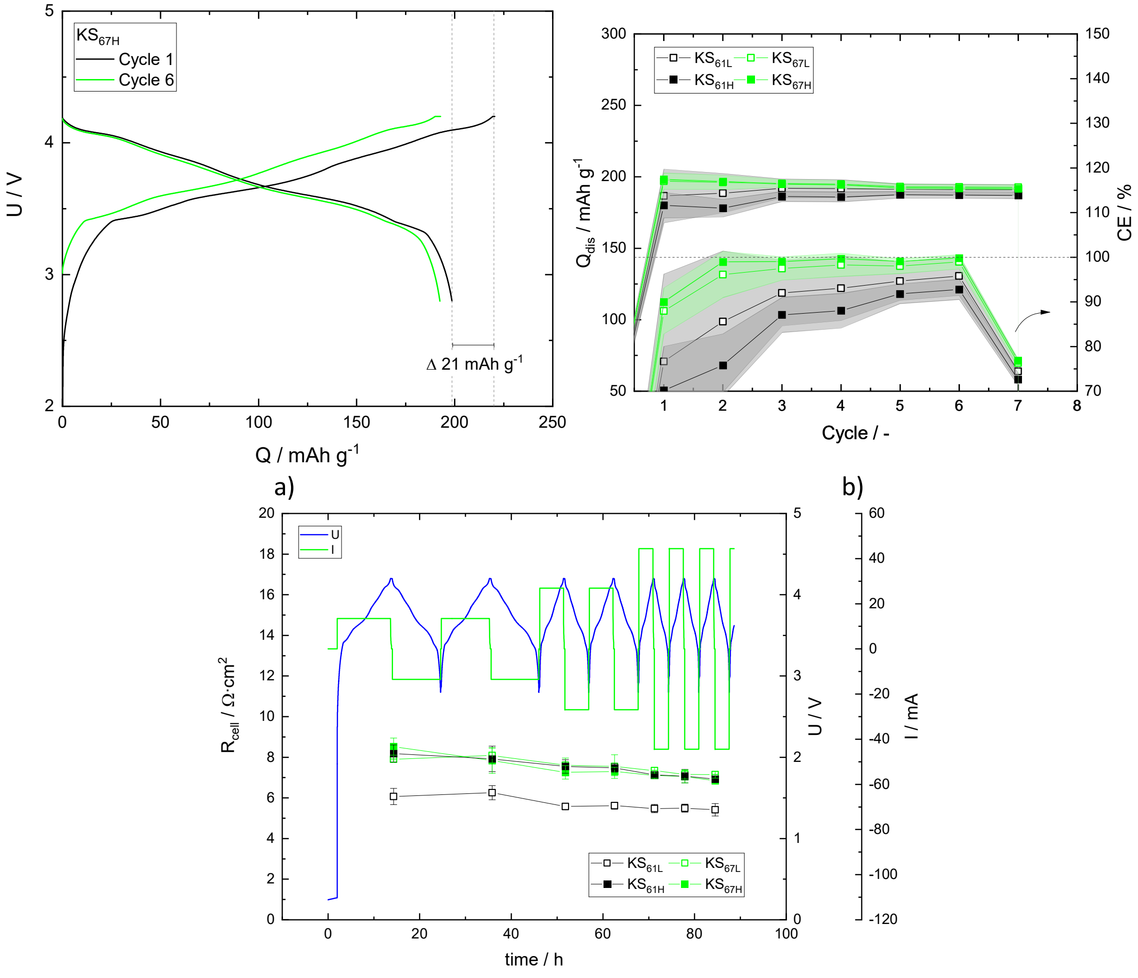

a)

b)

c)

Figure 7-17: a) Voltage profile of KS_{67H}; b) average Capacity of the Kneading-Series 1 FPC during formation; c) Voltage and current profile of a FPCs of Kneading 67H of the Kneading-Series 1 with the calculated cell resistance using simplified DCIR method (34)

Figure 7-17a illustrates the voltage profile of a representative cell derived from KS_{67H}. In the initial cycle, the value of Q_{cha} is 220 mAh g^{-1}, while Q_{dis} is approximately 199 mAh g^{-1}. This results in a net loss of approximately 21 mAh g^{-1}, leading to an estimated first-cycle efficiency (FCE) of 90.1 %. The other cells in the series demonstrate a relatively high standard deviation in FCE during the initial cycle, as illustrated in Figure 7-17b. It seems probable that this is the consequence of a lack of uniformity in the wetting of the FPCs electrodes by the electrolyte. This effect appears to diminish as the cycle count increases. This also elucidates the discrepancies observed between the samples during the initial four cycles. As the formation plan progresses, the cells exhibit a heightened degree of stability in their cycling behavior, particularly in cycles five and six. The initial cycle of KS_{67H} exhibited a Q_{dis} value of 198 ± 0.4 mAh g^{-1} and a coulombic efficiency (CE) of approximately 90 %. The lowest Q_{dis} value observed in KS_{61H} cells was 180 ± 8.9 mAh g^{-1}, accompanied by a CE of approximately 70 %. By the sixth cycle, the discrepancies are less pronounced. In this instance, the KS_{67H} cells exhibited a Q_{dis} of 192 ± 0.4 mAh g^{-1} and a CE of approximately 99.8 %, while the KS_{61H} cells demonstrated a Q_{dis} of 187 ± 2.3 mAh g^{-1} and a CE of approximately 92.8 %. The formation results suggest that the mixing procedure, which involved a higher energy input and a TSC of 67 wt% within the kneading sequence, resulted in the creation of a cell that exhibits the highest Q_{dis} and high CE. Nevertheless, an examination of the cells' resistance via the simplified DCIR method (Figure 7-17c) reveals that the cells belonging to the KS_{61L} variation exhibit a markedly lower R_{cell} value of 6.1 ± 0.8 Ω cm^2 in comparison to the other samples, such as those belonging to the KS_{67H} procedure, which displays an R_{Cell} value of 8.5 ± 0.9 Ω cm^2. This can be attributed to the formation's characteristic low current and constant current voltage (CCV) regimes, as indicated by R_{Cell}, which predominantly represents the electric resistance of the cell and has a minimal impact on the formation's Q_{dis}.

As illustrated in Figure 7-18a, the series cells operate at a rate of approximately 186 to 193 mAh g−1 during the initial two cycles of the C-rate test. The KS_{67H} configuration continues to demonstrate the highest Q_{dis}, as previously observed. As the C-rate is increased, the overall Q_{dis} value is observed to decrease. From 0.5C to 3.0C, the KS_{67L} configuration exhibits the highest Q_{dis}. At the commencement of 3.5C, the cells originating from procedure KS_{61H} are more dominant in terms of discharge capacity. This is illustrated in the figure's inlay. The Q_{dis} values of the KS_{61H} and KS_{67H} are both 150 mAh g−1. Furthermore, a slight degree of fading is discernible, indicated by a reduction in Q_{dis} within each step of constant C-rate. This behavior can be observed in both low and high energy input procedures of KS_{67}. This may be indicative of lithium plating due to elevated ionic resistances. At the subsequent C-rate step, 4.0C, the remaining samples also exhibited capacity fading. At the final check-up cycle (33 and 34), the cells KS_{61L} exhibited the highest Q_{dis} value of 180 mAh g^{-1}, while the KS_{67H} demonstrated the lowest value of 165 mAh g^{-1}. All electrodes and cells within this series were treated in an identical manner. The cell resistance data is shown in Figure 7-18b, it is eminent that cells of KS_{61L} hold the lowest cell resistance, this corresponds well with its higher performance level within the C-rate test.

It must be proposed that the disparate outcomes observed in these cells are a consequence of the differing mixing procedures employed. Consequently, the mixing procedure with a low TSC while kneading and a low tool speed, which consequently results in a reduced energy input, is beneficial in these pure graphite anodic electrodes. This results in an enhanced C-rate capability, discharge capacity and a reduction in capacity fading.

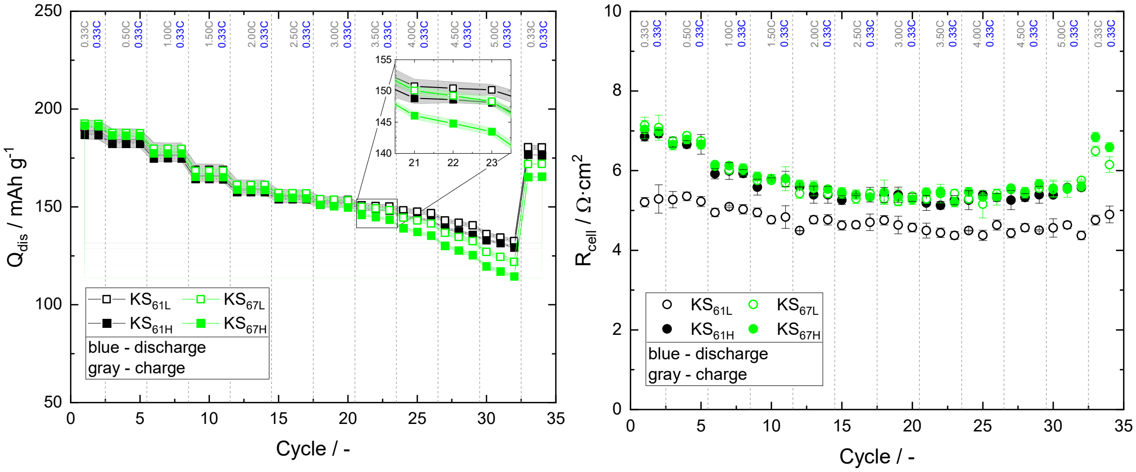

a) b)

Figure 7-18: Cell data of Kneading-Series 1; a) C-rate test b) calculated cell resistance using simplified DCIR method (34)

7.3.2. Kneading-Series 2

The electrodes of the Kneading-Series 2, procedures P_{60} to P_{69}, were employed in the construction of SPC_{20} full pouch cells, four cells per variation. The voltage profile of the most effective cell of the two-cell variations, P_{60} and P_{69}, are illustrated in Figure 7-19a. Cell P_{60} exhibits a slightly higher Q_{cha} than cell P_{69} (228 vs 225 mAh g^{-1}). The Q_{dis} of cell P_{60} was measured at 193 mAh g^{-1} and cell P_{69} at 188 mAh g^{-1}. Consequently, the first cycle efficiency was calculated to be approximately 84.7 % for cell P_{60} and 83.5 % for cell P_{60}. Given the use of silicon in the anodic electrodes employed here, the aforementioned first cycle efficiency appears to be reasonable. In addition to the minor fluctuations resulting from the diminished Q_{dis}, no notable discrepancies in the voltage profile are discernible between the two samples. The subsequent formation capacities (Figure 7-19b) of the series' cells exhibit a comparable trend in terms of Q_{dis} and coulomb efficiency. At the sixth cycle, the highest average Q_{dis} was observed for cells P_{63}, at approximately 171.2 mAh g^{-1}, while the lowest was observed for cells P_{69}, at 168.1 mAh g^{-1}. The cells exhibited a CE of 98.3 ± 0.4% for both.

The simplified DCIR method was employed to calculate the cell resistance, the results of which are presented in Figure 7-19c. The series R_{cell} was calculated to be between 6 and 11 Ω cm^2. At the seventh cycle, cells P_{63} exhibited the highest calculated R_{cell}, with an average of 9.8 ± 3.2 Ω cm^2, while cells P_{60} exhibited an average of 7.3 ± 2.1 Ω cm^2.

Figure 7-20a illustrates the C-rate test of the series' cells. In the initial segment of the test, a notable decline in discharge C-rate is evident, accompanied by a discernible reduction in capacity during the cathode lithiation phase. This may be attributed to ionic resistances associated with the cathode. This irreversible capacity loss results in a relatively low check-up cycle (cycles 33 and 34).

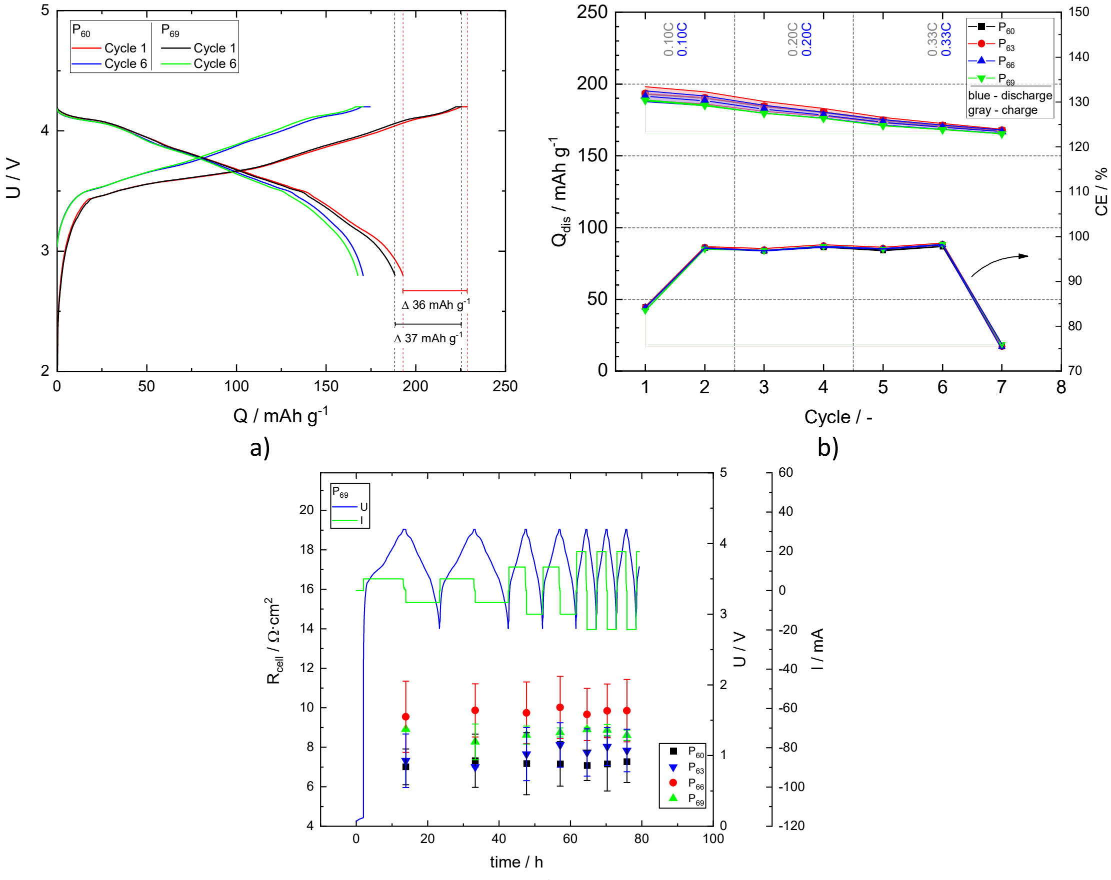

a)

b)

c)

Figure 7-19: a) charge and discharge curves of a FPC of Kneading 67H of the Kneading-Series 2; b) average Capacity of the Kneading-Series 2 FPC during formation; c) Voltage and current profile of a FPCs of Kneading 67H of the Kneading-Series 2 with the calculated cell resistance using simplified DCIR method

In this instance, cells P_{69} are operating at the highest Q_{dis} of 126.4 ± 0.8 mAh g^{-1}, while cells P_{60} are operating at 119.9 ± 0.8 mAh g^{-1}. At 0.5C, the cells Q_{dis} follow the same trend as the electrode resistance measurement of Figure 7-19a, although the cells' resistivity measurements of Figure 7-19c indicate that the anodic electrode's contribution is three orders of magnitude smaller than that of the R_{cell}, and therefore the cells resistance does not follow the same trend as the electrodes ρ. At higher C-rates, e.g. 4.0C cells of cells P_{69} exhibit the highest average Q_{dis} (66.3 ± 1.4 mAh g^{-1}), yet the standard deviation of the other cells, e.g. P_{66} (65.2 ± 11.8 mAh g^{-1}), is too high to allow for a meaningful comparison. In the final assessment conducted at cycles 65 and 66, cells P_{69} exhibited the highest average Q_{dis}, reaching approximately 128.8 ± 0.3 mAh g^{-1}, while cells P_{60} demonstrated a value of 121.2 ± 0.9 mAh g^{-1}.

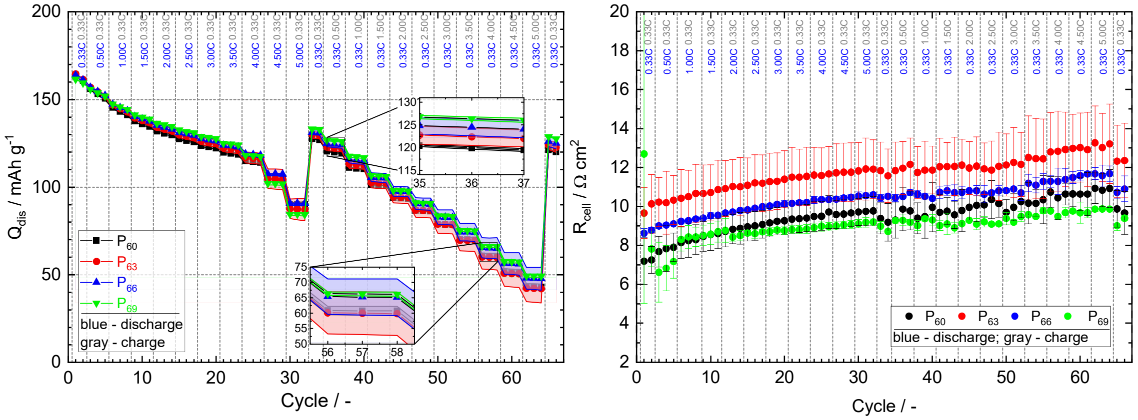

a) b)

Figure 7-20: a) C-rate test of the FPCs of Kneading-Series 2 ; b) calculated cell resistance using simplified DCIR method

7.4. Summary and conclusion

This chapter examined the effects and consequences associated with a change in TSC and the subsequent alterations in energy input. In pursuit of this objective, a series of experimental studies were conducted.

The initial series demonstrated that a slurry of the same final composition can be produced by either manual or mechanical mixing. The resulting slurries display markedly disparate viscosity profiles. The slurry produced by the machine exhibits a markedly lower viscosity, by a factor of several orders of magnitude. Moreover, the kneading sequence's TSC content was observed to influence latter slurry's viscosity function as well, as an increase in TSC resulted in a notably lower viscosity.

The apparent importance of TSC was further investigated by producing a series of slurries with a wide range of final solids content. As anticipated, the successive increase in slurry-TSC resulted in elevated slurry viscosity [14, 17]. The variation in TSC, was created by individual mixing procedures, hence the procedure's sequence TSC incrementally changed as well. The resulting slurries exhibited a segment of exponential low and high shear viscosity as a function of slurry TSC. However, in contrast to slurries that are created by dilution of a stock [157], a change in flow behavior was observed, once changed, the exponential correlation changed as well. As the procedures specific energy input did not increase in the same way the viscosity did, it was concluded that a different microstructure is formed as a consequence of the higher TSC values in both the procedure's sequences and the final TSC. In order to establish a relationship between TSC and energy input, the same material composition was used in another series of experiments.

Within this Kneading-Series 1, two procedures were investigated, one with short sequences and slow dispersion tool speeds and one with longer sequences and faster tool speeds, representing a low and high energy input procedure, while keeping the final composition of the slurry constant. The procedure variation concerned the kneading sequence's TSC and was carried out in four increments per procedure. It was shown that the low energy input procedure produced slurries of higher viscosity than the high energy input procedure. As for the changes in kneading sequence TSC, a decrease in viscosity was observed with increasing TSC. However, the increment with the highest TSC (70 wt%) in the kneading sequence did not follow this trend as their viscosity was elevated. It was assumed that the high TSC created a not flowable mass, hence no adsorption related change in flow behavior was observed. The slurries were treated in a centrifuge and the supernatant, which theoretically consists of a negligible proportion of solids and dissolved CMC within the continuous phase of the slurries, was compared with a range of CMC solutions. It was found that although the default concentration is high enough to be considered a semi-dilute polymer solution, most of the slurries' supernatants had a CMC concentration low enough to be considered a dilute polymer regime. This effect was attributed to the effect of polymer adsorption and occurred to varying degrees. Assuming no mechanical degradation occurred, it was found that as the energy input increased, so did the amount of CMC adsorption. Furthermore, it was theorized that very a high sequence TSC cause the mass to become non-flowable, resulting in an unexpected low energy input, causing less CMC adsorption, meaning the polymer regime stayed semi-dilute and did not change into a dilute one. It is well established that the adsorption of CMC on graphite-based slurries is contingent upon the ratio of polymer and graphite [91, 116, 158, 159] until a saturation limit was reached. These results suggest that the degree of adsorption is affectable by the mixing procedure's energy input.

Electrodes from the slurries with the highest and lowest viscosity, from both procedures, were used in full pouch cells. During the formation process, the cells originating from the high energy input process demonstrated superior coulombic efficiency in comparison to those from the low energy input procedure; however, the measured capacity of the cell was found to be very similar in both cases. The majority of the cells exhibited comparable cell resistance, yet the cells from the lowest energy input procedure exhibited significantly lower resistance. The charge-specific C-rate test demonstrated that the cells exhibited comparable performance up to a rate of 3.5C. However, increasing the C-rate resulted in significantly less charged capacity, with the cells exhibiting the lowest cell resistance demonstrating this behavior at 4.0C and to a lesser extent than the others. Subsequent to the C-rate variations, the cells subjected to the lower kneading TSC procedures exhibited a higher capacity within the check-up cycle, suggesting that the cells exposed to the higher kneading TSC procedures experienced a considerable permanent capacity loss. It is therefore reasonable to predict a reduction in cycle life.

With regard to the second series of kneading sequence variations, the same blend of graphite and SiO_x as that used in the Parameter Series was employed. In contrast to the initial kneading series, an alternative type of CMC was employed, distinguished by a markedly higher molar weight and an identical degree of substitution. The procedure Kneading-Series 2 was varied in four increments of TSC during the kneading sequence. To facilitate a more comprehensive interpretation of the procedure, a low-energy reference procedure was also employed. It is demonstrated that the combination of components and procedure settings is highly dependent on the TSC present within the kneading sequence. A change from approximately 60 to 69 wt% within the kneading sequence resulted in an increase of the energy input and a reduction in the low shear viscosity of the later slurry by an order of magnitude, as well as a change in its flow behavior. The initial linear shear thinning flow behavior underwent a transformation, giving way to an initial shear thinning trend at low shear rates, followed by a brief period of Newtonian behavior. This was succeeded by a shear thickening segment, which ultimately exhibited shear thinning behavior at high shear rates, dominated by hydrodynamic forces.

As with the first kneading series, the intricate alteration in flow behavior was postulated to be the consequence of extensive CMC adsorption. The supernatant from the slurry was investigated and compared to two series of CMC dilutions: the original high-molecular-weight CMC (875 kDa) and a low-molecular-weight CMC (500 kDa). It was demonstrated that as the concentration of TSC in the kneading sequence increased, both the degree of adsorption and the degree of mechanical degradation increased concomitantly. This was evidenced by the supernatant viscosity function, which exhibited a profile analogous to that of the low molar weight CMC, despite the slurry's composition being based on a high molar weight CMC. Mechanical degradation of polymers itself is no new observation, however, this topic and its consequences is rarely discussed in literature addressing LICs. The two slurries that exhibited the most pronounced differences in flow behavior were selected for examination on a pilot line scale roll-to-roll slot die coater. The stability limits of the coating process were determined and mapped for a broad range of machine settings, resulting in a map of the upper and lower stability limits. It was shown that, despite the significant differences in rheological behavior, both slurries were capable of being coated. However, the common linear shear thinning slurry displayed a wide range of stable settings, thereby allowing a corresponding freedom of process settings. In contrast, the slurry with the complex flow behavior demonstrated a narrow band of process settings that led to a stable coating. It was hypothesized that higher line speeds might not be feasible due to the slurry's complex flow behavior. Despite the fact that both slurries were coated without any defects, the visco-capillary model [129] was only able to predict the behavior of the linear shear thinning slurry, validating that the model does not cover every application case within electrode coatings [126]. The tailoring of slurry viscosities by changing the procedure parameters like the kneading sequence's TSC could serve as a potent method to lower low shear viscosities to a moderate extent, thereby mitigating coating defects believed to be induced by elevated viscosities [126, 160].

The subsequent electrodes demonstrated no damage at the level of the active material particles. It was demonstrated that the deagglomeration of the carbon black conductive additive increased in accordance with the increase in kneading sequences TSC, which corresponded to the energy input of the procedure. This incremental change in dispersion was also reflected in the electronic conductivity of the dry electrodes. The peel strength of the electrodes was found to be comparable for three out of the four variations. However, the procedure with the highest energy input resulted in electrodes that exhibited significantly reduced peel strength. This finding was attributed to the SBR dispersion sequence employed during the mixing procedure, which involved a substantially higher energy input compared to the other procedures. It was proposed that this phenomenon may be attributed to the agglomeration of SBR particles as they flocculated in their emulsified form as a consequence of the high shear forces. The formation of the full pouch cells in the series demonstrated minimal variation. The trend observed in the dry electrode resistance did not manifest at the cell level. The C-rate test demonstrated that the discharge rate is solely influenced by the paired anode at exceedingly high C-rates. The charge segment demonstrated differences. At low charge rates, an improve of the rate capability correlated with an increase of procedure energy input. However, at high C-rates, this trend could not be observed any more. In contrast to the cell formation, the C-rate tests final check-up cycle showed a trend whereby the higher the mixing procedure's energy input, the higher the discharge capacity.

The cell performance of the two kneading-series evidently demonstrates that there is no simple formula for designing a mixing procedure, and that fine-tuning is invariably a reciprocal process. On the one hand, the all-graphite electrode, originating from the low energy input procedure, exhibited superior C rate capabilities; on the other hand, the silicon-containing electrodes, originating from the high energy input procedures, also demonstrated beneficial capabilities. This finding underlines the existence of an optimal degree of conductive additive dispersity [75, 123]. Conversely, graphite-containing anodes typically exhibit excellent conductivity, and there have been instances that demonstrate an extensive mixing procedure might be harmful to tortuosity [124]. However, the majority of publications address cathodic mixing procedures (see Table 2-1), which use a less conductive active material and a different binder (PVDF), which typically does not adsorb on the particle surfaces [83]. This chapter therefore provides valuable insights into the design considerations of the compositional ratios within a mixing process dedicated to the production of anodic graphite-based electrode slurries. It highlights the rheological consequences of these and the impact on the electrode and subsequent cell.

8 Summary and outlook

8.1. Summary

In this work, the topic of producing lithium-ion electrode suspensions was investigated in a number of experimental series. To gain a broad understanding of the topic, different material compositions were investigated, utilizing compositions of both cathodic LFP and anodic graphite and SiO_x. The materials and machines utilized were chosen in accordance with current trends and applicational relevancy. It has been shown that the electrode suspensions, known as slurries, exhibit complex flow behavior as a result of a number of circumstances.

From a compositional standpoint, it was shown that the flow behavior is a superposition of viscous influences, originating from the solvent, the dissolved polymer, the sur-micrometer and the sub-micrometer particle fractions. However, the flow behavior of a slurry is not solely contingent on the intrinsic properties of its constituent materials, but also on the manner in which they have been processed and the subsequent microstructure that emerges. The cathodic experiments conducted in this work revealed that conductive additives, specifically particulate carbon black and single-walled carbon nanotubes, demonstrated a notable enhanced colloidal impact on flow behavior compared to the investigated LFP active material. This notable difference significantly influenced the slurry's flow behavior. On the anodic side, the interaction between the binder and the composition's components was of particular interest due to the considerable interaction between them. It was evidenced that carboxymethyl cellulose interacts with the components by adsorption, which not only reduces the viscosity of the slurry, but also alters its flow behavior. In extreme cases, this behavior changed from monotonous shear thinning to a multi-segment viscosity function that displayed shear thinning, plateau and shear thickening behavior throughout the spectrum of investigated shear rates. This behavior was attributed to the steric isolation of the particles by the adsorption of carboxymethyl cellulose, which either neutralized the Van der Waals forces that are always present or promoted a slightly repulsive particle-particle interaction. It was hypothesized that this would facilitate the formation of hydrodynamic clusters, which are associated with the shear thickening behavior. The investigation revealed, that the degree of adsorption is primarily influenced by the energy input associated with the mixing procedure. This was regulated by adjusting the total solids content of dedicated procedure sequences. This design consideration has been demonstrated to exert control over the degree of adsorption, to the extent that it even changed the polymer regime of the suspension's continuous phase from semi-dilute to dilute.

Further experiments have shown that rheological changes can be achieved by modifying the procedure's machine parameter, the dispersion tool's speed and the sequence duration. However, this was largely contingent on the sequence in which they were varied. E.g. a modification of machine parameters within a dry mixing sequence did not result in a notable impact on the flow behavior of the subsequent slurry when conducted on anodic compositions. The same results were observed for a sequence that disperses carbon black in a dissolved binder. Nevertheless, within the kneading sequence, alterations to the tool speed and, most notably, the sequence duration resulted in a change in slurry viscosity. This was due to the fact that these modifications led to a markedly higher energy input compared to the other parameter variations. This behavior was examined in two anodic compositions with distinct active materials and carboxymethyl celluloses and was associated with adsorption behavior and mechanical degradation of the carboxymethyl cellulose. At the micro structural level, variations in pore size distribution and in carbon black deagglomeration were observed. In terms of cell resistance and C-rate capabilities, discrete differences were observed, however, within the investigated anodic compositions the differences were rather small, underlining that the choice of machine-parameters should not be the highest priority, but the choice of sequencing, as will be explained later.

The complexity of the anodic slurries' flow behavior potentially presents a challenge when coating the slurries. On a larger scale, the processability of slurries exhibiting both typical and complex flow behavior was demonstrated on a roll-to-roll slot die setup. However, this was contingent upon the requisite adjustment of machine parameters. The mapping of settings that resulted in a set of stable coating windows indicated that it is possible to predict stable processing conditions of typical monotonous shear thinning slurries by using Ruschak's Visco-capillary model, despite its initial design for Newtonian liquids. Nevertheless, the results also suggested that there may be a limit in terms of line speed to the processability of slurries with complex flow behaviors, despite the ability to coat them in this experiment.

The cathodic LFP compositions also exhibited alterations in their flow behavior as a consequence of variations in the mixing procedures employed. The dispersion of carbon black as an initial sequence, followed by the active material and finished with a carbon nanotube dispersion, exhibited the highest viscosity values, indicating that attractive interactions are stronger than in other procedure variations. The subsequent electrode coatings exhibited markedly reduced mechanical resistance. Subsequently, microstructural changes were put forth as a potential explanation for this behavior. It was hypothesized that the weak mechanical strength is the result of a less pronounced dispersion of the conductive additives, which creates disruptions to the binder's network and thereby reduces the mechanical strength of the electrode. The pre-dispersion of both conductive additives prior to the active material resulted in a higher degree of dispersity and in the formation of web-like carbonous structures on the surface of the active particles. These electrodes display robust mechanical strength. The third procedure variation employed a dry mixing sequence comprising carbon black, the active material and a dry binder. This resulted in a slurry with markedly reduced viscosity compared to other procedures of the same composition, yet the peel strength was found to be comparable to that of the aforementioned procedure. The EDX-mapping results revealed that the electrode exhibited the highest degree of carbon dispersity across its entire surface. In accordance with the rheological data, it was postulated that this phenomenon is due to a sequence-induced carbon black coating onto the LFP particles. The absence of voluminous carbon black in the continuous phase resulted in lower viscosity values. Furthermore, the utilization of a dry mixing sequence resulted in the lowest specific energy input of the procedures.

Cell specimens derived from the aforementioned variations in the LFP mixing procedures were subjected to electrochemical testing. In the formation process, minor discrepancies in the initial cycle efficiency were discernible. However, more pronounced variations were evident in the C-rate capability tests. The procedure variations of the conductive additive sequences and the dry mixing sequence exhibited markedly inferior C-rate capability compared to the procedure that initially dispersed carbon black and added the carbon nanotubes in the final sequence. In addition, it was demonstrated that cells originating from the procedure variations were measured with a cyclability of roughly 1,000 cycles, whereas the procedure that first dispersed carbon black and lastly mixed in carbon nanotubes was calculated to reach the same capacity retention at approximately 2,000 cycles.

8.2. Outlook

In this study, a variety of experimental series comprising diverse compositions were employed to gain a comprehensive understanding of the correlation between the mixing procedure and the subsequent products, namely the slurry, the electrode, and the cell. Given the considerable time investment required for a single-factor analysis, there are numerous additional effects that warrant further investigation.

One of the current trends in the industry is the reduction of energy consumption throughout the production chain. One significant opportunity for improvement is the utilization of dry mixing sequences prior to a wet procedure. This work demonstrated that the energy consumption of the mixing procedure can be reduced, which provides a promising indication for further investigations. This was achieved using an industrially scalable mixer that is capable of providing the necessary shear force for this sequence in both wet and dry conditions. However, the scope for variation was limited, encompassing not only the machine parameters but also the compositions under investigation. Furthermore, it is well established that the utilization of a vacuum atmosphere within a dry mixing procedure markedly increases the particle-particle collision rate, thereby enhancing the effectiveness. Future studies should address these considerations when designing studies on this topic.

Given that the objective of this investigation was to establish a baseline and to gain insight into this topic, the variation in sequencing was largely limited to a relatively straightforward design of mixing procedure sequences, comprising primarily four sequences. This work revealed correlations between the anodic and cathodic compositions that have yet to be fully investigated. The high-energy input procedure resulted in the formation of anodes with markedly inferior peel strength. It is established practice to treat the SBR binder with care when mixing, yet there are white sport in literature in form of a comprehensive explanation for this behavior. With regard to the cathode, four of the five investigated mixing procedures exhibited remarkable mechanical strength, although the cell performance was deemed to be inferior to that of the procedure’s cells with the weaker mechanical strength. The combination of design considerations, for example the mixing of half of the conductive additives prior to finalization, could result in hybrid-like electrodes that exhibit both features. Also, it is unclear whether a similar behavior will be observed when utilizing different active materials, such as NMC or LMNO.

The variation of total solids content in this study was primarily focused on the limits of specific mixing procedure sequences. Nevertheless, the total solids content of the slurry may prove useful when confronted with unforeseen challenges. For instance, it is anticipated that the total solids content of the LFP slurries under investigation is sufficiently low to potentially cause issues such as drying-induced cracking of the coating on an industrial scale line speed. This may be mitigated by increasing the total solids content of the slurry, although this may have implications for the microstructure and the subsequent cell characteristics.

A significant corpus of research has been devoted to the dispersion of particular carbon blacks. In contrast, there is a paucity of literature addressing the dispersion of carbon nanotubes within a slurry. In this instance, a pre-dispersed product was employed. Nevertheless, the dispersion of dry carbon nanotubes offers tremendous economic benefits, while also presenting a number of challenging academic questions. It would be beneficial to examine the impact of utilizing dry mixing sequences that employ not only carbon nanotubes but also carbon nanofibers and graphene.

With regard to the subject of binders and mixing, numerous publications address the utilization of innovative polymers in lithium-ion cells. Nevertheless, there is a notable absence of dedicated research investigating the intricate nature of these molecules throughout the product-chain. The binder is subjected to intensive shear (mixing), then heat (drying), then deformation (calendering) and finally the potential difference within a potentiostatic cycling. It is evident that these subjects are addressed, albeit often in isolation and rarely in the context of technically relevant formulations and equipment.

The results and observations presented in this work may prove to be a useful collection of design considerations when designing electrodes out of novel materials.

9 Appendix

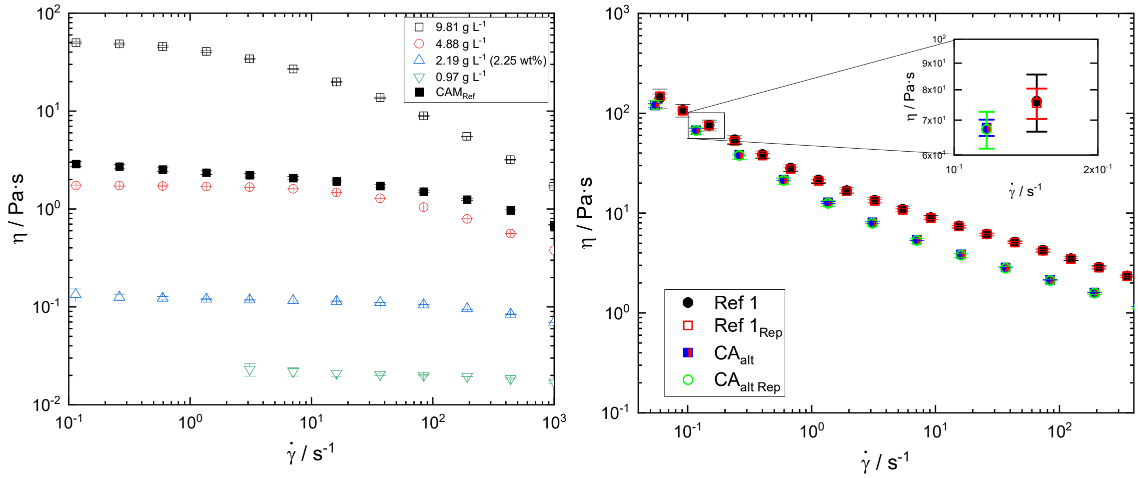

A 9-1: a) Viscosity function of PVDF solutions of various concentrations next to the flow curve of CAM$_{ref}$; b) Viscosity function of reproduced slurries, Ref 1 of Parameter-Series and CA$_{alt}$ (a.k.a. CB$_{1.5}$) of the Procedure-Series

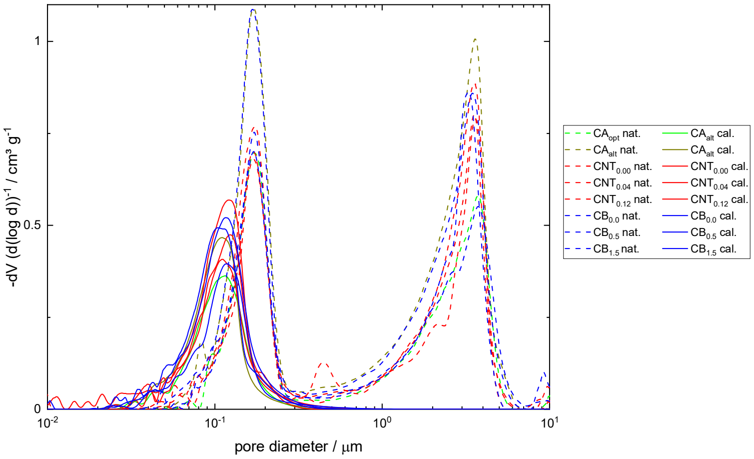

A 9-2: Mercury intrusion of CA-Series samples

A 9-3: TSC of supernatants of Kneading series 1

Sample	TSC / g g^{-1}
61L	0.08
64L	0.05
67L	0.04
70L	0.06
61H	0.05
64H	0.04
67H	0.04
70H	0.06

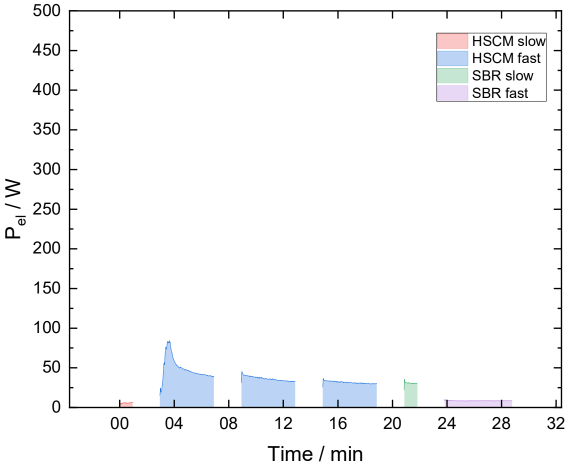

A 9-4: Total rotor power consumption for the low energy input reference P_{Low} of the Kneading-Series 2

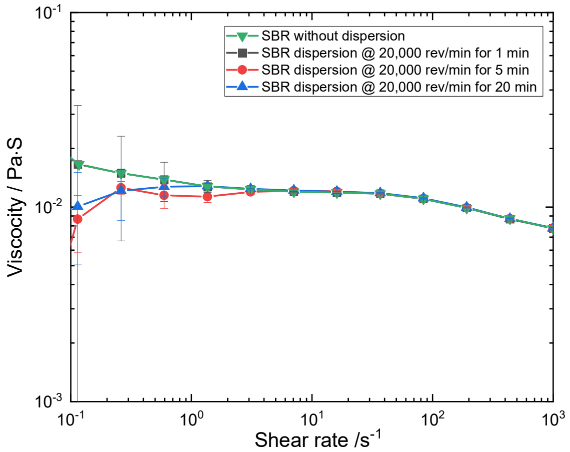

A 9-5: Viscosity function of SBR dispersion; green – without mixing; black – mixing with 20,000 rev/min for 1 min; red – mixing with 20,000 rev/min for 5 min; blue – mixing with 20,000 rev/min for 20 min; tool for dispersion: IKA T10 basic ULTRA-TURRAX (IKA-Werke GmbH & CO. KG, Staufen, Germany

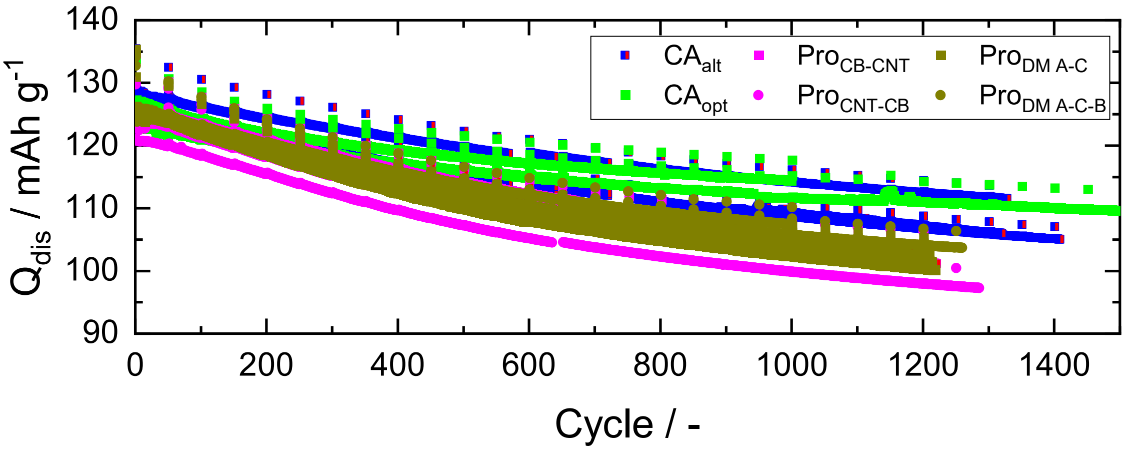

A 9-6: Charge and discharge curves of Procedure-Series cells

A 9-7: Post-measurement images of sample CB$_{0.0}$; row $\varrho_{CB_{0.0}}$ lists the columns electrode density; row i: image of current collector with the coating's remainder; row ii: top light microscope images after threshold filter application; row iii: color value spectrum of the original microscope image; row CC%: percentage of the remainder's occupied area (range 0-80)

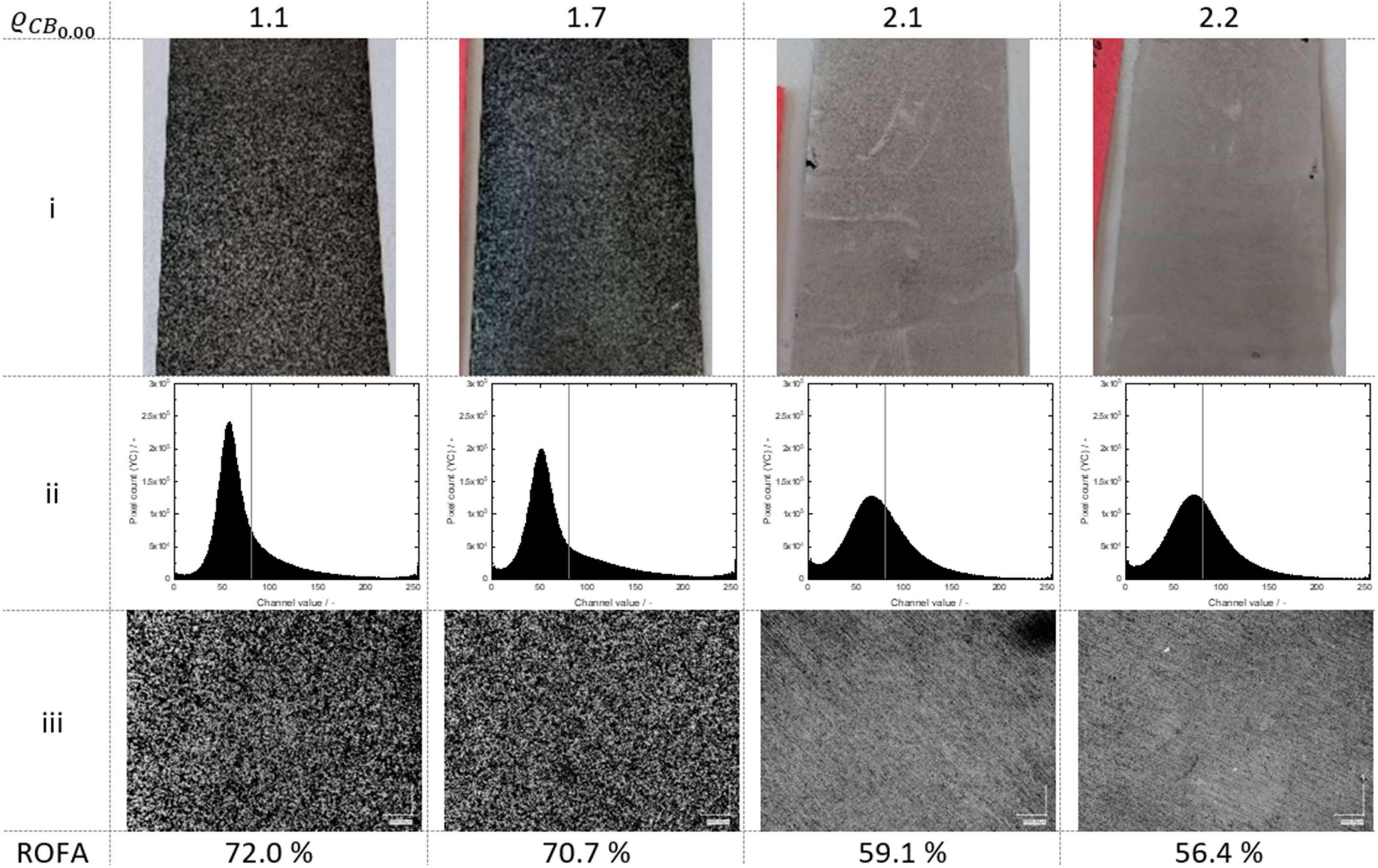

10 References

1. M. Hannan; M. Lipu; A. Hussain; A. Mohamed, A review of lithium-ion battery state of charge estimation and management system in electric vehicle applications: Challenges and recommendations*, Renewable and Sustainable Energy Reviews*, 2017, 78, 834–854.
2. M. Li; J. Lu; Z. Chen; K. Amine, 30 Years of Lithium-Ion Batteries*, Advanced Materials*, 2018, 30, e1800561.
3. M. Hannan; F. Azidin; A. Mohamed, Hybrid electric vehicles and their challenges: A review*, Renewable and Sustainable Energy Reviews*, 2014, 29, 135–150.
4. W. Budzianowski, Negative carbon intensity of renewable energy technologies involving biomass or carbon dioxide as inputs*, Renewable and Sustainable Energy Reviews*, 2012, 16, 6507–6521.
5. M. Shariq and D. Nemec, Modelling Approaches of the Dispersion Process for Conductive Slurries in Chemical Process Industries*, Advanced Engineering Materials*, 2024, 26, 2401089.
6. Thomas G. Mezger, *Das Rheologie Handbuch*. Hannover: Vincentz Network, 2016.
7. F. Morrison, *Understanding rheology*. New York: Oxford University Press, 2001.
8. R. Tanner, *Engineering rheology*. Oxford: Oxford University Press, 2002.
9. J. Mewis and N. Wagner, *Colloidal Suspension Rheology*. Cambridge: Cambridge University Press, 2011.
10. P. Hiemenz and R. Rajagopalan, *Principles of colloid and surface chemistry*. New York: Marcel Dekker Inc, 1977.
11. M. Rubinstein and R. Colby, *Polymer physics*. Oxford: Oxford University Press, 2014.
12. B. Kronberg; K. Holmberg; B. Lindman, *Surface chemistry of surfactants and polymers*. Chichester, West Sussex: Wiley, 2014.
13. C. Clasen and W.-M. Kulicke, Determination of viscoelastic and rheo-optical material functions of water-soluble cellulose derivatives*, Progress in Polymer Science*, 2001, 26, 1839–1919.
14. H. Laun, Rheological properties of aqueous polymer dispersions*, Angew. Makromol. Chem.*, 1984, 123/124, 335–359.
15. J. Melrose and R. Ball, “Contact networks” in continuously shear thickening colloids*, J. Rheol.*, 2004, 48, 961–978.
16. J. Bender and N. Wagner, Reversible shear thickening in monodisperse and bidisperse colloidal dispersions*, J. Rheol.*, 1996, 40, 899–916.
17. W. Russel; N. Wagner; J. Mewis, Divergence in the low shear viscosity for Brownian hard-sphere dispersions: At random close packing or the glass transition?*, J. Rheol.*, 2013, 57, 1555–1567.
18. A. Benchabane and K. Bekkour, Rheological properties of carboxymethyl cellulose (CMC) solutions*, Colloid and Polymer Science*, 2008, 286, 1173–1180.
19. H. Lekkerkerker; R. Tuinier; M. Vis, *Colloids and the Depletion Interaction*. Cham: Springer Nature Switzerland AG, 2024.
20. A. Garcıa; M. Culebras; M. Collins; J. Leahy, Stability and rheological study of sodium carboxymethyl cellulose and alginate suspensions as binders for lithium ion batteries*, Journal of Applied Polymer Science*, 2018, 135, 46217.
21. P. Kurzweil and O. Dietlmeier, *Elektrochemische Speicher*. Wiesbaden: Springer Fachmedien Wiesbaden GmbH, 2018.
22. A. Jossen and W. Weydanz, *Moderne Akkumulatoren richtig einsetzen*. Göttingen: MatrixMedia, 2019.
23. M. Wakihara and O. Yamamoto, *Lithium Ion Batteries: Fundamentals and Performance*. Weinheim: Wiley-VCH, 1998.
24. S. Petrovi´c, *Battery technology crash course*. Cham: Springer Nature Switzerland AG, 2021.
25. A. Wang; S. Kadam; H. Li; S. Shi; Y. Qi, Review on modeling of the anode solid electrolyte interphase (SEI) for lithium-ion batteries*, npj Comput Mater*, 2018, 4, 1–26.

26. Y. Chen; Y. Kang; Y. Zhao; L. Wang; J. Liu; Y. Li; Z. Liang; X. He; X. Li; N. Tavajohi; B. Li, A review of lithium-ion battery safety concerns: The issues, strategies, and testing standards*, Journal of Energy Chemistry*, 2021, 59, 83–99.
27. X. Zhang and T. Wierzbicki, Characterization of plasticity and fracture of shell casing of lithium-ion cylindrical battery*, Journal of Power Sources*, 2015, 280, 47–56.
28. S. Link; C. Neef; T. Wicke, Trends in Automotive Battery Cell Design: A Statistical Analysis of Empirical Data*, Batteries*, 2023, 9, 261.
29. N. Soldan Cattani; E. Noronha; J. Schmied; M. Frieges; H. Heimes; A. Kampker, Comparative Cost Modeling of Battery Cell Formats and Chemistries on a Large Production Scale*, Batteries*, 2024, 10, 252.
30. S. Zhang; T. Jow; K. Amine; G. Henriksen, LiPF6–EC–EMC electrolyte for Li-ion battery*, Journal of Power Sources*, 2002, 107, 18–23.
31. S. Kainat; J. Anwer; A. Hamid; N. Gull; S. Khan, Electrolytes in Lithium-Ion Batteries: Advancements in the Era of Twenties (2020's)*, Materials Chemistry and Physics*, 2024, 313, 128796.
32. T. Jaumann; J. Balach; U. Langklotz; V. Sauchuk; M. Fritsch; A. Michaelis; V. Teltevskij; D. Mikhailova; S. Oswald; M. Klose; G. Stephani; R. Hauser; J. Eckert; L. Giebeler, Lifetime vs. rate capability: Understanding the role of FEC and VC in high-energy Li-ion batteries with nano-silicon anodes*, Energy Storage Materials*, 2017, 6, 26–35.
33. X. Zhang; E. Sahraei; K. Wang, Li-ion Battery Separators, Mechanical Integrity and Failure Mechanisms Leading to Soft and Hard Internal Shorts*, Sci Rep*, 2016, 6, 32578.
34. Z. Zhang and P. Ramadass, Lithium-Ion Battery Separators in *Lithium-ion batteries: Science and technologies*, M. Yoshio, R. J. Brodd, and A. Kozawa, Eds., New York, NY: Springer, 2009, 1–46.
35. H. Lee; M. Yanilmaz; O. Toprakci; K. Fu; X. Zhang, A review of recent developments in membrane separators for rechargeable lithium-ion batteries*, Energy Environ. Sci.*, 2014, 7, 3857–3886.
36. S.-T. Myung; Y. Sasaki; S. Sakurada; Y.-K. Sun; H. Yashiro, Electrochemical behavior of current collectors for lithium batteries in non-aqueous alkyl carbonate solution and surface analysis by ToF-SIMS*, Electrochimica Acta*, 2009, 55, 288–297.
37. A. Frank; J. Sturm; M. Steinhardt; A. Rheinfeld; A. Jossen, Impact of Current Collector Design and Cooling Topology on Fast Charging of Cylindrical Lithium-Ion Batteries*, ECS Adv.*, 2022, 1, 40502.
38. P. Zhu; D. Gastol; J. Marshall; R. Sommerville; V. Goodship; E. Kendrick, A review of current collectors for lithium-ion batteries*, Journal of Power Sources*, 2021, 485, 229321.
39. J. Asenbauer; T. Eisenmann; M. Kuenzel; A. Kazzazi; Z. Chen; D. Bresser, The success story of graphite as a lithium-ion anode material – fundamentals, remaining challenges, and recent developments including silicon (oxide) composites*, Sustainable Energy Fuels*, 2020, 4, 5387–5416.
40. A. Padhi; K. Nanjundaswamy; J. Goodenough, Phospho-olivines as Positive-Electrode Materials for Rechargeable Lithium Batteries*, J. Electrochem. Soc.*, 1997, 144, 1188.
41. Y. Nishi, The development of lithium ion secondary batteries*, Chemical record (New York, N.Y.)*, 2001, 1, 406–413.
42. T. Tran and K. Kinoshita, Lithium intercalation/deintercalation behavior of basal and edge planes of highly oriented pyrolytic graphite and graphite powder*, Journal of Electroanalytical Chemistry*, 1995, 386, 221–224.
43. T Prem Kumar; T Sri Devi Kumari; Manuel A Stephan, Carbonaceous anode materials for lithium-ion batteries – the road ahead*, Journal of the Indian Institute of Science*, 2009, 89, 393–424.
44. M. Cermak; N. Perez; M. Collins; M. Bahrami, Material properties and structure of natural graphite sheet*, Sci Rep*, 2020, 10, 18672.
45. D. Billaud; E. McRae; A. Hérold, Synthesis and electrical resistivity of lithium-pyrographite intercalation compounds (stages I, II and III)*, Materials Research Bulletin*, 1979, 14, 857–864.

46. T. Placke; R. Kloepsch; S. Dühnen; M. Winter, Lithium ion, lithium metal, and alternative rechargeable battery technologies: the odyssey for high energy density*, J Solid State Electrochem*, 2017, 21, 1939–1964.
47. B. Boukamp; G. Lesh; R. Huggins, All-Solid Lithium Electrodes with Mixed-Conductor Matrix*, J. Electrochem. Soc.*, 1981, 128, 725–729.
48. M. Obrovac and V. Chevrier, Alloy negative electrodes for Li-ion batteries*, Chemical Reviews*, 2014, 114, 11444–11502.
49. K. Feng; M. Li; W. Liu; A. Kashkooli; X. Xiao; M. Cai; Z. Chen, Silicon-Based Anodes for Lithium-Ion Batteries: From Fundamentals to Practical Applications*, Small*, 2018, 14, 1702737.
50. Y. Jiang; G. Offer; J. Jiang; M. Marinescu; H. Wang, Voltage Hysteresis Model for Silicon Electrodes for Lithium Ion Batteries, Including Multi-Step Phase Transformations, Crystallization and Amorphization - IOPscience*, Journal of The Electrochemical Society*, 2020, 167, 130533.
51. H. Wu; G. Chan; J. Choi; I. Ryu; Y. Yao; M. McDowell; S. Lee; A. Jackson; Y. Yang; L. Hu; Y. Cui, Stable cycling of double-walled silicon nanotube battery anodes through solid-electrolyte interphase control*, Nature nanotechnology*, 2012, 7, 310–315.
52. J. Ryu; Jae Woo Kim; Y. Sung; Seung M. Oh, Failure Modes of Silicon Powder Negative Electrode in Lithium Secondary Batteries*, Electrochemical and Solid State Letters*, 2004, 7, A306-A309.
53. M. Armand; P. Axmann; D. Bresser; M. Copley; K. Edström; C. Ekberg; D. Guyomard; B. Lestriez; P. Novák; M. Petranikova; W. Porcher; S. Trabesinger; M. Wohlfahrt-Mehrens; H. Zhang, Lithium-ion batteries – Current state of the art and anticipated developments*, Journal of Power Sources*, 2020, 479, 228708.
54. E. Roduner, Size matters: why nanomaterials are different*, Chem. Soc. Rev.*, 2006, 35, 583–592.
55. J. Saint; M. Morcrette; D. Larcher; L. Laffont; S. Beattie; J.-.-P. Pérès; D. Talaga; Couzi; M.; J.-.-M. Tarascon, Towards a Fundamental Understanding of the Improved Electrochemical Performance of Silicon–Carbon Composites*, Advanced Functional Materials*, 2007, 17, 1765–1774.
56. D. Vrankovic; L. Reinold; R. Riedel; M. Graczyk-Zajac, Void-shell silicon/carbon/SiCN nanostructures: toward stable silicon-based electrodes*, Journal of Materials Science*, 2016, 51, 6051–6061.
57. Y. Yang; Y. Liu; X. Jiang; L. Zhao; P. Wang; Y. Zhang, Rational design of SiO x based anode materials for next generation lithium-ion batteries*, Mater. Adv.*, 2024, 5, 896–919.
58. W. Chen; R. Salvatierra; M. Ren; J. Chen; M. Stanford; J. Tour, Laser-Induced Silicon Oxide for Anode-Free Lithium Metal Batteries*, Advanced Materials*, 2020, 32, e2002850.
59. C. Heubner; T. Liebmann; O. Lohrberg; S. Cangaz; S. Maletti; A. Michaelis, Understanding Component-Specific Contributions and Internal Dynamics in Silicon/Graphite Blended Electrodes for High-Energy Lithium-Ion Batteries*, Batteries & Supercaps*, 2022, 5, e202100182.
60. N. Nitta; F. Wu; J. Lee; G. Yushin, Li-ion battery materials: present and future*, Materials Today*, 2015, 18, 252–264.
61. J. Molenda; A. Stoklosa; B. Tadeusz, Modification in the electronic structure of cobalt bronze LixCoO2 and the resulting electrochemical properties*, Solid State Ionics*, 1989, 36, 53–58.
62. L. Wang; J. Wang; L. Wang; M. Zhang; R. Wang; C. Zhan, A critical review on nickel-based cathodes in rechargeable batteries*, Int. J. Miner. Metall. Mater.*, 2022, 29, 925–941.
63. S. Wang; M. Yan; Y. Li; C. Vinado; J. Yang, Separating electronic and ionic conductivity in mix-conducting layered lithium transition-metal oxides*, Journal of Power Sources*, 2018, 393, 75–82.
64. S.-Y. Chung; J. Bloking; Y.-M. Chiang, Electronically conductive phospho-olivines as lithium storage electrodes*, Nature Mater*, 2002, 1, 123–128.
65. Contemporary Amperex Technology Co. Limited, *CATL Unveils Shenxing PLUS, Enabling 1,000-km Range and 4C Superfast Charging (Press release).* [Online]. Available: https://www.catl.com/en/news/6239.html (accessed: Mrz. 21 2025).

66. X. Su; S. Ha; M. Ishwait; H. Lei; M. Oljaca; B. Blizanac; D. Dees; W. Lu, Nonlinear Conductivities and Electrochemical Performances of LiNi0.5Co0.2Mn0.3O2 Electrodes*, Journal of The Electrochemical Society*, 2016, 163, A2720-A2724.
67. Q. Zhang; Z. Yu; P. Du; C. Su, Carbon nanomaterials used as conductive additives in lithium ion batteries*, Recent patents on nanotechnology*, 2010, 4, 100–110.
68. J. Baumgärtner; K. Kravchyk; M. Kovalenko, Navigating the Carbon Maze: A Roadmap to Effective Carbon Conductive Networks for Lithium-Ion Batteries*, Advanced Energy Materials*, 2024, 15, 2400499.
69. A. Mistry; S. Trask; A. Dunlop; G. Jeka; B. Polzin; P. Mukherjee; V. Srinivasan, Quantifying Negative Effects of Carbon-Binder Networks from Electrochemical Performance of Porous Li-Ion Electrodes - IOPscience*, Journal of The Electrochemical Society*, 2021, 168, 70536.
70. M. Kroll; S. Karstens; M. Cronau; A. Höltzel; S. Schlabach; N. Nobel; C. Redenbach; B. Roling; U. Tallarek, Three-Phase Reconstruction Reveals How the Microscopic Structure of the Carbon-Binder Domain Affects Ion Transport in Lithium-Ion Batteries*, Batteries & Supercaps*, 2021, 4, 1363–1373.
71. M. Chouchane; A. Rucci; T. Lombardo; A. Ngandjong; A. Franco, Lithium ion battery electrodes predicted from manufacturing simulations: Assessing the impact of the carbon-binder spatial location on the electrochemical performance*, Journal of Power Sources*, 2019, 444, 227285.
72. A. Gören; C. Costa; M. Silva; S. Lanceros-Méndez, State of the art and open questions on cathode preparation based on carbon coated lithium iron phosphate*, Composites Part B: Engineering*, 2015, 83, 333–345.
73. X. Lu; G. Lian; J. Parker; R. Ge; M. Sadan; R. Smith; D. Cumming, Effect of carbon blacks on electrical conduction and conductive binder domain of next-generation lithium-ion batteries*, Journal of Power Sources*, 2024, 592, 233916.
74. R. Dominko; M. Gaberscek; J. Drofenik; M. Bele; S. Pejovnik; J. Jamnik, The role of carbon black distribution in cathodes for Li ion batteries*, Journal of Power Sources*, 2003, 119-121, 770–773.
75. J. Mayer; L. Almar; E. Asylbekov; W. Haselrieder; A. Kwade; A. Weber; H. Nirschl, Influence of the Carbon Black Dispersing Process on the Microstructure and Performance of Li-Ion Battery Cathodes*, Energy Technol.*, 2020, 8, 1900161.
76. J. Heremans, Electrical conductivity of vapor-grown carbon fibers*, CARBON*, 1985, 23, 431–436.
77. I. Gogotisi, *Nanotubes and nanofibers*. Boca Raton, FL: CRC Taylor & Francis, 2006.
78. W. Haselrieder; B. Westphal; H. Bockholt; A. Diener; S. Höft; A. Kwade, Measuring the coating adhesion strength of electrodes for lithium-ion batteries*, International Journal of Adhesion & Adhesives*, 2015, 60, 1–8.
79. Johannes Landesfeind; Askin Eldiven; Hubert A. Gasteiger, Influence of the Binder on Lithium Ion Battery Electrode Tortuosity and Performance*, Journal of The Electrochemical Society*, 2018, 165, A1122-A1128.
80. Marcus Müller; Lukas Pfaffmann; Stefan Jaiser; Michael Baunach; Vanessa Trouillet; Frieder Scheiba; Philip Scharfer; Wilhelm Schabel; Werner Bauer, Investigation of binder distribution in graphite anodes for lithium-ion batteries*, Journal of Power Sources*, 2017, 340, 1–5.
81. N. Wang; Y. NuLi; S. Su; J. Yang; J. Wang, Effects of binders on the electrochemical performance of rechargeable magnesium batteries*, Journal of Power Sources*, 2017, 341, 219–229.
82. T. Nirmale; B. Kale; A. Varma, A review on cellulose and lignin based binders and electrodes: Small steps towards a sustainable lithium ion battery*, International Journal of Biological Macromolecules*, 2017, 103, 1032–1043.
83. S. Sung; S. Kim; J. Park; J. Park; K. Ahn, Role of PVDF in Rheology and Microstructure of NCM Cathode Slurries for Lithium-Ion Battery*, Materials*, 2020, 13, 4544.

84. D. Versaci; R. Nasi; U. Zubair; J. Amici; M. Sgroi; M. Dumitrescu; C. Francia; S. Bodoardo; N. Penazzi, New eco-friendly low-cost binders for Li-ion anodes*, Journal of Solid State Electrochemistry*, 2017, 21, 3429–3435.
85. *PFA ban proposal ECHA (Press release).* [Online]. Available: https://echa.europa.eu/de/-/echa-publishes-pfas-restriction-proposal (accessed: Jun. 11 2024).
86. D. Bresser; D. Buchholz; A. Moretti; A. Varzi; S. Passerini, Alternative binders for sustainable electrochemical energy storage - the transition to aqueous electrode processing and bio-derived polymers*, Energy Environ. Sci.*, 2018, 11, 3096–3127.
87. T. Heinze and A. Koschella, Carboxymethyl Ethers of Cellulose and Starch – A Review*, Macromolecular Symposia*, 2005, 223, 13–40.
88. B. Ghanbarzadeh; H. Almasi; A. Entezami, Physical properties of edible modified starch/carboxymethyl cellulose films*, Innovative Food Science & Emerging Technologies*, 2010, 11, 697–702.
89. S. Kim; T. Kim; Y. Kim; H. Choi; H. Lim; S. Yang; C. Park, Surface modifications for the effective dispersion of carbon nanotubes in solvents and polymers*, CARBON*, 2012, 50, 3–33.
90. C.-C. Li and Y.-S. Lin, Interactions between organic additives and active powders in water-based lithium iron phosphate electrode slurries*, Journal of Power Sources*, 2012, 220, 413–421.
91. R. Gordon; R. Orias; N. Willenbacher, Effect of carboxymethyl cellulose on the flow behavior of lithium-ion battery anode slurries and the electrical as well as mechanical properties of corresponding dry layers*, J Mater Sci*, 2020, 55, 15867–15881.
92. J. Li; R. Lewis; J. Dahn, Sodium Carboxymethyl Cellulose*, Electrochem. Solid-State Lett.*, 2007, 10, A17.
93. Z. Karkar; D. Guyomard; L. Roué; B. Lestriez, A comparative study of polyacrylic acid (PAA) and carboxymethyl cellulose (CMC) binders for Si-based electrodes*, Electrochimica Acta*, 2017, 258, 453–466.
94. F. Jeschull; F. Scott; S. Trabesinger, Interactions of silicon nanoparticles with carboxymethyl cellulose and carboxylic acids in negative electrodes of lithium-ion batteries*, Journal of Power Sources*, 2019, 431, 63–74.
95. H. Buqa; M. Holzapfel; F. Krumeich; C. Veit; P. Novák, Study of styrene butadiene rubber and sodium methyl cellulose as binder for negative electrodes in lithium-ion batteries*, Journal of Power Sources*, 2006, 161, 617–622.
96. J. Park; N. Willenbacher; K. Ahn, How the interaction between styrene-butadiene-rubber (SBR) binder and a secondary fluid affects the rheology, microstructure and adhesive properties of capillary-suspension-type graphite slurries used for Li-ion battery anodes*, Colloids and Surfaces A: Physicochemical and Engineering Aspects*, 2019, 579, 123692.
97. S. Lim; S. Kim; K. Ahn; S. Lee, The effect of binders on the rheological properties and the microstructure formation of lithium-ion battery anode slurries*, Journal of Power Sources*, 2015, 299, 221–230.
98. K. Habeeb Rahiman, G. Unnikrishnan, A. Sujith, C.K. Radhakrishnan, Cure characteristics and mechanical properties of styrene–butadiene rubber/acrylonitrile butadiene rubber*, Materials Letters*, 2005, Pages 633-639.
99. K. Hofmann; A. Hegde; X. Liu-Theato; R. Gordon; A. Smith; N. Willenbacher, Effect of mechanical properties on processing behavior and electrochemical performance of aqueous processed graphite anodes for lithium-ion batteries*, Journal of Power Sources*, 2024, 593, 233996.
100. Hawley; W. Blake; J. Li, Electrode manufacturing for lithium-ion batteries—Analysis of current and next generation processing*, Journal of Energy Storage*, 2019, 25, 100862.
101. Q. Feng; Y. Miyai; H. Kanoh; K. Ooi, Lithium(1+) extraction/insertion with spinel-type lithium manganese oxides. Characterization of redox-type and ion-exchange-type sites*, Langmuir*, 1992, 8, 1861–1867.

102. I. Shkrob; J. Gilbert; P. Phillips; R. Klie; R. Haasch; J. Bareño; D. Abraham, Chemical Weathering of Layered Ni-Rich Oxide Electrode Materials: Evidence for Cation Exchange*, J. Electrochem. Soc.*, 2017, 164, A1489-A1498.
103. S. Roberts; L. Chen; B. Kishore; C. Dancer; M. Simmons; E. Kendrick, Mechanism of gelation in high nickel content cathode slurries for sodium-ion batteries*, Journal of Colloid and Interface Science*, 2022, 627, 427–437.
104. N. Lingappan; L. Kong; M. Pecht, The significance of aqueous binders in lithium-ion batteries*, Renewable and Sustainable Energy Reviews*, 2021, 147, 111227.
105. S. Radloff; R.-G. Scurtu; G. Carbonari; M. Hölzle; T. Diemant; M. Bozorgchenani; F. Klein; M. Wohlfahrt-Mehrens, Mitigating water-induced surface degradation in water-based Ni-rich Li-ion battery electrodes*, Journal of Power Sources*, 2023, 580, 233314.
106. A. Kwade; W. Haselrieder; R. Leithoff; A. Modlinger; F. Dietrich; K. Droeder, Current status and challenges for automotive battery production technologies*, Nature Energy*, 2018, 3, 290–300.
107. M. Bouguern; Madikere Raghunatha Reddy, Anil Kumar; X. Li; S. Deng; H. Laryea; K. Zaghib, Engineering Dry Electrode Manufacturing for Sustainable Lithium-Ion Batteries*, Batteries*, 2024, 10, 39.
108. S. Wecker; T. Davidson; D. Baker, Preferred orientation of crystallites in uniaxially deformed polytetrafluoroethylene*, J. Appl. Phys.*, 1972, 43, 4344–4348.
109. D. Shin; J. Nam; C. Linh Nguyen; Y. Jo; K. Lee; S. Hwang; Y.-J. Kim, Design of densified nickel-rich layered composite cathode via the dry-film process for sulfide-based solid-state batteries*, J. Mater. Chem. A*, 2022, 10, 23222–23231.
110. X. Wang; S. Chen; K. Zhang; L. Huang; H. Shen; Z. Chen; C. Rong; G. Wang; Z. Jiang, A Polytetrafluoroethylene-Based Solvent-Free Procedure for the Manufacturing of Lithium-Ion Batteries*, Materials*, 2023, 16, 7232.
111. Y. Wang; J. Zhang; J. Xue; K. Zhang; L. Wen; G. Liang, Effect of particle dispersion on the properties of LiFePO4 slurry and the electrochemical properties of the battery*, Ionics*, 2022, 28, 1547–1558.
112. Q. Zhao; X. Li; Z. Shao; C. Liu; R. Zevenhoven, Effects of Tween 80 dispersant on LiFePO4/C cathode material prepared by sonochemical high-temperature ball milling method*, Ionics*, 2019, 25, 5565–5573.
113. J. Lee; P. Kumar; G. Lee; B. Moudgil; R. Singh, Electrochemical performance of surfactant-processed LiFePO4 as a cathode material for lithium-ion rechargeable batteries*, Ionics*, 2013, 19, 371–378.
114. H. Rumpf, Beanspruchungstheorie der Prallzerkleinerung*, Chemie Ingenieur Technik*, 1959, 31, 323–337.
115. W. Bauer; D. Nötzel; V. Wenzel; H. Nirschl, Influence of dry mixing and distribution of conductive additives in cathodes for lithium ion batteries*, Journal of Power Sources*, 2015, 288, 359–367.
116. J. Park; S. Kim; K. Ahn, Role of carboxymethyl cellulose binder and its effect on the preparation process of anode slurries for Li-ion batteries*, Colloids and Surfaces A: Physicochemical and Engineering Aspects*, 2023, 664, 131130.
117. D. Liu; L.-C. Chen; T.-J. Liu; T. Fan; E.-Y. Tsou; C. Tiu, An Effective Mixing for Lithium Ion Battery Slurries*, Advances in Chemical Engineering and Science*, 2014, 4, 515–528.
118. H. Nakajima; T. Kitahara; Y. Higashinaka; Y. Nagata, Effect of Electrode Mixing Conditions on the Performance of Lithium-Ion Batteries Analyzed by Fast Fourier Transform Electrochemical Impedance Spectroscopy*, ECS Trans.*, 87–95.
119. K. Kim; W. Jeon; S. Chang, Effect of mixing sequences on the electrode characteristics of lithium-ion rechargeable batteries*, Journal of Power Sources*, 1999, 83, 108–113.
120. M. Wang; D. Dang; A. Meyer; R. Arsenault; Y.-T. Cheng, Effects of the Mixing Sequence on Making Lithium Ion Battery Electrodes*, J. Electrochem. Soc.*, 2020, 167, 100518.

121. E. Tang; R. Chua; Y. Cai; Y. Guo; W. Chong; S. Winardi; T. Soh; R. Chaudhary; M. Srinivasan, Rheological Studies of LiNi 0.6 Mn 0.2 Co 0.2 O 2 -Based Slurry for the Development of Energy Dense Li-Ion Applications, *J. Electrochem. Soc.*, 2024, 171, 20518.
122. M. TAKENO; S. KATAKURA; K. MIYAZAKI; T. ABE; T. FUKUTSUKA, Relation between Mixing Processes and Properties of Lithium-ion Battery Electrode-slurry, *Electrochemistry*, 2021, 89, 585–589.
123. K. Kuratani; K. Ishibashi; Y. Komoda; R. Hidema; H. Suzuki; H. Kobayashi, Controlling of Dispersion State of Particles in Slurry and Electrochemical Properties of Electrodes, *J. Electrochem. Soc.*, 2019, 166, A501-A506.
124. K. Huber; A. Adam; D. Grießl; A. Kwade, Understanding slurry mixing effects on the fast charging capability of lithium-ion battery cells: Methodology and case study, *Journal of Power Sources*, 2022, 536, 231455.
125. K. Konda; S. Moodakare; P. Kumar; M. Battabyal; J. Seth; V. Juvekar; R. Gopalan, Comprehensive effort on electrode slurry preparation for better electrochemical performance of LiFePO4 battery, *Journal of Power Sources*, 2020, 480, 228837.
126. M. Schmitt; M. Baunach; L. Wengeler; K. Peters; P. Junges; P. Scharfer; W. Schabel, Slot-die processing of lithium-ion battery electrodes—Coating window characterization, *Chemical Engineering and Processing: Process Intensification*, 2013, 68, 32–37.
127. S. Kistler and P. Schweizer, *Liquid Film Coating*. Dordrecht: Springer Netherlands, 2012.
128. N. Pallas and Y. Harrison, An automated drop shape apparatus and the surface tension of pure water, *Colloids and Surfaces*, 1990, 43, 169–194.
129. K. Ruschak, Limiting flow in a pre-metered coating device, *Chemical Engineering Science*, 1976, 31, 1057–1060.
130. ITU-R, Parameter values for the HDTV standards for production and international programme exchange "Rec. ITU-R BT.709-6", *Electronic Publication, Geneva, 2015*, 2015.
131. C. Seidl; S. Thieme; M. Frey; K. Nikolowski; A. Michaelis, Comparison of Electronic Resistance Measurement Methods and Influencing Parameters for Lmfp and High-Nickel Ncm Cathodes, *Batteries*, 2024, 10, 105.
132. H.-G. Schweiger; O. Obeidi; O. Komesker; A. Raschke; M. Schiemann; C. Zehner; M. Gehnen; M. Keller; P. Birke, Comparison of several methods for determining the internal resistance of lithium ion cells, *Sensors*, 2010, 10, 5604–5625.
133. H. Bockholt; W. Haselrieder; A. Kwade, Intensive Dry and Wet Mixing Influencing the Structural and Electrochemical Properties of Secondary Lithium-Ion Battery Cathodes, *ECS Transactions*, 2013, 50, 25–35.
134. Henrike Bockholt; Wolfgang Haselrieder; Arno Kwade, Intensive powder mixing for dry dispersing of carbon black and its relevance for lithium-ion battery cathodes, *Powder Technology*, 2016, 297, 266–274.
135. M. Wang; K. Uzun; B. Frieberg; J. Hu; A. Li; X. Huang; Y.-T. Cheng, Influence of Mixing Process on the Performance of Electrodes Made by a Dry Coating Method, *J. Electrochem. Soc.*, 2023, 170, 10541.
136. A. Wang; C. Chen; L. Liao; J. Qian; F.-G. Yuan; N. Zhang, Enhanced β-Phase in Direct Ink Writing PVDF Thin Films by Intercalation of Graphene, *Journal of Inorganic and Organometallic Polymers and Materials*, 2020, 30, 1497–1502.
137. A. Ribeiro; R. Marques; A. Guastaldi; de Carvalho Campos, João Sinézio, Hydroxyapatite deposition study through polymeric process on commercially pure Ti surfaces modified by laser beam irradiation, *J Mater Sci*, 2009, 44, 4056–4061.

138. J.-T. Lee; Y.-J. Chu; F.-M. Wang; C.-R. Yang; C.-C. Li, Aqueous processing of lithium-ion battery cathodes using hydrogen peroxide-treated vapor-grown carbon fibers for improvement of electrochemical properties*, Journal of Materials Science*, 2007, 42, 10118–10123.
139. Peipei Su, Haitao Zhang, Lipeng Yang, Chunxian Xing, Shanshan Pan, Wei Lu, Suojiang Zhang, Effects of conductive additives on the percolation networks and rheological properties of LiMn0.7Fe0.3PO4 suspensions for lithium slurry battery*, Chemical Engineering Journal*, 2022, 433, 133203.
140. Gaikwad AM and Arias A. C., Understanding the Effects of Electrode Formulation on the Mechanical Strength of Composite Electrodes for Flexible Batteries - PubMed*, ACS Appl Mater Interfaces*, 2017, 9, 6390–6400.
141. M. Weber; R. Moschner; A. Kwade, Modifying the Network Structures of High Energy Anodes for Lithium-Ion Batteries through Intensive Dry Mixing*, Energy Technol.*, 2022, 11, 2200852.
142. N. Billot; T. Günther; D. Schreiner; R. Stahl; J. Kranner; M. Beyer; G. Reinhart, Investigation of the Adhesion Strength along the Electrode Manufacturing Process for Improved Lithium-Ion Anodes*, Energy Technology*, 2019, 8, 1801136.
143. G. Apachitei; M. Hidalgo; D. Dogaru; M. Lain; R. Heymer; J. Marco; M. Copley, Optimisation of Industrially Relevant Electrode Formulations for LFP Cathodes in Lithium Ion Cells*, Batteries*, 2023, 9, 192.
144. G. Liu; H. Zheng; S. Kim; Y. Deng; A. Minor; X. Song; V. Battaglia, Effects of Various Conductive Additive and Polymeric Binder Contents on the Performance of a Lithium-Ion Composite Cathode - IOPscience*, Journal of The Electrochemical Society*, 2008, 155.
145. J. Vogel; J. Sederholm; E. Shumway; Gabriel J. Abello; S. Trask; D. Wheeler; B. Mazzeo, Li-Ion Battery Electrode Contact Resistance Estimation by Mechanical Peel Test - IOPscience*, Journal of The Electrochemical Society*, 2022, 169, 80508.
146. G.-W. Lee; J. Ryu; W. Han; K. Ahn; S. Oh, Effect of slurry preparation process on electrochemical performances of LiCoO2 composite electrode*, Journal of Power Sources*, 2010, 195, 6049–6054.
147. D. Grießl; A. Adam; K. Huber; A. Kwade, Effect of the Slurry Mixing Process on the Structural Properties of the Anode and the Resulting Fast-Charging Performance of the Lithium-Ion Battery Cell*, Journal of The Electrochemical Society*, 2022, 169, 20531.
148. D. Grießl; K. Huber; R. Scherbauer; A. Kwade, Dispersion kinetics of carbon black for the application in lithium-ion batteries*, Advanced Powder Technology*, 2021, 32, 2280–2288.
149. A. Barai; K. Uddin; W. Widanage; A. McGordon; P. Jennings, A study of the influence of measurement timescale on internal resistance characterisation methodologies for lithium-ion cells*, Sci Rep*, 2018, 8, 1–13.
150. B. Bitsch; N. Willenbacher; V. Wenzel; S. Schmelzle; H. Nirschl, Einflüsse der mechanischen Verfahrenstechnik auf die Herstellung von Elektroden für Lithium-Ionen-Batterien*, Chem. Ing. Tech.*, 87, 2015, 466–474.
151. P. Novák; W. Scheifele; M. Winter; O. Haas, Graphite electrodes with tailored porosity for rechargeable ion-transfer batteries*, Journal of Power Sources*, 1997, 68, 267–270.
152. C. Clasen and W. Kulicke, Determination of viscoelastic and rheo-optical material functions of water-soluble cellulose derivatives*, Progress in Polymer Science*, 2001.
153. M. Pahl, *Mischen und Rühren*. Weinheim: Wiley-VCH, 2007.
154. M. Ndour; J.-P. Bonnet; S. Cavalaglio; T. Lombard; M. Courty; L. Aymard; C. Przybylski; V. Bonnet, The formulation of a CMC binder/silicon composite anode for Li-ion batteries: from molecular effects of ball milling on polymer chains to consequences on electrochemical performances*, Mater. Adv.*, 2022, 3, 8522–8533.
155. E. Soares, Review of mechanical degradation and de-aggregation of drag reducing polymers in turbulent flows*, Journal of Non-Newtonian Fluid Mechanics*, 2020, 276, 104225.

156. K. Park; S. Myeong; D. Lee; H. Yoo; J. Kim; C. Kim; J. Kim; S. Sun; J. Kwon; S. Kim; K. Lee; C.-W. Cho; U. Paik; T. Song, Improved Li-ion kinetics of the anode by kneading process of binder for lithium-ion batteries with high energy density, *Electrochimica Acta*, 2023, 464, 142900.
157. L. Ouyang; Z. Wu; J. Wang; X. Qi; Q. Li; J. Wang; S. Lu, The effect of solid content on the rheological properties and microstructures of a Li-ion battery cathode slurry, *RSC Adv.*, 2020, 10, 19360–19370.
158. J.-H. Lee; U. Paik; V. Hackley; Y.-M. Choi, Effect of Carboxymethyl Cellulose on Aqueous Processing of Natural Graphite Negative Electrodes and their Electrochemical Performance for Lithium Batteries, *Journal of The Electrochemical Society*, 2005, 152, A1763-A1769.
159. M. Ishii and H. Nakamura, Influence of molecular weight and concentration of carboxymethyl cellulose on rheological properties of concentrated anode slurries for lithium-ion batteries, *JCIS Open*, 2022, 6, 100048.
160. S. Spiegel; T. Heckmann; A. Altvater; R. Diehm; P. Scharfer; W. Schabel, Investigation of edge formation during the coating process of Li-ion battery electrodes, *J Coat Technol Res*, 2022, 19, 121–130.